Properties of dijets in pp, pPb and PbPb collisions

by

Doga C. Gulhan

Submitted to the Department of Physics
in partial fulfillment of the requirements for the degree of

Doctor of Philosophy in Physics

at the

MASSACHUSETTS INSTITUTE OF TECHNOLOGY

February 2016

Signature redacted

Author .....
Department of Physics
Jan 28, 2016

Signature redacted

Certified by .....
Gunther Roland
Professor
Thesis Supervisor

Signature redacted

Accepted by .....
Nergis Mavalvala
Associate Department Head

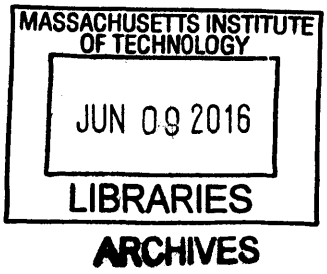

Properties of dijets in pp, pPb and PbPb collisions

by

Doga C. Gulhan

Submitted to the Department of Physics
on Jan 28, 2016, in partial fulfillment of the
requirements for the degree of
Doctor of Philosophy in Physics

Abstract

Two dijet measurements, one using 35 pb^{-1} pPb data at $\sqrt{s_{\text{NN}}} = 5.02$ TeV, and another with 166 μb^{-1} PbPb and 5.3 pb^{-1} pp data at $\sqrt{s_{\text{NN}}} = 2.76$ TeV collected with CMS detector at the LHC, are presented. In pPb collisions, the dijet p_{T} ratios, azimuthal angle differences and pseudorapidity distributions are measured and compared to PYTHIA and PYTHIA+HIJING simulations as well as NLO QCD predictions for the latter observable. No significant signs of final state interactions, such as a decrease in the mean dijet p_{T} ratios or a broadening in the correlation of the dijets in azimuthal angle, with increasing forward activity, are observed. The dijet pseudorapidity distributions are also measured, and are sensitive to nuclear PDFs for x values of $0.001 - 0.5$. Selections on event activity are found to yield unexpected centrality biases on dijet pseudorapidity distributions, which aided the interpretation of similar biases seen in inclusive jet measurements by ATLAS. In PbPb collisions, a detailed scan of charged particle distributions in correlation with the dijet system is carried out. The p_{T} projection of charged particles on the dijet axis is measured at different distances of $\Delta = \sqrt{(\eta_{\text{trk}} - \eta_{\text{jet}})^2 + (\phi_{\text{trk}} - \phi_{\text{jet}})^2}$ with respect to the leading and subleading jet axes. In this way, the spectra and angular distribution of the additional particles, which recover the overall event balance in dijet events with enhanced p_{T} asymmetry in PbPb compared to pp collisions, are obtained up to $\Delta = 1.8$ in steps of 0.2. A significant excess of low p_{T} particles associated with a subleading jet at large Δ values is observed, and this excess is shown to get larger for dijet events with p_{T} asymmetry. The scan is carried out for variety of anti-k_{T} R parameters, which provides a way of varying jet width and fragmentation. Medium response to jet quenching at wide angles for jets with different fragmentation is studied. Only an insignificant increase of the magnitude of low p_{T} particle excess at large angles, but a significant increase in the modification of the balance distribution close to the jet axes is observed by increasing R.

Thesis Supervisor: Gunther Roland
Title: Professor

Acknowledgments

To be a member of relativistic heavy ion group at MIT has been a very rewarding experience. I would like to thank Gunther Roland for welcoming me, the condensed matter theory student who had no idea about what was going on, to join the group and being my mentor through the years. With his trust, and with him pushing the limits I was able to leave behind each difficult step one by one and go further. He opened several doors for me and encouraged me to work on non-experimental projects. I was very lucky to have an overlapping time with Yen-Jie for the first year and half of my time at CERN, which gave me an unequal chance to ask him tons of questions. I owe him much of what I know today. Working with him over the past four years has been very fulfilling thanks to his excitement in physics and his endless energy. To Wit, thank you for asking "Why?" and make me step back and think. Thanks Bolek for watching out for us and trying to improve our working environment. Thanks to Ivan and Christof for sparing time to listen to me given how busy they are making sure we get data to analyse, and special thanks to George for his help with the writing process. I received a lot of support from our post-docs to whom I look up to, Camelia, Gian-Michele, Krisztian, and Yue Shi, and my comrade grad students Dragos, Alex, Mukund, Austin, Chris, Kaya, Ta-Wei, Jing and Bi Ran. Special thanks to Chris and Austin for two years of blood, sweat, and tears, that made missing p_{T} analysis possible. Thanks Dragos, for teaching me the basics when I first started working in this group, and his help over the years and during the graduation process. I am proud to be a part of the CMS Collaboration have a chance to use our excellent detector and collaborate with several talented physicists, special thanks to Eric, Matt, Yetkin and Stas.

Thanks to Krishna I had the opportunity to be a member of the Hybrid collaboration. I spent valuable time with him, Jorge, Guilherme and Dani. Over this time I gained new perspectives and familiarity with the theorist's approach to questions. Hybrid collaboration is the most friendly collaboration, and I am a lucky experimentalist, to have colleagues to whom I can ask questions after reading a new theory paper

and getting very confused. I had a similar experience collaborating with Guilherme and Nestor. I appreciate the attention of Guilherme and Nestor to our measurement, and the smart and simple explanation they came up with.

I would like to thank here to everyone who sacrificed a part of their soul to support me in the process. A lot came from my family, friends, and people I love. I was very lucky to be surrounded by wonderful people, and I hope that they all know how much I appreciate having them.

Contents

Chapter 1

Overview

The main focus of our field, ultra-relativistic heavy ion collisions, is to study the properties of quark gluon plasma (QGP), a strongly coupled color charged medium. QGP is the only form of plasma that exists in the universe in which interactions are described by a non-Abelian quantum field theory. We start this thesis with a description of QGP in Chapter 2. In heavy-ion collisions QGP is rapidly expanding and lives only for a very short time before turning into ordinary QCD matter, but long enough to create observable effects on jet production. To understand what happens inside QGP, we present some information on color confined QCD matter in Chapter 3. In this chapter jet properties in vacuum and properties of the nuclei in the initial state of the collisions are described. Jets in vacuum form a baseline to study jet quenching, i.e., modification by their interactions in the medium. Jet quenching measurements and theory are discussed in Chapter 4.

The aim of this document is to put two specific dijet measurements (one in pPb collisions, and the other in PbPb with a comparison to pp collisions) in context and present technical details involved in the analyses of the data. The measurements are carried out with the CMS, detector. The layout and compontents of the detector are presented in Chapter 5. In Chapter 6 we describe how to select collision events in PbPb, pPb and pp collisions. In addition selection of events with different impact parameters is discussed. In PbPb collisions, classification of events according to activity distinguishes collisions with different overlap areas between colliding nuclei.

A similar classification was attempted in pPb collisions. Definition of centrality of collisions in pPb and PbPb collisions are also described in Chapter 6. Dijet selection is also presented in this chapter, while the merit in studying dijet properties and the basic observables that can be constructed with dijets is discussed in Chapter 7.

In collisions with large overlap between Pb nuclei $\approx 1k$ binary collisions take place and tens of thousands of particles are produced, therefore standard reconstruction algorithms used by other physics groups in CMS do not work. The reconstruction algorithms for tracks and jets used in heavy ion collisions are described in Chapter 8, and their performance is presented in comparison to the standard reconstruction algorithm used in pp and pPb collisions in the same chapter.

Chapter 9 includes results of the measurements in pPb collisions, which are taken from Ref. [110]. A model explaining the kinematic biases seen in the results of CMS and ATLAS on jets in pPb is described in the same chapter, and is taken from [47]. While, Chapter 10 contains the analysis of dijets in PbPb collisions and is taken from Ref. [167], with additional discussion on fluctuations and corrections used for reconstruction biases. Conclusions of these analyses are discussed in the chapters they are presented and later summarized in Chapter 11.

In addition to the work presented here, I worked in developing a hybrid strong/weak coupling model for jet quenching described in Refs. [78, 79].

Chapter 2

Quark gluon plasma

Quark gluon plasma(QGP) is a term that was initially coined for a hypothetical state of matter with very similar properties to electromagnetic plasma with the difference that the electric charges are replaced with color charges [206]. In this plasma the color charges were expected to be weakly interacting as a result of asymptotic freedom. Therefore, the term QGP was first used for a gas of color charges. The measurements at RHIC revealed different properties for the form matter created in heavy ion collisions. The first measurements at RHIC showed that this new form of matter behaves almost as a perfect liquid[23, 30, 54, 4]. The original idea, that at high temperature there can be no hadrons because of the large number of quarks and gluons in what would be the volume of hadrons, is still true, but the interactions between these turned out to be different than what was expected. A medium in which color charges are interacting with a strong coupling is formed at large energy densities obtained in heavy ion collisions and we now call this liquid QGP. [1]

Below we give a summary of what is known about QGP, including key experimental observations and theoretical framework used in studying its properties.

[1]However, due to differences between the observed medium and the initial usage of "QGP", we will sometimes refer to the deconfined color charged liquid formed in the collision of nuclei simply as the "medium". These two terms will be used interchangeably to refer to the same thing.

2.1 Phase Diagram

The QCD phase diagram is unique, as QCD matter is the only way to study a non-Abelian gauge theory interactions in bulk at non-zero temperatures and densities. The phase diagram of QCD in the 2D plane of temperature and baryon chemical potential is shown in Fig 2-1. The QGP that is created in collisions at accelerators has low chemical baryon potential, shown as white lines in Fig. 2-1. As the collision energies increase chemical baryon potential gets smaller and T gets larger, which makes us closer to what universe is believed to be filled with shortly after big-bang. In early universe QGP had much higher T than what can be reached at accelerators, and it sits effectively on the limit of 0 baryon chemical potential. Apart from ordinary hadrons and QGP a third form of QCD matter is predicted, which might be observed in neutron stars, called color super conductor [33].

As measured in lattice QCD calculations, when the chemical potential is close to zero, the phase transition from hadrons to QGP is a cross-over transition, i.e. there are no discontinuities in any thermodynamical quantity. As stated in the white paper of STAR, "the possible absence of a first- or second-order phase transition reduces hopes to observe some well-marked changes in behavior that might serve as an experimental "smoking gun" for a transition to a new form of matter"[23]. In Fig. 2-2, the change in P/T^4 as a function of T is shown. In the ideal gas limit, one obtains the Stephan-Boltzmann expression for pressure,

$$\frac{P_{SB}}{T^4} = \frac{\pi^2}{90}\left(2(N_c^2 - 1) + \frac{7}{2}N_c N_f\right), \tag{2.1}$$

where N_c and N_f are the number of color charges and flavors, respectively. Therefore, P/T^4 is expected to show the increase in number of degrees of freedom by switching from a hadronic state to partonic state. The Stephan-Boltzman limit is indicated on Fig. 2-2 as arrows, and one can see that LQCD calculations are not yet at this limit even at $T = 600MeV$. The conclusion is that the partons are still interacting in QGP and can not to be treated as an ideal gas. However the sharp turn on in P/T^4 is a sign in increase in degrees of freedom and so a crossover in to QGP, which occurs

at $T_c \approx 150 - 170$ MeV [59, 40]. In fact, the medium created in heavy-ion collisions behaves like an ideal fluid, as demonstrated by the phenomenon of collective flow observed first by RHIC experiments [23, 30, 54] and discussed in the next section.

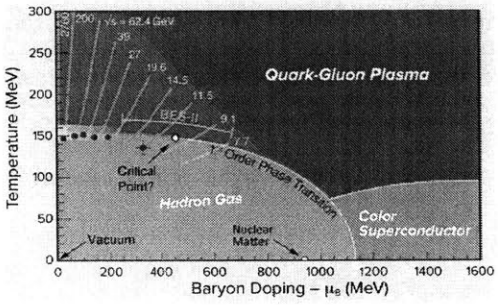

Figure 2-1: QCD matter phase diagram [147]

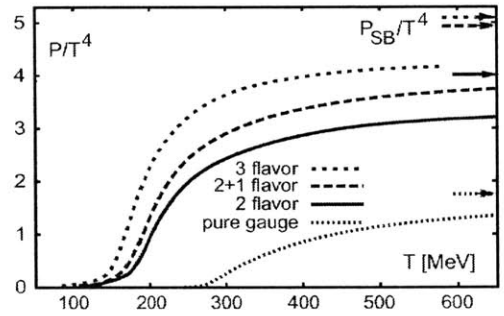

Figure 2-2: LQCD calculation from Ref. [192] for P/T^4 as a function of T.

2.2 Collective flow

Collective flow refers to the fact that particles pointing in the direction of the event plane, spanned by beam direction and impact vector as depicted in the cartoon left panel of Fig. 2-3, are enhanced. This is due to the modulation of the transverse pressure gradient, where the gradient is larger when the thickness of the medium the smaller, creating a flow of particles in the direction of this large pressure gradient. Collective flow produces a pattern that is flat across large η ranges, as at each longitudinal direction the particles are correlated with the event plane, which is a global

event property. Because of the fact that particles at different η have similar azimuthal modulation, flow can be observed in the dependence of the yield of pairs of particles on the azimuthal angle difference $\Delta\phi$ between them.

The correlation functions of pairs of particles are calculated in the 2D $\Delta\phi$ and $\Delta\eta$ plane. An example distribution for events where the nuclei overlap region is elliptic is shown for low p_{T} particle correlations (associated particle has $1 < p_{\mathrm{T}} < 1.5$ GeV) in the right panel of Fig. 2-3. A peak is observed in the region when particle pairs are aligned in both ϕ and pseudorapidity η, due to the jets in the event, sitting on top of a modulation in ϕ, which is flat in η. In order to avoid being sensitive to jet production, collective flow is studied at large $\Delta\eta$. [2] The medium modulation due to elliptic initial geometry has the functional form of $\cos(2\Delta\phi)$.

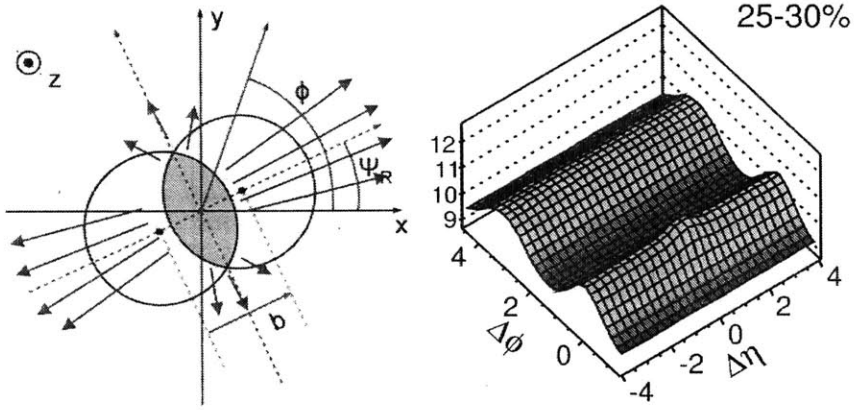

Figure 2-3: (Left) Event plane is shown as Ψ_{R} where beam direction z, and impact parameter are marked. The red arrows which denote the pressure gradient are not drawn according to scale, but are just a representation of the flow effect. Modified version of a figure in Ref. [102] (Right) Taken from Ref. [95], showing the correlation function for $3 < p_{\mathrm{T}}^{\mathrm{trig}} < 3.5$ and $1 < p_{\mathrm{T}}^{\mathrm{assoc}} < 1.5$ for 25-30 % centrality events, see Chapter 6 for definition of centrality classes.

The collective flow does not only result from an elliptic modulation in the initial overlap area, the modulation could also be triangular or tetragonal, etc., but the el-

[2]Note that this removes the effect of correlations of jet particles that belong to the same jet, but as jets are correlated in angle as well when they originate from the same hard scattering process, they can create azimuthal angle variations of particle distributions and this has to be taken into account.

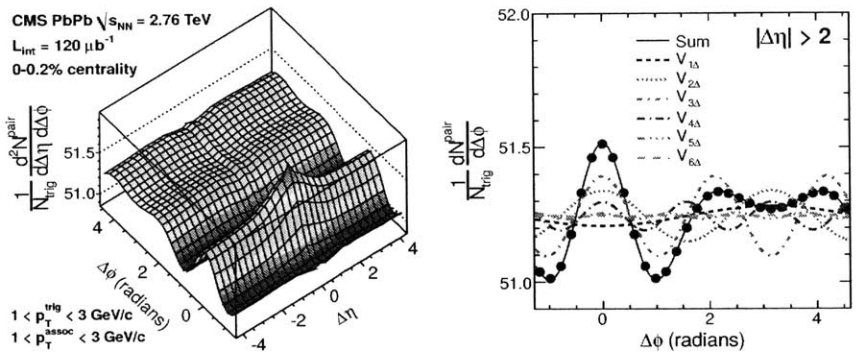

Figure 2-4: The 2D (left) and 1D $\Delta\phi$ (right) dihadron correlation functions for particles with $1 < p_T < 3$ GeV in $0.0 - 0.2\%$ central PbPb collisions at $\sqrt{s_{NN}} = 2.76$ TeV. The solid lines on the right panel show various orders of $V_{n\Delta}$, while the dashed line is the sum of all $V_{n\Delta}$ components. [109]

liptic shape usually dominates over the rest of the modulations because lead nuclei are approximately spherical in shape, unless a very central collision is considered, where elliptic modulation is suppressed. The correlation function for very small impact parameter collisions is shown in Fig. 2-4. The $\Delta\phi$ modulation at large $\Delta\eta$ can be decomposed into its Fourier components as given below:

$$\frac{1}{N_{\rm pair}}\frac{dN_{\rm pair}}{d\Delta\phi} = \frac{1}{2\pi}\big(1 + \sum_n 2V_{n\Delta}cos(n\Delta\phi)\big), \tag{2.2}$$

The two particle correlation decomposition is related to the coefficients, v_n for single particles which can be obtained by correlating each particle to the event plane, as $v_n = \sqrt{V_{n\Delta}}$

The first measurements were the calculation of v_2. Today, a lot more is known about the properties of the medium and it has passed several tests for hydrodynamics such as the higher order flow coefficients extracted from n-particle correlations, their dependence on p_T and mass of particles and centrality. The biggest next step has been the realisation of the importance of initial quantum fluctuations in the flow properties of each event, and the existence of v_3. Perfect spherical potentials colliding would not produce any $v_{\rm odd}$ components. However event-by-event initial state fluctuations can create triangular eccentricities, ϵ_3 which result in v_3 components in two particle

correlations. A generalized form of the eccentricities can be written as

$$\epsilon_n = \frac{\sqrt{\langle r^2_{\rm part} cos(n\phi_{\rm part})\rangle^2 + \langle r^2_{\rm part} sin(n\phi_{\rm part})\rangle^2}}{r^2_{\rm part}}, \tag{2.3}$$

where $r_{\rm part}$ and $\phi_{\rm part}$ are polar coordinates of participating nucleons.

Although, one it is explained it looks obvious, if the initial state fluctuations were washed out in the evolution of the medium it wouldn't have been possible to observe any v_3 components. The fact that fluctuations at initial collision geometry can still be observed after medium evolution indicates that the medium is very close to a perfect fluid, with minimal dissipation occuring as it flows

Flow in pp and pPb: Although collective flow is one of the strongest evidence of a discovery of a new medium, there are still remaining questions after the observation of flow in small systems at LHC by CMS, ATLAS and ALICE, pp [164], pPb[11, 18, 104], and later confirmed by RHIC in dAu and HeAu collisions [27, 22, 28]. This means that either a similar medium is formed in pPb collisions which is described well by hydrodynamics [224, 133], or initial state effects such as color condensation that are also present in pPb collisions are responsible for part of the flow effect observed in PbPb collisions [132]. Indeed, the two effects can be combined as discussed in Ref. [69]. The definition of initial state determines how much hydro has to contribute, as the eccentricities depend on the description of initial state and flow contribution has to cover for the observed flow coefficients in data. In general the observation of flow in smaller systems draw attention to better description of initial state geometry, and pre-equilibrium phase of evolution of QGP in heavy-ion collisions. These are discussed in the next section as well.

2.3 Dynamics of the medium

The dynamics of the medium formed in heavy ion collisions at very short times right after the collision are not very well understood. However, the rest of the medium evolution is well described by the hydrodynamics of relativistic fluids. The medium

is observed to be very close to ideal fluid, but the most accurate numerical hydrodynamics calculations are for viscous medium and they solve second order equations of motion. After the T falls below T_c, QGP turns into a gas of hadrons, which interact until the kinetic freeze-out temperature is reached.

2.3.1 Hydrodynamical evolution

Hydrodynamics of relativistic ideal fluid: The space time evolution of QCD matter is determined by conservation laws. In the ideal fluid approximation with zero viscosity, these are

$$\begin{aligned} \partial_\mu T^{\mu\nu}_{ideal} &= \partial_\mu\big((\epsilon + P)u^\mu u^\nu - P g^{\mu\nu}\big) = 0, \\ \partial_\mu J^\mu &= \rho \partial_\mu u^\mu = 0, \end{aligned} \tag{2.4}$$

where $T^{\mu\nu}$ is the energy momentum tensor, J^μ the baryon current. In the middle expressions these are written in terms of time-like flow 4-vector u^μ, energy density ϵ, baryon density ρ, and pressure P. The equations are to be solved for P, where P is a function of ρ and ϵ. With the assumptions of boost invariant expansion and a homogeneous medium in the transverse plane Eq. 2.4 can be solved analytically [62]. Boost invariant expansion is called as Bjorken expansion as he was the first to come up with a solution at this approximation.

Hydrodynamics at finite viscosity: The first order expression for the equations of motion at finite viscosity is given by the Navier-Stokes formalism [203]:

$$T_1^{\mu\nu} = T^{\mu\nu}_{ideal} + S^{\mu\nu}, S^{\mu\nu} = \eta\big(\nabla^\mu u^\nu + \nabla^\nu u^\mu - \frac{2}{3}\Delta^{\mu\nu}\nabla_\alpha u^\alpha\big), \tag{2.5}$$

These equations are simple but they result in numerical instabilities. Therefore, second order expansions are needed. These equations are rather lengthy, so they are not included here, but for further reading refer to [160, 221, 58].

Numerical hydro frameworks: Numerical hydro frameworks are needed to treat the transverse profile of the initial matter density and it's dynamics properly, and to incorporate event-by-event differences in the initial collision geometry. A group of hydro frameworks assume Bjorken expansion, and solve the medium evolution only in transverse plane and time, these hydro frameworks are called 2+1D hydro. Boost invariant Bjorken expansion is a valid approximation up to certain pseudorapidity ranges. The $dE_T/d\eta$ is flat up to $|\eta| < 2$ at RHIC decreasing by a factor of 2 at $\eta \approx 3.5$[53] and flat up to $|\eta| < 2.5$ at LHC decreasing by a factor of ≈ 2 at $|\eta| \approx 4$[99]. Keeping the Bjorken expansion and only modeling the transverse plane, successful hydrodynamic frameworks can be developed in 2+1D [211, 210]. However experimental data deviates from these calculations when forward measurements are done. Therefore the state-of-art hydrodynamics models are in 3+1D including the longitudinal dynamics as well [203, 161].

Apart from numerically solving the equations of state for viscous fluid dynamics at second order, these frameworks need two more ingredients, an event-by-event initial state generator that describes the evolution of the medium before the equilibrium is reached, and a description of what happens after the temperature goes below T_c. The description of pre-equilibrium dynamics differs from model to model. Moreover the evolution has to be terminated to simulate the hadronization once the T goes below T_c, this step is called the freeze-out.

Extracting viscosity values: The η/s values is one of the parameters of equations of motion and is given as input to hydro simulations. Experimental results are compared to hydrodynamics calculations with different η/s values to find the one matching the properties of the medium. It is found that using more than just v_2 but all the higher order flow coefficients and the correlations between them it is possible to significantly narrow down the range of allowed values. An example comparison of hydro simulations to data is shown in Fig. 2-5. The value extracted at RHIC and LHC energies is $\approx 0.08 - 0.12$ and $\approx 0.16 - 0.20$, respectively [144, 153]. These are surprisingly close to the limit obtained by string theory calculations $(\eta/s)_{AdS/CFT} = 1/4\pi$

[170].

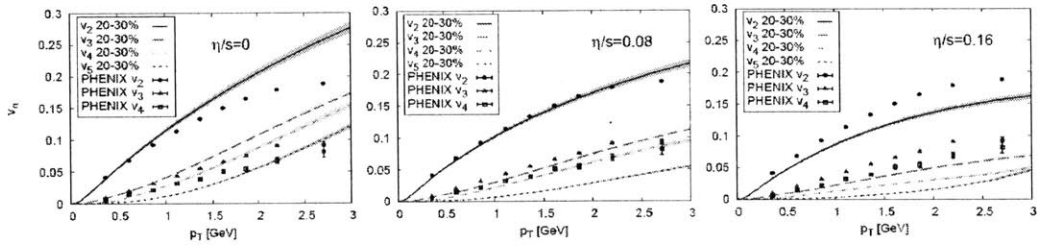

Figure 2-5: Taken from Ref. [202], v_2, v_3 and v_4 as a function of p_T for different η/s values used in 3+1D hydro simulation MUSIC.

2.3.2 Hydrodynamization

The pre-equilibrium phase of the medium evolution in heavy ion collisions is modelled commonly by two different approaches by interfacing numerical hydrodynamics with modelling the multi-particle production using Color Glass Condensate [148] and evolving it with Glasma gluon field solutions [145, 201], or by using the energy density obtained from numerical relativity solutions to AdS/CFT [218, 81, 112] before the equilibrium.

The length of pre-equilibrium phase, can be calculated in different ways. In weak coupling calculations that use turbulent flow thermalization is reached at $t_{\text{ther}} \approx 2$ fm/c[60]. In strong coupling calculations, not the thermalization time, but instead the time it takes for the the stress-energy tensor to converge to that of ideal fluid with viscous corrections is calculated, the time this occurs is called the hydrodynamization time[115]. Hydrodynamization is reached at much earlier times $t_{\text{hydro}} \approx 0.02$ fm/c [81]. One does not necessarily have to reach a thermal equilibrium for numerical hydrodynamics calculations to be applicable. In Ref. [172] a perturbative calculation of hydrodynamization time is found to yield $\lesssim 1$ fm/c, in agreement with the strong coupling approach.

Whether the initial state hydrodynamic calculations assume is the true initial state of the collisions is still an open question, but the answer of this question might

not have a big effect on experimental observables such as v_n as discussed in Ref. [187]. However, in Ref. [201] the lumpiness of initial geometry is shown to have larger effect on flow coefficients and eccentricities. The v_n and ϵ_2 values for different initial states that were used in Ref. [201] are shown in Fig. 2-6. The flow coefficients are used in the extraction of η/s from data, and therefore, the dependence of these on initial conditions reflect the uncertainty of the extracted viscosity value.

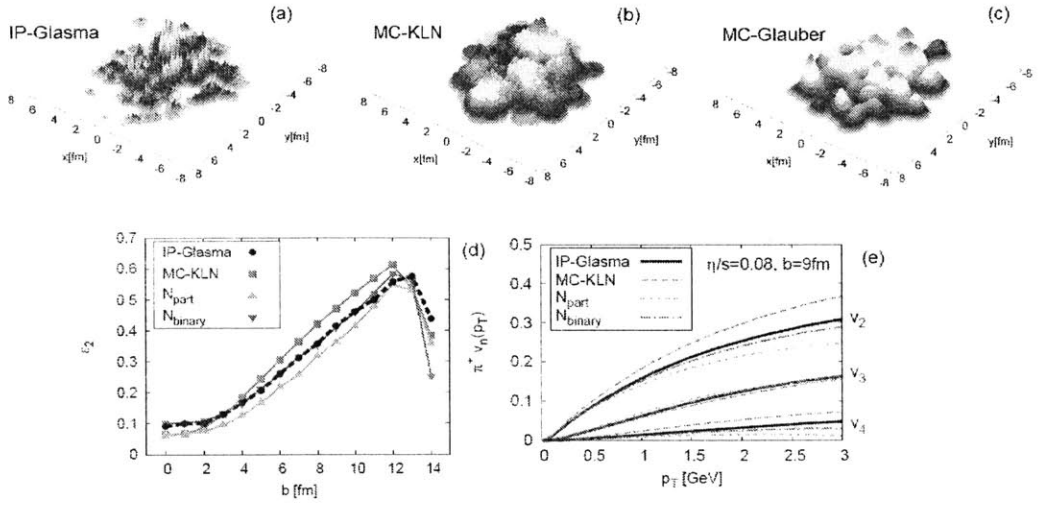

Figure 2-6: Elipticity (panel (d)) and v_n values (panel (e)) for different initial states (panels (a-c)) [201]

2.3.3 Freeze-out

After T falls below the temperature needed for color charges to exist in a deconfined state, hadronization takes place and QGP turns into a gas of hadrons. The conversion to hadrons is referred to as chemical freeze-out, taking place at temperature $T_{\rm chem}$, the hadron gas continues to interact elastically as a gas of hadrons, until the kinetic freeze-out temperature $T_{\rm kin}$ is reached.

Relative particle anti-particle production: Using statistical thermal model, in which one uses the generalized partition function at a fixed chemical freeze-out temperature, $T_{\rm ch}$, and baryon chemical potential, $\mu_{\rm B}$, the relative yields for particle

anti-particle production for different particle species can be calculated and compared to each other. Here the particle species are not assumed to change after chemical freeze-out. The particle ratios are sensitive to T_{ch} and are in good agreement with experimental results[38]. This procedure can be used to extract $T_{\rm ch}$ and $\mu_{\rm B}$, at RHIC the values correspond to $155 - 160$ MeV and $20 - 26$ MeV. At LHC T values are slightly higher, although compatible with no change, $156 - 164$ and baryon chemical potential values are significantly lower $0 - 1$ MeV [212, 17].

2.4 Quarkonia:

In hadronic collisions, the leading order process for the formation of heavy quark and anti quarks is in pairs, these pairs get dissociated by interactions with the medium and get unbound and lose their energy to it. The probability for them to stay bound increases as for more tightly bound mesons and as the radius of the meson gets smaller than the color screening radius of the medium, which is anti proportional to T.[39]

The yield of tightly bound $\rm Q\bar{Q}$ states such as Υ(1S) with binding energy of 1.10 GeV gets less suppressed in the medium with respect to vacuum compared to loosely bound Υ(2S) and Υ(3S), with binding energies of 0.54 and 0.20 GeV respectively. The larger suppression in quarkonia states with smaller binding energies, e.g. as in the case of three Υ upsilon states as shown in Ref. [100], is called sequential melting.

Similar behavior in pPb: As in the case of collective flow recent measurements from pPb run at LHC, showed that similar structure in suppression of quarkonia states has been observed in pPb collitions. This raises question marks about the interpretation of the same structure in PbPb in accordance with existence of QGP. The dependence of yields of $\Upsilon(2S)/\Upsilon(1S)$ on event activity, which is proportional to the size of the medium at least in PbPb collisions, is shown in Fig. 2-7.

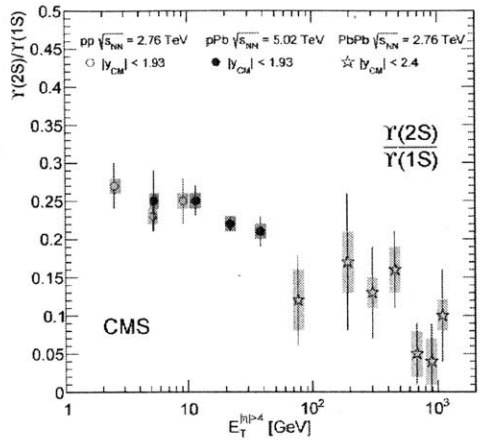

Figure 2-7: Yield ratios for $\Upsilon(2S)$ and $\Upsilon(1S)$ in pp, pPb and PbPb collisions as a function of activity in the event, which is assumed to correlate to the size of the medium produced in the collision [106]

2.5 Jet quenching:

Jet quenching is related to the modification of jets inside the medium as a result of interactions of partons that make up the jet with the color charged medium. Analyses presented in Chapters 9 and 10 are related to jet quenching. Therefore this discussion is left for Chapter 4, where we cover the subject in great detail. However, it is important to note in this context that unlike heavy quark sequential melting and flow no jet quenching is observed in smaller systems such as pPb, dAu or HeAu collisions. The effect might too small to observe, because effects of jet quenching build up over path length and in small systems the path length might not be large enough to see a turn on of these effects even if a small medium exists.

2.6 Photon spectrum

Thermal photons emitted in medium escape without further interactions as they only interact with electromagnetic interactions with the medium. However, these photons are emitted from all stages of collisions which evolves through different T as the medium expands and cools off [205]. The radial flow of the medium modifies the

spectrum of photons resulting higher T values. In addition, it has been observed that around T_c there is an enhancement of photon production and also that a significant fraction of photons comes from the pre-equilibrium and hadronic phases. Therefore, it is only possible to measure an effective temperature and not the T of the medium at its core. T_{eff}, at RHIC is extracted to be $221 \pm 19 \pm 19$ MeV for AuAu collisions and at LHC 304 ± 51 for PbPb collisions. They are above T_c by a significant margin therefore even taking into consideration all the complications it is a convincing sign of formation of QGP.[205, 219]

2.7 Chiral symmetry restoration

At T values above T_c chiral symmetry of quarks are predicted to be restored, in the chiral limit this produces a second order phase transformation more information of this phase can be found in Refs. [193, 143, 59]. A hope for marking a direct signature of phase transition to QGP, is the possibility to mark this transition by large fluctuations in relative abundance of charged and neutral pions only if the transition were far from equilibrium[194]. This has not yet been observed, which is consistent with the hydrodynamization of the medium.

Chapter 3

Jets in vacuum

Jets are remnants of highly virtual colour charged particles (quarks and gluons which are referred to as partons [1] when no distinction is made). High p_{T} partons turn into a spray of colour neutral particles as a result of QCD confinement that does not allow on shell color charges to exist. They turn into mature jets by showering into other partons and hadronize in $\approx 10^{-22}$ s. Parton shower formation is a perturbative process in which partons split into pair of partons and this happens several times successively, converting a single parton to a shower of partons. The splitting probability is given by DGLAP evolutions and is explained in Section 3.1.

When a single parton produces several partons the virtuality of each of these partons gets smaller. The coupling constant gets larger by going down in virtuality, and there comes a time that color charges cannot exist on their own, but they polarize the vacuum to create a pair of color charges and getting bound to one of these to neutralize (note that this picture is not completely realistic as when perturbation theory fails it is not possible to define the production of two partons). This process is called hadronization. Hadronization is a non perturbative process and models of hadronization are discussed in Section 3.4.

The association of a spray of color neutral particles to a color charge of interest

[1] Partons are representations of fundamental fields in perturbative QCD. Due to negative sign of β function of QCD, coupling constant is small at asymptotically high energies and at low energies it gets large and perturbative expansions can no longer be applied. Therefore, partons lose their physical meaning

is done through jet clustering algorithms which recognize the spiky patterns in geometrical distribution of momentum and group hadronic descendants of color charged parton into a single object. In Section 3.6, various jet clustering algorithms are discussed. The definition of jet depends on the clustering algorithm and using different clustering algorithms produce different jets. This is because a parton is not a well-defined particle: it radiates other partons with low momentum (infrared divergence), and in the same direction as itself (collinear divergence). Moreover, the radiation happens probabilistically. The jet definition is needed to overcome this ambiguity. There are commonly agreed criteria by experts in the field on how a jet should be defined [158] (taken from Ref. [196]):

1. Simple to implement in an experimental analysis,

2. Simple to implement in theoretical calculations,

3. Defined at any order of perturbation theory,

4. Yields finite cross sections at any order of perturbation theory,

5. Yields a cross section that is relatively insensitive to hadronization.

More than a single jet algorithm can satisfy all the needs above, but to overcome the ambiguity, a jet should be defined in a manner that provides the best sensitivity to the physics process that is under investigation. This usually means that one would like to calculate the cross-section of a certain matrix element that includes partons in some of its end products. As an example, for inclusive jet measurement the clustering algorithm should be sensitive to p_{T} of single partons while in hadronic Z decay measurements the aim is to increase the Z yield over the QCD dijet background and have a good quality mass peak. This requires sensitivity to the invariant mass of the two partons that the Z decays to instead of the p_{T} of a single parton. It turns out that these two measurements are performed better using different jet algorithms[196].

Although, what we said so far makes jets seem like monsters, as you can see in event display from ALEPH shown in Fig. 3-1, in many cases it is possible very

simple to spot jets in an event. At the LHC, energies jets are more collimated and therefore form even narrower structures. The difficulty at hadron colliders like LHC is the existence of several simultaneous interactions (Multi-Parton Interactions, MPI). Each of these interactions produce partons but with smaller energy scales. In e^+e^- colliders it is easier to define jets when a single QCD interaction is taking place.

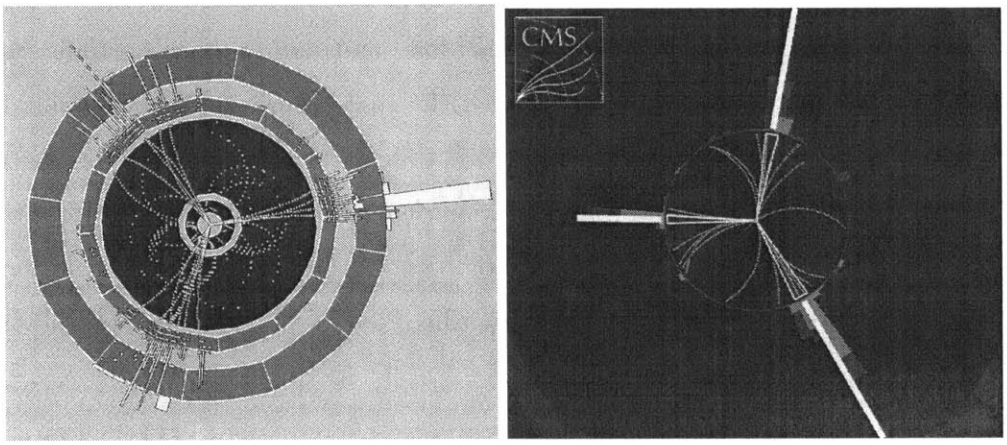

Figure 3-1: Event display from ALEPH experiment showing Z->3jet decays.[3]

3.1 QCD Factorization

Although jet evolution involves non-perturbative terms, thanks to the factorization of scales in QCD, it is possible to calculate cross-sections, hard scattering processes, and partonic shower formation of jets using perturbative QCD and then include the non-perturbative effects, the dependence of which on momentum scales are obtained from data, with convolution of these perturbative calculations with probability distribution functions.

The cross-section for a hard scattering QCD process in hadronic collisions, where a parton i with x_1 in hadron h_1 and a parton j with x_2 in hadron h_2 interact with a virtuality scale of Q_2 to produce a final state X, can be factorized into hard and soft scales at factorization scale of μ_F:

$$\sigma^{h_1 h_2 \to X}(p_1, p_2) = \sum_{i,j} f_i^{h_1}(x_1, (\mu_F)^2) \otimes f_j^{h_2}(x_2, (\mu_F)^2) \\ \otimes \sigma^{ij \to k}(x_1 p_1, x_2 p_2, \mu_F^2, Q^2) \otimes D_{k \to X}(z, \mu_F^2), \tag{3.1}$$

Here f_i and f_j are parton distribution functions (PDFs) of the hadrons that collide, $\sigma^{ij \to k}$ is the perturbative cross section for partons i and j to produce partonic state k, and $D_{k \to X}$ is the fragmentation function (FF) that describes the probability of production of X from parton k.

Both parton distributions and fragmentation depend on the probability for a parton k to split into partons l and m with momentum fractions z and $(1 - z)$, and a transverse momentum k_{T} with respect to the direction of k . The rate for splitting diverges as k_{T} goes to 0,

$$dw^{k \to l+m} = \frac{\alpha_s}{4\pi} \frac{d^2 k_{\mathrm{T}}}{dk_{\mathrm{T}}^2} dz P_{lk}(z), \tag{3.2}$$

where the $P_{lk}(z)$ are the splitting functions, which explain the splitting probabilities of partons to produce two other partons. The dependence of the splitting probability on k_{T} explains the collimated nature of jets. The splitting of a quark into a gluon and a quark happens with a different likelihood compared to the splitting of a gluon into a quark and anti-quark, or the splitting of a gluon into two gluons:

$$\begin{aligned} P_{\mathrm{q} \to \mathrm{qg}}(z) &= C_F \frac{1 + z^2}{1 - z}, \\ P_{\mathrm{g} \to \mathrm{gg}}(z) &= C_A \frac{(1 - z(1 - z))^2}{z(1 - z)}, \\ P_{\mathrm{g} \to \mathrm{q\bar{q}}}(z) &= T_R(z^2 + (1 - z)^2), \end{aligned} \tag{3.3}$$

In the above equation $C_F = 4/3$, $C_A = 3$, and $T_R = 1/2$. Notice that $\mathrm{g} \to \mathrm{q\bar{q}}$ is negligible compared to other processes for small z, as it does not diverge. Apart from these differences in factors and z dependencies, the divergence of Eq. 3.2 is very similar to QED. Parton evolution and its similarity to QED is discussed in detail

in Chapter 17 of Ref. [191]. It is handled in a similar way where NLO amplitudes cancel the singularities in LO terms, and the singularities can be factorized from the hard scattering amplitudes and combined with non-perturbative parton distributions instead. In analogy with QED: "The singular terms supply the kernel of an evolution equation for the parton distributions as a function of the logarithm of the momentum scale. Hard scattering with a momentum transfer Q probes the electron at a distance of order Q^{-1}. When the electron wavefunction is resolved to very small scales, it appears as a constituent electron, carrying only a fraction of the total longitudinal momentum, plus a number of constituents that carries a substantial fraction of the total electron momentum can initiate a hard scattering process. Precisely the same logic applies to the calculation of QCD cross sections. The contributions from the region of collinear gluon and quark emission should be associated with the parton distribution functions rather than with the hard scattering cross sections. If we make this association, we find that the parton distributions are no longer independent of the momentum Q that characterizes the hard scattering process; rather they now evolve logarithmically with Q."

In the quark-parton model the PDFs and FFs become independent of Q^2, $f_i(x, Q^2) \rightarrow f_i(x)$. This scaling is called Bjorken scaling. Although it does not look very accurate, for certain x ranges as indicated by the flatness of sets of points shown in Fig. 3-2, this scaling is violated due to the fact that when probed with large energies a particle turns into several particles as explained above. This is also the reason why PDFs are related to splitting probabilities. The space-like splittings describe the Q^2 evolution of PDFs, while time-like splittings describe the evolution of parton fragmentation into multiple partons (which is also called as parton showers).

Although, perturbative calculations allow to calculate the evolution of parton distributions in Q^2, at the low Q^2 region they are not applicable, so PDFs and FFs include non-perturbative physics. Therefore, parton distributions require input from data as boundary conditions. Given the boundary conditions at a factorization scale, their dependence on virtuality is described by Dokshitzer-Gribov-LipatovAltarelli-Parisi (DGLAP) equations:

$$\mu_F^2 \frac{\partial f_i(x,\mu_F^2)}{\partial \mu_F^2} = \sum_j \frac{\alpha_s(\mu_F^2)}{2\pi} \int_x^1 \frac{dz}{z} P_{ij}(z) f_j(\frac{x}{z}, \mu_F^2),$$
$$\mu_F^2 \frac{\partial D_i(x,\mu_F^2)}{\partial \mu_F^2} = \sum_j \frac{\alpha_s(\mu_F^2)}{2\pi} \int_x^1 \frac{dz}{z} P_{ij}(z) D_j(\frac{x}{z}, \mu_F^2), \tag{3.4}$$

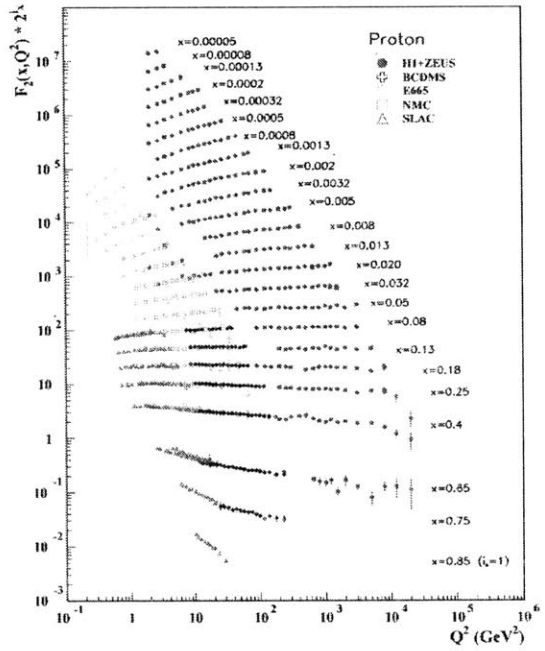

Figure 3-2: Taken from [136]: The proton structure function F_p^2 measured in electromagnetic scattering of electrons and positrons on protons (collider experiments H1 and ZEUS for $Q^2 > 2$ GeV^2), in the kinematic domain of the HERA data, and for electrons (SLAC) and muons (BCDMS, E665, NMC) on a fixed target

3.2 Color coherence

As partons are not well-defined objects the splitting of one parton into two can also be ambiguous. A more meaningful question is therefore, when do the two daughter partons start to behave as two separate sources of radiation? Assume that a g splits into a $q\bar{q}$ connected with color separated by an angle Θ from each other. We would like to know when the $q\bar{q}$ would radiate a gluon of transverse momentum $k_\perp$. The

transverse wavelength of this gluon is $1/k_\perp$ and its formation time is given as $t_f = k/k_\perp^2$. If $t_f\Theta$, i.e. the separation of the $q\bar{q}$ pair from each other at the end of the formation time of the gluon, is smaller than the transverse wavelength of the radiated gluon, then such radiation is cancelled by destructive interference and the $q\bar{q}$ pair acts as a single emitter. Therefore, large angle radiation happens first, two color charges radiate a gluon at larger angles than their separation as a single emitter, meaning that the color charge splitting happens after the radiation of gluon [83].

3.3 Parton disbribution functions

The PDFs describe the probability to find a parton i inside a particle a, with parton i carrying a fraction x of the total a momentum (Bjorken x) at a hard interaction scale of Q^2. As partons in vacuum only exist inside hadrons, they are crucial to understand QCD interactions and are involved in any experimental measurement. Measuring the PDFs is the focus of deep-inelastic scattering (DIS) experiments, where the inner charge structure of a hadron a (often a proton) is probed by a high energy electron beam. The electron creates a virtual photon (or weak bosons) transferring part of its energy to one of the partons in the a. The parton is knocked off and a breaks up forming hadrons. The values of x and Q^2, can be calculated with information at hand on kinematics of each collision. How to do so is described in "Structure Functions" review of Ref. [136].

Different collaborations generate global fits to QCD measurements independently from each, including DIS data from $e^{\pm}p$ collisions and more, such as asymmetry in rapidity of W boson production, rapidity distribution of Z bosons and inclusive jet production in $p\bar{p}$ collisions [173], to extract PDFs for species of quarks and gluons at a fixed energy scale ≈ 1 GeV/c, which can be evolved in Q^2 using DGLAP equations (See Section 3.1). Different sets of PDFs can be used to compare to data, in order to test the assumptions made during the fitting process. These fits were initially done based on LO perturbative calculations, later NLO order results have been established[173, 180] and recently there has been developments in moving forward in

NNLO PDFs[146, 181]. At NLO and NNLO it has been observed that at low Q^2, and x range there are instabilities caused by gluon radiation [214], and PDFs take negative values at these kinematics ranges, making an interpretation in terms of probability of finding a parton with given properties inside a hadron less applicable. In the analysis presented in Chapter 9, NLO CT10 PDF has been used, which is shown in Fig. 3-3 for different parton species. In the low x region, gluons dominate over valence quarks. The peak position of x value of valence quarks is slightly below 0.3. If quark-parton model was true these distributions would peak at $1/3$, but due to the momentum carried by gluons and sea quarks it happens at lower values.

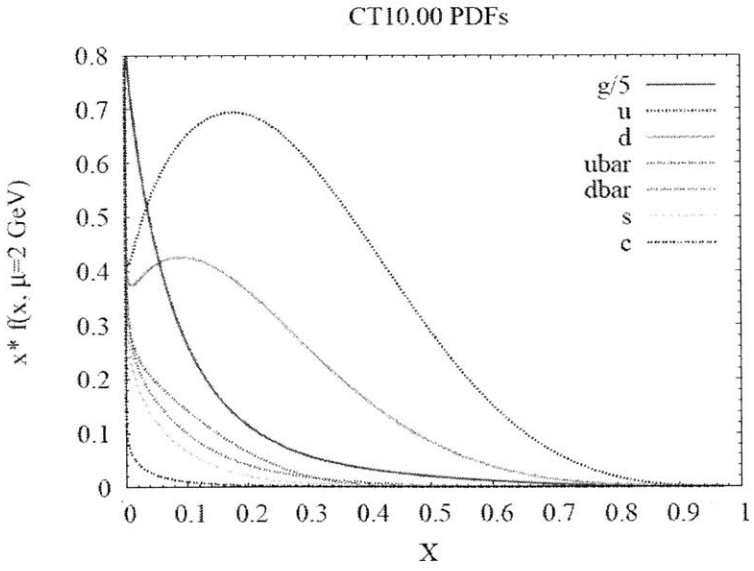

Figure 3-3: Parton distribution functions in the central fit for a scale of $Q^2 = 85 \times 85$ GeV^2 [2, 173].

3.3.1 Nuclear parton distribution functions

Inside the nucleus the interactions between nucleus effect the parton distributions inside the nucleons. The probability of finding a parton inside the nucleons of the nucleus at a given x is different than the probability of doing so for a free nucleon. The modification of PDFs for bound nucleons in nuclei (nuclear PDF - nPDF) is

observed as (i) suppression of low x partons, shadowing region, (ii) enhancement of partons with moderate x values, anti-shadowing region, (iii) suppression of large x partons, EMC region, and (iv) enhancement of very high x partons, inside the nucleus compared to proton. The regions become apparent when the ratio of nPDF and proton pPDF is calculated, $R_i^A(x,Q^2) = f_i^A(x,Q^2)/f_i^p(x,Q^2)$. In Fig. 3-4, R_u^{Pb}, R_d^{Pb} and R_g^{Pb} are shown, as can be seen from their dependence on x, the regions correspond approximately $x < 10^{-2}$, $10^{-2} < x < 10^{-1}$, $10^{-1} > x$. The plotting range is chosen to go up to $x = 0.5$ due to low statistics used to generate these figures, so Fermi region is not visible.

Nuclear parton distribution functions are mostly constrained by DIS experiments on heavy nuclei. In addition to data from DIS, measurements in pA collisions can also add constraining power on nPDFs, e.g. for EPS09 nPDF which is compared to data in Chapter 9 Drell-Yan dilepton production and pion production in pA collisions have also been used[134]. The data allows to constrain the on shell partons rather well. However, there are very large uncertainties for gluon PDFs. For $Q^2 = 2$ GeV/c, the uncertainty on gluon PDFs are as large as 40 % in the shadowing region and 50 % in the EMC region.

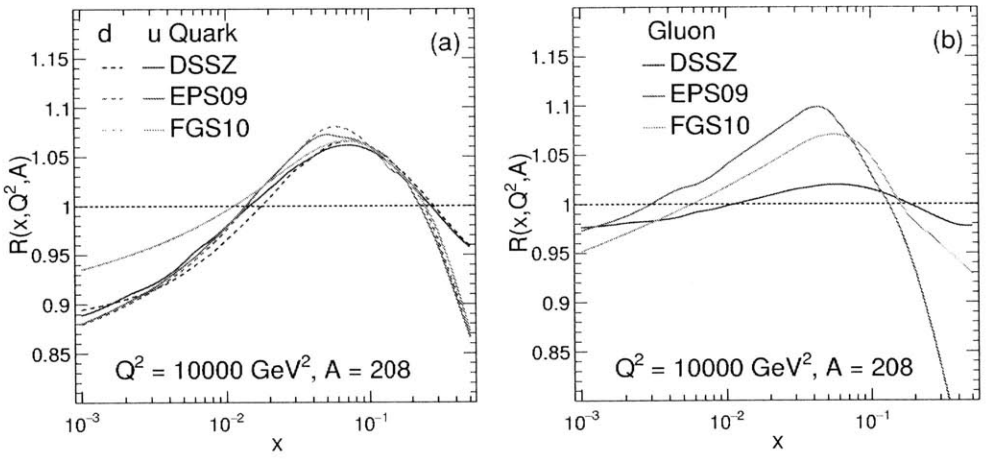

Figure 3-4: Ratio of nuclear PDFs and proton PDFs for global fits to data from different collaborations, DSSZ [127], EPS [134], FGS [141] for (panel (a)) u and d quarks, (panel (b)) gluons. Generated using Ref. [43].

Shadowing: Shadowing is a result of multiple scatterings of hadronic fluctuations of a virtual photon with several nucleons [45]. The inner nucleons are "shadowed" by the nucleons at the exterior. The cross-section of a projectile with a nucleus can be written as an expansion in the number of scatterings. For example, an interference term, $\exp(-i(x_{2+} - x_{1+})/l_c)$, is introduced in the expression of cross-section of scatterings at two points x_{1+}, and x_{2+}, where l_c is the coherence length (see Ref. [45] for definition of coherence length and derivation of the interference term). Coherence length gets smaller as Bjorken x and Q^2 gets larger, and therefore the shadowing gets smaller. When the coherence length is large, in the limit $exp(-i(x_{2+}) - x_{1+})/l_c) \rightarrow 1$, the cross section for two scatterings converges to $\sigma_A^{(2)} = -(A(A-1))/2 \int d^2x_T |T_A(x_T)\sigma|^2$, where $T_A(x_T)$ is the thickness function defined in Eq. 6.2, and σ is projectile-nucleon cross-section. The fact that this correction is negative explains why shadowing is observed as a depletion of low x partons. The values at which shadowing becomes effective can be estimated roughly by requiring the time of hadronic fluctuations to be larger than the time it takes for this state to span a nuclear radius, because for shadowing to appear the hadronic fluctuation has to interact with the nucleus as a whole. This consideration yields $x \lesssim 0.1A^{-1/3}$, so as nucleus gets larger the effects appear at smaller x values, but the magnitude is enhanced as the number of multiple scatterings is larger. The size of shadowing is model dependent, but the free fit parameters to data allows different models to converge to similar results.

Anti-shadowing: Anti-shadowing is a result of energy-momentum conservation. The depletion of the PDF at low x values due to shadowing results in an enhancement at x values above the threshold where the shadowing effects start to appear, because the momentum of all partons should add up to nucleon momentum.

EMC: There are different kinds of explanations for the EMC effect. The existence of nuclear binding, which reduces the mass of nucleons is one explanation, or in other words an excess pions a inside nucleus due to nuclear binding where part of the nucleon momentum is transferred to the virtual pions reducing the abundance

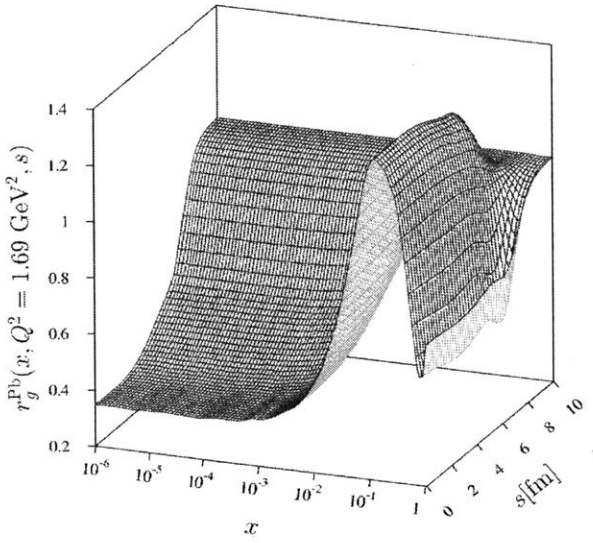

Figure 3-5: Taken from [154]: Shows modification of gluon PDF in Pb nucleus as a function of x and s.

of large x valence partons and increasing the number of partons with $x \approx M_\pi/M$. Alternatively, an increase in size of nucleons inside nucleus can result in a softening of the momentum distribution of partons [49].

Impact parameter dependence: A nucleon at the center of a nucleus is affected differently than a nucleon close to the surface. The nucleon at the edge has fewer neighbors and therefore the parton distributions inside should be more similar to a free nucleon. In Fig. 3-5, R_g^{Pb} is shown as a function of the position of a nucleon inside the nucleus, s and x. As can be seen it approaches to 1 at large s values. At larger Q^2 values the impact parameter dependent modification gets smaller as the overall R values are closer to 1 in general.

3.4 Hadronization

Hadronization is a non-perturbative process. Experimentally one can only reach the information of hadrons, while theoretical computations are with partons, as the QCD Lagrangian describes the dynamics of quarks and gluons. In a way hadronization

makes cross-sections "realistic" by reducing the effect of divergences, as collinear partons all end up inside the same hadron. Jets, are approximate handles on partons, but they also show sensitivities to hadronization, because hadrons are what jets are comprised off. Therefore, modelling of hadronization is an important ingredient in phenomenological studies of QCD. Monte Carlo generators first produce jet showers made out of partons down to a minimum virtuality scale, or p_{T} scale of order of $\approx$ 1 GeV, below which color neutral hadrons are formed by hadronization models. This cut off scale is not determined by theory, but based on how similar final hadron distributions can be to the initial parton distributions. A group of hadronization models describes the color flux between two partons as strings and another group treats each color charge pair as dipoles radiating other partons. Both methods aim to find a color neutral configuration while minimize change in the overall color flow.

In the Lund string model [37, 208], partons are connected by string that represents the flux of color force between them in a linear covariant approximation. As they move apart from each other string pulls them back, this pull is represented by infinitesimal losses of energy packages from the edges of the strings, i.e partons, to the string. This is a representation of color confinement in the sense that quarks cannot escape and are tied to each other. In the massless approximation, if strings are not broken into pieces, which is how hadronization takes place in these models, a $\mathrm{q\bar{q}}$ system would oscillate back and forth. The configurations are shown as line in Fig. 3-6, where each line is separated by equal time intervals.

Another simple color configuration is a $\mathrm{qg\bar{q}}$ system. In this configuration, the q and $\bar{\mathrm{q}}$ are attached to each other by a string that goes through the g, on the side without g there is no string, g is represented as a kink on the string instead of an edge. The fact that g has strings on both sides means that the force on g is twice as large as on a q or $\bar{\mathrm{q}}$, reflecting the ratio of color factors $C_A/C_F = 9/4$. In the case of no string break up, this system also oscillates back and forth, in a slightly more complicated way as shown in Fig. 3-6. Whenever a parton leaves all its energy on the string, i.e. the arrow in the figure disappears, the strings start growing in the direction of pull of the total energy density carried by the system. At the end $t = 15$,

the partons go back to a single point with the difference that q and $\bar{q}$ directions are flipped.

In the cases mentioned so far, partons are confined in the sense that they can't get too far away from each other, but of course this infinite oscillation cycle without the formation of hadrons is not realistic. Instead, strings are broken into pieces forming hadrons in a probabilistic manner. "The probability of a string breakup within a given small region (in space-time or energy-momentum, the two being simply related by the string constant κ) should basically be proportional to the probability of having a string there, i.e., that the string has not already broken up, times the phase space of the region." [208] The mass of hadrons come from the string energy stored in the string piece that is broken up, in order for hadrons to have mass the string cannot be broken into point like pieces. The break ups occur with the additional requirement of having on-shell hadrons.

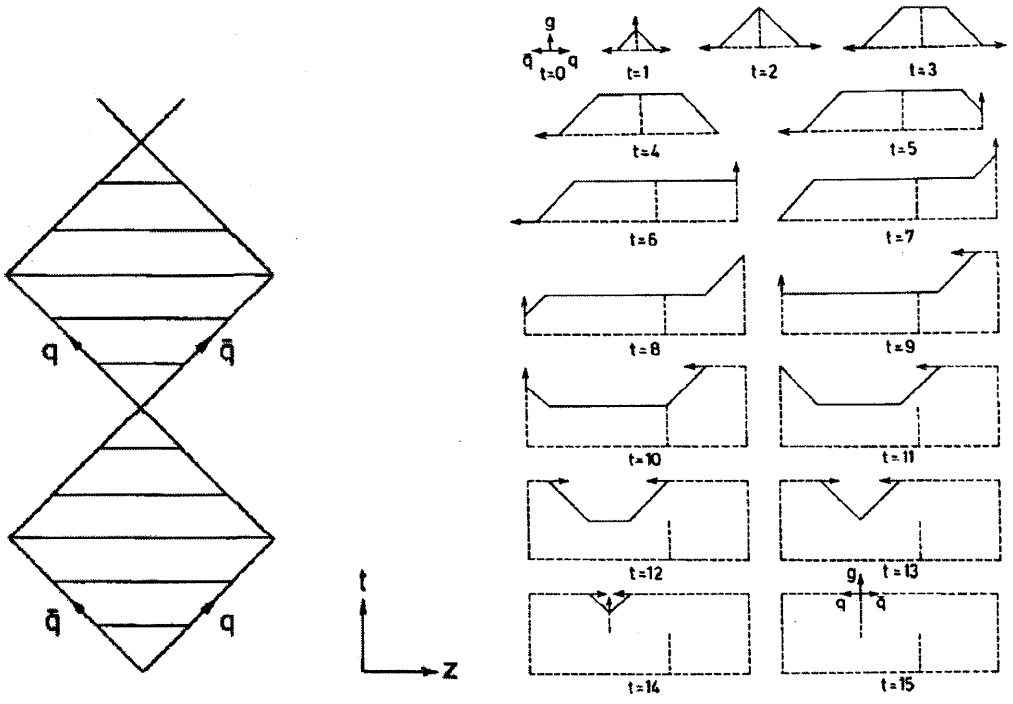

Figure 3-6: (Left) Time evolution of a string connecting a $q\bar{q}$ configuration. (Right) Time evolution of a string connecting a $qg\bar{q}$ configuration [208].

Another method used for hadronization is color dipole models, which model generation of several soft gluon emissions from dipoles of color charges. The generated gluons recoil the partons forming this radiation, the transverse recoil direction of gluon is distributed so that the disturbance of the color flow in neighboring dipoles is minimized[177]. Later these gluons are split into $q\bar{q}$ pairs. This model uses $p_\perp^2$ ordering, the emissions with larger $p_\perp^2$ are performed first.

3.5 Jets in PYTHIA

PYTHIA is one of the most well established Monte Carlo event generators used in high-energy physics at LHC. A similar generator is HERWIG [56], but it will not be discussed here. PYTHIA includes a wide range of functionalities, but in this section we will focus on implementation of the QCD framework concerning light flavor parton production. For more detailed information please refer to Ref. [209].

The main specialities of PYTHIA are initial state radiation (ISR), final-state radiation (FSR), multi-parton interactions (MPI), and hadronization with string fragmentation. It is built on LO machinery, but models higher order QCD processes through parton shower algorithms. It uses LO PDFs in ISR as boundary conditions to DGLAP and for MPIs where PDF is interpreted as number density of partons.

Hard-scatterings The hard process matrix elements at LO that are used in hard QCD interactions are $q_i q_j \to q_i q_j$, $q_i \bar{q}_i \to q_k \bar{q}_k$, $q_i \bar{q}_i \to gg$, $q_i g \to g q_i$, $gg \to q_k \bar{q}_k$, $gg \to gg$. Matrix elements are calculated for massless quarks, and the final quarks are then put on mass shell. The divergence as $k_\perp \to 0$, are overcome by setting a minimum threshold for the $\hat{p_T}^2 = \hat{t}\hat{u}/\hat{s}$ of the hard interaction, $\hat{p_T} > p_{\perp min}$.

Perturbative showers Although $2 \to 3$ or $2 \to 4$ matrix elements are not implemented in PYTHIA, the production of multi-jet events are accounted for via initial and final state radiation processes which utilize the same shower algorithm as the jet shower formation through splitting of single partons into many as a result of several

$2 \rightarrow 3$ processes based on dipoles[2]. Even if the matrix elements for higher order diagrams are not accessible in PYTHIA it is known that the outcome would be cancellation of $k_\perp \rightarrow 0$ singularities. Some approximations derived by simplyfying the kinematics, interference and helicity structure give good description of substructure of jets. The study of well-separated jets and α_s studies using multi-jet generation need to rely on higher order matrix element calculations and PYTHIA is expected to provide an limited description.

The parton showers in PYTHIA are $p_\perp$ ordered [207], allowing a natural implementation of coherence effects by the use of Sudakov factors [215]. Each splitting probability is governed by splitting functions that depend on z as given in Eq. 3.3. If these probabilities are put directly in practice, infinite number of partons would be produced due to divergences, but by assuming that the output of the parton generation will be used in study of jets via an IRC safe jet reconstruction algorithm it is possible to apply an effective cut-off of Q^2 for each emission.

FSR is a forward parton evolution, and ISR employs the same evolution but backwards, in the sense that, for FSR one tries to find partons b and c that parton a will branch into, while in ISR given parton b one searches for parton a that produced b. The two cases are shown in Fig. 3-7. The ISR and FSR takes place in the hard-scattering center of mass frame and the recoiler is defined as the rest of the particles produced in this process except the one whose evolution is being processed. The exact definition of $p_\perp$ is done in light-cone coordinate system for a moving in z^+, so that $p^\pm = E \pm p_z$ and $p^+p^- = m_\perp^2 = m^2 + p_\perp$. The splitting forms two partons with $p_b^+ = zp_a^+$ and $p_c^+ = (1-z)p_a^+$. Then by energy momentum conservation one gets $m_a^2 = (m_b^2 + p_\perp^2)/z + (m_c^2 + p_\perp^2)/(1-z)$. Using these for FSR, for which $Q^2 = m_a^2$ and $m_b = m_c = 0$, one finds that $p_\perp^{\text{evol}} = z(1-z)Q^2$. While for ISR one has $Q^2 = -m_b^2$ and $m_a = m_c = 0$, thus $p_\perp^{\text{evol}} = (1-z)Q^2$. In order to have Lorentz invariant when constructing the kinematics of daughter partons, z is calculated in radiator+recoil reference frame.

[2]Rather $1 \rightarrow 2$ processes where the effect of dipoles come into play at determination of phase space

Given the evolution scale $p_\perp$, Sudakov form factors, $\mathcal{P}_a^{no}$, are calculated which define the probability that no emissions occur between the initial maximum scale $p_\perp^{\max}$, and $p_\perp^{\rm evol}$. The probability of no splitting to occur is given by the inverse exponential of the integral of probability of emission to occur above the scale $p_\perp^{\rm evol}$, $d\mathcal{P}_a(p_\perp^{\rm evol}, z)$:

$$\begin{aligned} \mathcal{P}_a^{no} &= \exp\Big(\int_{p_\perp^{\rm evol}}^{p_\perp^{\max}} \int_{z_{\min}}^{z_{\max}} d\mathcal{P}_a(p_\perp^{\rm evol}, z)\Big), \\ d\mathcal{P}_b(p_\perp^{\rm evol}, x) &= \left|\frac{dp_\perp^2}{p_\perp^2}\right| \frac{\alpha_s}{2\pi} \int dz \frac{x' f_a(x', p_\perp^{\rm evol})}{x f_b(x, p_\perp^{\rm evol})} P_{a\to bc}(z), \end{aligned} \tag{3.5}$$

where $x = zx'$. The largest $p_\perp^{\rm evol}$ is picked by throwing dice and comparing to the value of the Sudakov form factors. Later, for the given z and $p_\perp^{\rm evol}$ values daughter partons are generated, and Q^2 is calculated. Given Q^2 and z, the rest of the kinematics of daughter partons are set and the above procedure is repeated until $p_\perp^{\rm evol}$ of next splitting goes below $p_\perp^{\min}$. This kind of evolution where splittings with larger $p_\perp^{\rm evol}$ occur first and the phase space is determined using dipoles is enough to satisfy angular ordering that is required by color coherence. The dipole phase space factors are described in Ref. [177].

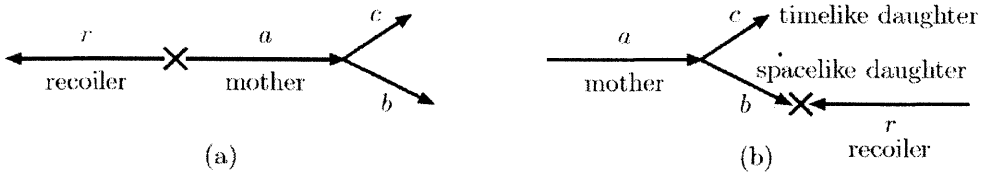

Figure 3-7: Taken from [207], on panel (a) FSR and on panel (b) ISR is demonstrated.

The showering procedure is ambiguous: shuffling ISR and FSR can still create the same final state configuration. The talk between the two is done by first creating ISR and associate a $p_\perp$ scale for each of the partons generated in ISR, and color connecting all of the final state partons and partons from hard scattering in forms of dipoles. The partons are coupled after they are ordered in $p_\perp$, each parton forms a dipole with

other partons with closest $p_\perp$ values and these dipoles cannot radiate with $p_\perp$ values that are greater than the minimum of $p_\perp$ of a pair of partons. Therefore, initially the partons coming from the hardest interaction scale radiate, once these are evolved downwards in $p_\perp$ and reach the $p_\perp$ values of partons from ISR these dipoles also start to contribute to FSR

3.6 Jet clustering algorithms

As discussed in Section 3.1, splitting probability diverges in soft and collinear limits. However, because the definition of p_{T} of the initial parton is independent of these splittings, so should be the jet clustering algorithm. Jet clustering algorithms that produce same set of jet in an event with and without an additional collinear or soft splitting are called infrared collinear (IRC) safe. The most commonly used IRC safe algorithm at LHC is the anti-k_{T} algorithm [72]. Analyses described in Chapters 10 and 9 both employ this algorithm. Some other commonly used IRC safe algorithms are SISCone, k_{T} and Cambridge/Aachen [168, 131, 87].

The ancestor of jet clustering algorithms [213] was a simple cone algorithm aimed to search for back to back parton production, i.e., dijet production. This algorithm functioned in a very intuitive way of grouping particles together and tagged them a jet if the total energy contained in two cones with openning angle δ is larger than $1-\epsilon$ times total event energy. In this algorithm, δ and ϵ are free parameters that do not have well defined constraints on which values they can have. Today, we expect more from clustering algorithms. They do not assume a fixed number of jets and they do not make use of the total event energy, as in hadron collisions the energy that goes into hard scattering process is not same as the total event energy due to MPIs.

3.6.1 Infrared collinear safety

Experimentally all jet algorithms are IRC safe, as the jet reconstruction is done using objects, such as tracks and calorimeter towers with minimum p_{T} and E_{T} thresholds. However, for experimental observables to be comparable to the theoretical calcula-

tions, algorithms used by both parties should be IRC safe. Theoretically the problem arises when IRC divergences are cancelled by different order diagrams analytically but the jet clustering algorithm treats these two cases not in the same way, resulting in two sets of different jets for different order processes so that the cancellation in the sum of these cannot take place even if both describe the same amplitude. The best way to describe what IRC safe algorithms are expected to do is by showing how the IRC unsafe algorithms are effected by such radiation.

Iterative cone algorithms reconstruct cones around high p_{T} seeds, recalculate a new seed with the momentum sum of all the particles inside the cone and iterate the construction of the cone. All the stable cones in the event are reconstructed in this manner. However, in order not to use one particle for two jets, either particles associated to a jet are removed from the event (iterative cone with progressive removal, IC-PR) or the jets that overlap are merged (iterative cone with split-merge, IC-SM). IC-PR algorithm is not collinear safe, as one of the high p_{T} seeds might have split into two smaller p_{T} particles in the same direction by collinear radiation, this would result of another particle in the event to be picked up as the highest p_{T} seed and particles associated to this real highest p_{T} jet might have been removed, resulting in change its p_{T}. The IC-SM algorithms are not infrared safe, because an infrared radiation can make two jets that did not initially overlap overlap with each other and get merged into a single jet[196]. Iterative cone algorithms reconstruct cones around high p_{T} seeds, recalculate a new seed with the momentum sum of all the particles inside the cone and iterate the construction of the cone. All the stable cones in the event are reconstructed in this manner. However, in order not to use one particle for two jets, either particles associated to a jet is removed from the event (iterative cone with progressive removal, IC-PR) or the jets that overlap are merged (iterative cone with split-merge, IC-SM). IC-PR algorithm is not collinear safe, as one of the high p_{T} seeds might have split into two smaller p_{T} particles in the same direction by collinear radiation, this would result of another particle in the event to be picked up as the highest p_{T} seed and particles associated to this real highest p_{T} jet might have been removed, resulting in change its p_{T}. The IC-SM algorithms are not infrared safe,

because an infrared radiation can make two jets that did not initially overlap overlap with each other and get merged into a single jet[196].

In order to be IRC safe an algorithm should group collinear particles together and recombine them into a single particle, and soft particles radiations at large angles should not be able to combine two jets into a single jet.

3.6.2 Sequential recombination and anti-k_{T} algorithm

A general class of jet clustering algorithms are the sequential recombination algorithms. These algorithms compare two distance measures for an entity j, which can be a particle or a pseudojet: d_{ij} distance between j and all the other entities i in the event, and d_{iB} distance of entity i to the beam axis, B. If $d_{ij} < d_{iB}$, i and j are combined into a single entity by combination of 4-momentum vectors, or else i is removed from the list of entities for j. Recombination might start from the particle with lowest d_{iB} measure (as is the case for k_T and CA algorithms) or it might start from the particle with largest d_{iB} measure as is the case for anti-k_{T} algorithm. After each recombination d_{ij} and d_{iB} is recalculated and the procedure is repeated.

The distances are defined in the general form given below for the clustering algorithm power value n:

$$\begin{aligned} d_{ij} &= min\{k_{\mathrm{T}i}^{2p}, k_{\mathrm{T}j}^{2p}\}\frac{\Delta_{ij}^2}{R^2}, \\ d_{iB} &= k_{\mathrm{T}i}^{2p} \end{aligned} \tag{3.6}$$

where $\Delta_{ij} = \sqrt{(\eta_i - \eta_j)^2 + (\phi_i - \phi_j)^2}$. Note that the d_{ij} expression is very similar to the divergence of splitting probability shown in Eq. 3.2. Here $k_{\mathrm{T}}^2 R_{ij}^2$ replaces $k_\perp^2$, in order to define a boost invariant angular projection, because in hadron colliders the hard scattering interactions take place in boosted frames with respect to the lab frame as a result of the composite nature of proton. Having the divergent term in the expression is what lies behind the IRC safety of these algorithms. The same expressions that appear in the denominator of splitting probabilities which get arbitrarily small

resulting in it to diverge appears in the numerator of d_{ij}, and as the clusterring is first done for small d_{ij} values these splittings are combined before other combination steps.

For k_T algorithm $n = 1$, for C/A $n = 0$ and for anti-k_T $n = -1$. The advantage of anti-k_T is that as the clustering grows outward around the highest p_T cores of jets, it is less sensitive to perturbative effects from hadronization and pileup. The other sequential reconbination algorithms first find the soft subjets inside a jet and at the end combine these with the higher p_T subjet. [72].

3.7 Jet shapes and fragmentation functions

After explaining the theoretical mechanism behind jet formation, implementation of these in MC and clustering algorithms, we would like to demonstrate how an average jet looks like. The most commonly used ways of calculating jets is by means of measurement of energy density distribution as a function of distance to the jet axis, jet shapes, and distribution of momenta of constituents of the jet when projected on the jet axis, fragmentation functions. Note that the use of fragmentation functions here is an overload of terminology, as we do not refer to D_k in Eq. 3.1, because we cannot access partonic information directly. This is instead an approximatation of fragmentation functions which are often measured by experiments.

A jet is a very collimated object, as indicated by divergences shown in splitting probabilities in Eq. 3.2. The collimation results in the exponentially falling shape shown in 3-8, where,

$$\rho(r) = \frac{1}{\delta r}\frac{1}{N_{\text{jet}}}\sum_{\text{jets}}\frac{\sum_{\text{tracks}\ \in\ [r_a,\ r_b)} p_T^{\text{track}}}{p_T^{\text{jet}}} \tag{3.7}$$

About 90% of the momentum of the jet is contained in 10 % of its area. The R parameter of jet clustering algorithm coupled with a p_T cut on the jet results in different shapes of jets. By varying R and keeping the p_T threshold fixed different parton p_T values are probed. Only a fraction of parton's p_T from three level hard

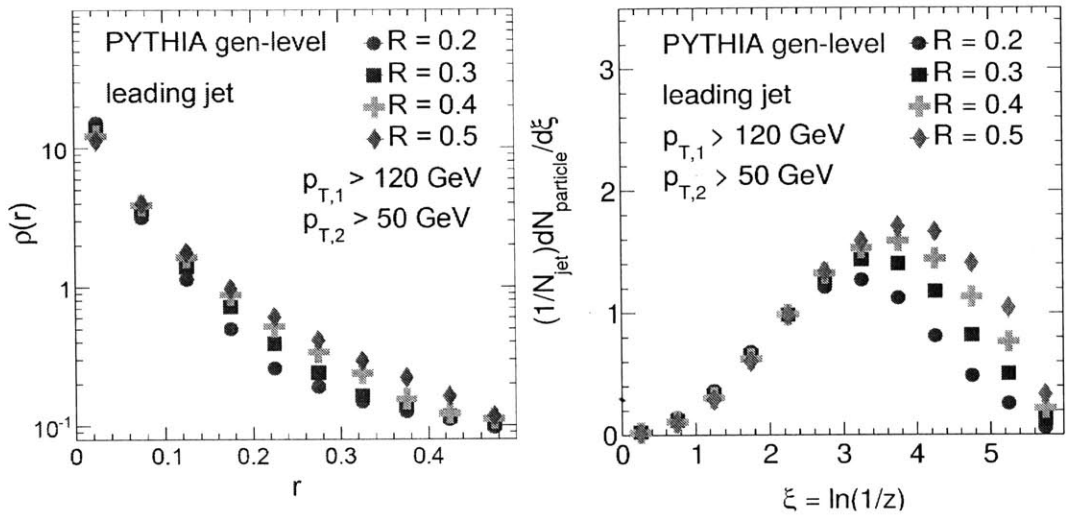

Figure 3-8: Charged particle shapes (left) and fragmentation (right) of jets with different anti-k_T R parameters in PYTHIA events generated with Z2 tune [1]. Only charged particles with $p_T > 0.5$ GeV are used.

scattering interaction is available in clustered jets with small R parameters, and cut on jet p_T translates into higher values for the parton p_T for these small R jets. Higher p_T partons have a more collimated shower pattern resulting in the observed effect for smaller R values. Therefore, it is favorable to use large R values. However this is not applicable in hadron collisions with large underlying event, and especially not in heavy ion collisions. Therefore, common choices of R values are $0.2 - 0.5$.

The radiation from higher p_T partons are more collimated than lower p_T partons, when a clusterred jet is required to be greater than a value this translates into higher requirements for on parton p_T for smaller R parameters. On the left panel of Fig. 3-8, jet shapes are shown for the leading jet in the event for a variety of R parameters, and smaller R parameter jets are naturally narrower. Another consequence of increasing R parameter while keeping clustered jet p_T fixed is adding softer fragmenting jets of same total p_T, because at the outskirts of the jet the composition of particles is softer. The dependence of FF of leading jet on R parameter is shown on right panel of Fig. 3-8.

Chapter 4

Jet quenching

4.1 Observation

Jet quenching, is the name attributed to the concept that jets traversing the QGP get modified. It was discovered as suppression of high-p_{T} hadrons at RHIC [29, 30, 52, 55, 23, 31]. Other measurements that show jet quenching at RHIC are the disappearance of the away-side jet peak in correlations of high-p_{T} hadrons, and modification of the away side fragmentation in gamma-hadron correlations. At the LHC, clustered jets were used for the first time to demonstrate the effect of jet quenching in addition to high-p_{T} charged hadrons. The first observation was the enhancement of imbalanced dijet pairs[8, 94, 97]. The variety of observables increase significantly once jet clustering is done. Inclusive jet spectra[10], shape and fragmentation modifications [108, 98, 12, 67], suppression of number of jets associated to photons and the p_{T} imbalance of the gamma-jet pair[101] are some of the measurements that are aimed to shed light to underlying mechanisms that cause the observed modification of jets in heavy ion collisions.

Jets and medium are both made out of QCD matter. There are no sharp boundaries between a parton that belongs to a jet and a parton that belongs to the medium from the perspective of partons. The medium and the jet are modified mutually by changing each other simultaneously. Therefore, an interesting set of measurements are those that look at global event properties around the jet, and that try to determine

how far in angular distances do jet quenching effects extend. One such measurement that provides a very detailed description of global event modification is the "missing p_{T}" measurement that is described in Chapter 10.

4.2 Theory of jet quenching

This is a very wide topic to cover as whole in a few pages, which is what I will attempt to do. For detailed information please refer to Refs. [184, 128, 179] and to the relevant section in the book Ref. [82].

Before going into the details of interaction mechanisms of jets and medium, one can try to match the time scales involved in medium evolution and jet evolution to get an idea of where do these overlap and how much time do jets spend inside the medium. First splittings for partons produced in a hard scattering process of virtuality $\approx$ 100GeV occur at time scales $\approx 1/Q = 0.002$ fm/c. As discussed in Section 2.3 thermalization occurs at $t_{\mathrm{ther}} \approx 2$ fm/c according to pQCD calculations and hydrodynamization occurs $t_{\mathrm{hydro}} \approx 0.02$ in strong coupling regime and $\lesssim 1$ fm/c in weak coupling regime. All these values are larger than the time it takes for the first hard splitting to occur forming the multi-jet angular structure in the event. Therefore the very beginning of jet formation takes place effectively in vacuum, resulting in azimuthal correlation of jets in PbPb collisions to be similar to that in pp collisions. However, when the medium is formed the jets are still in the early stages of their evolution, and a significant portion of shower formation occurs inside the medium, allowing jets to spend enough time inside the medium to show the effects of jet quenching. In Ref. [84], the probability of splitting to occur outside of QGP is calculated based on PYTHIA showers, and there is $\approx 20\%$ probability for a splitting to occur after propagation time of 30 fm/c since the formation of initial parton that creates the shower. The typical lifetime of QGP is ≈ 10 fm/c. Therefore, even after the medium has disappeared shower formation might continue for some jets.

Effects of medium interactions are often seen as corrections on top of the vacuum structure of jets [78, 185, 183], because these interactions are soft and cannot compete

with the hard structure of the vacuum radiation. Vacuum branching of jets determines the main skeleton of jets and the probabilistic nature of this structure causes a large variance on how jet and medium interacts depending on how splittings occur. This variance gets even larger when one considers all the factors in the variation of the matter density seen by a jet over its path. The total matter density, related to the energy density and temperature, seen by the jet on its path, depends on whether the hard collision occurs at the center of overlap of two nuclei or close to the surface, whether the jets are boosted, and on the shower structure of jets. As the number of partons increase so does the matter seen by the jet, but keeping in mind that each parton in a jet cannot be considered as separate emitter due to coherence effects.

The effective matter density increases with number of partons but it is not a straightforward sum of the matter density over each parton. The number of emitters is also related to local medium properties and the resolution power of the medium. In addition to having large variations of due to fluctuations in jet showers and medium properties on the path of jets, the actual difficulty in having a complete model of jet quenching arises due to the several competing mechanisms of jet-medium interactions that are also probabilistic in nature and correlated to each other in ways that are not fully understood. Initially the theoretical study of jet quenching was focused on single parton energy loss, but as described above the complexity of the problem seeks for a more global picture of jet-quenching. Monte Carlo studies are therefore very crucial for jet phenomenology.

Partons traversing the medium Transport coefficients, $\hat{q}$ and $\hat{e}$ explain the average effect of the medium on a single parton:

$$\hat{q} = \frac{\langle k_\perp^2 \rangle_L}{L}, \hat{e} = \frac{\langle \Delta E \rangle_L}{L}, \tag{4.1}$$

where $k_\perp^2$ is the momentum component that parton acquires transverse to its initial direction by medium interactions and ΔE is the energy it loses over the length of L.

A single parton, that starts existing when created by a radiation (vacuum or medium-induced) until the end of its propagation when it splits into other partons,

interacts with the medium which results in a change in its:

- **Energy:** Parton loses energy to the medium through elastic scatterings (pQCD) or drag force (AdS/CFT).
- **Color:** In pQCD, the same mechanisms described above changes the color of the parton as well, because the energy is transferred with a gluon.
- **Direction:** Each scattering causes the direction of the parton to be tilted in pQCD and energy distribution in the field theory projection to broaden in AdS/CFT. It is usually safe to assume that the change in direction of the parton due to collisions is small, this limit is the eikonal limit, "when the energy of the quark is much larger than any other scale in the problem, the longitudinal and transverse degrees of freedom decouple - here longitudinal refers to the direction along the propagation of the quark." [198].
- **Propagation time:** In pQCD, the probability of each parton to undergo a splitting changes due to medium induced gluon radiation, which occurs as a result of an increase in the virtuality of the parton after the energy momentum transfer in elastic scatterings. The DGLAP evolution in vacuum is modified inside the medium. The propagation time is given by the formation time of radiation, and $k_\perp$ can be replaced with the expression of $\hat{q}$ given in Eq. 4.1, then $t_f = k/k_\perp^2 = k/\hat{q}t_f$, as a result $t_f = \sqrt{k/\hat{q}}$. As $\hat{q}$ increases propagation time gets smaller.

However considering the modification of single parton is not sufficient due to color coherence effects, which are discussed in the next subsection.

4.2.1 Perturbative calculations

There are various approaches on how to model jet-medium interactions with pQCD. These models differ on the approximations used in calculations. Approximations are needed, because of the limitation of cases where first-principle analytical calculations are possible. The precision of calculations improve systematically as higher order

corrections are calculated. One approach is to focus on multiple soft scatterings, and take averages over length to define transport coefficients which allows to resum all the interference terms (e.g. ASW[199], AMY[51]). This approximation ignores the hard scatterings. Another approach, opacity expansion, takes into account the hard scatterings but the interference terms are calculated order by order and the expansion is over number of scattering centers, so at first order there are no interference effects and just one scattering (HT[222], DGLV[225]). Often it is assumed that the medium is composed of static scattering centers (as in the BDMPS-Z formalism [57, 226], note that ASW and DGLV solve BDMPS-Z path integrals under different assumptions), and for some cases it is assumed to be composed of thermal plasma but of infinite length ([51]).

In the BDMPS-Z formalism, the small angle gluons are suppressed for in medium radiation due to the equivalent of Landau-Pomeranchuk-Migdal effect in medium. The suppression is a result of gluon formation times of collinear gluons being larger than the distance between successive scatterings, i.e, mean free path, in the medium. The diagrams resulting to suppression of small angle radiation by interference are shown in Fig. 4-1. The BDMPS-Z formalism explains single medium-induced gluon emissions from a single parton that undergoes successive multiple scatterings, but the correlation between two gluons emitted according to BDMPS-Z gets suppressed for large medium lengths. The color coherence between two gluons is lost at a length scale that is comparable to the formation time.[63] Therefore, multiple medium-induced gluon emissions and their cascade can be studied making use of the single medium-induced gluon emissions.

There have been recent developments in understanding of the color coherence between multiple medium-induced gluon emissions and the correlation of these with vacuum radiation [50, 86]. Such radiation was previously studied without considering the interplay with the vacuum radiation for a dense medium [138]. According to these calculations, the LPM effect can be generalized to multiple gluon emissions but the explanation is not as simple as in the single gluon case and involves more than the comparison of the time scale of the formation of the medium and the mean free path.

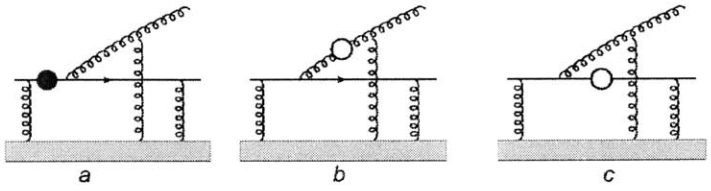

Figure 4-1: Taken from Ref. [179], diagrams that contribute to LPM effect.

As in the vacuum, the study of color coherence in emission of a gluon from two close-by color sources can also be studied with color dipoles in the medium. In vacuum, using color dipole antennas as building blocks of jets rather than partons leads to a natural implementation of the study of color coherence effects, as discussed for the case of vacuum in Section 3.2 and modelling of jets showers in PYTHIA in Section 3.5. Similarly, color coherence effects can studied by a color dipole antenna inside the medium, where a new angular scale $\Lambda_{\rm med}$ is introduced to the problem [83]. The $\Lambda_{\rm med}$ characterizes the resolution power of scattering centers in the medium.

The calculations show that quarks in a color dipole radiate gluons with k_T separately from each other (color decoherence) if the angle between them Θ is larger compared to $\Lambda_{\rm med} = 1/\sqrt{\hat{q}t_f}$ for a gluon radiation of $t_{\rm f} = k/k_\perp^2$. If the transverse size of the antenna at the formation time of this radiation $r_\perp = \Theta t_{\rm f}$ is much smaller than $\Lambda_{\rm med}$, then the emission occurs coherently, if $r_\perp \gg \Lambda_{\rm med}$ then the color charges in antenna radiate decoherently. This explains that medium causes the color dipoles to lose their coherence for large angle radiation but the hard core of the jet stays coherent and the branchings occur in a way that is similar to the vacuum.[83]

4.2.2 AdS/CFT correspondence

AdS/CFT correspondence allows to calculate interaction of partons with strongly coupled SYM plasma classically by making use of the dual black hole description. The parton's interaction with the medium is described by the dynamics of a string with one end attached to a brane, which is at a distance that is inversely proportional to their mass from the black hole in the holographic dimension. The other edge of the

string is inside the black hole dragging behind. The energy loss was first calculated for quarks with infinite mass going at constant velocity by three different groups [175, 149, 156]. The energy loss per unit length

$$\frac{dE}{dt} = \frac{E}{t_0}, t_0 = \frac{2}{\pi\sqrt{g^2_{YM}N}}\frac{m}{T^2}, \tag{4.2}$$

is anti-proportional to mass of the parton. This expression diverges as m $\to$ 0, as the approximation is no longer valid for a massless quark. Later the light parton energy loss is calculations were done [111, 150], the form of energy loss per unit time is more complicated for light quarks and it depends on the time parton travels in the medium as shown in Fig. 4-2.

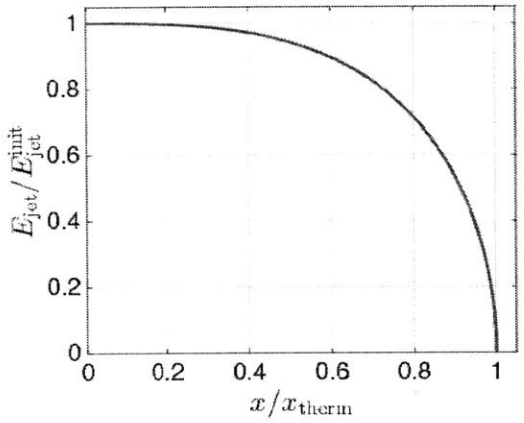

Figure 4-2: Taken from Ref. [113]: Shows the energy lost by light quark per unit time in $\mathcal{N} = 4$ SYM plasma.

Since the results above on parton energy loss the field has developed in a direction where numerical calculations make it possible to calculate quenching in a finite medium [113] and an expanding medium[112]. The calculations of jet quenching with holographic models are described in detail in [82].

4.2.3 Comparison

Although energy loss of single partons are different in terms of expressions of transport coefficients. The two very different approaches to jet quenching predict some qualitatively similar consequences for modification of jets:

- **Energy goes to large angles** In a pQCD, medium induced gluon radiation is suppressed at small angles due to the LPM effect. Moreover, the radiated gluons form a cascade[159, 65] and thermalize in the medium, carrying the lost energy to large angles. Other mechanisms such as collimation [76] can cause energy to go to large angles in weakly coupled plasma, where soft particles are stripped off the jet by getting stopped by medium interactions and carried to larger angles. In strongly coupled plasma, partons traversing the medium generate sound waves exciting hydro modes, generating diffusion wakes and mach cones. Heating the plasma creates an effect that extends over large pseudorapidities. In addition, depending on the time these sound waves have to travel (they propagate with $c = 1/\sqrt{3}$ [186]) they can carry the energy to large angles.

- **Wider jets are quenched more** In pQCD, color dipole antenna radiates decoherently when the angle gets larger than the medium scale, wider jets are composed of color dipoles with larger angular separations and therefore would act as more than a single emitter losing more energy. A recent calculation [114] showed that in $\mathcal{N} = 4$ SYM theory the angle of a "jet" is the driving parameter for how much energy will be lost per length as well, such that two jets with different initial energy but same trajectory and opening angle lose same amount of fractional energy.

- **Jet structure is not modified significantly** In weakly coupled calculations the core of jets are not modified because medium cannot resolve the partons that are close to each other and the shower development in the core is like in the vacuum. In AdS/CFT calculations, parton splittings do not exist [157, 152]. In any case, qualitatively a package of energy shot a slab of $\mathcal{N} = 4$ SYM plasma comes out with a shape that is same as before up to a scale [113].

All the items listed above are rather qualitative, which is not sufficient to distinguish signatures of different quenching mechanisms in data. For that quantitative comparisons between data and theory are needed. However, the quantitative comparison to data requires a full-fledged MC implementation, which is not yet available and which cannot easily be developed because of gaps in our understanding of interactions in QGP. In the future it might be possible to distinguish between the contribution of different quenching mechanisms even for the cases for which they predict similar qualitative behavior. Instead, at the moment all these models could be seen as different approximations of reality and therefore components of it or different ways of saying the same thing rather than being made to compete with each other.

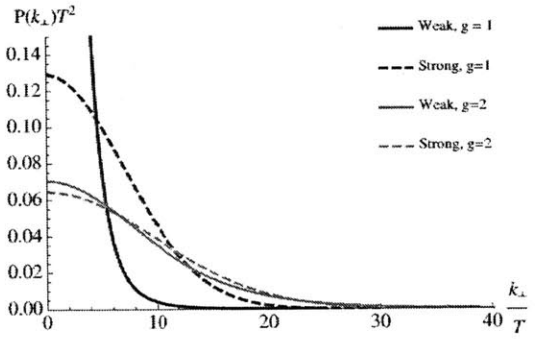

Figure 4-3: Taken from Ref. [129]: Shows distributions of $k_\perp$ kicks for strong and weak coupling calculations.

It is more likely to observe one of the mechanisms in action if one of them creates an effect the other does not predict, below we list one such item for each approach:

- **Large transverse kicks** As shown in Fig. 4-3 the transverse kicks partons get in weakly coupled plasma have a tail for large kicks which does not exist in strongly coupled plasma. Therefore scatterings analogous to Rutherford scattering can be signature of scattering centers in the plasma so a signature of pQCD [129].

- **Cherenkov meson radiation** Observing a conical enhancement of heavy flavor mesons around quenched jets would be a signature measurement in the

opposite direction, as this radiation is created only when partons go faster than the characteristic speed of sound of the strongly coupled plasma. [77]

4.3 Monte Carlo implementations

Jet quenching MCs are essential in the phenomenology of jet quenching in order to model the interaction of the jet with the medium event-by-event, having a realistic description of the geometry of the collision and the path the jets take inside the medium. It also lets one to study the modification of the medium and not only the modification of jets due to jet propagation. A good example with this functionality is JEWEL [229], where medium back-reaction is modelled by generating source terms. Moreover, MCs allow the study of fluctuations, depending to what extent the causes of fluctuations are implemented, and not only the averaged quantities, for quantities such as dijet asymmetry the fluctuations in energy loss due to probabilistic nature of jet formation has been studies in Ref. [185]. Below you can find an non-comprehensive list of available jet quenching MC models (see more in Refs. [200, 151, 176] and a comparative list can be found Ref. [228]), to give a taste of how the mechanisms discussed above were implemented by MC developers in real life.

Q-PYTHIA: Q-PYTHIA[46] modifies PYTHIA at the level of splitting functions. The total spectrum is given as sum of the vacuum and medium induced spectra:

$$\frac{dI^{\text{total}}}{dzdp^2_{\text{perp}}} = \frac{dI^{\text{vac}}}{dzdp^2_{\text{perp}}} + \frac{dI^{\text{med}}}{dzdp^2_{\text{T}}}, \tag{4.3}$$

where p_{T} is the In vacuum spectrum and the splitting probability are related as:

$$\frac{dI^{\text{vac}}}{dzdp^2_{\text{perp}}} = \frac{\alpha_2}{2\pi}\frac{1}{p^2_{\text{perp}}}P_{\text{vac}}(z), \tag{4.4}$$

The vacuum splitting probability is modified by an additive term,

$$\Delta P = \frac{2\pi(1-z)zp^2_{\text{perp}}}{\alpha_s} I_{\text{med}}, \tag{4.5}$$

similar to the relationship in vacuum but with additional factor of $(1-z)z$ and the difference in spectrum where I_{med} is described by the BDMPS-Z formulation.

JEWEL: JEWEL [227, 229] implements BDMPS-Z radiation incorporating LPM interference effects. Jets see the medium as a collection of partons, assuming that the momentum transfers involved in jet medium interactions are hard enough to resolve the partonic structure of the medium. A number of scattering centers are created based on density of the medium and the momentum distribution of these scattering centers are created according to the temperature. The same mechanism which is used for $2 \rightarrow 2$ processes in MC generators such as PYTHIA describe the medium jet interactions, i.e. with an initial state and a final state parton shower (See Section 3.5). The several overlapping scattering processes are combined based on the formation times associated to the processes, such that the process with shorter formation time takes place instead of the longer one when two of the formation times overlap and the process with longer formation time is reset in the case that does not generate any effect. This results in vacuum evolution dominating over the medium induced radiation because of the shorter formation times associated to vacuum processes with higher momentum exchanges. The LPM effect is implemented probabilistically based on an iterative algorithm that compares emission times and calculates the coherent momentum transfer based on this. In the modelling of coherent emission from multiple scattering centers an effective momentum transfer is used in the $2 \rightarrow 2$ processes. The emission probability is adjusted according to BDMPS-Z in the eikonal limit and assumed to hold in the non-eikonal case of the implementation.

YAJEM: YAJEM [195] Modifies the shower of partons by reducing their propagation time in medium based on the virtuality partons acquire over a path length based on a $\hat{q}$ parameter. The $\hat{q}$ value is obtained from the medium based on the energy density on the path of the parton, and the medium is modelled by 3d hydrodynamical evolution. The parton showers generated by modifying a PYTHIA shower algorithm, specifically the propagation time if change in virtuality due to $\hat{q}$ is large

or by keeping the virtuality to share it among the daughter partons. The shower is formed based on angular ordering in PYTHIA, and the effects such as the LPM effect and the modification in angular ordering for medium induced radiation are assumed to be small. In addition while the virtuality is acquired from the medium through $\hat{q}$ parameter due to multiple scatterings, these scatterings are assumed to cause no change in longitudinal momentum of that parton.

Hybrid model: The Hybrid model[79, 78], which I am a coauthor of, is based on the observation that quenching effects are corrections to vacuum showers in terms of the structure of the shower. It aims to test the effects of dE/dx for massless parton obtained from AdS/CFT for $\mathcal{N} = 4$ SYM theory. The expressions of energy loss per unit length are applied, up to a scale factor that allows the translation to QCD which is also used as the only fitting parameter to data, to each parton in the shower based on the medium energy density and temperature. The medium is modelled by hydro [71]. The vacuum showers that are directly obtained from PYTHIA without modifications due to effects such as medium induced radiation. The propagation time of each parton is calculated according to $E/2Q^2$ based on the values in unquenched PYTHIA shower. Recently, new features were implemented such as medium backreaction, by making the medium locally hotter due to energy lost to it by the partons from PYTHIA shower. Additional, thermal particles are generated based on Cooper-Frye formula which conserve 4-momentum of the quenching process[80].

The basic observables such as the modification of inclusive jet spectra, dijet asymmetry are modelled well with the existing jet quenching MCs. These models do not reproduce some of the more detailed jet observables with same level of agreements, such as fragmentation functions and jet shapes. Moreover, the medium response to quenching has been realised to be a necessity, except some models [116], for a better description of these observables [80, 220].

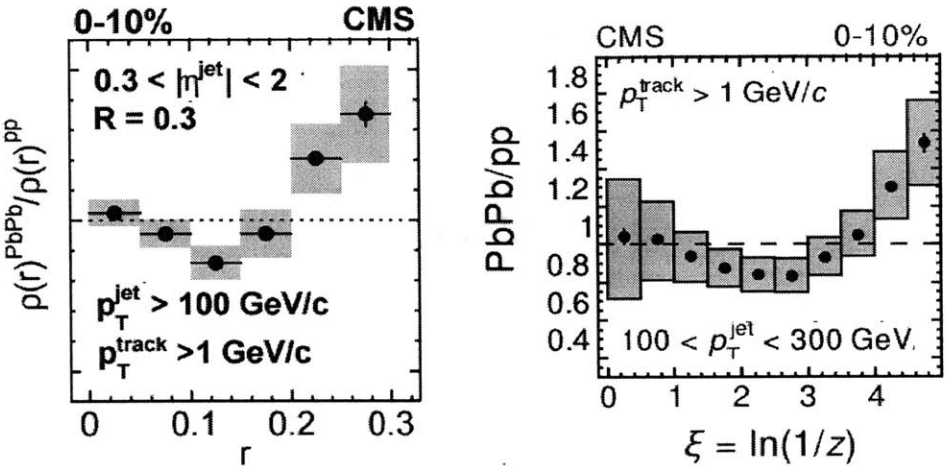

Figure 4-4: Jet shape (left) and fragmentation functions (right) modification in head on PbPb collisions collisions compared to pp collisions. Taken from Refs. [108, 107].

4.4 Experimental tests of predictions

After going through the theoretical predictions, let us go back now to how jet quenching is observed experimentally and compare the qualitative predictions listed in Section 4.2 to experimental measurements. When we say that jets lose energy we directly imply that the energy that would be radiated by the parton inside a "cone" of R in vacuum now goes outside of this cone after the interactions with the medium. Otherwise, after clustering the particles generated in interactions would contribute to the p_{T} of the jet without resulting in a depletion of its energy. A medium induced effect that is contained in the vicinity of jet axis, i.e, inside the jet cone would not show up as a significant change in jet p_{T}, but rather as a modification of its inner-structure. In Fig. 4-4, the ratio of PbPb and pp fragmentation functions and shapes are shown for $R = 0.3$ jets. Noting that the jet energy is mostly contained at the center, the change at the outskirts of the jet $R > 0.2$ only corresponds to redistribution of ≈ 1 GeV energy (to see how energy is distributed inside a jet in vacuum please refer to Fig. 3-8), so a 1% modification of a 100 GeV jet. Instead, p_{T} balance in dijet and gamma jet events show that the energy loss is $\approx 10 - 20$ GeV. Therefore, a significant portion of jet energy goes outside at angles larger than at least the size of the jet.

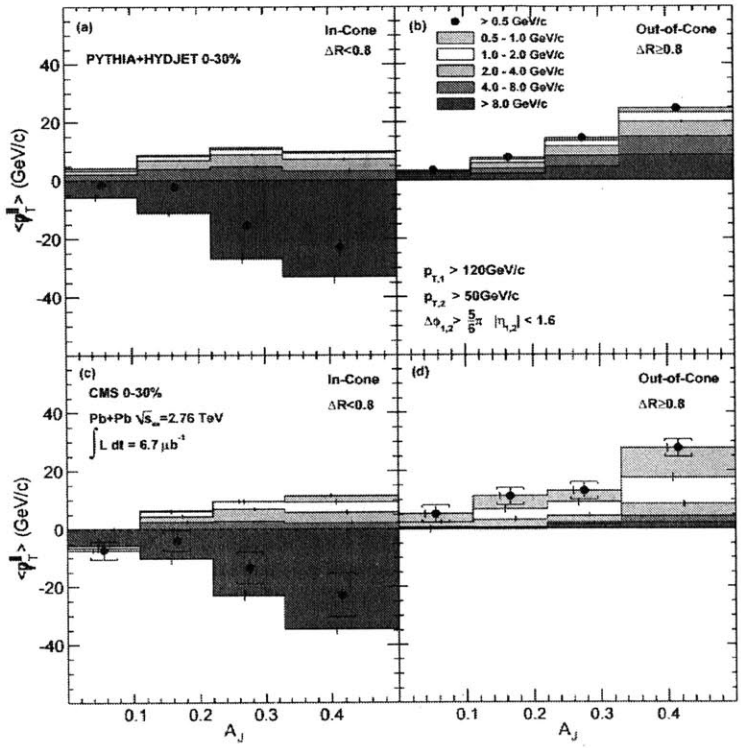

Figure 4-5: "Missing p_{T}" for $\Delta < 0.8$ and $\Delta > 0.8$ for PYTHIA+HYDJET MC simulations (top) and for PbPb collisions (bottom). Taken from Ref. [94].

Third item on our list of qualities expected from quenched jet by both strong and weak coupling approaches, seems to be true given the little modification in shapes and fragmentation, but it is important to note that the inclusive jets for which these measurements are carried out for might be less quenched than the recoiling jet from a high p_{T} gamma or leading jet.

Identifying the distribution of energy that goes out of the jet is challenging, as the underlying event (UE) in a head-on (central) PbPb collision is about three orders of magnitude larger [91, 99] than the magnitude of the lost energy. One advantage we have is that the UE is uncorrelated in angle with respect to the dijet direction, therefore the vectoral p_{T} sum of particles associated to the UE can be large but it points to random directions with respect to the dijet axis. The "missing p_{T}" method of CMS makes use of this fact to calculate the contribution of only the correlated

particles. For different p_{T} intervals, the p_{T} of charged particles are projected on the dijet axis in order to measure the spectra of particles that are correlated to the jet. This measurement showed that the spectrum of particles that contribute to the p_{T} balance in the event at $\Delta = \sqrt{(\eta^{trk} - \eta^{jet})^2 + (\phi^{trk} - \phi^{jet})^2} > 0.8$ [1] in PbPb collisions is softer with respect to MC simulations that do not have quenching effects, as shown in Fig. 4-5. This means that quenching effects extend above $\Delta = 0.8$. Therefore, the first item in the list is verified by experiments, but the differences between different mechanisms can show up at more quantitative level of how the p_{T} spectrum of out-of-jet-cone dissipation look like as a function of Δ. The large angle particle enhancement is observed also at RHIC by jet-hadron [20], and γ-hadron correlations[24], where the peak formed hadrons on the away side of triggered objects get broader and the particles at larger angles from this back-to-back peak have a softer spectrum.

There has been no direct measurement on the second common prediction, but there has been indications of it. The dijet asymmetry measurement by STAR shows that when jets with hard fragmentation are selected no dijet asymmetry enhancement is observed in AuAu collisions compared to pp collisions[162], while we know that jets at RHIC energies are quenched similarly as the jets in LHC when no fragmentation biases are introduced with the selection based on the results of inclusive jet spectra[204]. This is a sign that jets with smaller mass than average, are not getting as quenched and needs to be followed up with more direct measurements in which jet quenching effects are studied as a function of jet mass.

[1] Δ is denoted as ΔR in Ref. [99]

Chapter 5

CMS Detector and Software

5.1 CMS Detector

CMS detector is one of the four experiments placed on the ring of the Larger Hadron Collider (LHC).

The detector is named as Compact Muon Solenoid after its purpose of measuring momentum of muons very precisely thanks to the solenoid providing large magnetic field. The magnet is a superconducting solenoid of 6 m internal diameter, providing a magnetic field of 3.8 T. Although the measurements presented here are not using muons, every measurement benefits greatly by the opportunity of measuring momentum of charged particles with good precision. Muons are measured in gas-ionization detectors in the steel flux-return yoke outside the solenoid. Within the superconducting solenoid volume are a silicon pixel and strip tracker, a lead tungstate crystal electromagnetic calorimeter (ECAL), and a brass and scintillator hadron calorimeter (HCAL), each composed of a barrel and two endcap sections. Forward calorimeters extend the pseudorapidity [88] coverage provided by the barrel and endcap detectors. A drawing of the detector is shown in Fig. 5-1.

The measurements that will be discussed in the proceeding chapters use a large portion of the sub-detectors of the CMS detector, and these subdetectors are detailed below. A more detailed description of the CMS detector, together with a definition of the coordinate system used and the relevant kinematic variables, can be found in

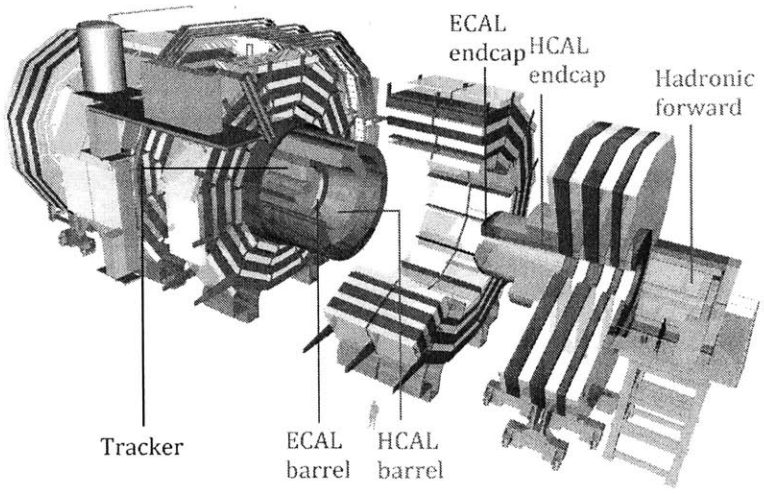

Figure 5-1: Drawing of CMS and its sub-detectors

Ref. [88].

5.1.1 Tracker

Tracker is used in finding the position of collision vertex, reconstruction of charged particles, muons and electrons, and indirectly in the reconstruction of neutral hadrons through the particle flow algorithm described in Section 8.2.1. Therefore it has central importance to the physics performance of the detector.

Tracker is composed of an inner pixel detector, and outer strip detector, both of these cover $|\eta| < 2.4$. The layout of the tracker is shown in Fig. 5-2.

Silicon Pixel Detector Silicon pixel detector is composed of 3 barrel cylinders and 2 forward disks. The closest pixel barrel cylinder is located at a 4 cm distance from the interaction point, the proximity of this layer allows good vertex resolution. These layers are composed of 65 M pixels. In the barrel, each pixel has an area of $100\mu m \times 150\mu m$ and a Lorentz angle of 23° at 3.8 T. The holes and electrons created by ionization during the charged particle passage diffuse towards the two ends of the sensor, top and bottom, and as they do so they drift with the Lorentz angle and this results in charge sharing on different readout modules. The analogue readout of the

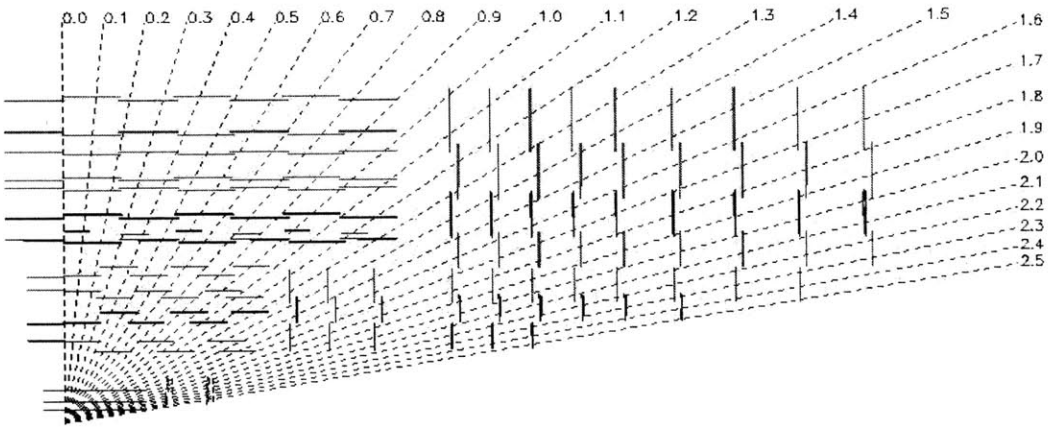

Figure 5-2: Layout of tracker demonstrating from bottom left (inside), top right(out) 3 layers of pixel barrel, 2 layers of pixel forward, 4 layers of tracker inner barrel, 3 disks of tracker inner disk, 6 layers of tracker outer barrel and 9 disks of tracker endcap. [117]

charge lets one to calculate the weighted center of the charge distribution. Therefore the passage of particles inside a sensor can be measured with much better spatial resolution then a binary readout would allow, the r-ϕ resolution obtained with this setup is 10 μm, and z resolution is 20 μm. In order to make use of the Lorentz drift also at the forward disks, the disks are tilted by and angle of 20°, so that magnetic field has a vertical component with respect to the electric field also in this region.

Silicon Strip Detector Silicon strip detector is composed of 4 parts, tracker inner barrel (TIB), tracker inner disk (TID), tracker outer barrel (TOB), tracker outer endcap (TEC), these layers add up to 10 M strips. Unlike the pixel detector one layer of silicon strip detector, provied 1D information on the hit of the track. However if two layers of strips are put one after the other with an angle between these layers 2D information can be obtained. Layers demonstrated with blue color in Fig. 5-2 are layers composed of double silicon strip layers. However, as shown in left panel of Fig. 5-3, if two particles pass through nearby strips the 2D information is blurred as there are 2 possible configurations which can create the same pattern, by the empty dots or by crosses. The filled crosses are where the particles passed through and the empty ones are called ghosts hits. In order to reduce the ghost hits the two

layers of strips are placed with a small angle (100 mrad) between the orientation of strips in a stereo format, rather than vertically, as shown in right panel of Fig. 5-3. The pitch of strips vary between 81 to 183 μm, and thickness between 320 to 500 μm providing a hit position resolution of $23-52$ μm in the $r-\phi$ and z directions.

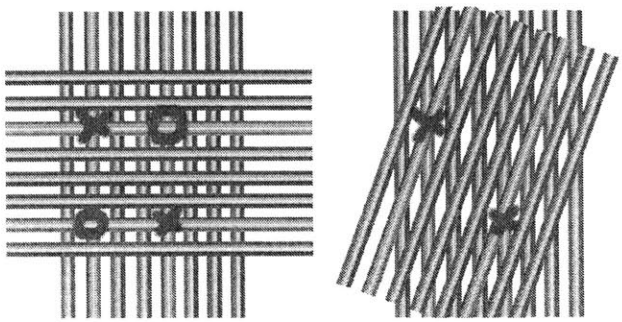

Figure 5-3: (Left) Drawing demonstrating the ghost hits (empty circles) that are formed by two layers of strips, when two particles hit these layers (hits shown with crosses). (Right) Cartoon showing the lack of ghost hits when two layers are placed in stereo configuration instead of vertically. The angle between strip directions is exaggerated in this drawing. In CMS the angle between strip directions in stereo layers is only 100 mrad.

The layout of the tracker is very important to understand the track reconstruction. Some particle trajectories coincide with larger number of layers than the others depending on their pointing direction and p_{T}. Having more layers on their trajectory these particles leave behind more hits and are reconstructed with more accurate p_{T}values. Moreover, The material budget needs to be kept low in order to avoid multiple scattering that would result in a radical deviation in the direction of the particle direction. The largest contributor of the material budget is the cooling system and the readout cables associated to the barrel sensors which pass in between barrel and forward tracker layers. In Fig. 5-4, where material budget as integrated over the path of the particle normalized by the interaction length (right panel) and radiation lenght (left panel) are shown, one can see that there is a peak in the material budget between $1.0 < \eta < 2.0$. A similar shape is observed in terms of the radiation length. Following the dashed lines marking these η values in Fig. 5-2, it can be seen that this

coincides with the zig zag empty space between disks in forward region and cylinders at barrel, these spaces shown empty in the drawing are filled with readout cables and cooling systems.

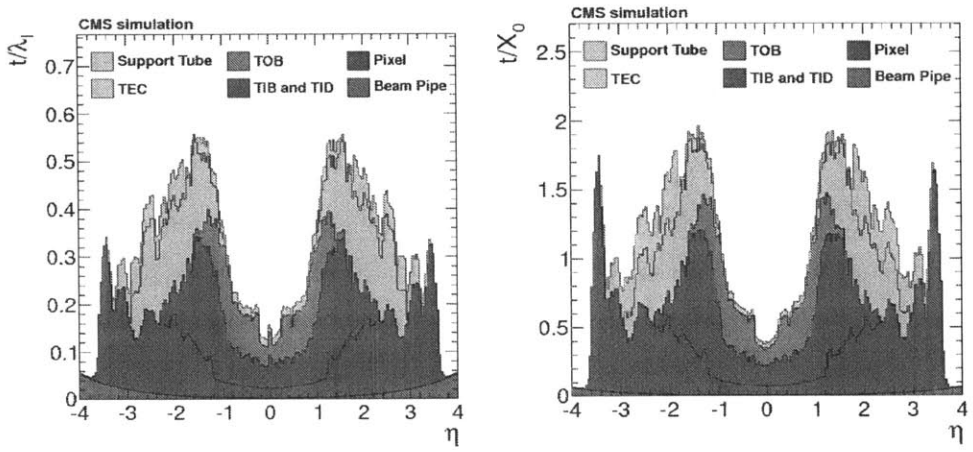

Figure 5-4: Integrated path of particle through material over its trajectory is shown function of η normalized to interaction lenght (left) and radiation length (right). [117]

Readout of tracker Before the electronic signal in pixel and silicon detector can be interpreted as a sign of particle passing through it, noise cleaning is carried out. The noise cleaning is called zero-suppression (ZS).

In pp collisions, strips are read if the signal is 5 times higher than the average noise, and pixels are read with a signal threshold of 3200 electron equivalent signal. The clusters formed by multiple sensors readouts have further thresholds, for pixels the clusters are required to have more than 4000 electron equivalent signal, for strip clusters the signal is required to be 3 times larger than the channel noise.

In PbPb collisions, for pixels same ZS as in pp collisions is applied, but for strips a different ZS algorithm is used. Although it is commonly referred as ZS it contains more parts then just ZS. This algorithm has three steps; subtraction of common mode, pedestal subtraction and finally ZS. In PbPb collisions strip detectors are exposed to large rate of particle passage resulting in highly-ionized particles which causes shifts and slopes in a group of 128 strips (a single APV) to build a common shift in their

baseline. The common mode is calculated using iterative median method in which the median adc count of all strips is calculated, then recalculated using only strips with an signal below the calculated median plus 2σ times the strip noise, and then recalculated a third time in the same manner. This value is subtracted from all the strips in the APV.

The pedestal subtraction is done where average signal in each strip is set to zero, and finally ZS is applied by each strip signal to be greater than 3 times the noise, and strip clusters to be 2 times greater than the average noise in the clusters. The final cluster is removed if the total signal in this is less than 5 times the quadratic sum of noises in each strip belonging to it.

Hit reconstruction Once the signal is read and noise is cleaned this signal is turned into hits with central points and widths. Pixel hits are 1-D and strip hits can be 1-D or 2-D. Hit positions are calculated by the geometric center of the cluster taking into account the Lorentz drift. The effective widths are calculated by subtraction the effect of diffusion with Lorentz drift and spread in length due to the thickness of the sensor and so the path the particle takes inside the sensor horizontally inside the sensor. All pixels that carry information of a single hit are clustered together. The cluster shape of an example hit in pixel barrel detector is shown in Fig. 5-5. After the local hits positions are determined within layers of detectors, it is translated to global CMS coordinates, using the information of alignment of each of the layers. Alignment is calculated using cosmic rays passing through the detector with 3-4 μm precision, as explained in Refs. [89].

5.1.2 Calorimeters

Calorimeters of CMS are aimed to measure photons, electrons and jets, and they have a hermetic design that would allow the measurement of precise missing E_T for neutrinos to be used in SM measurements, and for SUSY and beyond standard model searches. The hermeticity was not designed for heavy-ion collisions, but we also benefit from this design as it lets us study the jets production to large η, and

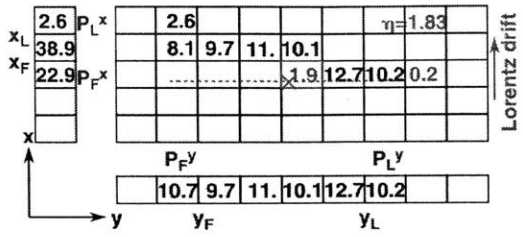

Figure 5-5: Cluster shape for a barrel hit where the signals in each pixel are given in kiloelectrons is shown. Those shown in green are below the readout threshold. The track projection is shown as the dashed red line. The x- and y-projections are also shown as one-dimensional arrays. The coordinates of the boundaries between the first and second pixels (x_F/y_F) and the next-to-last and last pixels (x_L/y_L) and the charges of the first and last pixels $P_{F/L}^{x/y}$ are also shown. [216]

collective medium effects that extend over large η ranges.

The different parts of calorimeter are listed below.

Pre Shower (PS) PS is used for identification of electrons in the barrel and for identification of neutral pions in the endcap regions. It is composed of 2 layers of lead radiators, each of which are followed by a silicon strip sensor. Lead radiators are used to initiate the electromagnetic shower.

ECAL ECAL is composed of lead tungstate crystals with silicon avalanche photodiodes in barrel and vacuum phototriodes in the endcap to multiply the photons from the crystals. Crystals have radiation lengths of $X_0 = 0.89cm$, and Moliere length of 2.2 cm. In the barrel, the depth of crystals is 25.8 X_0, and it allows good containment of electromagnetic showers. In $\Delta\phi$ and $\Delta\eta$ each crystal covers 0.0174. In the endcap the depth of crystals is $24.7X_0$. Due to the rapid change of η in forward region the crystals are not arranged in constant intervals of $\Delta\eta$, instead they have equal cross section in x and y ($28.6 \times 28.6mm^2$). ECAL barrel reaches $|\eta|$ of 1.479 and endcap extends this range up to $1.479 < |\eta| < 3$.

HCAL HCAL is a sampling calorimeter composed of brass layers interlaid with scintillator tiles. In the barrel which extends up to $|\eta| < 1.3$, the scintillator tiles have a surface of $\Delta\eta - \Delta\phi$ of 0.087.087. The end cap covers $1.3 < |\eta| < 2$, granularity of tower size is same as in barrel for $1.3 < |\eta| < 1.74$ and $\Delta\eta$ size increases above this value.

HF HF is a very important detector for PbPb collisions, because it is used to reject the non-collision events and in determination of collision centrality classes. HF is a part of the hadronic calorimeter system, but it is better to consider it as a separate sub-detector, because it is not a brass/scintillator sampling detector as HCAL barrel and endcap. It is a Cherenkov steel/quartz fibre where detection of signal is done with Cherenkov light produced in quartz fibres. Fibers are bundled into towers of 0.175×0.15 in $\Delta\eta \times \Delta\phi$.

Chapter 6

Event selection and centrality classification

In this Chapter, we go through the selections that allow us to select good collision events to analyze and methods of selecting on different initial collision geometries in PbPb collisions, and efforts to extend those methods to pPb collisions. The collision event selection is discussed in Section 6.1. The cause of differences in initial state geometries are discussed in Section 6.2. The experimental methods used by CMS to select on different geometries are discussed in 6.3.

6.1 Selection of collision and dijet events

Triggers: The CMS online event selection employs a hardware-based Level-1 trigger and a software-based high-level trigger (HLT). Events used in dijet analyses are selected using an high-p_{T} inclusive single-jet trigger in the HLT, requiring a calorimeter-based jet with transverse momentum above a given threshold. The momentum threshold used in analysis of pp, and PbPb events are chosen to be 80 GeV and for the analysis of pPb events it is chosen to be 100 GeV. For all the collision systems the trigger becomes fully efficient for events with a leading jet with $p_{\mathrm{T}} > 120$GeV with all the anti-k_T R parameters used in offline reconstruction of jets.

Dijet selection: The pseudorapidity range for jets in pPb collisions extend up to $|\eta| < 3$. In pp and PbPb collisions, leading and subleading jets are selected among the set of jets within $|\eta| < 2$ sorted in p_{T}, because of lack of sufficient control on JES above this range in PbPb multiplicities. Jets in the event are ordered in p_{T} to find the highest, leading, and second highest, subleading jet. Further selections of η values are applied on η_1 and η_2, where index 1 always refers to leading and 2 to subleading jet, when necessary. The specific requirements of η of individual jets are described later during the definition of each observable in Section 10.1.

In the light of our physics goals (see Chapter 9) dijet events are chosen to allow a sufficient gap between the leading and subleading jet p_{T} for the study of asymmetric dijet events in search for jet quenching effects. Dijet events are required to have a leading jet with $p_{\mathrm{T},1} > 120$ GeV and subleading jet with $p_{\mathrm{T},2} > 50$ GeV in pp and PbPb collisions, while in pPb collisions a lower threshold of $p_{\mathrm{T},2} > 30$ GeV is picked. In addition, to enhance a dijet topology jets are required to be back to back in azimuthal angle. In pp and PbPb collisions azimuthal angle difference is required to satisfy $\Delta\phi_{1,2} > \phi_1 - \phi_2 > 5\pi/6$, and in pPb collisions $\Delta\phi_{1,2}$ is required to be greater than $3\pi/2$.

Collision selection in PbPb: A minimum bias event sample is selected by employing the cleaning procedure to remove background, beam gas, PKAM (Previously Known As "Monster") events and ultra-peripheral-collision events from the selected events standardized by previous analyses. The procedure includes the following,

1. Events where any of the beam scintillator counter (BSC) halo bits fired (L1 Technical Trigger bits 36, 37, 38 or 39) were excluded from the analysis. This happens only in 0.1% of the events triggered by the HLT jet trigger with 80 GeV threshold, thus any possible biases are negligible.

2. A reconstructed primary vertex with at least 2 tracks was required, removing collisions which were not inelastic hadronic interactions(e.g. beam-gas, UPC, calorimeter).

3. The cut used to remove PKAM events in PbPb collisions is a compatibility requirement between first layer pixel cluster length and angle with respect to the vertex location, the cluster compatibility is check is done the same way as in the first step of vertex reconstruction we described in Section 8.1.

4. At least 3 towers in the HF detectors on both sides of the interaction point, with at least 3 GeV total deposited energy per tower, were required in the PbPb (pp) analysis .

5. In order to remove events with residual HCAL noise that are missed by the calorimeter noise rejection algorithms [119, 120]

Collision selection in pp and pPb: Step 2, 4 and 5 listed for PbPb collisions are applied, with a small difference in 4 where only a single tower is required to have energy greater than 3 GeV. In addition, the standard beam scraping filter is used[163]. This filter removes events where the number of reconstructed tracks is larger than a certain threshold but the fraction of google quality tracks is low. If the events contain a minimum of 10 tracks, the minimum fraction of good quality tracks is required to be larger than 25%, where good quality refers to the satisfaction of the "high purity" requirement, which is discussed in Chapter 8.

In pPb collisions, there is a $\sim$3% probability of at least one additional interaction occurring in the same bunch crossing. Events with more than one interaction are referred to as "pileup events". A pileup rejection algorithm developed in Ref. [103] is employed to select a clean single-collision sample, which removes 0.01 % of events without pileup while cleaning $>$ 90% with pileup. In pp collisions, the pileup probability is significantly larger ($\approx$ 23%). However, due to the nature of the analysis a pileup rejection filter algorithm was not needed. Also the pileup events are used in the analysis, but charged particles coming from pileup vertices are rejected by requiring each particle to come from a restricted distance within the primary vertex. The reason why pileup in pPb collisions needs to be cleaned is because the analysis in pPb collisions were done as a function of activity in the forward calorimeter, and the high

activity events were of special interest. The pileup contribution in the calorimeters cannot be cleaned, because the vertex information is not available as in the case of tracks. If pileup events are not cleaned this causes large systematic uncertainties in such events because forward energy produced by pileup interaction adds up to the interaction of interest with dijet production. In the highest activity events used in the analysis the probability of contamination with pileup events after the rejection filter is found to be smaller than 2% [110].

Further information on event selection can be found in Refs. [101, 96, 98, 94].

6.2 Selecting different initial state configurations

In relativistic collisions, the interaction of nuclei and hadrons happen in a snapshot. At this moment in time each collision can be described as a frozen configuration of nucleons inside the nuclei and frozen configurations of partons inside these nucleons. Experimental observables sample these configurations based on their properties at the end of their evolution in time, with the aim of measuring average behavior of collisions with different initial states, for example the region of overlap between two nuclei for studies as a function the size of the medium formed in heavy-ion collisions.

The question is whether or not the evolution of very different initial configurations can lead to similar final states. The answer is "not very often" if the amount of variation among the initial configurations for events in a given class of final state events is smaller than the variations of that initial state property for events in different final state classes, i.e. when fluctuations are smaller than the separation of mean values. In fact, the term fluctuation only makes sense in this case. If an initial state property gets washed out by competing initial state effects or final state interatctions, the possible initial configurations for a final state class follow wide probability distribution and the answer of the question becomes "very likely". In order to be able to interpret results of measurements correctly and factorize the initial or final state effect of interest, it is crucial to understand the initial state distributions and their final state outcomes.

In the next chapters we will investigate three types of colliding species; pp, pPb and PbPb collisions. The basic distribution functions that govern probabilistically how the snapshot will look like, are the parton distribution functions (PDFs), nuclear modification of these and the distribution of nucleons inside nucleus. Parton distribution functions are discussed in Section 3.3 and also later in Section 3.1 govern initial state of pp collisions. The effective influence of neighboring nucleons is described by a modification in PDF in nucleus compared to nucleon is described by nuclear PDF (nPDF), governing the initial state of pPb collisions. In PbPb collisions on top of these the of position of nucleons are taken into account ignoring the interactions between them, where the effect of having multiple nucleons is contained in nPDF.

6.2.1 Glauber model

The Glauber model describes the spatial distribution of nucleons inside the relativistic nucleus and the number of collisions, assuming that each nucleon-nucleon interaction happens with same cross-section, σ_{NN}. The probability density of having a nucleon is given by the nuclear potential described by Wood-Saxon distribution

$$\rho(x, y, z) = \frac{1}{e^{(r-R)/\delta} + 1}, \tag{6.1}$$

where $R = (1.2\mathrm{fm})A^{1/3}$ is the nuclear radius and δ which is typically 0.5 fm is the thickness which determines how smoothly the potential turns on at the edges of nuclei. The Lorentz contracted nuclei become planar, and the density of nucleons in this 2D surface is described by the thickness function

$$T_A^{x,y} = \int dz \rho(x, y, z), \tag{6.2}$$

For two colliding nuclei with mass numbers A and B separated in x direction by an impact parameter b, number of nucleons per area that participate in the interaction is

$$N_{\rm part}^{AB}(x,y,b) = AT_A(x-b/2,y)(1-e^{-B\sigma_{\rm NN}T_B(x+b/2,y)}) + BT_B(x-b/2,y)(1-e^{-A\sigma_{\rm NN}T_A(x+b/2,y)}), \tag{6.3}$$

$N_{\rm part}$ is what drives the soft particle production in heavy ion collisions, as shown in Fig. 6-1. The cross section for hard interactions is driven by the number of binary collisions. For processes with small cross section,

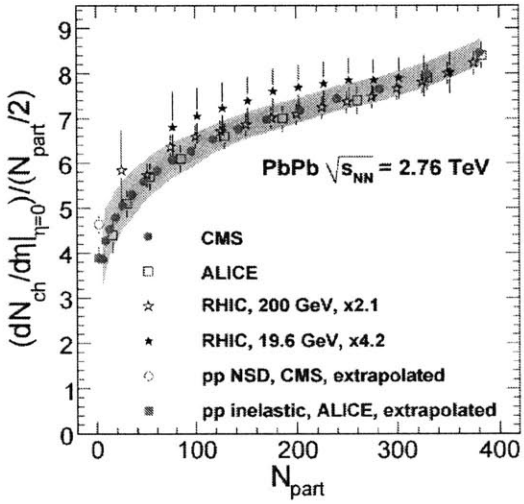

Figure 6-1: $N_{\rm part}$ dependence of particle production per pseudorapidity at RHIC and LHC, taken from Ref. [90].

$$N_{\rm coll}^{AB}(x,y,b) = \sigma ABT_A(x-b/2,y)T_B(x+b/2)y, \tag{6.4}$$

In MC implementations, nucleon configurations are created randomly according to $T_A(x,y)$ and pairs of nucleons from each nuclei are checked for overlaps with each other for an impact parameter b. Nucleons are approximated as solid spheres with $R=\sqrt{\sigma_{NN}}$ and collision happens if the spheres touch each other. The input of these MC implementations are σ_{NN}, nucleon species and a parameter that does not allow the position of two nucleons to be closer than a certain value to each other, in order to avoid overlaps which are not allowed because of Fermi exclusion principle.[34] It is

also possible to model the nucleons with smooth density distributions.

In order to demonstrate the arbitrariness of choice of using solid spheres for nucleons, the distribution of N_{part} and N_{coll} for an example PbPb collision with $b = 3.4$ fm is shown in Fig. 6-2 for solid sphere nucleons and for nucleons wrapped with Gaussian density distributions colliding with each other. The choice of a Gaussian distribution here is not based on measured nucleon density profiles, but a way to show that smoothing nucleon profiles effect the initial overlap area, therefore ϵ_n values that are defined as in Eq. 2.3. This in turn produces different v_n values by hydrodynamic evolution given that there are tuning parameters such as viscosity in the hydro models. The lumpy profiles obtained by Glauber model were shown to give larger eccentricity values and produce the p_{T} dependent v_n values more accurately than some models that model the color charges within the nucleons. Models that accounts for the color charges inside the nucleon with tunable parameters, which allows to determine how lumpy the collision profile will be, can reproduce large eccentricities obtained by Glauber initial state and agree with data for v_n values obtained [145].

In Fig. 6-3 correlation between impact parameter and integrated N_{part} values are shown in pPb and PbPb collisions as a function of impact parameter at 5.02 and 2.76 TeV corresponding to $\sigma_{NN} = 70$ mb and $\sigma_{NN} = 64$ mb, respectively, for colliding solid spheres. It can be seen that the root mean square of this mean value is larger for pPb collisions than PbPb collisions.

Gribov model In the Glauber model subsequent interactions between nucleons take place without a change in σ_{NN}. In Gribov theory, the subsequent interactions are suppressed and each intermediate states collisions have modified cross-sections with nucleons in the target. This treatement is rather complicated involves Reggeon calculations, for a review on Gribov's work see Ref. [130].

6.2.2 Initial state of proton

In a Glauber model, each binary collision is assumed to happen with the same cross-section, and the variety of different nucleon-nucleon collision configurations are not

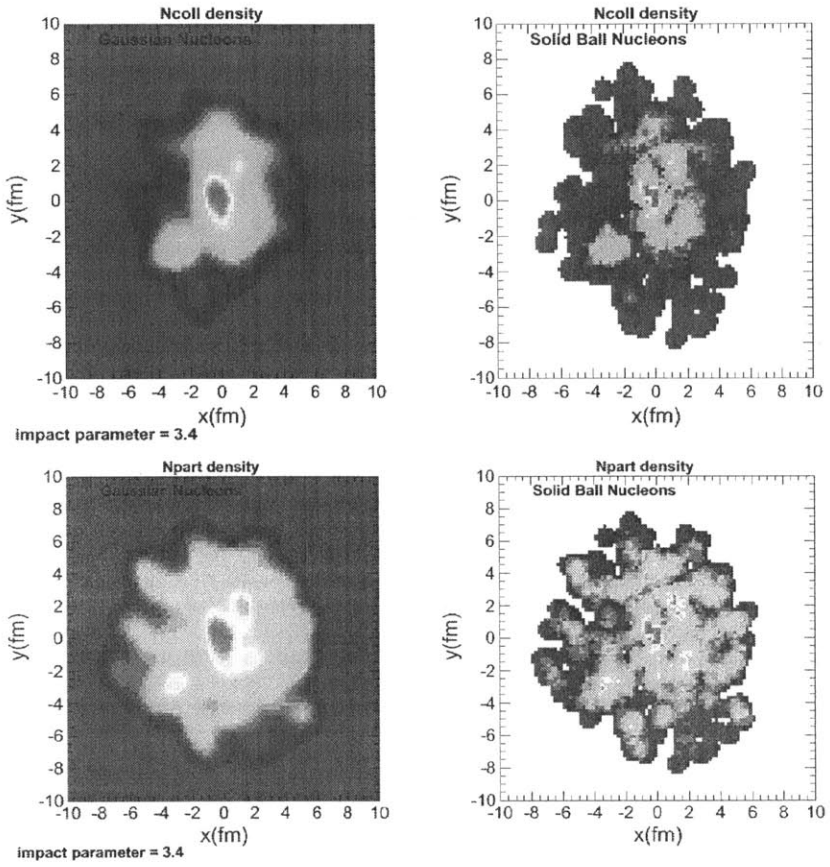

Figure 6-2: N_{part} and N_{coll} distributions in a single event for two nucleon descriptions, gaussian energy densities and solid spheres.

taken into account, which is not an accurate description for collision of smaller systems such as pPb collisions, but work efficiently for nucleus-nucleus collisions. Below we list some reasons proton-proton collisions differ from each other.

Constraints of total available energy We have discused earlier in Section 3.3 that the initial state of proton collisions have a wide range of distributions at least for interactions where momentum transfer is large. It is natural to observe that a proton where most of the energy is carried by a valence quark with $x \approx 1$ would not have a wide spatial energy distribution, because of the lack of available energy. A parton like this would also not produce a significant amount of ISR. Thinking about how this is implemented in PYTHIA, i.e. the downward evolution in virtuality from

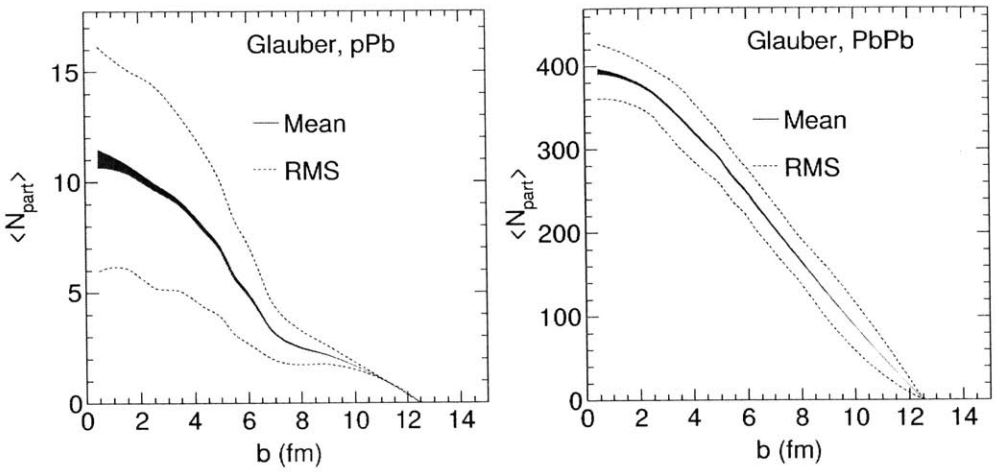

Figure 6-3: Number of participating nucleons, in (left) pPb and (right)PbPb collisions. The filled line shows the mean the width of it the statistical uncertainty and the dashed lines show the RMS of the distributions.

maximum energy scale to the scale of interaction, when a parton carries most of the proton energy not much phase space is left for ISR. These: The fluctuations in spatial distribution of color charges inside proton, the parton distribution functions (generalized parton distribution functions to be more accurate), and the amount of ISR multi parton interactions in MC generators are all related and are different expressions of same phenomenon.

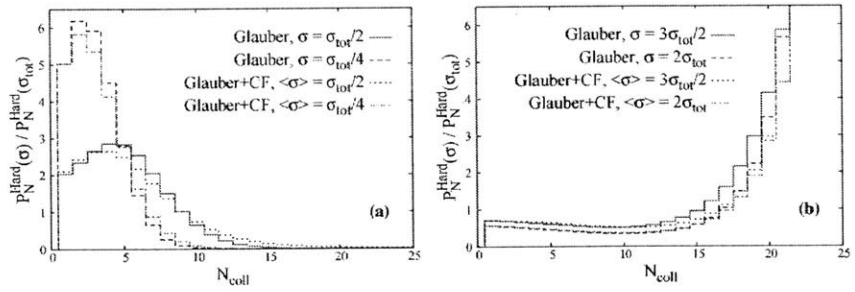

Figure 6-4: Ratio of the probabilities PN of having $N = N_{\rm coll}$ wounded nucleons for configurations with different $\langle\sigma(x)\rangle$ and $P_{\rm N}$ for $\sigma = \sigma_{\rm tot}$, for cross-sections (a) smaller and (b) larger than average.

There are models [35], where fluctuations of proton size is allowed to be a free parameter, and a relationship produced between size of proton and probability of

having a hard-scattering collision with a given x value are correlated. The change in size of the proton then reflects to the number of collisions in the Glauber model, as shown in Fig. 6-4. For protons with large x partons, $< \sigma >< \sigma_{\rm tot}$ as in panel (a), and $N_{\rm coll}$ distribution shift towards smaller values compared to $\sigma_{\rm tot}$, and vice versa for protons with small x. In Section 9.6, a toy model which produces a similar effect i.e. anti correlation between x and $N_{\rm coll}$ is explained.

Impact parameter of proton-proton collisions It is true that once most of proton energy is taken by a single parton not much energy is left for the rest of the interactions. However, it is also possible to have a proton configuration that has a small size and a large x parton without this parton interacting during the collision. Having more energy produced in a collision is an indication of more multiple interactions, and implies that the impact parameter between the two protons are small. The high x partons, which are most likely to be located at the center of the proton, have higher chances of interacting when the impact parameter of proton proton collision is small. In such cases an opposite effect is produced, i.e. a direct correlation between soft particle production and high $p_{\rm T}$ jet events. This correlation is also produced by PYTHIA as shown in Fig. 6-5.

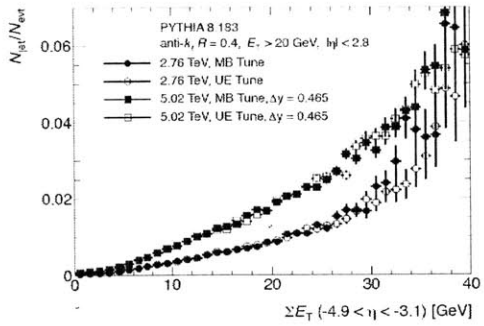

Figure 6-5: Taken from Ref. [190], number of jets per event as a function of total forward E_T in PYTHIA simulations.

To summarize, the initial state of collisions have several sources of fluctuations, although in some cases it is not fair to call these fluctuations, because the deviations

from a "mean" are large and the form of distributions start matter, as in the case of parton distribution functions. In probing the final state effects due to medium formed in heavy-ion collisions, initial state configurations are not expected to have a large impact on jet quenching effects we are interested in studying and the correlations between hard scattering process and soft particle production get washed out as a result of large number of collisions that take place. However for smaller collision systems, such as pPb, if one tries to make measurements on different initial colision geometries these effects need to be considered.

6.3 Centrality classification

After choosing events with collisions and which has a dijet pair produced, we would also like to have control of the impact parameter of collision, so that in PbPb collisions size of the medium will be larger and therefore the effects of jet quenching we are interested in studying can be enhanced. Moreover, as discussed in Chapter 2, the observation of flow effects in pPb collisions have raised the question of whether a similar medium is formed in small colliding systems as well. Therefore, having a control of impact parameter of pPb collisions and studying events where many collisions happen in one event is of interest as well. Selecting on certain impact paramer ranges would also let us measure impact parameter dependent nPDFs, in case there no jet medium interaction is observed.

In general particle multiplicity scales with N_{part}, which is correlated to impact parameter in Glauber model as shown in Fig. 6-3. Therefore, selecting on events in which large number of particles are produced one can obtain a set of collisions with small impact parameter. However selecting on multiplicity in the region of measurements might bias the observables, as an example by requiring a large particle multiplicity in mid-rapidity region one might favor the events containing multiple jets, which will have different than average dijet properties. In order to avoid correlation between centrality selection and the measured observable events are classified according to their activity in the forward region. To define the centrality classes

transverse energy in the HF is used.

6.3.1 Centrality in PbPb

In PbPb collisions the centrality is determined using the total sum of transverse energy of calorimeter towers in the HF region (covering $2.9 < |\eta| < 5.2$). The distribution of this total transverse energy was used to divide the event sample into bins, each representing 0.5% of the total hadronic nucleus-nucleus interaction cross section. Fig. 6-6 shows in the left panel the centrality variable for the collection of minimum bias events (black open histogram) and the jet-triggered sample (red cross-hatched histogram). The minimum bias histogram exhibits a flat shape by construction, while the jet-triggered events are weighted towards more central events. The shift in the jet triggered sample is a result of increase in number of binary collisions as overlap between two nuclei increase. As the number of binary collisions get larger so does the probability of having a hard scattering interaction in one of those. The right panel of Fig. 6-6 shows the actual distribution of the total HF energy of these same two samples.

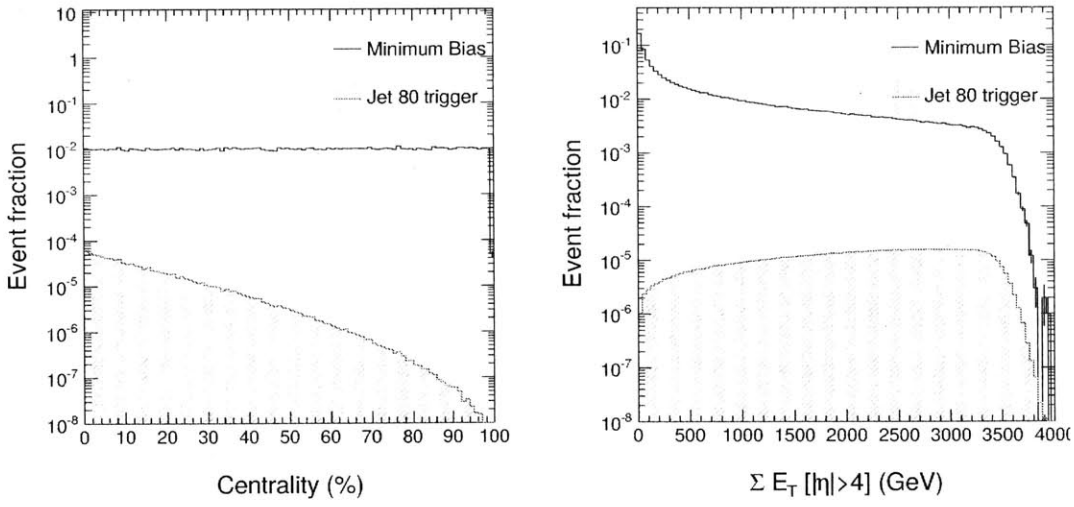

Figure 6-6: Centrality distributions for minimum bias and jet-triggered events. The latter tend to be biased towards more central events where the number of binary collisions is large. This effect is taken into account when constructing the MC reference plots.

In PbPb events, the properties of selected event classes in percentages of cross-section do not change significantly based on the variable used for centrality classification. This is due to the tight correlation between multiplicities of particles produced in different η regions, because of the coherent particle production in PbPb collisions which is a result of strongly coupled nature of the medium that also generates flow as discussed in Chapter 2. As an example, in Fig. 6-7 the correlation between total E_{T} in HF on two sides and of the detector and the correlation between total HF E_{T} and number of pixel hits are shown.

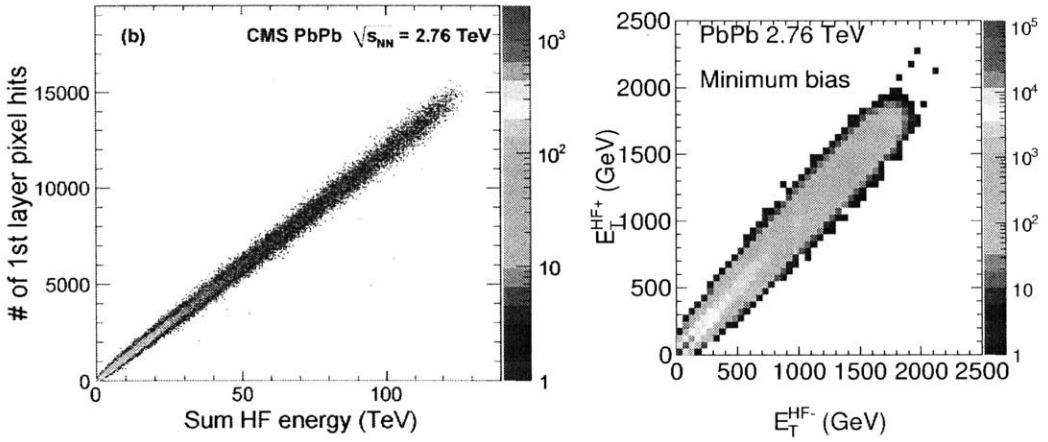

Figure 6-7: (Left) Correlation between the number of pixel hits and HF total energy, and (Right) correlation between total E_{T} in HF in $+z$ direction, i.e. $\eta > 2.9$, and total E_{T} in HF in $-z$ direction, i.e. $\eta < -2.9$ in PbPb collisions.

6.3.2 Centrality in pPb

Centrality in pPb collisions is a misnomer, in the sense that we apply a very similar procedure to what is used in PbPb collisions to define subsets of events according to activity in the HF, but in pPb collisions, the resulting event classes do not correlate with impact parameter or other geometric quantities like N_{part} as they do in PbPb collisions. The name given to this event selection is simply inherited from PbPb collisions, and the initial aim of choosing on different impact parameter events, which experiments failed to achieve in this way. Still this classification showed interesting effects related to proton structure. Keeping this in mind here is how the centrality in

pPb is defined in intervals of the raw transverse energy measured in the HF detectors within the pseudorapidity interval $4.0 < |\eta| < 5.2$, denoted as $E_{\mathrm{T}}^{4<|\eta|<5.2}$. The HF transverse energy distribution for the selected dijet events in comparison to that for minimum bias events is shown in Fig. 6-8 in the left panel, and can be compared to 6-6 for PbPb collisions. It can be seen that similar to the PbPb case the selection of a high-p_{T}dijet leads to a bias in the $E_{\mathrm{T}}^{4<|\eta|<5.2}$ distributions toward higher values. The η interval used in the selection is slightly different than in PbPb collisions, this pseudorapidity interval is chosen in order to separate the transverse energy and dijet measurements by a pseudorapidity gap of at least one unit ($3.0 < |\eta| < 4.0$).

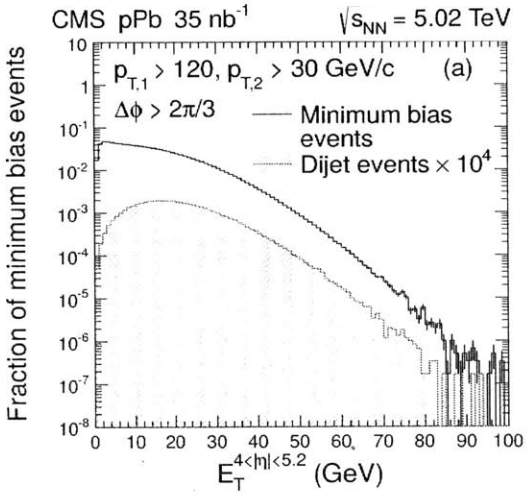

Figure 6-8: (Left) Raw transverse energy measured by the HF detector in the pseudorapidity interval $4.0 < |\eta| < 5.2$ for minimum bias collisions (black open histogram) and dijet events passing the dijet selection defined in this analysis (red hatched histogram).

The ambiguity in definition of event classes can be seen by the large width of the correlation between a variety of possible choices of parameters that could be used to define event activity, e.g. in Fig. 6-8 the correlation between $E_{\mathrm{T}}^{4<|\eta|<5.2}$ and the raw number of tracks originating from the primary vertex ($N_{\mathrm{trk}}^{\mathrm{offline}}$) with $|\eta| < 2.4$ and $p_{\mathrm{T}} > 0.4$GeV (before the tracking efficiency correction) is shown in the left panel. A broad correlation between the two quantities is observed in the inclusive pPb collisions. Similarly, the correlation between the raw transverse energy measured by

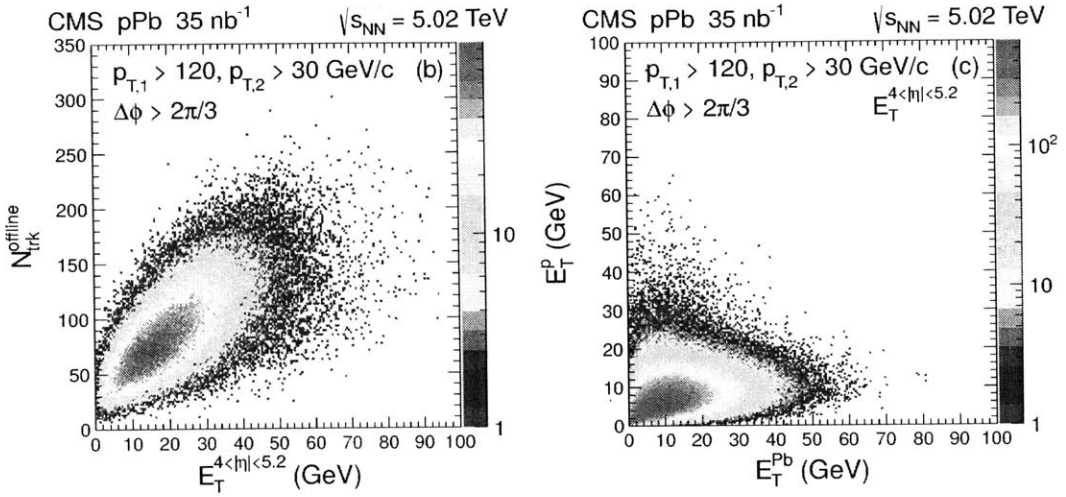

Figure 6-9: (Left) Correlation between the raw number of reconstructed tracks from the primary vertex ($N_{\rm trk}^{\rm offline}$) with $|\eta| < 2.4$ and $p_{\rm T} > 0.4$GeV and raw transverse energy measured by the HF detector in the pseudorapidity interval $4.0 < |\eta| < 5.2$ ($E_{\rm T}^{4<|\eta|<5.2}$)(Right) Correlation between the raw transverse energy measured by the HF in proton ($E_{\rm T}^{p}$, measured in the pseudorapidity interval $4.0 < \eta < 5.2$) and lead ($E_{\rm T}^{\rm Pb}$, measured in the pseudorapidity interval $-5.2 < \eta < -4.0$) directions.

the HF detector in the pseudorapidity interval $4.0 < \eta < 5.2$ (in the proton direction, $E_{\rm T}^{p}$) and in the pseudorapidity interval $-5.2 < \eta < -4.0$ (in the lead direction, $E_{\rm T}^{\rm Pb}$) shown in Fig. 6-8 in the right panel is not as tight as it was in PbPb collisions. To see the difference between pPb and PbPb collisions compare Figs. 6-7 and 6-9.

Table 6.1: Fractions of the data sample for each HF activity class calculated for the minimum bias data passing DS selection and for the jet-triggered data passing dijet selection. The fourth column shows the average multiplicity of reconstructed charged particles per bin with $|\eta| < 2.4$ and $p_{\rm T} > 0.4$GeV ($N_{\rm trk}^{\rm corrected}$). The fifth column gives the mean HF activity in each class calculated from DS events.

$E_{\rm T}^{4<|\eta|<5.2}$ range (GeVns)	Fraction of DS data	Fraction of dijet data	$\langle N_{\rm trk}^{\rm corrected}\rangle$ in DS data	$\langle E_{\rm T}^{4<|\eta|<5.2}\rangle$ (GeV) in DS data
<20	73.1%	52.6%	33 ± 2	9.4
20–25	10.5%	16.8%	75 ± 3	22.4
25–30	7.1%	12.7%	89 ± 4	27.3
30–40	6.8%	13.0%	108 ± 5	34.1
>40	2.5%	4.9%	140 ± 6	46.3

In order to demonstrate the insensitivity of event activity selection on geometric quantities, $N_{\rm part}$ distributions for different centrality classes, boundaries of which

are listed in 6.1, are shown in Fig. 6-10 according to implementation of Glauber model and particle generation in HIJING simulations. This distribution depends on the model, but in all generators similar wide correlations were observed. The highest activity 2.5 % events have large overlaps in N_{part} with lower activity classes.

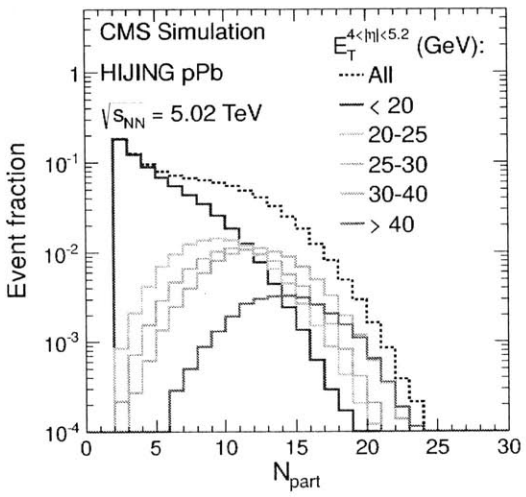

Figure 6-10: Number of participating nucleons (N_{part}) in the HIJING MC simulations for five different $E_{\text{T}}^{4<|\eta|<5.2}$ bins and the cumulative distribution without any requirement on $E_{\text{T}}^{4<|\eta|<5.2}$.

6.4 Summary

Using CMS detector, especially the forward calorimeter HF, it is possible to select collision events and our high-level-trigger allows us to obtain a large collection of jet events. In addition, in PbPb collisions it is possible to select collisions with different impact parameters based on the fact that particle production is correlated with the number of wounded nucleons, N_{part}, which in turn is correlated to impact parameter. Total forward E_{T} in the event is commonly used to select collisions with different centralities, instead of particle production in mid-rapidity which might bias the observables one wants to study as a function impact parameter.

However, in pPb collisions applying same machinery does not provide as tight

correlations as observed in PbPb collisions between impact parameter and N_{part}, nor between N_{part} and number of produced particles. Therefore, the definition of centrality classification becomes ambiguous. For these small systems, number of particles produced in the event are largely effected by the properties of proton such as its size and parton distributions inside proton. The size of proton and distribution of momentum of partons is inversely related, meaning that when the proton is wide the partons are softer. Large total E_{T} produced in the forward detector is an indication of a fat proton for which partons are more likely to have smaller x values. There is an additional factor which produces an opposite effect, the fact that large x partons are more likely to be found at the center of the proton. This produces a positive correlation between forward E_{T} production and x values. The model described in Chapter 9 addresses the former effect, i.e., negative correlation between E_{T} and x values.

Chapter 7

Dijets

Back-to-back parton production is the most basic hard QCD process which appears in standard QFT text books such as Ref. [191]. As a result, and back-to-back jet production is well understood. This can be seen in left panel of Fig. 7-1 where the azimuthal angle difference between dijets are shown to agree very well with NLO QCD calculations whenever the jets are close to being back-to-back. Because dijet properties are shown to be well described by QCD calculations and produced in copious amounts at hadron colliders, in pp collisions they are often used in searches for new physics [15, 165] at LHC. Instead, for our purposes dijet production in pp collisions serve as a QCD reference to study jet production without jet quenching effects. The aim is to compare them to measurements in PbPb collisions collected at same $\sqrt{s_{\mathrm{NN}}}$ and isolate the effects of the medium, keeping in mind that nuclear effects that are present in the initial state of collisions can also result in modifications of dijet properties in PbPb collisions.

Jet production in heavy ion collisions, which includes the effects of jet quenching, are often compared to jet production in pp collisions with same kinematic cuts on jets, i.e. requirements on p_{T} and η. However, this comparison is not quite fair, as we are comparing quenched jets which relate a particular initial parton energy to jets in vacuum with lower parton energies. The development of parton showers for initiating partons with different p_{T} are already different in vacuum, as a result part of the differences in jet properties in PbPb and pp collisions source simply due to

the fact that we are not using a perfect reference for our purposes. It is possible to avoid this by tagging the hard scattering event with a photon, which does not interact with the medium and study the recoiling jets with an as low as possible jet p_{T} selection. The parton initiating the jet which is quenched in the medium has an initial $p_{\mathrm{T}} \approx p_{\mathrm{T}\gamma}$, up to semi-hard splittings forming third (and multi) jets. Therefore, comparing jets in medium to jets in vacuum for events with same $p_{\mathrm{T}\gamma}$ allows us to make a better comparison. The study of dijet events is motivated by a similar idea, where γ is replaced by the leading jet. The leading jet interacts with the medium as well, as a result it is not as good reference as γ. However, on average leading jets loose less energy compared to subleading jets, which lets us tag the quenched low p_{T} jet with it.

In this chapter, basic dijet observables and their use in the field are discussed.

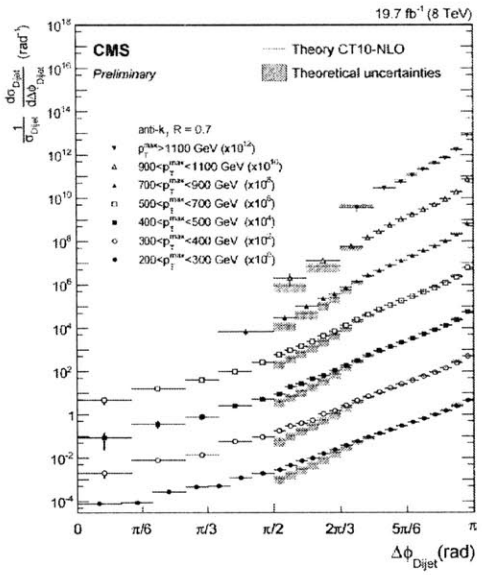

Figure 7-1: Taken from Ref. [124], azimuthal angle correlations between leading and subleading jet compared to NLO calculations

7.1 Basic observables

7.1.1 Dijet p_{T} asymmetry

In vacuum, at tree level jets in dijet events have equal p_{T} pointing in opposite direction in azimuth. However, semi hard splitting of one of the back-to-back partons, can cause significant asymmetry in the p_{T} of the leading and subleading jet in the event. In pp collisions, it is the semi-hard splittings, forming a third jet that drives the asymmetry in dijet events. In addition to effect of third jet, clustering jets with R parameters that are smaller than the width of the shower of the parton can cause significant change in the p_{T} of each jet, resulting in differences in dijet asymmetry and asymmetry of leading and subleading partons after the semi hard splitting process. Therefore, dijet asymmetry depends on the R parameter and dijet events get more balanced using larger R parameters, which capture larger fraction of p_{T} of partons as shown in Fig. 7-2.

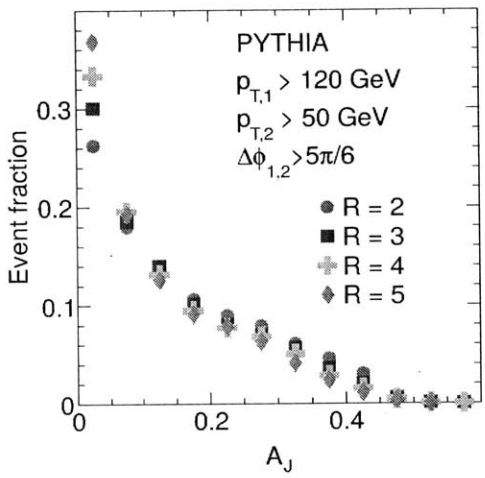

Figure 7-2: Dependence of A_J on anti-k_{T} R parameter for generator level PYTHIA events.

In PbPb collisions, due to jet quenching all the jets in the event are modified. The amount of modification of each jets is different depending on its fragmentation, fluctuations in energy loss processes and due to the difference of path length they travel [185]. Jets with more quenching are more likely to end up being subleading jet,

which results in an overall increase in the imbalance of the dijet pair, where imbalance is quantified by the dijet p_{T} asymmetry,

$$A_J = \frac{p_{\mathrm{T},1} - p_{\mathrm{T},2}}{p_{\mathrm{T},1} + p_{\mathrm{T},2}}, \tag{7.1}$$

Dijet asymmetry in central PbPb collisions can be compared to MC simulations and pp collisions, these distributions are shown in Fig. 7-3. The increase in simulations compare to pp reflect the effects of larger jet energy resolution in central collision compared to pp collisions. However, the shift in PbPb collisions is larger than the resolution effect observed in simulations. This shift corresponds to $\approx$ 10 GeV more energy loss by the subleading jet compared to leading jet.

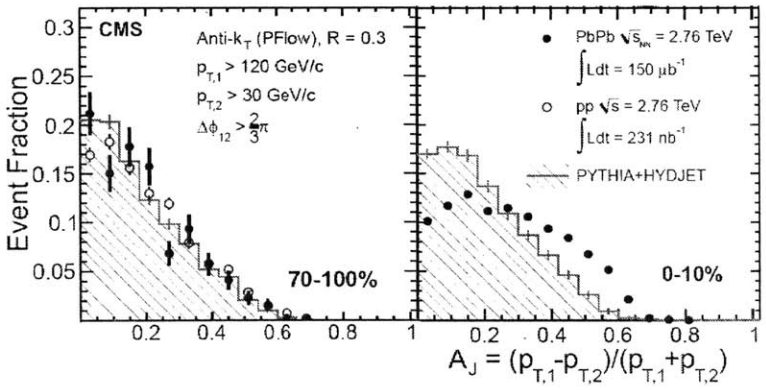

Figure 7-3: Dijet p_{T} asymmetry distributions in pp collisions, and PbPb collisions with 0-10% and 70-100% centrality. The data is compared to PYTHIA+HYDJET simulations. Taken from [96].

The dependence of increase in A_J on path length or rather the integrated matter effects over the path-length, which may depend also on the energy density and temperature of the medium as well, can be tested by centrality dependent measurements or by the correlations with the angle with respect to the event plane, due to more medium crossed by jets when they are perpendicular to event plane. Measurement of dijet asymmetry with respect to the event plane shows very small modulations in dijet [125], while the centrality dependence of A_J enhancement is larger. This is expected as central collisions are hotter and denser in general, while the event plane depen-

dence at fixed centrality mostly only varies the path length without changing the properties of plasma. It is however hard to tell whether the larger imbalance in dijet system as medium size gets larger is due to a surface bias, where leading jet is close to the exterior escaping the medium earlier than leading jet or not. Larger medium results in larger enhancement in dijet asymmetry, but one should not interpret this as difference in path length of two jets, because the fluctuations in fragmentation and energy loss is the dominant effect in making one of the jets lose more energy than the other [185]. Even if both jets travel the same path length if one of them loses more energy per path length it would get quenched more, and the differences in the lost energy between the two jets would also get larger as medium size and density is larger because it builds up over time.

Many different jet quenching MC models can reproduce the dijet asymmetry quite well, some with more free fit parameters than others. This observable is for searching for existence of jet quenching, but not to study the mechanisms involved in depth. It can be used to select on events with significantly quenched subleading jet. While being sensitive to final state effects on jets such as jet quenching, dijet asymmetry is insensitive to nuclear effects in the initial state, which makes it a good observable to search jet quenching effects in pPb collisions. As shown in Fig. 7-4 A_J is independent of the x values of partons that participate in the hard scattering process in PYTHIA events.

7.1.2 Azimuthal dijet correlations

Although balance of jets are modified by interactions with the medium, no significant modification was observed in the azimuthal correlations of jets defined by,

$$\Delta\phi_{1,2} = |\phi_1 - \phi 2|, \tag{7.2}$$

As shown in Fig. 7-5 in 0-10 % central events agree with pp collisions and PYTHIA+HYDJET simulations. This implies that the semi hard splittings happen before medium parton interactions can cause significant modification. It has been

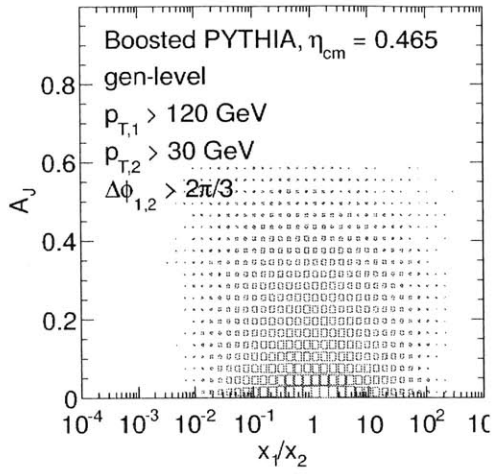

Figure 7-4: Dependence of A_J on parton x ratios in PYTHIA.

discussed in Chapter 4 that partons get transverse kicks as they propagate through the medium and broaden, the effect of broadening is small compared to the p_{T} of the jet[68]. The decorrelation in $\Delta\phi$ caused by a third jet is an order of magnitude larger. Another use for measuring azimuthal angle correlations is to look for large angle scatterings of jets created by a parton hitting a scattering center in the medium head on as in the case of Rutherford experiment. However, this effect is expected to be rare, and again not easy to observe due to the decorrelation caused by the semi hard splittings.

In order to see effects of broadening the width of the exponentially falling distribution at $\Delta\phi_{1,2} = \pi/2$ is measured, by fiting the distribution with,

$$\frac{1}{N_{\mathrm{dijet}}}\frac{dN_{\mathrm{dijet}}}{d\Delta\phi_{1,2}} = \frac{e^{(\Delta\phi-\pi)/\sigma}}{(1-e^{-\pi/\sigma})\,\sigma} \tag{7.3}$$

The γ-jet azimuthal correlations are more suited for the study of angular broadening than dijets, because γ direction does not get effected by medium, and moreover, γ does not undergo semi-hard splittings in vacuum. The width as described above has been measured in γ-jet events, and as shown in Fig. 7-6. In $0-10\%$ events with $N_{\mathrm{part}} = 355$ the PbPb value agrees with the pp and is even slightly lower.

Therefore, azimuthal angle correlations between jets are robust even in the exis-

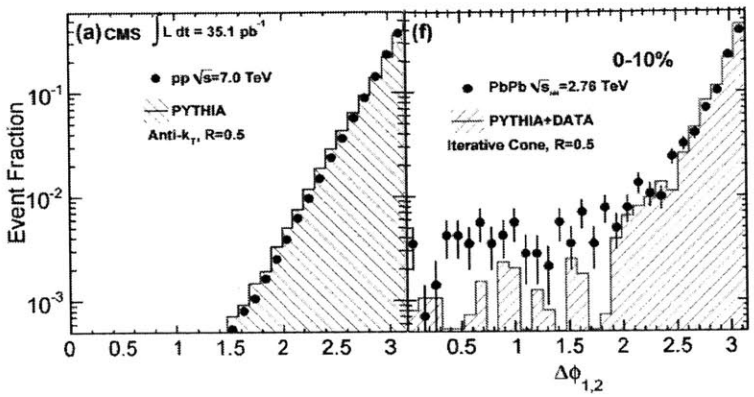

Figure 7-5: Distributions of azimuthal angle correlations between leading and subleading jet in pp and central PbPb collisions, compared to PYTHIA and PYTHIA+HYDJET simulations. Taken from Ref. [94]

tence of medium, and a requirement on back-to-back-ness of a dijet pair can therefore be useful to remove the combinatorial background one observes in central PbPb collisions due to jets formed in binary collisions of other nucleons or due to fake jets which are caused by fluctuations of UE energy. The combinatorial jet background in central collisions can be seen in the right panel of 7-5 as a flat background of dijet production becoming dominant for $\Delta\phi < 2$.

7.1.3 Dijet pseudorapidity

Inclusive jet η has been suggested as an observable that is sensitive to nPDF and for different x regions[197]. Dijet pair includes more information from the hard scattering process than single jets, as a result dijet pseudorapidity defined as,

$$\eta_{\text{dijet}} = \frac{\eta_1 + \eta_2}{2}, \tag{7.4}$$

is even more sensitive to the Bjoerken x values of partons participating in hard interaction. Assuming that two massless partons (one with x_1 in proton going in $+z$ direction and with $p_1^\mu = (Ex_1, 0, 0, Ex1)$ and other with x_2 in the other colliding nucleon going in $-z$ direction inside Pb nucleus and with $p_2^\mu = (Ex_2, 0, 0, -Ex_2)$)

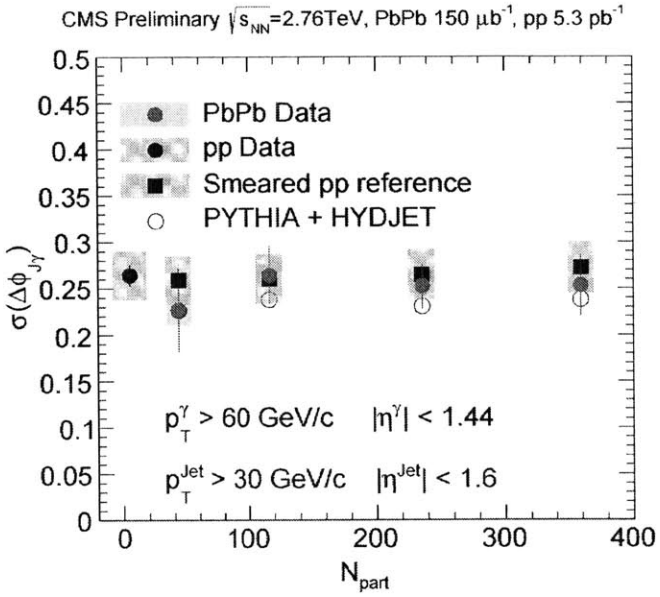

Figure 7-6: Taken from [123], Comparison of $\Delta\phi_{J\gamma}$ width in PbPb and pp collisions.

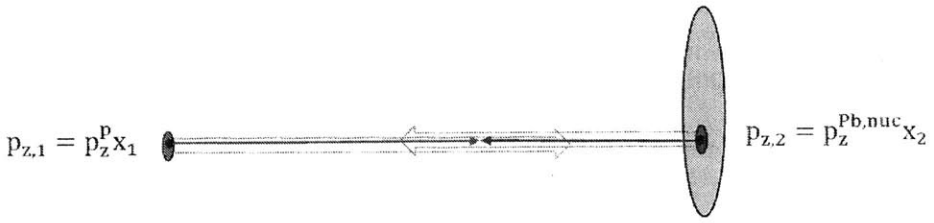

Figure 7-7: Drawing which demonstrates collision of two partons in pPb collisions one with Bjoerken x value x_1 in proton and the other with x_2 in Pb.

collide as depicted in Fig. 7-7 the total momentum of the outgoing jets will be $p^{\mu}_{\rm dijet} = (E(x_1 + x_2), 0, 0, E(x_1 - x_2))$. Pseudorapidity of the dijet pair is then $\eta_{dijet} = 0.5ln((E_{\rm dijet} + p_z^{\rm dijet})/(E_{\rm dijet} - p_z^{\rm dijet}) = 0.5ln(x_1/x_2)$. Of course, there are several approximations in this derivation, e.g. jets being identical to outgoing partons produced in $2 \rightarrow 2$ QCD process, partons being massless, partons not having momentum component transverse to nucleon momentum direction, and so on. However, even when these are taken into account there is still a tight correlation between $ln(x_1/x_2)$ and η_{dijet}. Shown in left panel of Fig. 7-8 is the correlation between η_{dijet}

and ratios of x values in PYTHIA events, which can be compared to the correlation with leading jet η instead, which is shown in the right panel.

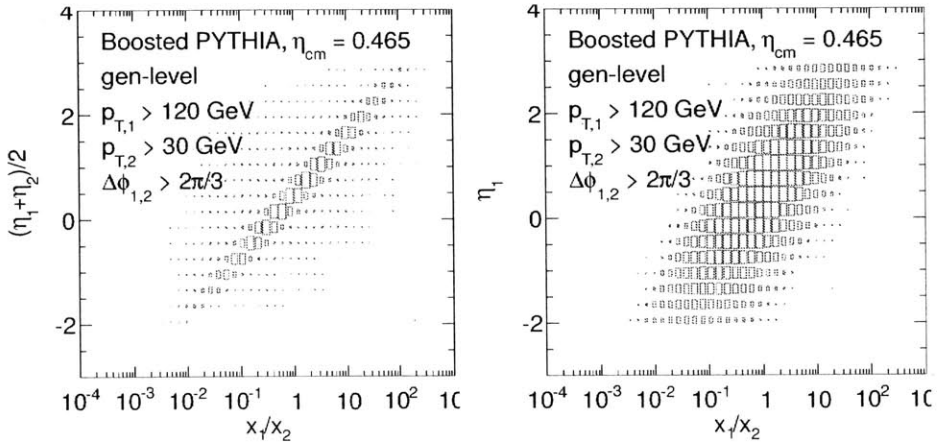

Figure 7-8: Dependence of η_{dijet} (Left) and η_1 (Right) on x ratios of partons.

In pPb collisions, the colliding beams have different momenta 4 TeV for proton and 1.58 TeV per nucleon for pPb, as a result in lab frame the center of mass of collisions are boosted by $\eta_{\text{cm}} = 0.465$ and the correlation with η_{dijet} in the lab frame is therefore $\eta_{\text{dijet}} \approx 0.5ln(x_1/x_2) + 0.465$. Dijet pseudorapidity interval of $|\eta_{\text{dijet}}| < 3$ together with the p_{T} cuts used in the selection of dijets, is sensitive to x region of $10^{-3} - 0.5$.

7.2 Summary

Measurement of dijets provide a wide range of possibilities. We can control the amount of quenching of jets, know the energy scales involved in the hard scattering process by using the leading jet as a tag jet, remove the combinatorial jets contributions from other collisions using the azimuthal correlations, and probe nuclear PDFs with dijet pseudorapidity.

Chapter 8

Reconstruction performance

In this chapter we go the through track and jet reconstruction in pp and PbPb collisions, in Sections 8.1 and 8.2, respectively. In Sections 8.4 and 8.5 the performance of these algorithms are presented. In pPb collisions the multiplicity generated in each event is small enough that the standard pp reconstruction sequence can be employed. In the analysis of dijets in pPb, track distributions were not studied, and PF jets are used in the measurement. Therefore, for pPb dijet analysis is only the standard jet energy correction strategy described in 8.5.1 is relevant. The tracking performance in pPb is not included as the correponding measurement only concerns jets.

For the "missing-p_{T}" analysis in PbPb collisions presented in Chapter 10, track distributions around a dijet system are measured, which is a more challenging measurement considering the large UE generated in heavy-ion (HI) collisions and the correlations that exist between track and jet reconstruction. The large fraction of this chapter is devoted to understanding the jets and tracks well enough to be able to carry out the "missing-p_{T}" measurement. For reconstruction of pp events, pp tracking is employed and for reconstruction of PbPb events HI tracking is employed, for both cases calorimeter jets with special corrections described in 8.5.2 are used. For jets in pp collisions UE subtraction algorithm for jets is not applied, while in PbPb collisions HF/Voronoi algorithm that we described in Section 8.2.3 is employed.

8.1 Track reconstruction

Track reconstruction employs a pattern recognition algorithm that converts hits in the tracker into trajectories that resemble charged particles propagating in the magnetic field of CMS detector. A charged particle follows a helix path in a uniform magnetic field, for the reconstruction algorithm a more realistic description of magnetic field instead of a uniform one is used, and the matter content on the path of charge particles is also considered. The trajectories are still helical to first approximation with small deviations.

8.1.1 Vertex reconstruction

Track and vertex reconstruction is a chicken-egg problem: position of vertices are determined by using the extrapolated position of the track trajectories to the interaction point, and iterative tracking needs an intelligent guess of where the tracks are coming from at least in the initial iteration. Different solutions are used for pp and PbPb tracking. In PbPb collisions there is no significant pileup unlike in pp collisions, and in PbPb collisions the multiplicity produced is much larger than in pp collisions. This points to finding vertices last in pp, because one needs to be accurate in their resolution to be able to distinguish different pileup vertices. Instead, in PbPb this points to a direction of finding vertices first in order to simplify the combinatorial problem by restricting the possible trajectories using the information of their starting point, i.e., the vertex.

Vertexing in pp collisions Vertex reconstruction is done after track reconstruction. All tracks within 5 standard deviation of BS in transverse direction, that has ≥ 2 hits at pixel and > 5 hits in strip tracker, and trajectory of which has $\chi^2 < 20$ are used to determine the position of vertices.

As the first step, an annealing algorithm, which minimizes a function:

$$F = -T \sum_{i}^{\#\text{tracks}} p_i \log \sum_{k}^{\#\text{vertices}} p_k \exp\left[-\frac{1}{T}\frac{(z_i - z_k)^2}{\sigma_i^{z\,2}}\right], \tag{8.1}$$

that has a direct analogy with free energy in statistical mechanics, is used to determine the z positions of vertices. In this expression z_i is the z position of tracks and z_k are the z positions of vertices p_i and p_k are weights for tracks and vertices, respectively. In this equation the number of vertices are allowed to vary. In the analogy with statistical mechanics the role of E in F is taken by χ^2 of compatibility of z position of tracks with z positions of vertices.

The free parameter T in F defines how spread the track positions with respect to vertices can be. When T is infinite it means that tracks associated to a vertex can appear anywhere, and therefore all the tracks are compatible with a single vertex. Initially p_i and p_k are equal and constant. As T value is reduced having more vertices become more favourable therefore the number of vertices increase.

Taking the limit all the way to zero, when each track is assigned the same weight factors, is not desirable because it results in unrealistic vertex splitting where the vertex of a single interaction is split into many artificially and each track has its own vertex. Therefore this limit is truncated at a point that balances between merging of vertices into one and splitting of a single vertex into multiple vertices ($T_{min} = 4$). Below this value the and additional weight, $Z_i = \exp(-\mu^2/T)$ per track is inserted in Eq. (8.1), the tracks that are μ standard deviations away from the nearest vertex does not play a significant role in the value of F.

Once the z positions for vertices are estimated as described above, a final fit to vertex position in x, y and z is done with an adaptive vertex fitter, described in Refs. [142, 118]. A position resolution of 10-12μm in each of the three spatial dimensions is obtained (for more detailed discussion see Ref. [105]).

Vertexing in PbPb collisions For PbPb collisions, vertex is finding precedes track reconstruction, because without using an accurate vertex position track reconstruction consumes unaffordable computational time. Due to the small probability of having a pile up interaction only a single vertex is reconstructed. As a first step, a rough estimate of z position of the vertex is done. The z values from -30 to 30 cm around BS are scanned in steps of 0.1 cm, according to compatibility of the pixel clusters

in the first layer of the pixel detector with the z value at each step of the scan. The compatibility check is done by comparing of the size of the pixel clusters with a particle generated at this point. [42]

The z value of vertex found in this way is used as an input to pixel track reconstruction, where the strip detector is not used to speed up the process. To get a finer estimate of the z position the closest approach of these pixel tracks to z axis is calculated an a fit to the distribution of closest approach is done around the median track. The refined z positions of vertices are used to filter pixel tracks to remove the outliners and the remaining tracks are fed in an adaptive vertex fitter[142, 118] to produce the final x, y and z coordinates of the vertex.

8.1.2 Iterative track reconstruction

In each PbPb collision, there are tremendous amount of hits produced in the tracker (The average particle multiplicity of 0–10% central PbPb collision is $\approx$ 35000, each of these particles leave behind $\approx$ 15 hits adding up to $\approx$ 500000 hits. With this many dots to connect one cannot consider all possibilities of combination and pick the ones that resemble a particle. The combinatorial problem associated to this many hits requires a smart approach so that we can find as many particles as possible within the limits of a reasonable computing time. To do so one has to realize that some particles simply will be missed.

CMS track reconstruction is based on an iterative algorithm that repeats some basic blocks of track finding described below, but only considering a subset of hits. After each iteration the hits that are used up are removed and the remaining hits are considered for the next step of search for particles in order to simplify the combinatorial problem. Each iteration of the algorithm is composed of seeding, trajectory building, fitting, filtering:

Seeding Only the hits in pixel detector are used as seeds the starting point for tracks, because of the finer granularity and better point resolution of pixel detector compared to strips. Moreover the vertex position or beam spot(BS) can be used

together with the hits in the pixel to further restrict the possible track seeds and speed up the algorithm. The p_T of the track constructed only from pixel and its displacement from the vertex are some of the tunable parameters. Seeds are later extended into full trajectories in the next steps described below. Note that the building and fitting steps are also used in the seed building process using only a subset of the tracker defined as the seeding region, which is usually just the pixel detector.

Building Trajectory builder takes as input track trajectories that are produced from N layers of the tracker to calculate a new set of possible hits that can be used to fit a new trajectory adding the information from the N+1st layer. The most compatible hits in the closest layer with respect to the direction of the input trajectory (or layers if more than a single layer satisfies this property, e.g. one barrel layer and one endcap layer) are added to the hit collection associated to a given track candidate. Not only the best candidates from the previous N layers is considered, but top 3-4 best input trajectories, because if at each layer only the best trajectory is kept, one of the worse trajectories might be corresponding to a real particle and we would lose it.

Fitting Combinatorial Kalman Filter is used in fitting on the set of hits that are obtained from the builder. Kalman Filter applies and iterative fitting procedure where the outlining hits are removed and trajectory is refit from inside-out and outside-in until a fit with a good χ^2 is obtained. Trajectories are built by propagating the trajectory of the particle in realistic particle propagation in CMS magnetic field with Runge Kutta Propagator. Also, the material content is considered in the propagation.

Filtering Filtering step decides on which of the final set of trajectories obtained after fitting are more likely to correspond to a real particle. It is not possible to know this directly, but one can check if the trajectory to be a good fit with tight requirements on parameters of the fit and increase he likelihood of a track to be a combinatorial coincidence. The quality selection used to do so is discussed further in Section 8.4. Only the hits used by good quality tracks are removed, as the hits are passed to the next iteration of tracking.

The steps given above are repeated for each iteration. The choice of seeding region is what makes one iteration different than the other and lets more tracks that were missed by the previous steps to be found.

Merging At the end of all iterations, tracks from each of these need to be merged as more than a single iteration might find the same particle. Merging is done such that if two tracks that match with each other both have good quality or both have bad quality the track coming from the earlier iteration is kept, if one of them has good quality while other doesn't the good quality track is kept instead.

Detailed information about tracking used in pp collisions can be found in [105]. A short summary: it is composed of 11 iterations, and the tracks p_{T}goes down to 200 MeV. The primary particles as well as the particles displaced from primary vertex are reconstructed.

Iterative tracking in PbPb collisions is different from that used in pPb and pp collisions, due to the larger multiplicities associated to former. In pPb collisions, multiplicities are still small enough that one can use "pp reconstruction", the default reconstruction used by the other physics groups analysing only the data from pp collisions. The iterative PbPb tracking follows the footsteps of pp tracking, in terms of the ordering of iterations with different purposes, but the ranges allowed for seeding are usually narrower in order to have good timing, and some iterations in pp reconstruction are omitted.

Iterative tracking used in PbPb collisions has three iterations and minimum $p_{\mathrm{T}}$for tracks seeds that goes down to 400 MeV. Recently an iteration aiming to recover displaced tracks and and another recovering high p_{T} jets inside the jet core were added. In Table 8.1 the seeds, parameters used in each iteration are shown as well as the tracks these iterations aim to reconstruct. The iterations that are marked as "New" did not exist at the time of the measurements described in Chapter 10. The three iterations are detailed below and the parameters for their seeding region is listed in Table 8.1.

Initial iteration For seeding pixel tracks with $p_T > 0.9$ GeV are used. The pixel tracks are similar to those used in vertexing with tighter compatibility requirements with the vertex as vertices are known in this case.

Low p_T iteration The multiplicity increases by a large amount by going from 0.9 GeV to 0.4 GeV. It was observed that, although reconstructing pixel tracks first then using these as seeds instead of using pixel hits takes additional time for pixel track reconstruction, the timing of this iteration is reduced by an order of magnitude when pixel tracks are used instead of pixel triplet seeds, because the resolution of pixel tracks in p_T is much smaller than pixel triplets. When a threshold of 0.4 GeV is set on pixel triplets a considerable amount of lower p_T tracks pass this cut due to resolution, such tracks are reduced by the use of pixel tracks seeds.

High p_T pixel pair iteration After hit cleaning for the previous two iterations, the pixel triplet seeds become scarce, it is possible to gain efficiency by using pixel pair seeds. The problem is that the combinatorial possibilities of combining two hits on three layers is much more time consuming then combining three hits compatible with each other. Therefore this iteration has seeds with a threshold of 4 GeV and is aimed to find only the high p_T tracks.

Table 8.1: Parameters used in each iteration of track reconstruction in PbPb collisions.

Iteration	Target	Seeding	$p_T >$ (GeV)	d_0 (cm)	d_z (σ_{BS})
Initial Step	high p_T prompt	Pixel track	0.9	0.1	3
Detached Step (New)	displaced prompt	triplets	0.9	0.5	4
Low p_TStep	low p_T prompt	triplets	0.4	0.02	4
Pixel Pair Step	recover high p_T prompt tracks	pairs	4 (New: 0.9)	0.005	4
Jet core (New)	regional around high p_T jets	triplets	10	0.2	3

8.2 Jet reconstruction

Jet reconstruction is done using the anti-k_{T} algorithm. The constituents that are fed in the clustering differ among types of jets. Two types of jets are used in the analyses presented in the next chapters, particle-flow jets and calorimeter jets. In PbPb collisions constituents are different than in pp collisions, as a result of the underlying event subtraction step applied a prior to clustering.

8.2.1 Particle flow candidates

Particle-flow (PF) algorithm, described in detail in Refs. [7, 5], combines information from different sub-detectors to identify types of particles such as charged and neutral hadrons, muons, electrons and photons, and associate the signs these particles leave in different parts of the detectors to each other to avoid double counting of energy associated to a single particle. The only signature of neutral hadrons, the deposits left at the calorimeters, can therefore be identified as the left over clusters after the ones associated to charged ones are removed.

In addition, it allows cleaning of misidentified tracks, and decomposition a single tower energy into multiple particles making best use of the knowledge at hand. For example two tracks with p_{T} 62.1 and 14.3 GeV, and at (η, ϕ) coordinates (-0.78,1.73) and (-0.79, 1.75), therefore only separated by $\Delta < 0.02$, which is much smaller than the HCAL tower granularity get associated to $\mathrm{E_T}$ values of 15.8 and 3.6 at ECAL and 61.6 and 14.2 at HCAL respectively. The combination of charged particles to ECAL and HCAL is done by extrapolating the trajectory of the track into the calorimeters. From the last hit position of the track at the tracker to the closest calorimeter clusters. The energy in ECAL within an expected maximum depth for a typical longitudinal electron shower and the energy at HCAL within an interaction length at HCAL is taken into account. After the matching in $\eta - \phi$ space also the energies are required to be compatible.

8.2.2 Calorimeter vs. PF jets

Calorimeter jets These jets are reconstructed using clustering algorithms on calorimeter towers. Calorimeter towers are defined by the overlapping ECAL and HCAL cells, and have the granularity of HCAL cells as ECAL are smaller. A tower is composed of 5×5 ECAL cells and a single HCAL cell.[121] The typical cell size is 0.02 in the ECAL and 0.1 in the HCAL.[7]

PF jets Jets are made out of particles, therefore, using the good p_{T} resolution of track we can simply add up the p_{T} of track constituents of the jet to learn about its p_{T}. In fact, this can readily be done using the PF candidates. However, only about 65% of jet energy is associated to the charged hadrons, and there are $\approx 10-20$ charged particles inside a jet. It means that the resolution of total p_{T} carried by charged particles in a jet is $\sqrt{10}-\sqrt{20}$ larger than track resolution. Moreover, the 65 % is only an average value, if one of the high p_{T} particles is not reconstructed, the p_{T} sum of charged particles vary significantly. Finally, 35% of the p_{T} of the jet belongs to neutral particles and the energy resolution of these is worse than track resolution because of the shower shape fluctuations in calorimeters.

8.2.3 Jet reconstruction in heavy ion environment

In the high multiplicity environment of heavy ion collisions jet reconstruction requires additional steps, in which the particles around a jet that do not come from the hard interaction but that are produced in other collisions in the event are cleaned. This is somewhat similar to proton-proton collisions that suffer from pile-up, but the number of simultaneous collisions (1k in central PbPb collisions) is much larger than 20-30 which is the maximum reach of pileup in high luminosity proton-proton collisions at LHC so far, and moreover all the particles come from a single vertex unlike in pile-up collisions in pp making the subtraction more challenging.

HF/Voronoi algorithm The underlying event E_{T} in a 0-10% central PbPb collision is as large as 10 GeV in a random cone of $\Delta = \sqrt{\Delta\phi^2 + \Delta\eta^2} < 0.3$. Moreover

there are large modulations in azimuthal angle in a given event due to ellipticity, i.e. the overlap between two Pb nuclei having an elliptic shape, and higher order eccentricities in an event. The largest modulations in underlying event (UE) energy in azimuthal angle occur in mid-central collisions where the overlap of the nuclei is still large but the nuclei are not head-on so the geometry deviates from a circular shape [13]. The difference in total E_{T} inside a cone that is parallel and perpendicular to event plane was found to be ≈ 4 GeV in 20-30 % centrality events with significant eliptic flow ($v_2 > 0.1$). Therefore, in order to measure the energy of jets, an underlying event subtraction algorithm that takes into account these modulations is needed. In addition to the modulations caused due to physics of particle production, there are other modulations to be considered caused by the detector. The detector response is not linear as function of E_{T} and this nonlinearity and functional dependence on E_{T} depends on η, because different sub-detectors cover different η ranges.

HF/Voronoi is an algorithm that subtracts the UE from calorimeter towers and PF candidates a prior to jet clustering. It takes into account the azimuthal angle variations of the underlying event.

- In order not to be sensitive to the energy of jets themselves, energy profile at HF is used to estimate the energy profile in mid-rapidity. The algorithm is trained on minimum bias (MB) PbPb collisions and HYDJET for data and simulations, respectively, to create a map of energy density as a function of η and ϕ given the energy profile at HF (This is where the "HF" in the name of the algorithm comes from). A polynomial fit to $\mathrm{E_T}$ and Q vector (See Ref. [61] for definition) is done in bins of η and the values of these parameters at HF region are associated to values in mid-rapidity.

- After the training, algorithm is applied on events with jets. For a given high p_{T} jet event, the $\mathrm{E_T}$ and Q vector at HF are calculated and the energy density at mid-rapidity is estimated based on the map previously derived on MB events. A voronoi map is built that assigns an area per PF candidate which described by lines passing through mid points of the lines connecting this PF candidate

to all of its closest neighbors. In the case of calorimeter jets Voronoi map is not built and detector cell granularity is used as a map.

- For calorimeter jets the step above is modified where Voronoi map is replaced by a grid that has same granularity as the calorimeter towers.

- After subtraction of some PF candidates/towers are left with non-physical negative energies, due to lower fluctuations below the average value and vice versa some PF candidates/towers constitute the upper fluctuations above the average energy density and therefore even if they belong to UE they are left with positive energies. An "equalization" procedure is applied to redistribute the energy of lower fluctuations and upper fluctuations. This is done by minimizing a metric that describes the energy difference before and after the process with the condition that at the end all towers have positive energy.

- The equalization is done in cones of $\Delta = \sqrt{\Delta\eta^2 - \Delta\phi^2}$, which is chosen to be defined as $\Delta < R$, where R is the distance parameter of anti-k_t jet reconstruction algorithm for PF jets and $R+1$ for calorimeter jets in order to take into account the larger granularity involved with these jets that might result in part of the calorimeter cells to fall outside of the circular Δ region.

Because of the interaction between the medium and partons created in hard scattering processes, there is no clear way of telling which particle belongs to the medium and which particle belongs to the jet. The underlying event subtraction technology used by experiments at LHC, e.g. HF/Voronoi algorithm for CMS, works based on event averaged estimates of what is likely to be associated to underlying event. This algorithm assumes that energy created in HF is not effected significantly by medium response to jet quenching. Indeed, if the total energy lost by the jet which is of order 10 GeV is distributed in such a large phase space the effect on the energy at HF is expected to be small.

8.3 Monte Carlo Generators

Testing the performance of reconstruction depends heavily on MC generators. In order to test the reconstruction algorithm under realistic conditions, MC generators need to resemble data and create similar particle production. PYTHIA generator (specifically the PYTHIA version 6.423 with the Z2 tune [139, 1]) is used as a baseline for pp collisions. In order to put reconstruction algorithms to more stringent tests and understand how they behave in pPb and PbPb collisions where $N_{\text{coll}} > 1$ and UE is more pronounced, the PYTHIA events are often superposed with other MC generators which describe the particle production minimum bias collisions reasonably well.

HIJING: For understanding reconstruction in pPb collisions, HIJING [223, 151] (version 1.383) generator is used to reproduce the UE created by multiple nucleon nucleon collisions in pPb collisions. The particle production in a single nucleon-nucleon collision in HIJING is based on a combination of three types of interactions single hard scatterings, multiple mini-jet production, and interactions at soft scales. The hard scatterings depend on PYTHIA packages, as well as some kinematic properties of mini-jet formation. Interactions with small momentum transfers depend on a phenomenological multiple string model. The final set partons produced at the end are color connected with strings to the partons from the initial nucleon they originated from. To extend the implementation in nucleon-nucleon collisions to systems such as pA and AA collisions, the probability of having multiple nucleon-nucleon scatterings are implemented based on a Glauber type model. The hard-scattering happens first consuming part of nucleons energy and the rest of the collisions happen according to the remaining kinematics. Nuclear shadowing effect was accounted for using nPDFs, assuming that it is independent of A and Q^2, but it was considered to be impact parameter dependent. The showering of partons and hadronization is based on a variation of Lund string model.

HYDJET: For PbPb collisions HYDJET generator is used to simulate the effects of UE created by thousands of binary nucleon interactions that take place in a sin-

gle central PbPb collision. HYDJET is initially developed to model jet quenching by medium induced gluon radiation driven by scatterings off from partons in QGP as well as collisional energy loss associated to these scattering processes. Hard scatterings are simulated by PYQUEN generator which implements the quenching events by modifying PYTHIA version 6.2. It produces a soft hydro-type background, which is our main interest in this context, accompanying the hard process. The medium is modelled as a boost invariant expanding plasma in Bjoerken expansion approximation, and the freeze out conditions determined by three parameters: freeze out temperature, and maximum allowed longitudinal and transverse flow rapidities. Once the freeze out is reached hadron spectrum is generated according to the liquid hadron model, which randomly generates the 4-momentum of hadrons according to Boltzmann distribution at rest frame of liquid. The ellipticity of the freeze-out region is taken to be proportional to the ellipticity in the initial collision up to a scale, and azimuthal flow is created as a modulation in angle with respect to the event plane based to this ellipticity. The hadrons associated to the hard part of the event can be transferred to soft part if they go below certain threshold. The hard part of the generator is not used in studies of jet reconstruction, and $\hat{p}_{\mathrm{T,min}}$ is set to a low value. It models the combinatorial jets that are produced from the other binary collisions in addition to the scattering we are interested to study.[176]

In addition to having good description of particle production, it is necessary to have the detailed simulation of detector which describes all its imperfections to best of our knowledge. Particles from generators are propagated through detector using the GEANT4 package built for CMS [32]. The simulated detector signals are then processed through the same chain of steps as if it was data.

The pp and pPb collisions are processed with the standard pp reconstruction procedure, with pp tracking and no underlying event subtraction for jets, while PbPb collisions are processed with HI reconstruction which includes different vertexing, tracking and underlying event subtraction for jets as we discussed in Chapter 5. As MC simulations aim to provide a baseline to study the reconstruction effects in data, they are processed with matching reconstruction algorithms based on which collision sys-

tem they aim to be reference for, therefore PYTHIA, HIJING and PYTHIA+HIJING simulations are processed with pp reconstruction, while HYDJET and PYTHIA+HYDJET simulations are processed with HI reconstruction. These samples are used to carry out the performance tests described below.

8.4 Performance of track reconstruction

A track is a collection of hits, that are grouped together by a trajectory, a fit that goes through these hits to define a hypothetical particle path through the detector. A good track reconstruction algorithm produces tracks with trajectories similar to underlying particle trajectories for as many charged particles as possible. In collisions the underlying particle trajectories are not known. However, simulations are used to check the performance of tracking.

Tracks and particles are matched based on certain criteria. In CMS, a track is matched to a charged particle if 75% of reconstructed hits that are associated to a track to be compatible by hits created in the simulation of a particle going through the detector. There are other ways one can do this, such as reducing this requirement and qualifying tracks which has 50% of their hits matched to a simulated particle to be real, or by comparing the χ^2 of tracks to the matched particles.

Once a matching criteria is picked the following quantities can be defined:

- **Efficiency:** The fraction of primary particles, i.e., charged particles that are produced in the interaction or are remnants of particles with a mean proper lifetime of less than 1 cm/s, that are matched to at least one track.

- **Misidentification rate:** The fraction of reconstructed tracks that do not match any charged particle (primary or otherwise).

- **Multiple reconstruction rate:** The fraction of primary particles that are matched to more than one reconstructed track.

- **Secondary particle rate:** The fraction of tracks matched to a non-primary

particle, that is created by interactions of the primary particles with the detector.

The performance of the algorithm can be tested by how close the efficiency is to 1, and how close misidentification, multiple reconstruction and secondary particle rates are to 0. These parameters are correlated, in the sense that having larger efficiency usually comes with the cost of having large fraction of misidentified tracks and multiple reconstructed tracks. The optimization of efficiency versus misidentification rate is done using quality criteria. The quality selection is coupled the reconstruction at the filtering step applied at the end of each iteration. The main effect of the quality selection comes at the analysis level, as only "good enough" tracks are used in measurements. We discuss track quality selection next.

Selection Criteria There are three different selection criteria on tracks, that is "loose", "tight" and "high purity". Most of the analysis use the high purity tracks which puts the most stringent requirements on the tracks aiming to minimize the misidentification rate. In the analysis presented in Chapter 10 a cut based quality selection criteria is applied, high purity selection has been recently updated by a multi-variant analysis (MVA) based training showing significant improvement (up to 10% increase in efficiency), proving the importance of a good quality selection for tracks. The MVA track quality selection will not be covered here.

The cut based selection simply applies hard cuts on five parameters:

1. $|z_{\rm vtx} - z_{\rm trk}|/{\rm err}^{err}_{z,{\rm trk}} < 3$, the numerator is the distance in z position of the track from the closest primary vertex, and the denominator is the error for z position of track due to uncertainties on the trajectory,

2. $|r_{\rm vtx} - r_{\rm trk}|/{\rm err}^{err}_{r,{\rm trk}} < 3$, same as above but in the transverse direction $r = x^2 + y^2$,

3. $N_{hit} > 13$, number of hits,

4. $\chi^2/(N_{\rm dof}N_{\rm layer}) < 0.15$, normalized χ^2 per layer,

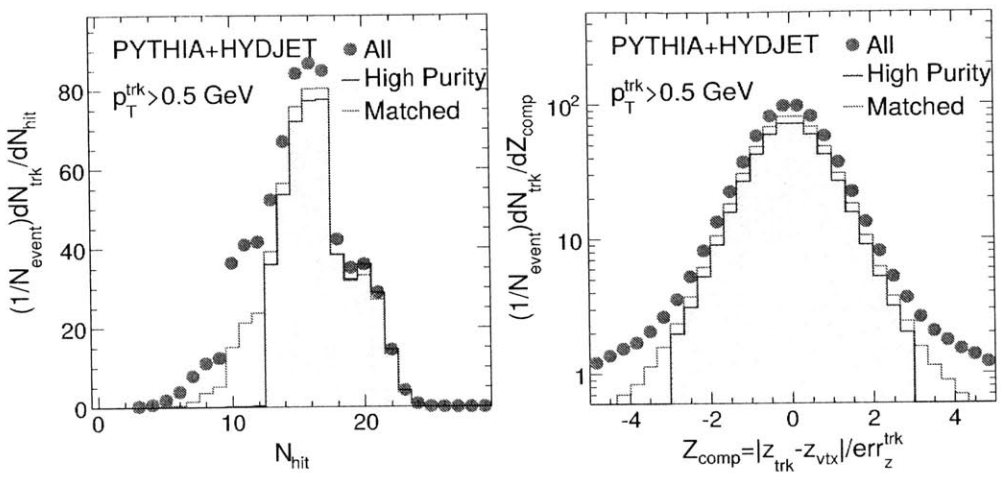

Figure 8-1: Distributions of (left) number of hits in the tracker and (right) track-vertex compatibility parameter for all reconstructed tracks, tracks matched to primary particles and for tracks with high purity selection.

5. $p_{\mathrm{T}}^{\mathrm{err}}/p_{\mathrm{T}} < 0.05$, fractional p_{T} error obtained from track's trajectory.

The cuts are chosen by comparing the distributions related to quality of trajectories for tracks that matched to primary particles and those that are misidentified. In Fig. 8-1 the distributions of number of hits and vertex z position compatibility are shown for all reconstructed tracks and a subset of these which are matched to primary particles. These are two of the parameters used in the definition of high purity. The distributions with high purity selection are shown on top of these two sets of distributions. As can be seen, regions that are dominated by matched tracks are chosen for the high purity definition.

The efficiency and misidentification rates for high purity tracks are shown in left panel of Fig. 8-2 for HI tracking in PYTHIA+HYDJET on top row can be compared to pp tracking performance shown in middle row for pp tracking in PYTHIA events. The dependencies in the rest of the panels are discussed in the proceeding section. There is a significant reduction in efficiency and increase in misidentification rate for $p_{\mathrm{T}} < 1$ GeV for HI tracking, while for pp tracking the performance is does not vary significantly. The drop in efficiency by going to low p_{T} is also observed in PYTHIA events reconstructed with HI tracking (see Fig. 8-2 bottom row), but the increase in

misidentification rate is not observed. Therefore, we conclude the source of increase in misidentification rate at low p_{T} is due to the large combinatorial background in PYTHIA+HYDJET events, that is not present in PYTHIA events. The lower efficiency in HI tracking compared to pp is due to less number of iterations, tighter quality selections that one can afford due to the higher rate of misidentified tracks, and due to less flexible seeding regions chosen for reconstruction. Having more iterations with more flexible tracking regions increases efficiency in pp tracking, but also the multiple reconstruction and secondary particle rates. In HI tracking these are $< 0.5\%$, while they are $\approx 1-2\%$ in pp tracking as shown in Fig. 8-3.

An additional concern in judging the performance of tracking is having the p_{T} of the track to be as close as possible to the p_{T} of the matched particle. The track p_{T} scale and p_{T} resolution are defined as $\langle p_{\mathrm{T}}^{\mathrm{track}}/p_{\mathrm{T}}^{\mathrm{particle}}\rangle$ and σ, where σ is the parameter of the Gaussian fit to the distribution $p_{\mathrm{T}}^{\mathrm{track}}/p_{\mathrm{T}}^{\mathrm{particle}}$ at a fixed $p_{\mathrm{T}}^{\mathrm{particle}}$. The distribution is not exactly Gaussian, but becomes more Gaussian when high purity selection is applied. The tail of the distribution can be checked by calculation root-mean-square(RMS) of the distribution instead of checking the width of the Gaussian. The RMS and σ values are shown in Fig. 8-4 for HI tracking. The resolution is $\approx 1-2\%$ up to large values of p_{T}. The width of Gaussian fits agree well for all tracks and high purity selection, but the RMS value is significantly reduced by high purity selection as the tail of this distribution is removed. The resolution is better for tracks at midrapidity with $|\eta| < 1$. A similar resolution is observed for pp tracking, more information can be found in Ref. [105].

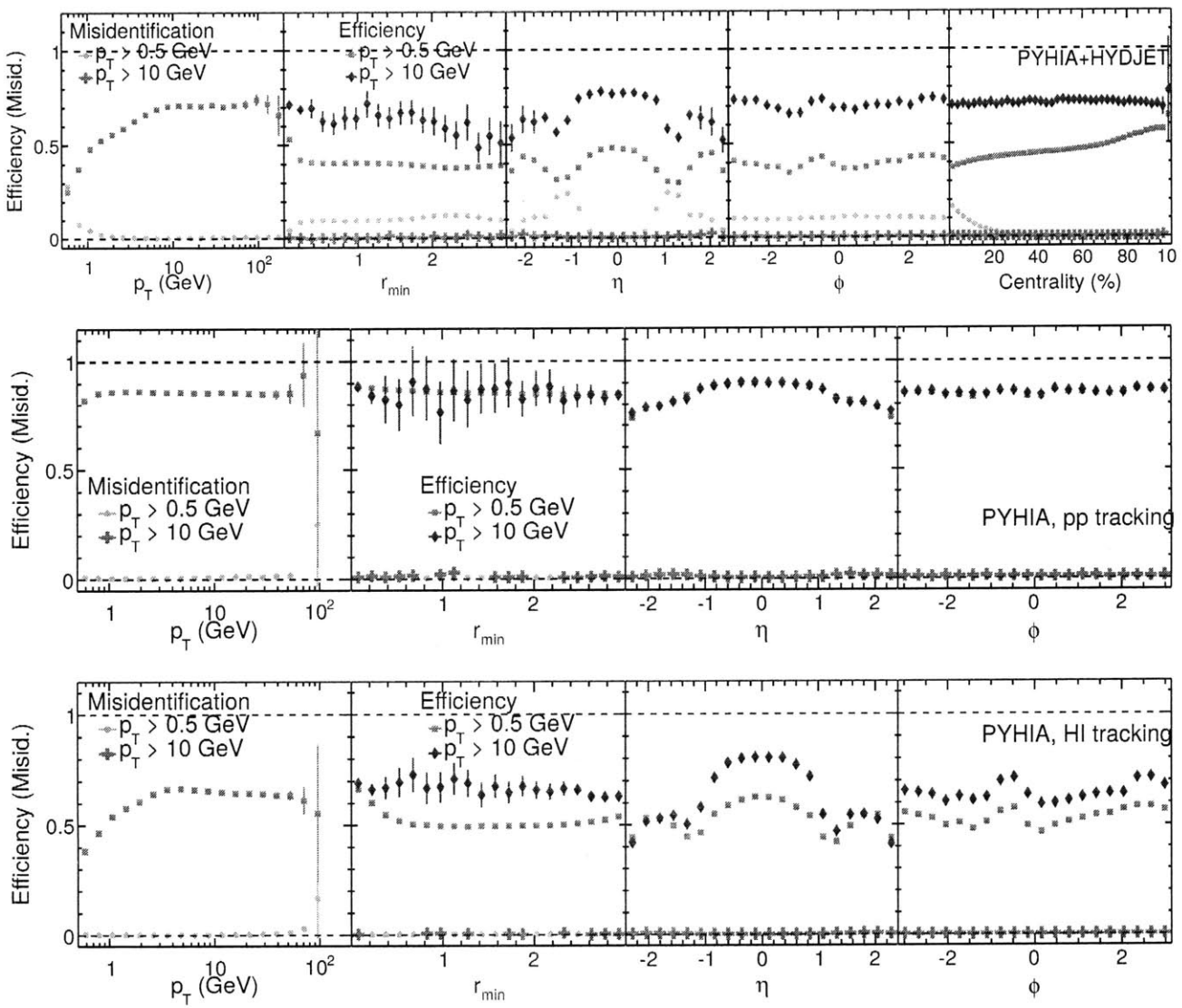

Figure 8-2: Efficiency and fake rate for HI and pp tracking.

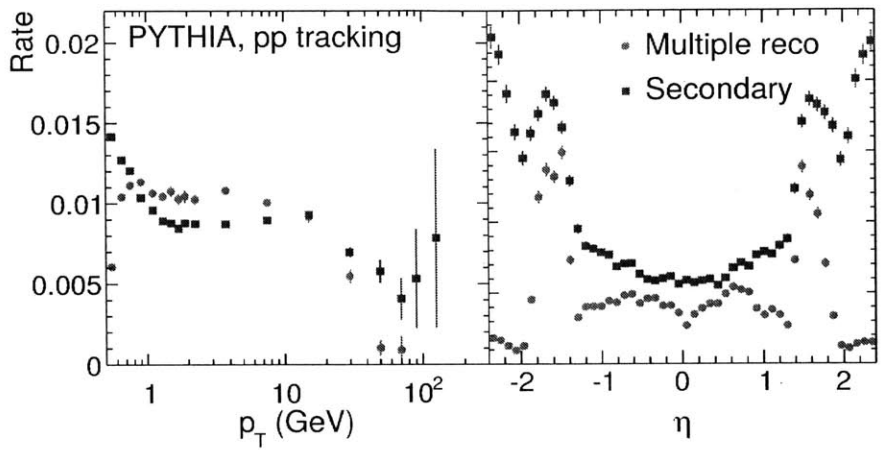

Figure 8-3: Multiple reconstruction and secondary particle rates in pp collisions as a function of η and p_{T}

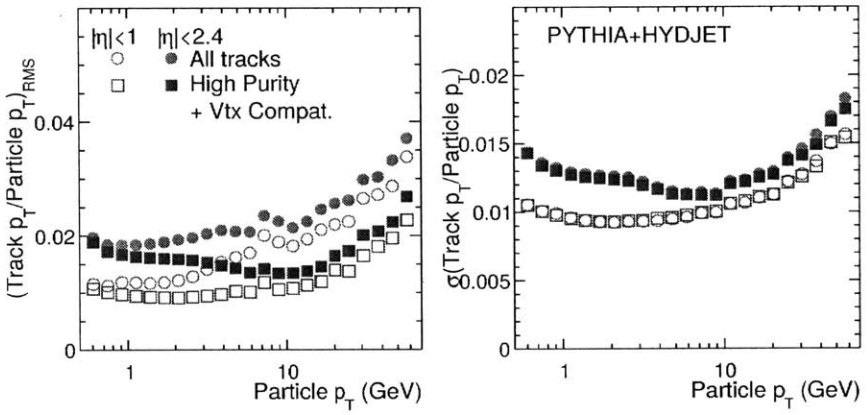

Figure 8-4: (Left) RMS of ratios of track p_{T} and matched particle p_{T}. (Right) Track p_{T} resolution defined as the σ of the Gaussian width to those distributions.

For small values of resolution, track distributions can be corrected by applying a multiplicative correction:

$$c^{\mathrm{trk}} = \frac{(1 - \text{misreconstruction}) \times (1 - \text{secondary-particle})}{(\text{efficiency}) \times (1 + \text{multiple-reconstruction})}, \tag{8.2}$$

Resolution needs to be considered here, because when reconstructed tracks are corrected for reconstruction efficiency and multiple reconstruction rate the correction

is derived as a function of particle p_{T} and later applied according to the p_{T} values of tracks. For large resolution $p_{\mathrm{T}}^{\mathrm{track}}$ values would have to be mapped to $p_{\mathrm{T}}^{\mathrm{particle}}$ values by unfolding or by a simple mapping function. However, no significant effect is observed due to the interplay between resolution and reconstruction effects, and therefore we assume efficiency($p_{\mathrm{T}}^{\mathrm{track}}$) $\approx$ efficiency($p_{\mathrm{T}}^{\mathrm{particle}}$). For pp tracking all of these correction factors are applied, while for HI tracking secondary particles and multiple reconstruction rates are set to zero. The derivation of corrections are discussed further in the next subsection.

Varying the matching criteria changes the quantities defined above. A tighter matching criteria results in lower track reconstruction efficiency and higher misidentification rate. A particle that would be matched to a reconstructed track with a loser requirement is no more matched and this reduces the reconstruction efficiency at the same time the track is tagged as misidentified. The misidentification rate and the reconstruction efficiency change with the requirements on track to match it to a particle, this is acceptable as long as the numbers add up, so that different matching criteria give same number of particles after the reconstruction effects are corrected. In Fig. 8-5, the efficiency and misidentification rate and overall corrections are shown for different 75% hit matching compared to 50% hit matching, as can be seen even if the definition of whether or not a track is associated to a charged particle is ambiguous. However, if the corrections are applied systematically using Eq. 8.2, same overall correction is observed, the inverse of c^{trk} are shown as lines on Fig. 8-5, and they agree perfectly even if efficiency and misidentification rate varies individually.

8.4.1 Track corrections

Tracker has several "holes", regions without sensors where a particle might escape the tracker without hitting any layer or, more likely, may miss some layers resulting in failure of the trajectory building process. The maps of the tracker in η and ϕ plane as seen by tracks with $p_{\mathrm{T}} > 0.5$ are shown for PbPb collisions and for HYDJET simulation in Fig. 8-6. They track each other reasonably well with some remaining differences. The effect of these differences can be checked using procedures described

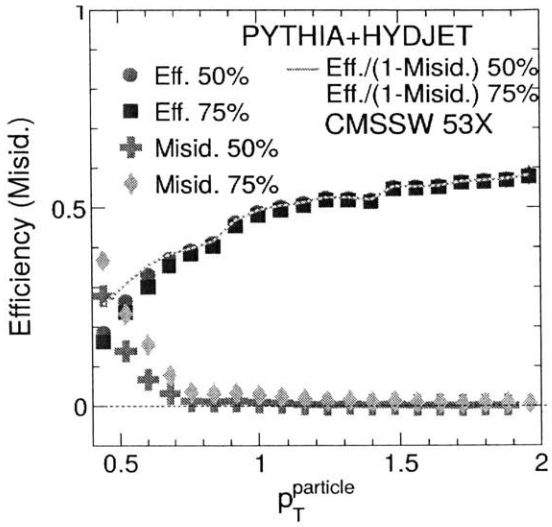

Figure 8-5: Efficiency, misidentification rate and the combination of two correction factors for two different particle track matching criteria.

in Ref. [6]. The similar have not been done for HI reconstruction yet due to limited statistics of D mesons. Instead we quote a conservative 5% uncertainty due to these residual differences instead of 3.8%, after comparing effect of a change in track quality selection in data and MC.

The size and shape of holes depend on the p_T of the particle, because of the change in the curvature of the track trajectory. In Fig. 8-7 the ratios of maps for tracks with $p_T > 10$ GeV and $p_T < 10$ GeV are shown. Particle production at different p_T has different η shapes, therefore in this plot the η dependence is mostly caused as a result of difference in production mechanisms, but the ϕ dependence is solely caused by the difference in how holes effect track reconstruction for different p_T tracks. As you can see the higher p_T tracks usually are less effected by holes, therefore the map ratio takes higher values around the holes because a larger fraction of low p_T tracks are lost. What one can tell simply by looking at these raw track distributions is that η, ϕ and p_T parameters are coupled to each other by the tracker geometry. Therefore, one has to consider these parameters in three dimensional arrays in correcting for reconstruction effects.

The dependencies do not get exhausted by only three dimensions, as shown in

Fig. 8-2, in HI tracking reconstruction effects also depend on centrality, and this dependence is different for high and low p_{T} tracks, meaning that centrality needs to be considered as a fourth parameter. As centrality increases local density of tracks and hits increase. In this high density environment local hit reconstruction of strip and pixel hits start to fail, merging two hits into one because they overlap. Merged hits result in a drop in efficiency because of misplaced location of merged hits compared to their original position, and because of the removal of hits associated to one of the tracks after the merged hit is used by the other track trajectory. Moreover, combinatorial background in trajectory building increase as well resulting in a higher misidentification rate. Another case where hit density is high is the core of a jet, because as we discussed is composed of several collimated high p_{T} particles. These two dependencies are similar but not the same because a jet is composed of high p_{T} tracks while the central events are composed of low p_{T} tracks. Low p_{T} tracks have larger curvature in magnetic field and are confined in the inner layers of the detector, while high p_{T} tracks are almost linear, so for these two cases the directional density from interaction point maps differently on layers of tracker and local hit densities at each layer. In the second panel in Fig. 8-2, the distance of a track to the closest jet with $p_{\mathrm{T}} > 50$ GeV, $r_{\mathrm{min}} = \sqrt{(\phi_{\mathrm{track}} - \phi_{\mathrm{jet}})^2 + (\eta_{\mathrm{track}} - \eta_{\mathrm{jet}})^2}$, is shown. The dependence of efficiency and fake rate on this parameter is different for different p_{T} ranges. Therefore, this parameter adds a fifth dimension to our correction tables.

Some measurements might not require to correct for all the dependencies, but the analyses that involve measurement of angular correlation of jets and tracks or jet fragmentation functions, require a good treatment of $\eta - \phi$ correlations, as well as correlations with jet direction. If the measurement is insensitive to the azimuthal angle, as in the case of track spectra the correction can be done binned in η ignoring variations in ϕ.

8.4.2 Iterative factorized corrections

We discussed the necessity of having corrections in multiple dimensions. Although having a multi-dimensional correction table would be optimal, it is not possible in

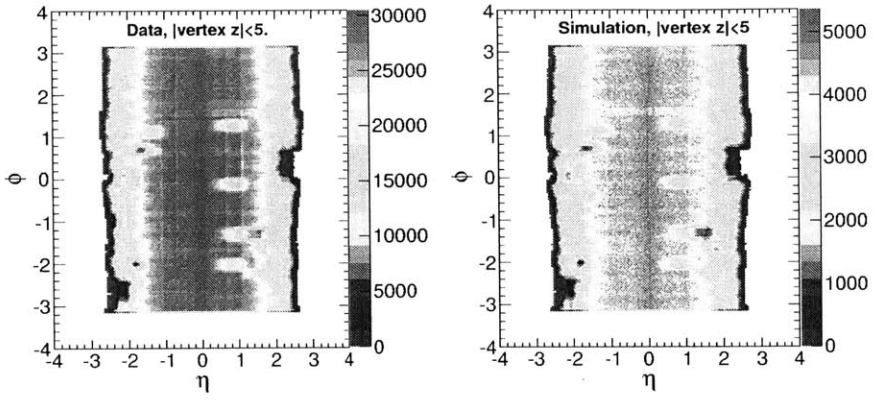

Figure 8-6: Tracker map, i.e., distribution of tracks in $\eta - \phi$ (left) in PbPb collisions, and (right) in PYTHIA+HYDJET simulations.

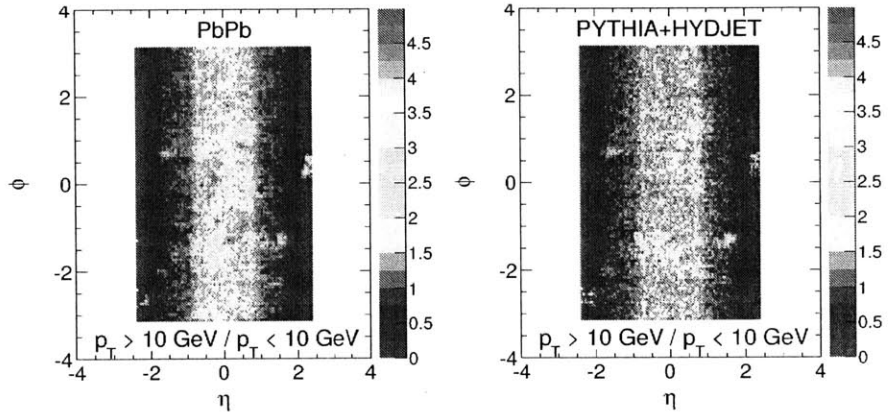

Figure 8-7: Ratio of tracker map for tracks with $p_T > 10$ GeV divided by that for tracks with $p_T < 10$ GeV (left) in PbPb collisions, and (right) in PYTHIA+HYDJET simulations.

terms of statistics of simulated samples needed to achieve this. Fortunately, it is possible overcome this conflict by determining what part of the dependencies on these parameters can be factorized from the rest, and use factorization whenever possible and using an iterative procedure which is described below.

An algorithm is developed to overcome the statistical limitations and consider several parameter dependencies of reconstruction effects at the same time. The sample is first divided into a minimal number of bins in p_T and centrality based on regions with large correlations between observables. Then in these large bins of p_T and centrality

factorization is assumed, i.e. efficiency is given as $E_{\rm total}({\rm centrality}, \eta-\phi, p_{\rm T}, r_{\rm min}) = E_{\rm centrality} \times E_{\eta,\phi} \times E_{p_{\rm T}} \times E_{r_{\rm min}}$ (misidentification rate is $F_{\rm total}({\rm centrality}, \eta-\phi, p_{\rm T}, r_{\rm min}) = F_{\rm centrality} + F_{\eta,\phi} + F_{p_{\rm T}} + F_{r_{\rm min}}$). The following procedure is iteratively applied after initially setting $E_X = 1$ (and $F_X = 0$) for all parameters, at $(n+1)^{\rm st}$ iteration:

1. For each particle calculate $E_{\rm total}$. Compare centrality distribution of particles matched to tracks with good quality selection with a weight of $1/E_{\rm total}$ to all primary particles. The discrepancy between the two gives $E_{[n+1,n,n,n]}$ where indices refer to centrality, $\eta-\phi$, $p_{\rm T}$ and $r_{\rm min}$. Set $E^{(n+1)}_{\rm centrality} = E_{[n+1,n,n,n]} \times E^{(n)}_{\rm centrality}$.

2. Recalculate $E_{\rm total}$, apply it on tracks and calculate the same discrepancy between corrected matched particles and particles as a function of $\eta-\phi$ this time to obtain $E_{[n+1,n+1,n,n]}$, set $E^{(n+1)}_{\eta-\phi} = E_{[n+1,n+1,n,n]} \times E^{(n)}_{\eta-\phi}$.

3. Recalculate $E_{\rm total}$, apply it on tracks, calculate the discrepancy between $p_{\rm T}$ distribution of corrected matched particles to all primary particles to obtain $E_{[n+1,n+1,n+1,n]}$, set $E^{(n+1)}_{p_{\rm T}} = E_{[n+1,n+1,n+1,n]} \times E^{(n)}_{p_{\rm T}}$.

4. Break if desired closure is reached in all parameters. Otherwise recalculate $E_{\rm total}$, apply it on tracks, calculate the discrepancy between $r_{\rm min}$ distributions of corrected matched particles to all primary praticles to obtain $E_{[n+1,n+1,n+1,n+1]}$. Set $E^{(n+1)}_{r_{\rm min}} = E_{[n+1,n+1,n+1,n]} \times E^{(n)}_{p_{\rm T}}$.

In Fig. 8-8 the above procedure is drawn, the parameters in each box or number of parameters is also variable. These parameters were simply chosen based on the discussion in the previous Section. The reason why the algorithm is terminated after $p_{\rm T}$ is because for physics purposes we would like to have a very good agreement between $p_{\rm T}$ spectra of tracks and particles. For misidentification rate, the multiplication is replaced by summation and at each step instead of comparing matched corrected particle distributions to distributions of all particles, the distributions of quality selected tracks corrected by $(1-F_{\rm total})$ are compared to distributions of quality selected tracks that are matched to a primary particle. The rest of the procedure is the same.

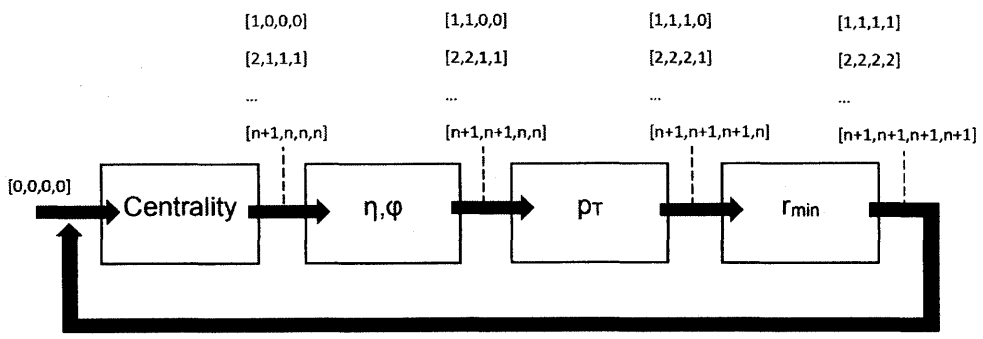

Figure 8-8: Drawing describing iterative factorized track corrections.

Trying to factorize the reconstruction effect in different parameters one quickly notices the deterioration in the performance of correction in one parameter when the correction depending on another correlated parameter is applied on top of it. Fortunately, when this procedure is repeated meaning that the deterioration is corrected iteratively on top of first order corrections, it is possible to get good performance in all parameters after fourth or fifth iteration. An example is shown for a prototype correction table with smaller number of parameters, i.e. no r_{min} dependence, in Fig. 8-9 for a small range of track p_{T}.

A failure in factorization assumption can be observed by a check as follows follows: Events are divided in two subsets with a certain requirement on one parameter and the performance of corrections as a function of the other variables are checked. For example assume that no initial coarse binning is applied based on centrality, and centrality is assumed to factorize completely from other variables. Then the final corrected sample can divided in two bins in centrality $0-10\%$ and $10-100\%$, for these two subsets the closure in another parameter, e.g. η is checked, one can then see large non closures in these two subsets that are in opposite direction, so when averaged over they give good closure. Therefore, instead of assuming complete factorization, a minimal binning is applied, bins boundaries in $p_{\mathrm{T}}$are chosen to be 0.5, 0.55, 0.65, 0.8, 1, 3, 8,300 GeV/c. As statistics is not a problem at low p_{T} and because the curvature of tracks change more rapidly at this kinematic range, a large number of bins are picked for low-pt tracks. For low p_{T} tracks events are further divided in

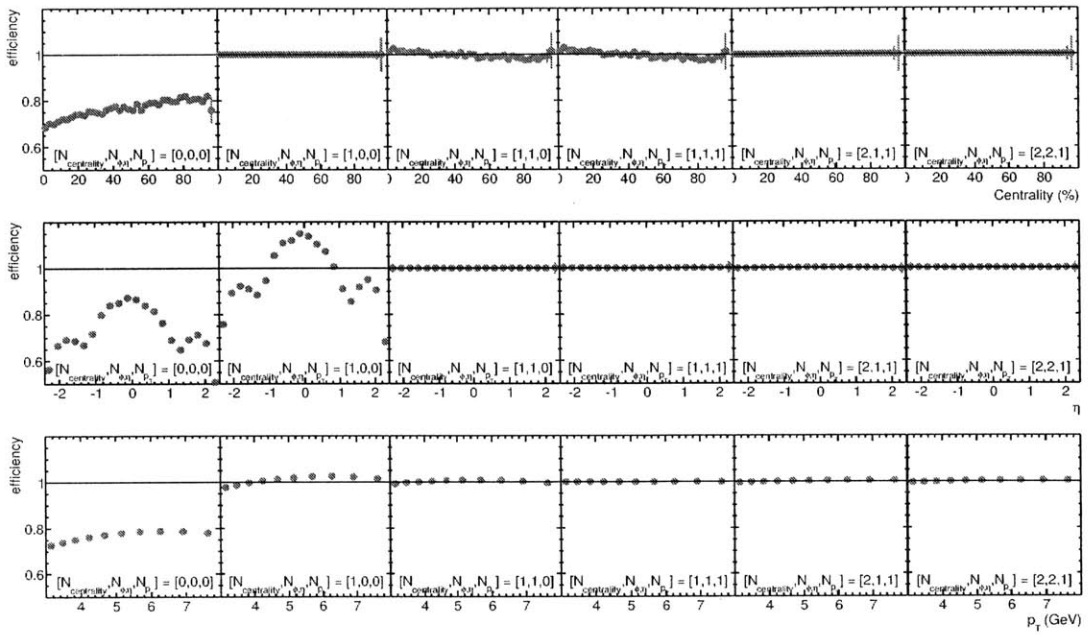

Figure 8-9: Step by step convergence of an iterative correction table for 3 factorized dimensions on 4 parameters, first centrality, then $\eta - \phi$ and then p_{T}, is corrected. Each panel shows one iteration, and first panels are before correction. Note that the selection, parameters and binning used here is not the final choice and this aims to serve as an example.

centrality due to the same non-factorization issue, the centrality bins are chosen to be 0-10, 10-20, 20-30, 30-50 and 50-100 % for $p_{\mathrm{T}} < 3$ GeV, 0-10, 10-20 and 20-100 % for $3 < p_{\mathrm{T}} < 8$ GeV/c and no binning in centrality is applied for larger p_{T} values. In total there are 29 bins in ($p_{\mathrm{T}}\times$ centrality), and in each of these the iterative factorized correction is carried out. Further factorization tests, where further binning is introduced did not show any nonclosure larger than 3% in all the bins. Therefore, the performance is considered to be sufficient.

The performance of the iterative factorized track correction table used in analyses [167, 166] is shown in Fig. 8-10 where corrected track distributions are compared to particle distributions. They agree with each other within 5%. For pp tracking a similar iterative procedure is applied without the centrality dimension, and in total 4 bins were found to be sufficient in p_{T} (0.5-1, 1-3, 3-8 and 8-300 GeV). Meaning that factorization assumption causes less problems in pp tracking, which is almost

perfectly factorizable.

8.5 Performance of jet reconstruction

Jet reconstruction involves challenges of different nature compared to track reconstruction. For tracks the difficulty is finding the particle and making sure it is not a random combination of hits. A very high-p_{T}, e.g. 100 GeV, jet is very hard to miss and it is also not likely for another object or detector noise to mimic a jet at this p_{T} without an actual jet in place. Therefore, at least for high p_{T} jets the reconstruction efficiency and misidentification rates are not big concerns. Jet reconstruction efficiency is 100% for jets above 50 GeV. Fake jet problems exists up to higher p_{T} ($\approx$ 80 GeV) for inclusive jets. However, finding a back-to-back dijet pair significantly reduces the probability of jets being fake. As shown in Fig. 8-11, down to 50 GeV the probability of a subleading jet being fake is $\approx$ 0.001-0.002 %.

Instead, the challenge for a jet reconstruction algorithm is calculating the p_{T} of the jet accurately, for tracks this is not an issue as can be seen in Fig. 8-4.

8.5.1 Jet energy correction procedure

Jet energy corrections aim to correct the raw jet p_{T}, calculated by clustering raw detector objects such as calorimeter tower E_{T} and PF candidate p_{T}, to obtain the "real" jet p_{T} we would have found if we had a priori access to information of all the particles produced in the collision. The correction is a multiplicative factor that depends on η and $p_{\mathrm{T}}^{\mathrm{raw}}$, $p_{\mathrm{T}}^{\mathrm{reco}} = C(p_{\mathrm{T}}^{\mathrm{raw}}, \eta) p_{\mathrm{T}}^{\mathrm{raw}}$. The aim is to have $< p_{\mathrm{T}}^{\mathrm{reco}} > = < p_{\mathrm{T}}^{\mathrm{real}} >$.

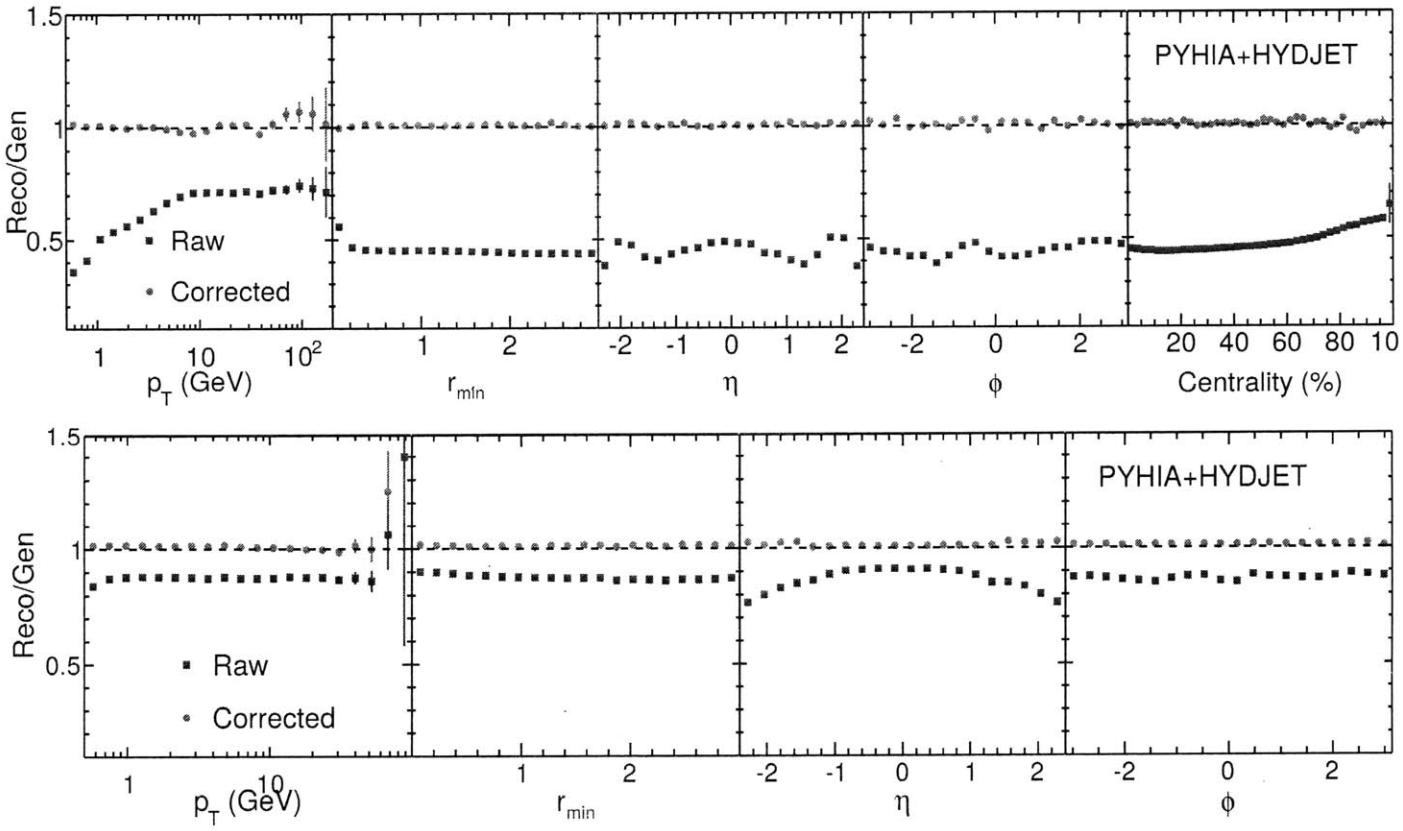

Figure 8-10: Ratio of track and primary particle distributions before and after track corrections in PYTHIA+HYDJET simulations with HI tracking on top and in PYTHIA simulations with pp tracking, shown as blue and red markers respectively, as a function of p_{T}, r_{min}, η and ϕ, and in addition to that centrality for PYTHIA+HYDJET

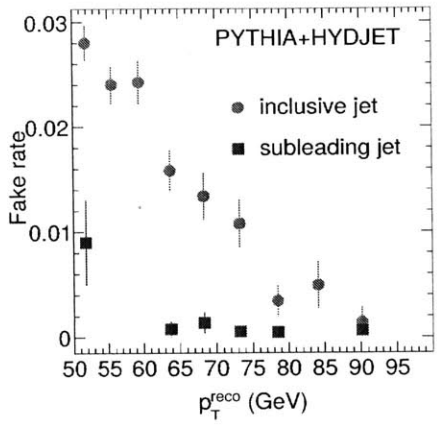

Figure 8-11: Fake rate for inclusive jets and subleading jets with $R = 0.3$ in PYTHIA+HYDJET simulations. For dijet selection leading jet is required to have $p_T > 120$ GeV and the two jets are required to have an azimuthal angle difference greater than $5\pi/6$.

The standard procedure for jet energy corrections in CMS follows the stepwise technique described in Ref. [122]:

- **L1 correction,** $C_{\text{offset}}(p_T^{\text{raw}})$**:** Offset that is caused due to pile up and detector noise is corrected to obtain $p'_T = C_{\text{offset}}(p_T^{\text{raw}})$ assuming it is constant in η. The correction is derived in a data driven way, either with fast jet area method event-by-event, or by correcting event averaged offset. Due to the event-by-event HF/Voronoi background subtraction applied in PbPb collisions L1 corrections are not necessary. In pp collisions at 2.76 TeV and pPb collisions at 5.02 TeV, the pileup probability is small therefore $L1$ corrections are not needed for these collisions systems either.

- **L2-L3 corrections,** $C_{\text{MC}}(p'_T)$: These corrections account for the discrepancy between the p_T of gen-jets obtained by clustering all generated particles except neutrinos in MC generators, p_T^{gen}, and the p_T obtained by clustering reconstructed objects after full chain of detector simulations are applied, p_T^{raw}, [1]. The reconstructed jets are matched to gen-jets by requiring $\Delta = \sqrt{\Delta\eta^2_{\text{reco-gen}} - \Delta\phi^2_{\text{reco-gen}}} < R$. The correction factors are derived as a

[1] $p'_T = p_T^{\text{raw}}$ in MC

function of $p_{\mathrm{T}}^{\mathrm{raw}}$ for different η bins. The functional form used to fit the response, $p_{\mathrm{T}}^{\mathrm{raw}}/p_{\mathrm{T}}^{\mathrm{gen}}$, are the ones used by the JetMET group Eq. 8.3 and Eq. 8.4 describe the these forms for PF jets and Calo jets respectively. The A_i fit parameters are obtained with the ROOT fitting procedure. Different fitting functions are used for PF and calorimeter jets, shown in Eq. 8.3 and 8.4 respectively,

$$[A_0] + \frac{[A_1]}{(log_{10}(x)^2 + [A_2])} + [A_3] * e^{(-[A_4]*(log_{10}(x)-[A_5])^2)} \tag{8.3}$$

$$[A_0] + \frac{[A_1]}{(log_{10}(x))^{[A_2]} + [A_3])} \tag{8.4}$$

These corrections are applied on top of L1 corrections in data if applicable, but for all the analyses presented in following chapters, L2-L3 corrections constitute the initial step.

- **Relative L3 correction, $C_{\mathrm{rel}}(\eta)$:**

  Bulk of the jet energy corrections comes from the L2-L3 step described above, but these corrections rely on a realistic simulation of detector repsonse in MC. Any discrepancy between the response in MC and data are accounted for this and next step of the correction procedure, where a residual data driven correction is calculated.

  The dijet p_{T}-balance technique is used to measure the response of a jet at any η relative to the jet energy response in the region $|\eta| < 1.3$ which is well calibrated. For the measurement of relative jet energy response, 2 leading jets are selected in the pseudorapidity interval of $|\eta| < 3.0$. The reference jet is required to be within $|\eta^{\mathrm{ref}}| < 1.3$, and the probe jet is at arbitrary η^{probe}. If both leading jets are in the pseudorapidity range of $|\eta| < 1.3$, one jet is randomly chosen as the reference jet. On the other hand, if both leading and subleading jets are not in the pseudorapidity range of $|\eta| < 1.3$, this event is not used in the final analysis. To study the relative detector response, a dijet balance quantity B is defined as:

$$B = \frac{p_T^{\text{probe}} - p_T^{\text{ref}}}{p_T^{\text{avg}}} \tag{8.5}$$

where p_T^{avg} is the average p_T of the two jets:

$$p_T^{\text{avg}} = \frac{p_T^{\text{probe}} + p_T^{\text{ref}}}{2} \tag{8.6}$$

Variables $\alpha = p_T^{\text{third}}/p_T^{\text{avg}}$ and $|\Delta\phi_{jj}| = \phi^{\text{probe}} - \phi^{\text{ref}}$ are used to suppress the three-jet events. Events with $|\Delta\phi_{jj}| > 2.5$, $\alpha < 0.2$ and $100 < p_T^{\text{avg}} < 140$ GeV/c are selected for final relative jet energy scale analysis. Figure 8-12 shows the example dijet balance distributions from data and MC. The width of the data is $\sim 7\%$ larger than MC. A significant shift in distribution is also observed in the $\eta^{probe} > 1.3$ region.

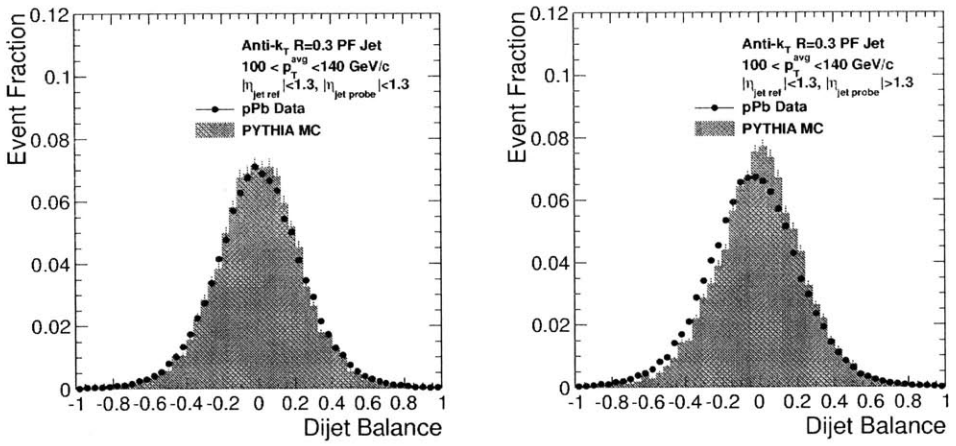

Figure 8-12: Example distributions of the dijet balance quantity B for PF jets with $R = 0.3$ in two η regions in pPb collisions.

The average value of the B distribution, $\langle B \rangle$ in a given η^{probe} bin, is used to determine the relative response R_{rel}:

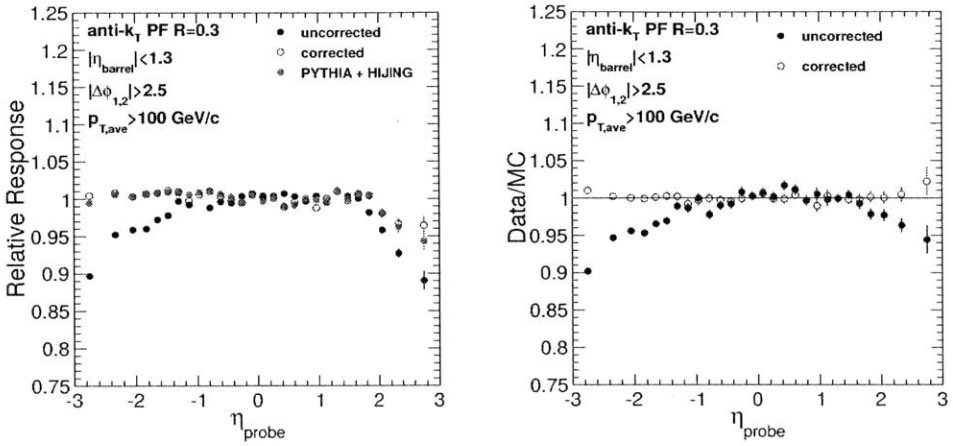

Figure 8-13: (Left) Relative response for pPb, PYTHIA+HIJING sample and pPb after correction. (Right) Ratio of relative response of data and MC before and after the correction with $C_{\mathrm{asym}}(\eta)$.

$$R_{\mathrm{rel}}(\eta^{\mathrm{probe}}) = \frac{2 + \langle B \rangle}{2 - \langle B \rangle} \tag{8.7}$$

Figure 8-13 shows the relative response evaluated in data and PYTHIA+HIJING MC. Correction factors $C_{\mathrm{asym}}(\eta^{\mathrm{probe}}) = R_{\mathrm{rel}}^{MC}(\eta^{\mathrm{probe}})/R_{\mathrm{rel}}^{data}(\eta^{\mathrm{probe}})$ are derived and applied on all reconstructed jets in pPb data. The relative response after correction is also shown in Figure 8-13. As can be seen from the right panel of the figure after the correction the agreement between data and MC is within 2%.

The relative data driven corrections are not applicable in PbPb collisions because they depend on balance of dijets, which are modified by jet quenching effects. Relative L3 corrections are necessary when jets in the forward regions are studied, i.e., $|\eta| > 2$, this is why in PbPb collisions none of the analysis has crossed this limit so far. If pp collisions are used as a reference to PbPb collisions, the same η selection is chosen and these corrections are therefore often omitted in pp collisions as well. Size of relative L3 corrections have been

checked in pp and peripheral, i.e., with large impact parameter, PbPb events, and as shown in Fig. 8-14 the relative L3 correction is $< 2\%$ for $|\eta| < 1.6$, the range used in the analyses described in Chapter 10. Note that the Relative L3 corrections depend on the detector conditions during the data taking period, and on how well these conditions are simulated in MC. This is why relative response differences in data and MC are different in Fig. 8-13 and 8-14. Moreover, nonlinearities can depend on the occupancy effects resulting in differences between these corrections in pp, pPb and PbPb collisions.

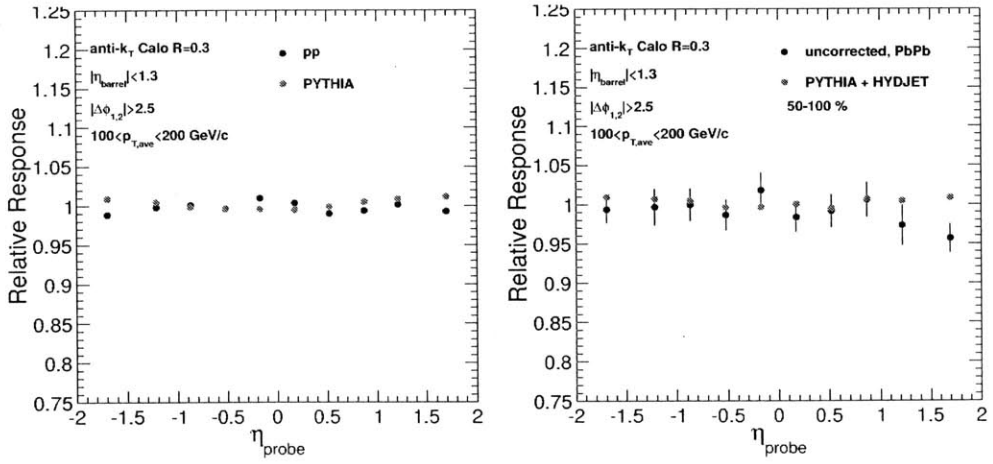

Figure 8-14: (Left) Relative response in pp and PYTHIA simulations. (Right) Relative response in 50-100 % peripheral PbPb and PYTHIA+HYDJET events.

- **Absolute L2 correction,** $C_{\rm abs}(p''_{\rm T})$

  The absolute jet energy response is measured using γ+jet events. Events with a photon in the barrel region $|\eta| < 1.479$ and $p_T^\gamma > 40$ GeV/c are selected. The jets used in the γ+jets sample are required to lie in the pseudorapidity interval $|\eta^{\rm probe}| < 3$ and $\Delta\phi_{j\gamma}(= |\phi^\gamma - \phi^{probe}|) > 0.3$ region. The leading away side jet with $p_T^{\rm probe} > 15$ GeV/c are selected as the probe jet. The γ+jets sample are dominated by dijet background, where a jet mimics the photon. To suppress this background, the photon candidate is required to be isolated (SumIso$^{\rm UE-sub} < 5$ GeV) and the show shape is required to be photon-like ($\sigma_{\eta\eta} < 0.01$). Details of

those requirements can be found the isolated photon analysis [101].

To reject γ+2 jets events, variables $\alpha^{\gamma} = p_T^{\text{subleading}}/p_T^{\gamma}$ and $\Delta\phi_{j\gamma}$ are used. Events with $|\Delta\phi_{j\gamma}| > 2.5$ and $\alpha^{\gamma} < 0.2$ are selected for final absolute jet energy scale analysis.

The average value of the transverse momentum ratio $p_T^{\text{probe}}/p_T^{\gamma}$ distribution in a given η^{probe} bin, is used to determine the absolute response R_{abs}. Figure 8-15 shows the absolute response evaluated in data and PYTHIA+HIJING MC where the data and MC are in good agreement. The ratio of the R_{abs} in data and MC is found to be 0.999 ± 0.005 which is consistent with 1. $C_{\text{abs}} = 1$ is used for final jet energy correction.

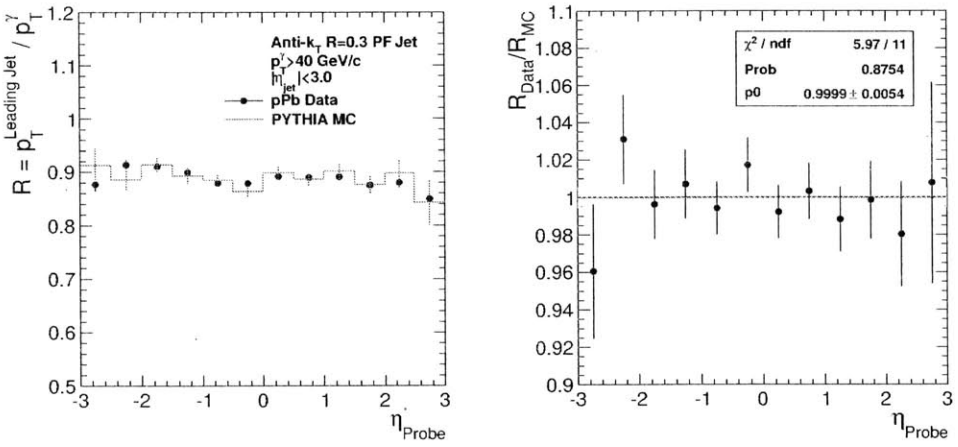

Figure 8-15: (Left) Absolute response for pPb, PYTHIA+HIJING γ-jet sample and pPb after correction. (Right) Ratio of absolute response of data and MC after the correction with $C_{\text{asym}}(\eta)$. The result is fit with a constant and the statistical error of this constant is shown as the yellow band in the plot.

This correction requires large statistics of γ-jet events and due to statistical limitations they have not been used in any collision systems used by the heavy ion group. However they have been checked and they agree with unity within the statistical fluctuations.

- The overall correction is calculated as $C(p_{\text{T}}^{\text{raw}}, \eta) = C_{offset}(p_{\text{T}}^{\text{raw}}) \times C_{\text{MC}}(p'_{\text{T}}, \eta) \times C_{\text{rel}}(\eta) \times C_{\text{abs}}(p''_{\text{T}})$. However, in our analyses we use a subset of the standard

corrections in pPb collisions ($C(p_{\mathrm{T}}^{\mathrm{raw}}, \eta) = C_{\mathrm{MC}}(p_{\mathrm{T}}^{\mathrm{raw}}, \eta) \times C_{\mathrm{rel}}(\eta)$) and some additional specialized ones in pp and PbPb collisions, which are discussed in the next section.

Additional analysis specific corrections are used for "missing-p_{T}" analysis described in Chapter 10, these are discussed next.

8.5.2 Fragmentation dependent jet energy corrections

For certain analyses that measure charged particle distributions around jets [167, 166] feeding in the track reconstruction effects during jet reconstruction, as PF algorithm does, is not favourable. PF jets suffer from a large change in jet p_{T} when a high p_{T}particle is failed to be reconstructed by the tracking algorithm. On the other hand, calorimeter jets suffer from fragmentation biases caused due to calorimeter response being non-linear as a function of particle energy. Many particles with low energy create a smaller response than a single particle carrying the total energy of these particles. Therefore, jets that fragment softer are under-corrected while jets that fragment hard are over-corrected.

In order to minimize the jet and track reconstruction biases without introducing large correlations between the two, calorimeter jets were used in the "missing-p_{T}" analysis with additional corrections which improve the performance and correct for the fragmentation biases. The fragmentation dependent JEC, FF JEC, accounts for the dependence of calorimeter jet energy on number of PF candidates above 2 GeV, N_{PF} inside a cone of $\eta - \phi$, $\Delta < R$, around jet axis. For PbPb collisions, the PF candidate p_{T} after HF/Voronoi subtraction is used in the count of particles inside the cone. As mentioned earlier the p_{T} of PF candidates after HF/Voronoi subtraction do not reflect their original p_{T}. However, this is found to correct for the fragmentation bias for all collision centrality ranges. In pp and PbPb collisions overall correction is given as $C(p_{\mathrm{T}}^{\mathrm{raw}}, \eta) = C_{\mathrm{MC}}(p_{\mathrm{T}}^{\mathrm{raw}}, \eta) \times C_{\mathrm{FF}}(p_{\mathrm{T}}'', N_{\mathrm{PF}}, centrality)$.

8.5.3 Jet energy scale and resolution

Jet energy scale (JES) describes the jet-averaged agreement between $p_{\mathrm{T}}^{\mathrm{real}}$ and $p_{\mathrm{T}}^{\mathrm{reco}}$. For the case of L2-L3 corrections, the true p_{T} is $p_{\mathrm{T}}^{\mathrm{gen}}$, which is the p_{T} of jets obtained by clustering all generated particles except neutrinos in PYTHIA simulations. Not to be sensitive to the tail of the distribution JES is calculated fitting a Gaussian function to $p_{\mathrm{T}}^{\mathrm{reco}}/p_{\mathrm{T}}^{\mathrm{gen}}$ distributions in intervals of $p_{\mathrm{T}}^{\mathrm{gen}}$, or η. The μ parameter of the Gaussian fit is used instead of the mean of the distributions. The width of these Gaussian fits σ parameter defines the jet energy resolution.

In Fig. 8-16 the dependence of JES on N_{PF} is shown for calorimeter jets before and after FF JEC correction, as can be seen the dependence is flattened after the corrections are applied. In the same figure in right panel, the dependence of JES on N_{PF} is shown for PF jets. PF algorithm does not introduce any significant fragmentation dependent bias on JES. Therefore, using these corrections for PF jets do not add to the performance of jet reconstruction. One might notice that there is an offset from 1 for calo jets with FF JEC and for PF jets in Fig. 8-16, but this offset is a result of resolution effects introduced by selection on $100 < p_{\mathrm{T}} < 140$ GeV to demonstrate the fragmentation bias in calorimeter jets, and it is not reflecting a problem in the correction procedure.

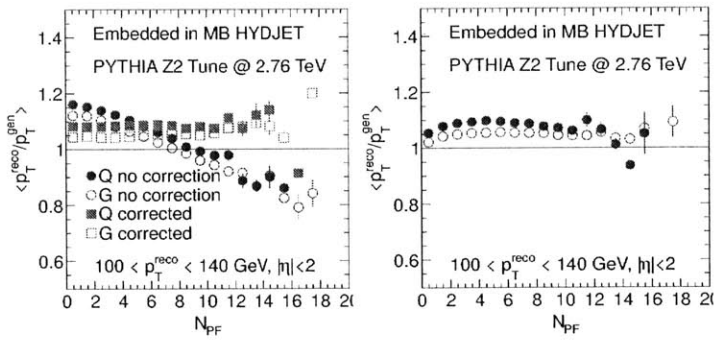

Figure 8-16: The dependence of JES on number of PF candidates with $p_{\mathrm{T}} > 2$ GeV inside the jet cone.

For g initiated jets N_{PF} values are larger on average compared to q initiated jets as shown in Fig 8-17. Therefore, g jets are significantly under-corrected for calorimeter

jets without FF JEC, but the separation between q-g JES improves significantly after these corrections. The JES for q and g jets are shown separately before and after FF JEC in Fig. 8-18 for PYTHIA simulations. The difference in JES of q and g jets at 100 GeV before FF JEC is $\approx 10\%$ and it is reduced to 4% after the correction. In the same figure the JES for inclusive parton flavor is also shown and the agreement with 1 is better than 1-2 %.

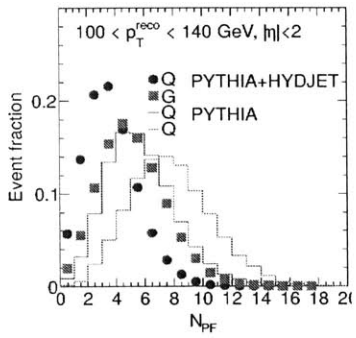

Figure 8-17: Distribution of number of PF candidates with $p_{\mathrm{T}} > 2$ GeV inside the jet cone for q and g initiated jets. The distributions for PYTHIA+HYDJET simulations use PF candidate p_{T} after HF/Voronoi subtraction, while the distributions for PYTHIA simulations are without any subtraction.

Calorimeter jets have worse resolution compared to PF jets, because of the fluctuations in shower formation in calorimeters. In addition to correcting for the fragmentation bias in calo jets FF JEC improves the resolution of jets as well. The resolution of PF and calorimeter jets with and without FF JEC are shown in Fig. 8-19. For peripheral events PF jets have the best resolution, but in central event calorimeter jets with FF JEC perform better.

Resolution can be parameterized with a function of the form:

$$\frac{\sigma}{p_{\mathrm{T}}(\mathrm{GeV})} = C \oplus \frac{S}{\sqrt{p_{\mathrm{T}}/(\mathrm{GeV})}} \oplus \frac{N}{p_{\mathrm{T}}/(\mathrm{GeV})} \tag{8.8}$$

where $\oplus$ indicates a sum in quadrature. Each of these term have a physical meaning, C is caused by electronic noise and tracking inefficiencies, S accounts for shower fluctuations, and N is the noise associated to underlying event or pile-up.

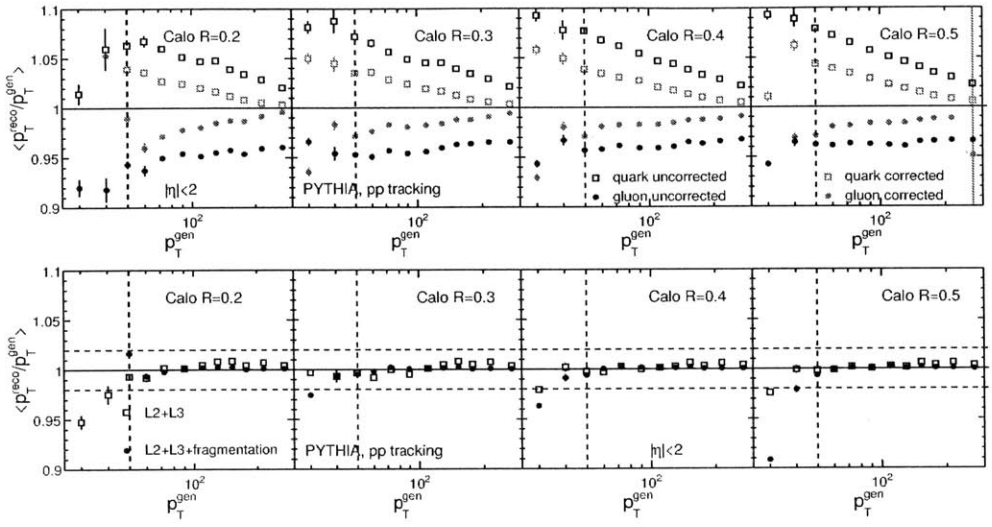

Figure 8-18: (Top) Jet energy scale as a function of p_{T}^{gen} for q and g jets before (black markers) and after (red markers) the fragmentation dependent correction for jets with $R = 0.2 - 0.5$ in PYTHIA simulations. (Bottom) Jet energy scale for inclusive jet flavor.

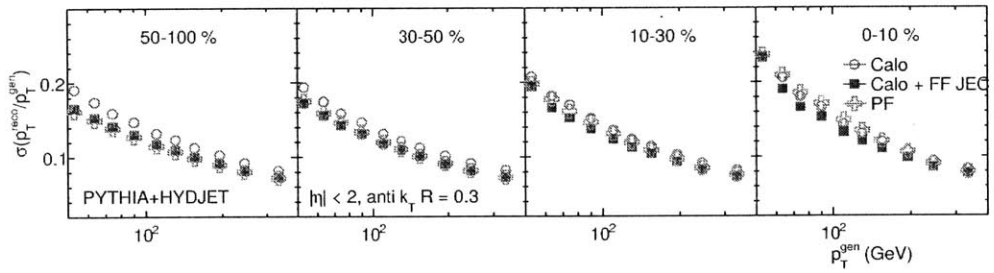

Figure 8-19: Jet energy resolution for $R = 0.3$ PF jets, and calorimeter jets with and without fragmentation dependent jet energy corrections in bins of collision centrality.

Using fits to $\sigma(\mathrm{p_T(GeV)})$ of the form as given above we obtained the parameters for pp collisions and for different centrality classes in PbPb collisions. For pp collisions the noise term, N, is set to zero since it is negligible compared to the noise in PbPb collisions. The values obtained for C in pp collisions is used in fits for PbPb collisions as well. However, separate S terms are calculated for pp and PbPb. In PbPb, S term fixed to be constant across all centrality ranges. The N parameter in PbPb collisions is calculated in bins of centrality used in the measurements. The values of resolution parameters are listed in Table 8.2. Resolution in PYTHIA+HYDJET in bins of collision

centrality as a function of $p_{\mathrm{T}}^{\mathrm{gen}}$ is shown in Fig. 8-20 together with the fits, as expected resolution gets worse by going to central events and to larger R parameters because of the increase in the N value. In each panel resolution in PYTHIA is shown as well in order to provide a reference to the corresponding curves in embedded events.

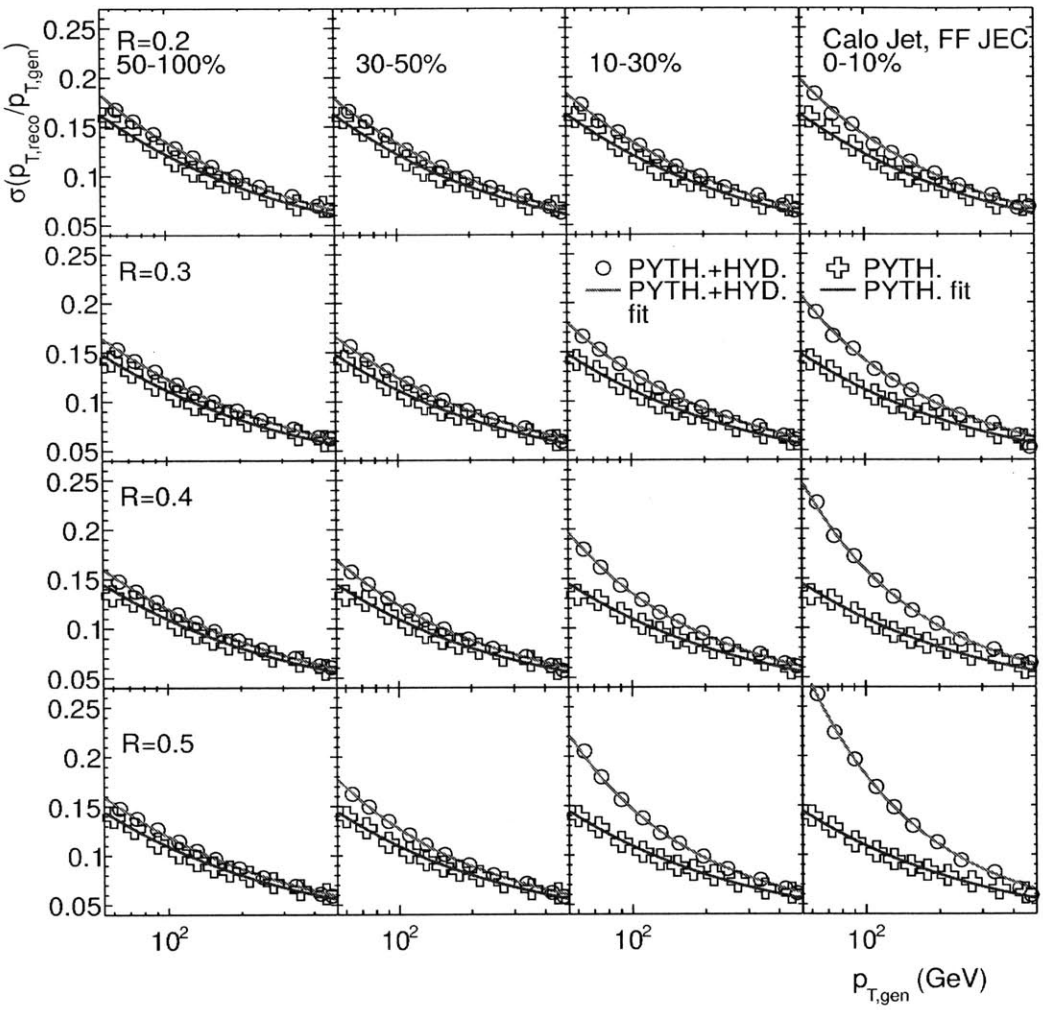

Figure 8-20: Jet energy resolution for jets with $R = 0.2 - 0.5$ in PYTHIA and PYTHIA + HYDJET simulations. From top row to bottom R parameter increases, while from left to right collisions become more central. The values for PYTHIA do not have any centrality selection but are repeated in each panel to enable a comparison to PYTHIA + HYDJET curves.

Table 8.2: Parameters of the functional form for the jet energy resolution $\sigma(p_{\mathrm{T}}^{\mathrm{reco}}/p_{\mathrm{T}}^{\mathrm{gen}})$ given in Eq. 8.2, obtained from GEANT4 simulation of PYTHIA pp jets and from PYTHIA jets embedded in HYDJET events for various PbPb centralities (indicated by the % ranges in parentheses).

R	C	S (pp)	S (PbPb)	N			
		$\sqrt{\mathrm{GeV}}$	$\sqrt{\mathrm{GeV}}$	50-100%	30-50 %	10-30 %	0-10 %
0.2	0.034	1.19	1.29	1.0	1.1	1.6	2.8
0.3	0.031	1.08	1.20	1.0	1.3	2.9	5.0
0.4	0.029	1.05	1.15	2.5	3.4	5.5	8.5
0.5	0.025	1.05	1.14	2.7	4.6	7.7	11.7

8.5.4 Performance of HF/Voronoi algorithm

The performance of the subtraction is studied in MB events where after subtraction the energy inside a random cone should be zero if UE is successfully subtracted. The energy in a random cone in MB events after background subtraction (before the equalization step) is shown in Fig. 8-21 and pointing to the success of the UE subtraction algorithm these are Gaussian distributions centered around 0. The distributions are similar for data and simulations, with slightly larger fluctuations in data.

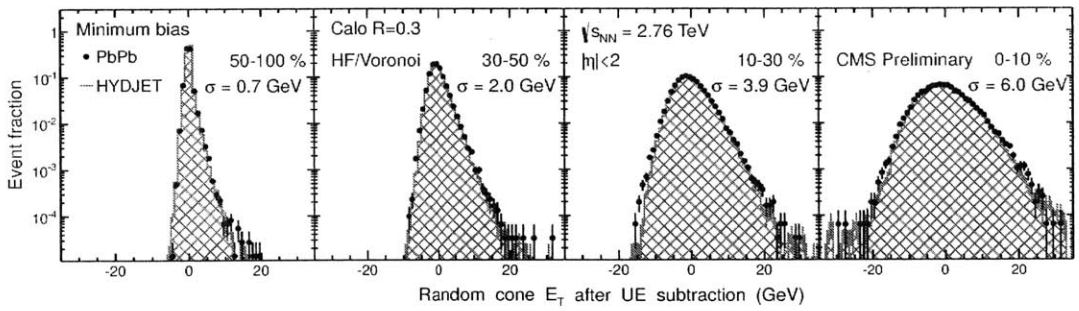

Figure 8-21: Distributions of sum of transverse energy in a random cone of R=0.3 in minimum bias PbPb events and HYDJET events after HF/Voronoi subtraction for four centrality classes 50-100 %, 30-50 %, 10-30 % and 0-10 %.

One might argue that the η dependence of the energy production is almost flat as the results by ALICE, CMS and ATLAS shows [90, 9, 16]. Therefore a simpler background subtraction could be used, such as fastjet background subtraction method [73]. The advantage of HF/Voronoi algorithm is that η dependent nonlinearities are

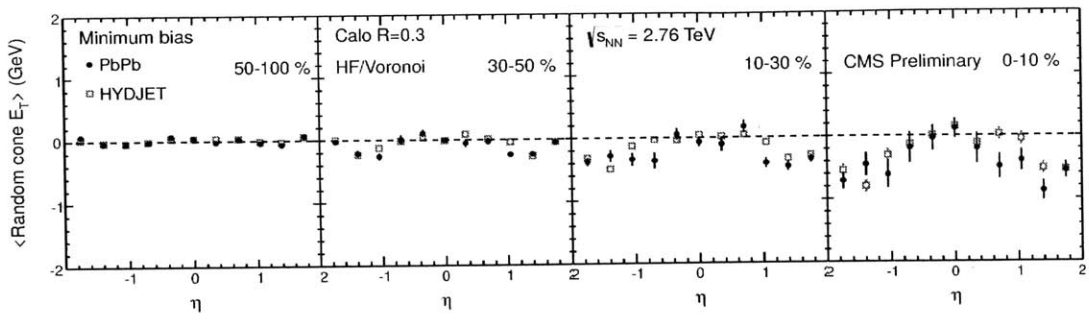

Figure 8-22: Mean sum of transverse energy in a random cone of R=0.3 as a function of Îů in minimum bias PbPb events and HYDJET events after HF/Voronoi subtraction for four centrality classes 50-100 %, 30-50 %, 10-30 % and 0-10 %.

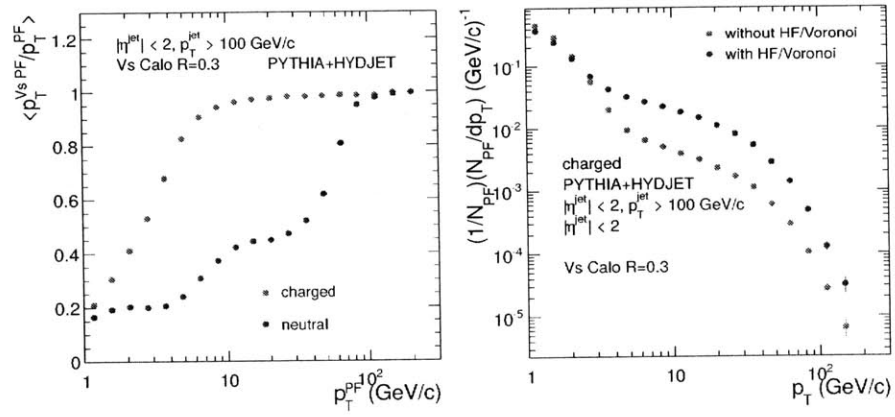

Figure 8-23: The change in the p_T of the PF candidates with HF/Voronoi subtraction for charged and neutral particles above 2 GeV/c(left). The comparison of spectrum of charged PF candidates before and after HF/Voronoi subtraction(right).

taken into account, see the talk by Lai in Ref. [174] for the comparison between the two algorithms. In Fig. 8-22, the mean random cone energy as a function of η is shown to check the agreement with 0 better, and even in $0-10$ % events the agreement is better than $1-2$ GeV over the full η range.

It is important to note that this algorithm leaves the vector sum of transverse momentum in cones of Δ unchanged, but it modifies the p_{T} of each jet constituent. Therefore p_{T} information of individual PF candidates are washed out. HF/Voronoi algorithm modifies the p_{T} of the PF candidates depending on the granularity of

the object, therefore neutral particles which have granularity of calorimeter cells are effected more than the charged PF candidates. For this reason only the charged PF candidates are used in this study. The change in the p_{T} of the PF candidates with HF/Voronoi subtraction is shown in left panel Fig. 8-23. The comparison of spectrum of PF candidates before and after HF/Voronoi subtraction is shown on the right panel of Fig. 8-23.

8.6 Dijet specific reconstruction biases

The physics motivation of studying dijets is discussed in Chapter 7. In terms of technical implications, dijets simplify the analyses procedure by getting rid of certain reconstruction effects, as an example it allows one to go to low p_{T} without suffering from fake jets and increase the phase space for quenched jets. However, the additional complication in dijets is the need for knowing the order of the two jets in the pair, i.e. which jet is the one with highest p_{T} and which one is the one with second highest p_{T}. As JES is a quantity defined on jet averages and because there is 10-20 % resolution around this mean value, some jets have their p_{T} over-corrected and some under-corrected. When one sorts the jets in the event according to their p_{T} due to resolution leading jets p_{T} has larger likelihood of be over-corrected, while subleading jet p_{T} is more likely to be under-corrected. Reconstruction effects on dijets with large A_J are often different from those with small A_J. For small A_J events

Below, we discuss the effect of resolution on dijet p_{T} asymmetry, swapping of order of jets, and finally how track reconstruction effects couple to dijet selection and energy scale.

8.6.1 Jet swapping

Already without reconstruction effects fluctuations in fragmentation of partons can cause ordering of partons in p_{T} to be different than the ordering of p_{T} of jets because part of partons energy might be radiated at angles larger than R parameter used in clusterring. Detector effects produces additional fluctuations in measured p_{T}

compared to gen.

In Fig. 8-24, the probability for leading jet to be matched to a leading jet at gen-level is shown as a function of A_J. This probability is not dependent on centrality for small R values as shown in the left panel and is very similar to the probability in pp. For larger R values as both pointing resolution and p_{T} resolution gets worse the swapping probability increases, i.e. the probability of leading jet to be matched to a gen-level leading jet decreass.

When dijet asymmetry is large leading subleading jet swapping becomes less likely. However, in this case subleading-third jet swapping probability starts to become significant. The probability of subleading jet to be matched to a gen-level subleading jet given leading jets are also matched can be calculated similarly. We observed that this has a very similar dependence on $A_J^{2,3} = (p_{\mathrm{T},2} - p_{\mathrm{T},3})/(p_{\mathrm{T},2} + p_{\mathrm{T},3})$, as the dependence of P_{matched} on A_J. Fraction of events with a subleading and third jet p_{T} close to each other happen with much less frequency compared to the events where there is a leading and subleading jet that have similar p_{T} values.

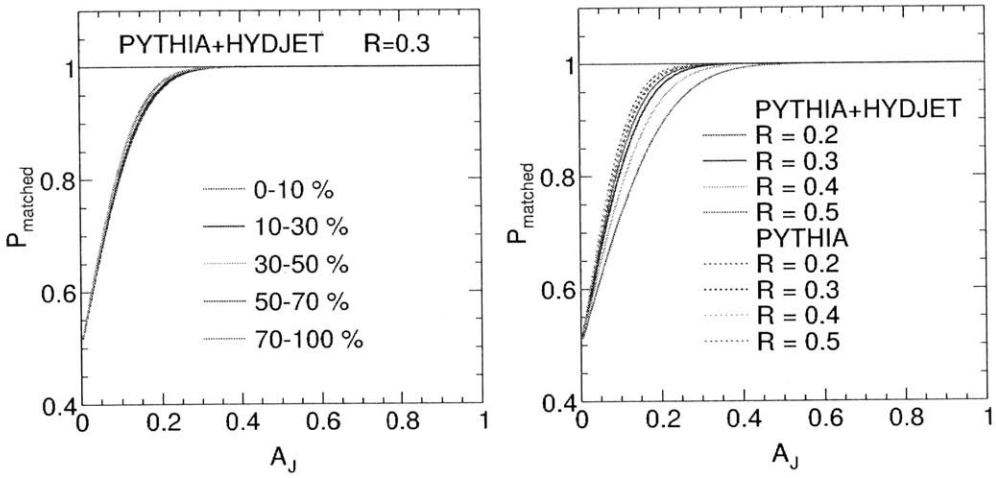

Figure 8-24: (Left) Probability for leading and jet to be matched to leading jet in bins of collision centrality in PYTHIA+HYDJET simulations for $R = 0.3$ calorimeter jets with HF/Voronoi subtraction. (Right) Same probability for jets with $R = 0.2-0.5$, for calorimeter jets in PYTHIA and PYTHIA+HYDJET simulations with 0-10% centrality.

8.6.2 Resolution of dijet asymmetry

The resolution of p_{T} of leading and subleading jet results in smearing of A_J values, andl eading and subleading jet produces additional smearing for balanced jets. In Fig. 8-25, the correlation between A_J^{reco} and A_J^{gen} is shown for all dijets with and without swapping on the left panel. The effect of swapping on this correlation is shown in the middle panel, where the distribution is shown only for those jets whose order is swapped. As the $A_J < 0.1$ range has significant contribution from swapping, the A_J resolution is calculated for values above these by fitting the $A_J^{\mathrm{reco}}/A_J^{\mathrm{gen}}$ distributions with Gaussian functions. In the right panel of Fig. 8-25, $\sigma(A_J^{\mathrm{reco}}/A_J^{\mathrm{gen}})$ is shown on for $R = 0.2 - 0.5$, and it is found to be insensitive to the R parameter. The resolution is similar in PYTHIA+HYDJET events for calo jets HF/Voronoi subtraction.

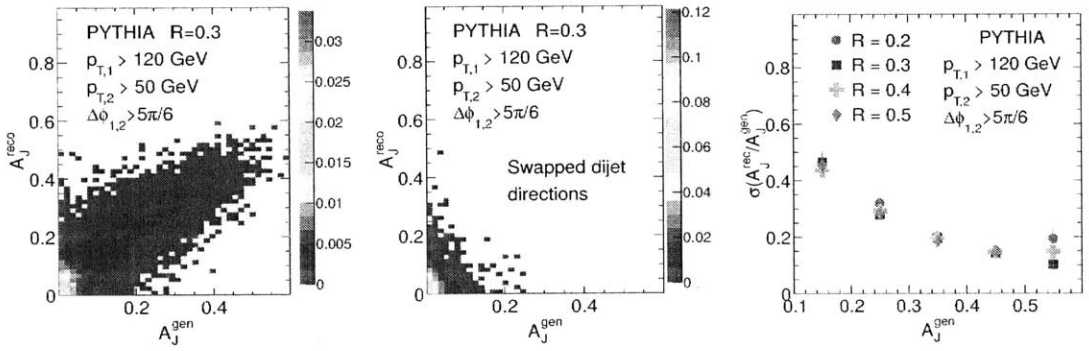

Figure 8-25: (Left) Correlation between A_J^{reco} and A_J^{gen} for R=0.3 Calo jets in PYTHIA events, (Middle) Same correlation for dijets where ordering of the pair is swapped with respect to that for gen-jets. (Right) Resolution of A_J for different R parameters.

8.6.3 Correlation between jet an track reconstruction biases

When a high p_{T} track inside the jet is lost either due to scattering in the detector which changes its direction, or because of track reconstruction algorithms failing to find it, this effects the p_{T} of the reconstructed jet. PF jets are the ones that are the most affected by this, while calorimeter jets still show the same effect in the case of change in the direction of the track because of interactions with the detector

material. This effect is not very important effect for inclusive jets, but when dijets are considered it again produces opposite effects for leading and subleading jet p_{T} values, and therefore the problem is enhanced for large A_J events.

A jet which loses a track inside its cone is more likely to become the subleading, and the higher the p_{T} of the track the more likely this is to happen. As a result the track correction tables which are derived for inclusive jets, under-estimate the inefficiencies in subleading jet cones and over estimate the efficiency in leading jet cones. To account for this a residual track correction table only for tracks inside $\Delta R < 0.2$ of leading and subleading jet was derived. In Fig. 8-26 the difference in these two tables are shown, i.e. the residual track correction for subleading jet minus correction for leading jet. This bias depends on the p_{T} of the track and the also on the reconstructed A_J of the dijet pair, increases as a function of both of these parameters. The bias is rather small for calorimeter jets with FF JEC corrections in pp which is shown on top left panel, because track reconstruction is much more efficient in pp collisions. In top right panel of Fig. 8-26, the corresponding plot is shown for calorimeter jets with FF JEC in PbPb collisions, which are the final jet collections used in the analysis, and this can be compared to calorimeter jets without FF JEC in the bottom left panel and to PF jets in the bottom right panel. The bias is larger for PF jets and goes as high as 22 % for large A_J events and for high p_{T} particles. The bias is smaller without FF JEC, but FF JEC reduces the jet reconstruction systematics significantly, therefore this improvement is not considered to be sufficient to change the choice of jet collection.

In Fig. 8-27 a more direct representation of the bias can be found. As the bias is largest in large A_J events only events with $A_J > 0.22$ are considered for this check. The maximum p_{T} of lost particle is found and when it is required to be large $10 < p_{\mathrm{T}} < 50$ GeV, the reco to gen p_{T} ratios shift towards smaller values both for leading and subleading jet. Meaning that when a high p_{T} track inside the jet is not found its energy shifts to smaller values on average. Although this shift is not as large as the overall resolution effect which makes subleading jets to be under- and leading jets to be over-corrected. Therefore, instead of comparing to unity, the curves

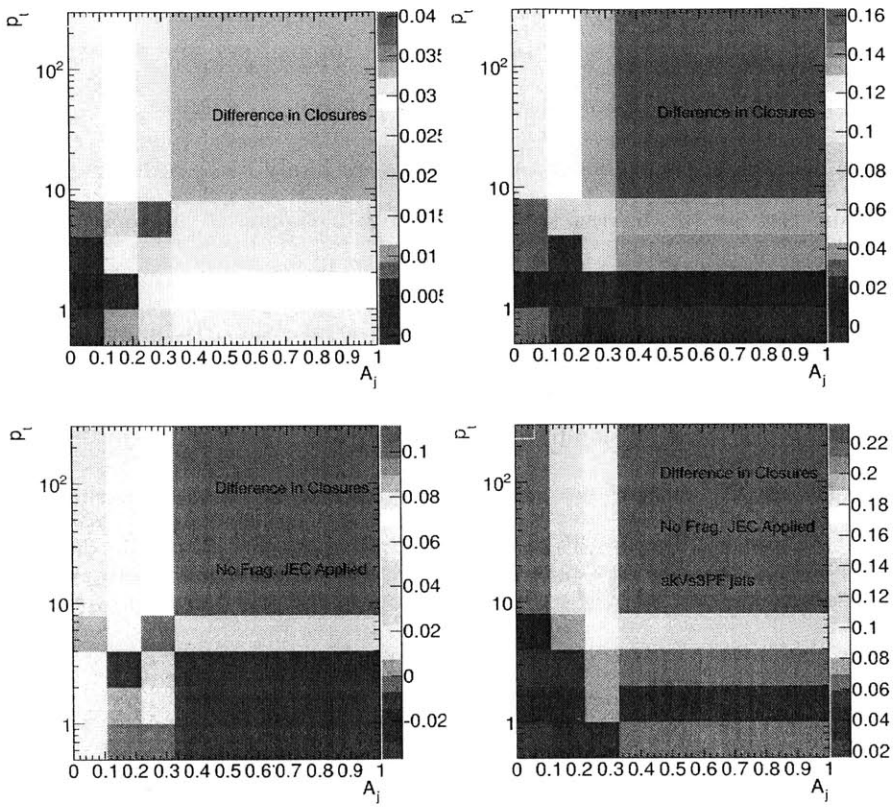

Figure 8-26: Incone track correction differences for subleading jet and leading jet. The corrections are shown for (top-left)calorimeter jets with FF JEC in pp, (top-right) same in PbPb, (bottom-left) calorimeter jets with standard corrections, (bottom-right) PF jets.

associated to jets with a lost a high p_{T} track, should be compared to those the highest p_{T} value of a lost track if any is 10 GeV.

8.6.4 Underlying event fluctuations and jet energy

HF/Voronoi algorithm subtracts the UE based on event averages. However there are event-by-event fluctuations that cause differences in energy densities in mid-rapidity at a given HF energy, and on top of that there are local density fluctuations. A jet might be ovelapping with an upper energy fluctuation or a lower energy fluctuation, and its energy might be over- or under-corrected, respectively. This results in leading

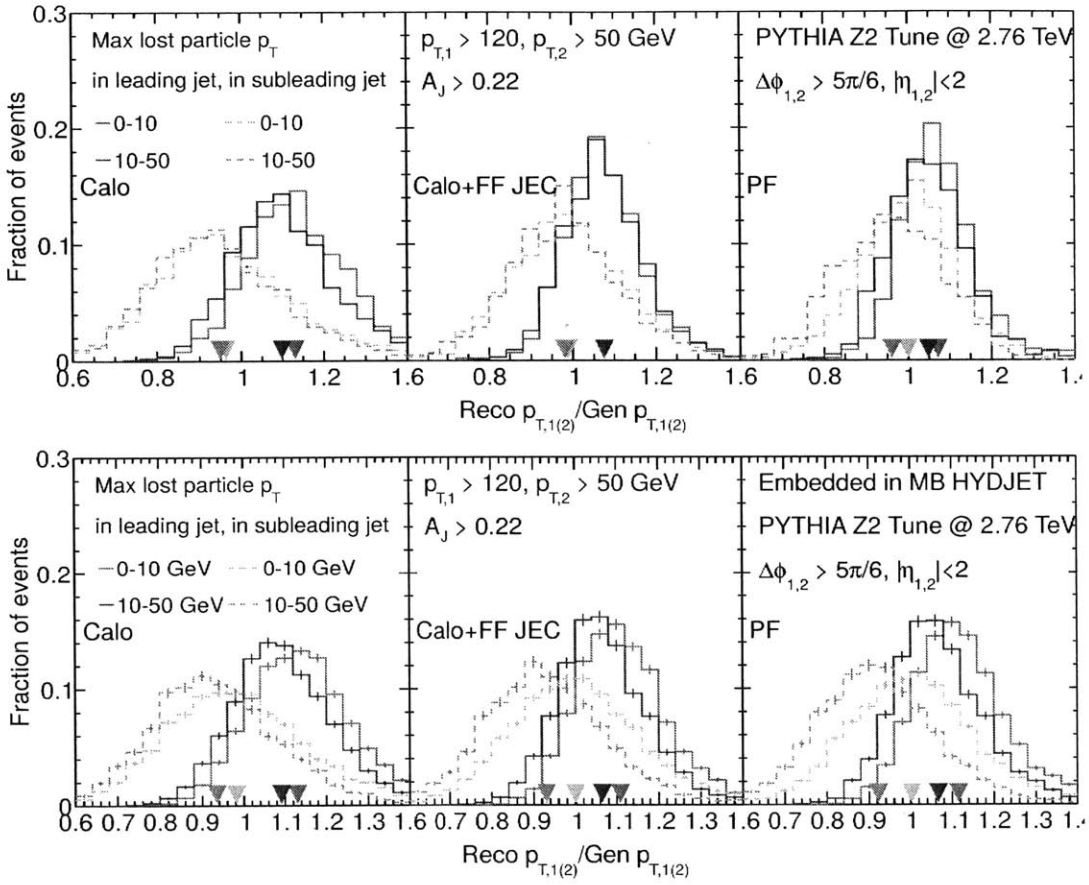

Figure 8-27: JES for leading (points) and subleading (histograms) jet in asymmetric ($A_J > 0.22$) dijet events in PYTHIA simulations. Blue points and histograms show the JES for events where inside the cone ($\Delta R < 0.3$) of leading and subleading jet all the gen particles above 10 GeV are reconstructed. Red points and histograms belong to events where there is a particle with $10 < p_T < 50$ that is not matched to a reconstructed track.

jet being more likely to be located in the direction of a upper density fluctuation.

8.7 Summary

Track and jet reconstruction algorithms used in heavy-ion collisions are specialized to work in high multiplicity environment. The correction of reconstruction effects is done in several steps for both reconstructed objects, and the final agreement after corrections compared to generator level event information in MC is found to be $< 5\%$

for track corrections and $< 2\%$ for jet energy corrections. Two special corrections were developed for analysis presented in Chapter 10, iterative factorized track correction tables that allows us to derive corrections in 5 dimensions, and fragmentation dependent jet energy corrections that corrects for the under- and over- correction of soft and hard fragmenting jets, respectively. The latter correction reduced the systematic uncertainties in final results for analyses presented in Chapter 10 by a factor of 3, and allows us to minimize the autocorrelation between jet and track reconstruction biases. Dijet specific reconstruction effects are discussed in Section 8.6, which is mostly related to reconstruction effects which result in over-corrected jets to become leading jet and under-corrected jets to become subleading jet. Based on the causes of this over- and under- corrections measurements are biased differently, therefore to minimize these biases it is important to understand the problem and apply dijet specific analysis procedures.

Chapter 9

Dijets in pPb

Studying pPb collisions at LHC at $\sqrt{s_{NN}}$ TeV scales, provides the opportunity to test the evolutions of nPDFs that are extracted from low energy DIS data, and pAu collisions at RHIC at $\sqrt{s_{NN}} = 200$ GeV. In addition, pPb collisions provide a reference for PbPb collisions. Measurements in PbPb collisions are often compared to pp collisions to observe modifications in properties of jets due to the effects of the medium. However, these modifications can be partly due to cold nuclear effects such as nuclear modification of parton distributions which we discussed (refer to Section 3.3), Cronin effect[169, 126] and saturation[137]. pPb collisions allow us to factorize cold nuclear effects from final state ones that are associated to the medium. This common view on usefulness of measurements in pPb collisions has developed a new direction with the observation of flow in pPb collisions which is very similar to flow in PbPb collisions which we interpretted as a sign of medium formation. Therefore, a recent question that needs to be answered before one can use pPb data to constrain nPDF and as a baseline with cold nuclear effects for PbPb is whether or not there are final state effects in pPb collisions as well.

In analysis of dijet properties in pPb collisions, we have two main aims: To search for final state effects that might modify jet properties, and to measure dijet properties that are sensitive to nPDFs as an input to future nPDF fits. The final state effects are addressed by the measurement of $p_{T,2}/p_{T,1}$, which is simply a variant of dijet p_{T} asymmetry, which was discussed in Section 7.1 aiming to measure imbalance induced

by jet quenching, and $\Delta\phi_{1,2}$ as defined in Eq. 7.2 to check broadenning effects. The initial state effects are probed by η_{dijet} as defined in Eq. 7.4. Sections 9.1, 9.2, 9.3 and 9.5 are taken from Ref. [110]. The kinematic model used in explaining the large modifications in η_{dijet} distributions as a function of event activity is taken from [47] with small additions.

9.1 Systematic uncertainties

The major systematic uncertainty for the $\langle\eta_{\text{dijet}}\rangle$ measurement comes from the uncertainty in the jet energy correction. Varying the transverse momentum of the jets by <2% up (down) for the jet at positive (negative) η results in a shift of the $\langle\eta_{\text{dijet}}\rangle$ value by ± 0.03. The uncertainty associated with the HF activity selection bias is estimated from the difference between PYTHIA without HF activity selection and PYTHIA + HIJINGwith HF activity selection. The uncertainty is found to be in the range 0.002–0.020. The uncertainty associated with the UE subtraction is studied by comparing the results with and without subtraction, which causes a shift of 0.01 in the two highest HF activity classes. Due to the normalisation to unity, a change in one data point moves the other points in the opposite direction on average, which results in a correlation of the systematic uncertainties at different η_{dijet} value

The main contributions to the systematic uncertainties of $\langle p_{\text{T},2}/p_{\text{T},1}\rangle$ include the uncertainties in the jet energy scale, the jet reconstruction efficiency and the effects of the UE subtraction. The uncertainty in the subtraction procedure is estimated by considering the difference between the p_{T} ratio results from reconstructed jets with and without UE subtraction, which is close to 1%. The residual jet energy scale uncertainty is estimated by varying the transverse momentum of the leading and subleading jets independently and is found to be at the $1-2\%$ level. Uncertainties associated with jet reconstruction efficiency are found to be at the 0.1% level based on Monte Carlo simulation.

9.2 Search for final state effects

This part of the analysis, is motivated by the observation of transverse momentum imbalance in PbPb collisions [93], aims at measuring the dijet transverse momentum ratio and the azimuthal angle correlation in pPb collisions. The dijet pseudorapidity distributions in pPb collisions, which are sensitive to a possible modification of the parton distribution function of the nuclei (nPDF) with respect to that of the nucleons, are also studied.

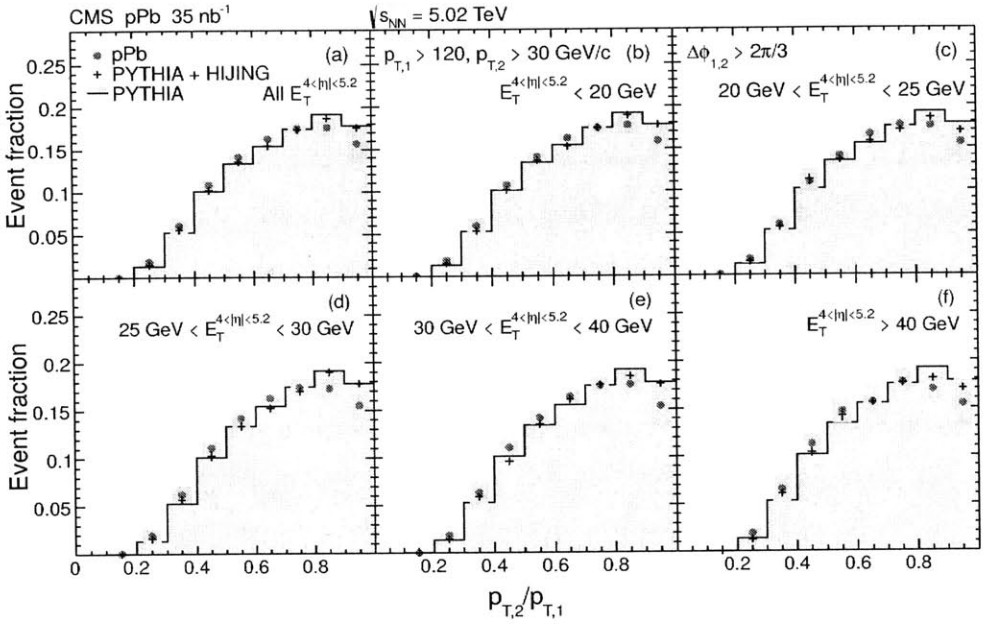

Figure 9-1: Dijet transverse momentum ratio ($p_{T,2}/p_{T,1}$) distributions for leading jets with $p_{T,1} > 120$GeVc, subleading jets with $p_{T,2} > 30$GeVc, and $\Delta\phi_{1,2} > 2\pi/3$ are shown (a) without any selection on the HF transverse energy $E_T^{4<|\eta|<5.2}$, and (b)–(f) for different $E_T^{4<|\eta|<5.2}$ classes. Results for pPb events are shown as the red solid circles, while the crosses show the results for PYTHIA + HIJINGsimulated events. Results for the simulated PYTHIA events are shown as the grey histogram which is replicated in all the panels. The error bars for the statistical uncertainties are smaller than the marker size and the total systematic uncertainties are shown as yellow boxes.

As a function of collision centrality (i.e. the degree of overlap of the two colliding nuclei), dijet events in PbPb collisions were found to have an increasing transverse momentum imbalance for more central events compared to a pp reference [93, 97, 8]. The same analysis is performed in pPb collisions. To characterize the dijet transverse

momentum balance (or imbalance) quantitatively, the dijet transverse momentum ratio $p_{\mathrm{T},2}/p_{\mathrm{T},1}$ is used. As shown in Fig. 9-1, $p_{\mathrm{T},2}/p_{\mathrm{T},1}$ distributions measured in pPb data, PYTHIA and PYTHIA + HIJINGagree within the systematic uncertainty in different $E_{\mathrm{T}}^{4<|\eta|<5.2}$ intervals, including the event class with the largest forward calorimeter activity. The residual difference in the dijet transverse momentum ratio between data and MC simulation can be attributed to a difference in the jet energy resolution, which is better in the MC simulation by about ~1–2% compared to the data [92].

In order to compare results from pPb and Pbp data, Pbp events which pass the same dijet criteria are selected for further analysis with an additional requirement on the forward activity $E_{\mathrm{T}}^{4<|\eta|<5.2} < 60\mathrm{GeV}$, since the bulk of the pPb events satisfy this condition, as can be seen in Fig. 6-8(b). The measured mean value of $p_{\mathrm{T},2}/p_{\mathrm{T},1}$ from these PbPb data is 0.711 ± 0.007 (stat.) ± 0.014 (syst.), which is slightly higher than that in inclusive pPb collisions (0.689 $\pm$ 0.014 (syst.), with a negligible statistical uncertainty). The difference between the $E_{\mathrm{T}}^{4<|\eta|<5.2}$ distributions for pPb and PbPb data, which results in a higher mean $E_{\mathrm{T}}^{4<|\eta|<5.2}$ value for PbPb events (35GeV), as well as the difference in centre-of-mass energy, should be taken into account in this comparison. The predicted $\langle p_{\mathrm{T},2}/p_{\mathrm{T},1}\rangle$ is 6% higher at $\sqrt{s_{\mathrm{NN}}} = 2.76$ than that at 5.02TeV in PYTHIA MC simulations.

Earlier studies of the dijet and photon-jet events in heavy-ion collisions [93, 97, 101, 8] have shown very small modifications of dijet azimuthal correlations despite the large changes seen in the dijet transverse momentum balance. This is an important aspect of the interpretation of energy loss observations [85].

The distributions of the relative azimuthal angle $\Delta\phi_{1,2}$ between the leading and subleading jets that pass the respective p_{T} selections in six HF activity classes, compared to PYTHIA and PYTHIA + HIJINGsimulations, are shown in Figure 9-2. The distributions from pPb data are in good agreement with the PYTHIA reference. To study the evolution of the shape, the distributions are fitted to a normalized exponential function, given as in Eq. 7.3.

The fit is restricted to the region $\Delta\phi_{1,2} > 2\pi/3$. In the data, the width of the

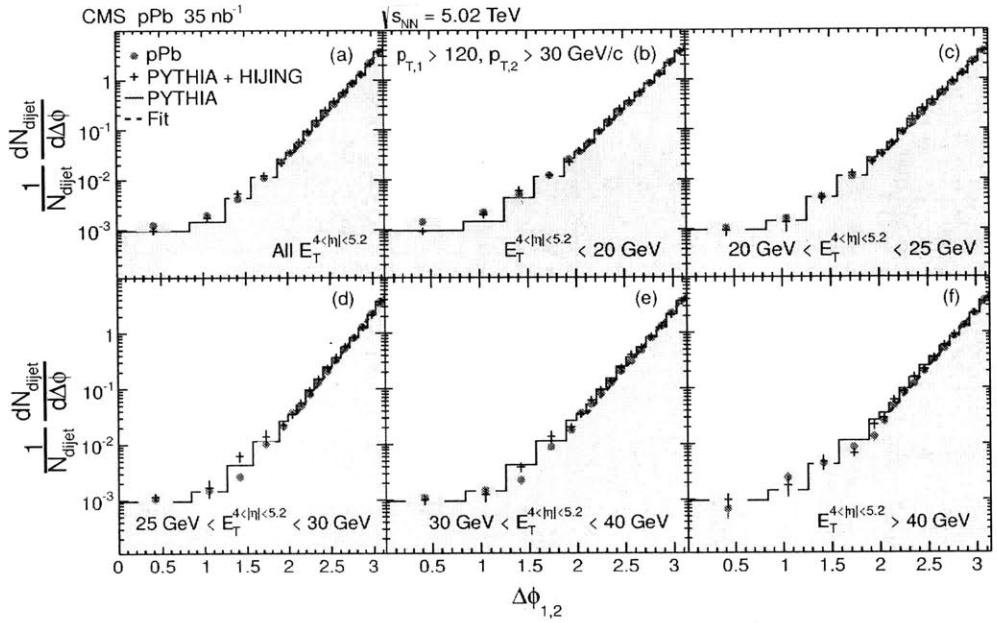

Figure 9-2: Distributions of the azimuthal angle difference $\Delta\phi_{1,2}$ between the leading and subleading jets for leading jets with $p_{T,1} > 120$GeVc and subleading jets with $p_{T,2} > 30$GeVc are shown (a) without any selection on the HF transverse energy $E_T^{4<|\eta|<5.2}$, and (b)–(f) for different $E_T^{4<|\eta|<5.2}$ classes. The range for $\Delta\phi$ in this figure extends below the lower bound of $2\pi/3$, which is used in the selection of the dijets for the other observables. Results for pPb events are shown as the red solid circles, while the crosses show the results for PYTHIA + HIJINGsimulated events. Results for the simulated PYTHIA events are shown as the grey histogram which is replicated in all the panels. The error bars for the statistical uncertainties are smaller than the marker size and the total systematic uncertainties are shown as yellow boxes.

azimuthal angle difference distribution (σ in Eq. (7.3)) is 0.217 ± 0.0004, and its variation as a function of $E_T^{4<|\eta|<5.2}$ is smaller than the systematic uncertainty, which is 3–4%. The width in the data is also found to be 4–7% narrower than that in the PYTHIA simulation.

9.3 Sensitivity to initial state

The normalized distributions of dijet pseudorapidity η_{dijet}, that we introduced in Chapter 7, are studied. Since η_{dijet} and the longitudinal-momentum fraction x of the hard-scattered parton from the Pb ion are highly correlated, these distributions

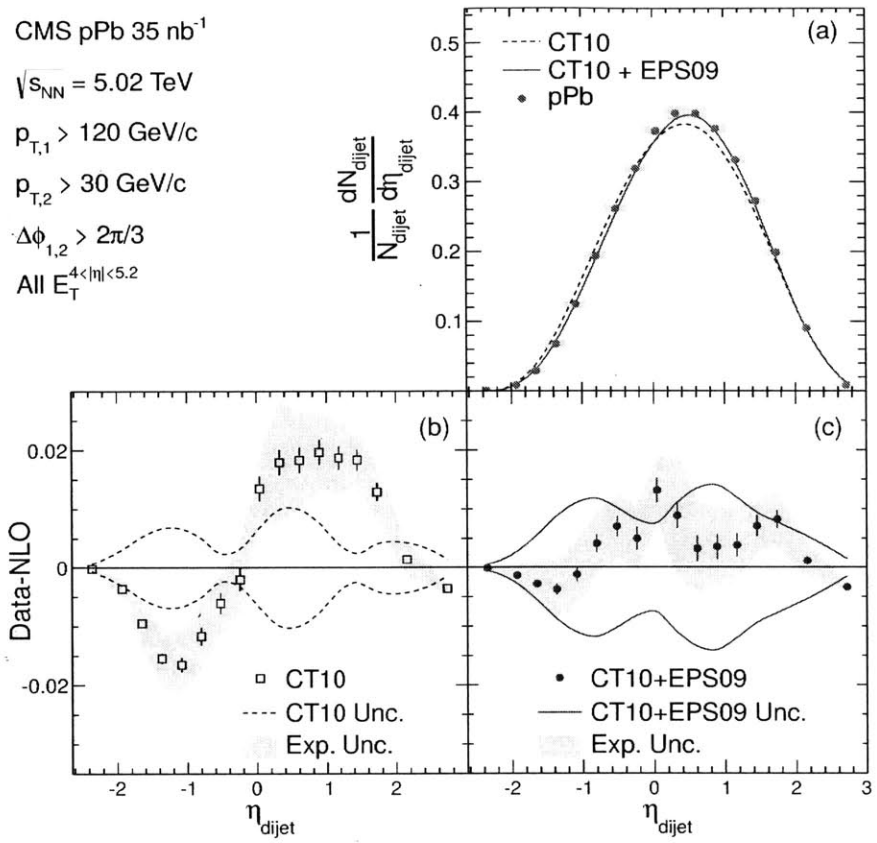

Figure 9-3: (a) Distribution of dijet pseudorapidity ($\eta_{\text{dijet}} = [\eta_1 + \eta_2]/2$) is shown for pPb dijet events with $p_{\text{T},1} > 120$GeVc, $p_{\text{T},2} > 30$GeVc, and $\Delta\phi_{1,2} > 2\pi/3$ as the red solid circles. The results are compared to NLO calculations using CT10 (black dashed curve) and CT10 + EPS09 (blue solid curve) PDFs. (b) The difference between η_{dijet} in data and the one calculated with CT10 proton PDF. The black squares represent the data points, and the theoretical uncertainty is shown with the black dashed line. (c) The difference between η_{dijet} in data and the one calculated with CT10+EPS09 nPDF. The blue solid circles show the data points and blue solid curve the theoretical uncertainty. The yellow bands in (b) and (c) represent experimental uncertainties. The experimental and theoretical uncertainties at different η_{dijet} values are correlated due to normalization to unit area.

are sensitive to possible modifications of the PDF for nucleons in the lead nucleus when comparing η_{dijet} distributions in pp and pPb collisions. As discussed previously, the asymmetry in energy of the pPb collisions at the LHC causes the mean of the *unmodified* dijet pseudorapidity distribution to be centred around a positive value. However, due to the limited jet acceptance (jet $|\eta| < 3$) it is not centred around $\eta = 0.465$, but at $\eta \sim 0.4$.s.

The normalized η_{dijet} distribution measured in inclusive pPb collisions, which is compared to next-to-leading-order (NLO) perturbative QCD predictions [135] using the CT10 [173] and EPS09 [134] PDFs, is shown in Fig. 9-3. The measurement and the NLO calculation based on CT10 + EPS09 PDFs are consistent within the quoted experimental and theoretical uncertainties in the whole η_{dijet} range. On the other hand, the calculation using CT10 alone, which did not account for possible nuclear modifications of the PDFs, gives a poorer description of the observed distribution.

9.4 Constraints on nPDFs

In Ref. [48] the agreement of pPb data at LHC from Run 1 with two sets of nPDFs, DSSZ and EPS09, is tested and data is used to reweight the nPDFs to check the improvements in the theoretical uncertainties. The dijet data presented above is shown to be compatible with EPS09 nPDFs while disfavoring proton PDF results as well as DSSZ results. The ξ^2/N_{data} values are shown in Table 9.1. Other jet data from LHC do not show sensitivity to nPDFs in the sense that they agree equally well (and sometimes even better) with only proton PDF[48].

The ability of dijet pseudorapidity distributions tell apart nPDF and no nPDF cases and even show better agreement with one EPS09 compared to DSSZ is thanks to the sensitivity obtained by cancellation of systematic uncertainties with area normalization. This normalization also cancels a large fraction of theoretical uncertainties from proton PDFs. This is in the lines of commonly used forward-to-backward ratios in pseudorapidity, but the correlation between uncertainties needs to be considered for that observable to be well constraining. However, as shown in Table 9.1 using CT10 PDF versus MSTW makes a factor of 2 difference in χ^2 values, meaning that the proton PDF effects are not cancelling completely. Therefore, it would be useful to make measurements of normalized dijet pseudorapidity distributions in pp collisions to constrain proton PDFs better.

Table 9.1: Taken from [48], showing the χ^2/N_{data} values for 15 points of dijet data used in the reweighting of two different nPDF sets (DSSZ and EPS09) based on two different proton PDFs(CT10 and MSTW2008).

PDF + nPDF	χ^2/N_{data} of fits before reweighting CMS dijet
CT10 + DSSZ	6.3
CT10 + EPS09	0.7
CT10 only	7.7
MSTW2008+ DSSZ	3.8
MSTW2008 + EPS09	0.4
MSTW2008 only	4.5

9.5 Dijet pseudorapidity with centrality selection

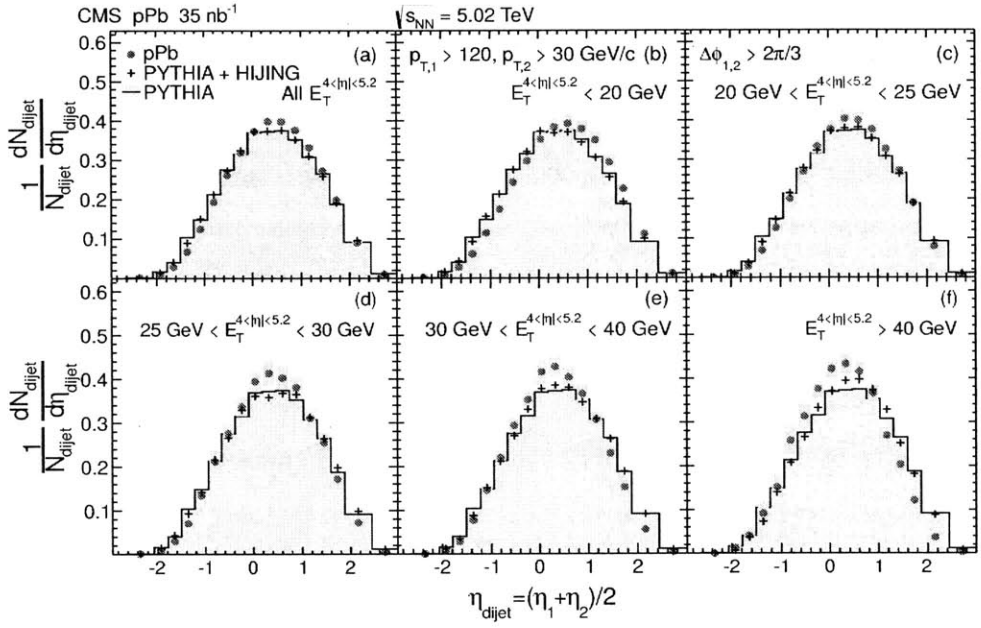

Figure 9-4: Distributions of the dijet pseudorapidity (η_{dijet}) for leading jets with $p_{\text{T},1} > 120$GeVc and subleading jets with $p_{\text{T},2} > 30$GeVc are shown (a) without any selection on the HF transverse energy $E_{\text{T}}^{4<|\eta|<5.2}$, and (b)–(f) for different $E_{\text{T}}^{4<|\eta|<5.2}$ classes. Results for pPb events are shown as the red solid circles, while the crosses show the results for PYTHIA + HIJING simulated events. Results for the simulated PYTHIA events are shown as the grey histogram which is replicated in all the panels. The error bars for the statistical uncertainties are smaller than the marker size and the total systematic uncertainties are shown as yellow boxes.

The η_{dijet} distributions are also studied in different HF activity classes, as shown in

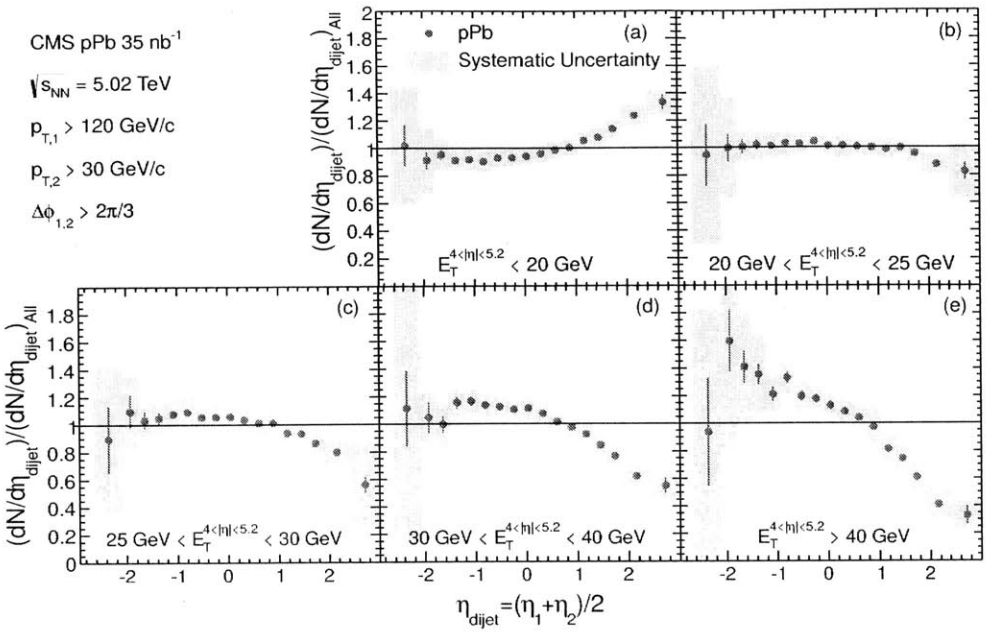

Figure 9-5: Ratio of the dijet pseudorapidity distribution from each $E_{\mathrm{T}}^{4<|\eta|<5.2}$ class shown in panels (b)–(f) of Fig. 9-4 to the spectrum from the inclusive $E_{\mathrm{T}}^{4<|\eta|<5.2}$ bin shown in panel (a). The error bars represent the statistical uncertainties and the total systematic uncertainties are shown as yellow boxes.

Fig. 9-4. The pPb data are compared to PYTHIA and PYTHIA + HIJINGsimulations. Deviations of the η_{dijet} distributions in each class are observed with respect to the PYTHIA reference without HF activity selection. The analysis was also performed using the PYTHIA + HIJINGsimulation in the same HF activity classes and no sizable deviation was observed with respect to the PYTHIA reference. This shows that the PYTHIA + HIJINGembedded sample, which assumes that hard and soft scatterings are independent, does not describe the correlation between the dijet pseudorapidity distribution and forward calorimeter energy. To illustrate the observed deviation in each HF activity class with respect to that in the inclusive pPb collisions, the ratio of the dijet pseudorapidity distribution from each $E_{\mathrm{T}}^{4<|\eta|<5.2}$ class to the distribution without HF requirements is presented in Fig. 9-5. A reduction of the fraction of dijets in the $\eta_{\mathrm{dijet}} > 1$ region is observed in events with large activity measured by the forward calorimeter. The magnitude of the observed modification is much larger than the predictions from the NLO calculations based on impact-parameter

dependent nPDFs [155] in the region $x < 0.1$ for partons in lead nuclei. Note that theory calculations are based on impact parameter, which can take a large range of values in each HF activity class.

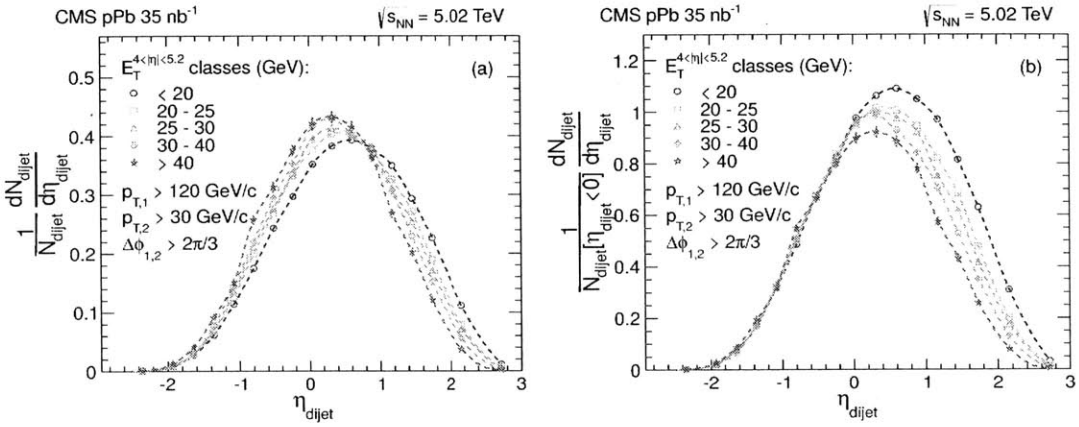

Figure 9-6: Dijet pseudorapidity distributions in the five HF activity classes. (a) The distributions are normalized by the number of selected dijet events. (b) The distributions are normalized by the number of dijet events with $\eta_{\text{dijet}} < 0$. The error bars represent the statistical uncertainties and the dashed lines connecting the data points are drawn to guide the eye.

The pPb distributions for different HF activity classes, from panels (b)–(f) of Fig. 9-4, are overlaid in Fig. 9-6. As shown in Fig. 9-6a, a systematic monotonic decrease of the average η_{dijet} as a function of the HF transverse energy $E_{\text{T}}^{4<|\eta|<5.2}$ is observed. A decrease in the longitudinal momentum carried by partons that participate in hard scattering coming from the proton, or an increase in the longitudinal momentum of partons from the lead nucleus, with increasing HF transverse energy $E_{\text{T}}^{4<|\eta|<5.2}$ would result in a shift in this direction. In order to compare the shape of the η_{dijet} distributions in the interval $\eta_{\text{dijet}} < 0$ the spectra from pPb data are normalized by the number of dijet events with $\eta_{\text{dijet}} < 0$ in the corresponding HF activity class. In inclusive pPb collisions, this interval roughly corresponds to $x > 0.1$ for partons in lead, a region where the measurement is sensitive to the nuclear EMC effect [188]. Using this normalization, the shapes of the η_{dijet} distributions in the region $\eta_{\text{dijet}} < 0$ are found to be similar, as is shown in Fig. 9-6(b).

One possible mechanism which could lead to the observed modification of the η_{dijet}

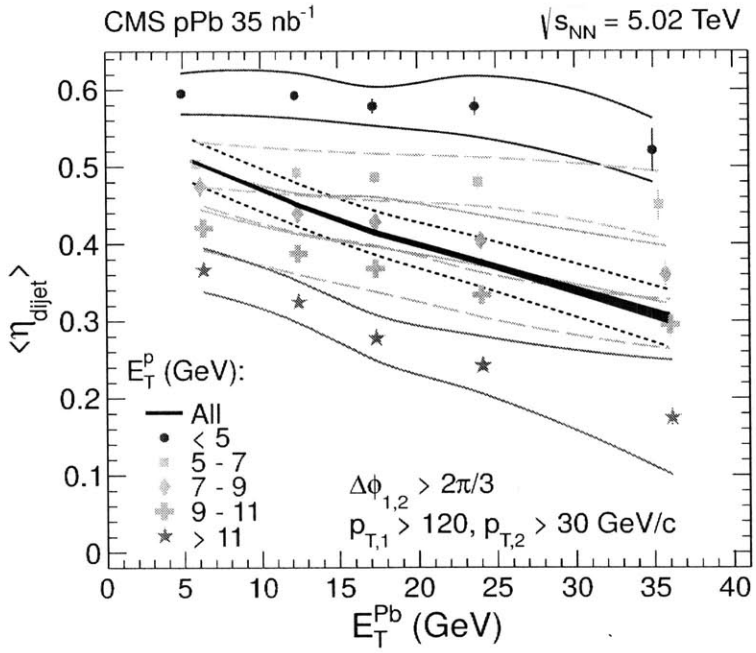

Figure 9-7: Mean of η_{dijet} distribution as a function of the raw transverse energy measured in the HF calorimeter in the lead direction (E_{T}^{Pb}) in bins of forward transverse energy in the proton direction (E_{T}^{p}). The lines indicate the systematic uncertainty on the points with matching color, and the error bars denote the statistical uncertainties. The results without selection on (E_{T}^{p}) are also shown as a solid black line with statistical uncertainties represented by the line width. The dashed black lines indicate the systematic uncertainty on the solid black line.

distribution in events with large forward activity is the kinematical constraint imposed by the selection, which is discussed in detail in 9.6. Jets with a given transverse momentum at larger pseudorapidity will have a larger energy ($E = \cosh(\eta)p_{\text{T}}$). If a large part of the available energy in the collision is observed in the forward calorimeter region, jets above a certain transverse momentum threshold are restricted to be in mid-rapidity, which leads to a narrower dijet pseudorapidity distribution. Moreover, the modification of the PDFs due to the fluctuating size of the proton, as well as the impact parameter dependence of the nuclear PDFs, may further contribute to the observed phenomenon. Therefore, the $\langle \eta_{\text{dijet}} \rangle$ is also studied as a function of the forward calorimeter activity in the lead direction (E_{T}^{Pb}) at fixed values of forward activity in the proton direction (E_{T}^{p}).

The correlation between $\langle\eta_{\text{dijet}}\rangle$ and E_{T}^{Pb} in different E_{T}^{p} intervals is shown in Fig. 9-7. With low forward activity in the proton direction ($E_{\text{T}}^{p} < 5\text{GeV}$, blue circles and solid lines near the top of the figure), the $\langle\eta_{\text{dijet}}\rangle$ is around 0.6 and only weakly dependent on the forward activity in the lead direction. The observed high $\langle\eta_{\text{dijet}}\rangle$ indicates that the mean x of the parton from the proton in the low E_{T}^{p} events is larger than that in inclusive pPb collisions. With high forward activity in the proton direction ($E_{\text{T}}^{p} > 11\text{GeV}$, red stars and solid lines near the bottom of the figure), the $\langle\eta_{\text{dijet}}\rangle$ is found to be decreasing as a function of E_{T}^{Pb}, from 0.37 to 0.17. These results indicate that the degree of modification of the η_{dijet} distribution is highly dependent on the amount of forward activity in the proton direction.

9.6 Modelling the kinematic biases

The classification of events according to some measurement of their activity (energy, multiplicity, etc.) in some region of phase space, what is commonly referred to as centrality selection, is extensively used in the study of nuclear collisions. Naively one expects that to events within a given centrality class correspond similar conditions, say of energy density or temperature. The dependence of specific observables on centrality should then yield information on their sensitivity to the properties of the system (energy density, temperature, etc.). Further, centrality should provide a link, albeit in a model dependent way, to theoretically well-defined quantities such as the impact parameter of the collision.

The usefulness of centrality selection relies, however, on how robustly it can be defined. Specifically, whether the centrality selection (and its link to some theoretical quantity as the impact parameter) depends (i) on the centrality criterium; and (ii) on the observable under consideration i.e. whether there is a correlation between the characteristics of the events under consideration, say the requirement of presence of jets, and the centrality criterium.

While in non-peripheral collisions between heavy ions the classification of centrality classes appears to be robust, in proton-lead collisions at the Large Hadron Collider

(LHC) the situation is far more problematic[1]. Whereas for both dijets [110] and single jets [14] the minimum bias results are well reproduced by standard pQCD with nuclear modification of parton densities [189], the centrality-selected results show a strong dependence on centrality that cannot be accommodated by the existing ideas on the impact parameter dependence of nuclear parton densities [44, 141, 155]. There is an ongoing discussion on the definition of centrality in such asymmetric systems [26, 19].

A numbers of factors can conceivably be at the origin of the observed effects. Fluctuations in the number of partipating nucleons are much larger in proton-nucleus than in nucleus-nucleus collisions and certainly confound the connection of centrality to collision impact parameter. Further, energy-momentum conservation poses significantly more stringent demands in the case of asymmetric collisions. Ultimately the problems can be traced back to our lack of understanding of the detailed microscopic dynamics underlying soft particle production in hadronic and nuclear collisions, and its coupling to hard subprocesses. These issues have been discussed in several recent works [182, 70, 36, 190].

In this short note we address solely, and in a simplistic framework, the role of kinematic constraints on the energy-momentum of the proton. We ask to what extent the requirement of a hard subprocess restricts the soft particle production which will eventually determine the centrality of the event[2].

We focus on CMS dijet [110] and ATLAS single-jet [14] results in pPb collisions at 5.02 TeV/nucleon. We find that our simplistic implementation leads to large effects in good agreement with data. Importantly the model fails to describe data when the implementation is evidently deficient, that is when energy-momentum constraints on the Pb nucleus are expected to play a role.

[1]The problem also exists in dAu collisions at the Relativistic Heavy Ion Collider (RHIC), see e.g. [25, 21].

[2]Take for example the production of a dijet pair at pseudorapidity $\eta_{\rm dijet} = 2$ with leading jet $p_T = 120$ GeV. The minimum momentum fraction taken from the proton is then $x_p \sim 0.35$.

9.6.1 Description of the model

The model that we employ uses PYTHIA [209] for the hard scattering and HIJING [223, 151] for the underlying event. Each event (our results are based on samples of 10^5 for dijets and $2 \cdot 10^6$ for single jet spectra) is generated according to the following procedure:

1. generate a pp event in PYTHIA with no underlying event (for a proton beam of $E_p = 4$ TeV and a Pb beam of $E_{\rm Pb} = 1.58$ TeV/nucleon, $\sqrt{s_{NN}} = 5.02$ TeV) with the required characteristics: jets or dijets within the experimental kinematic cuts, and extract the momentum fraction x_p of the hard parton from the proton participating in the $2 \to 2$ hard subprocess. The nuclear modification of parton densities was not taken into account because for this kinematics their effect, as discussed previously (see also [189]), is much smaller than the one observed in data;

2. generate a minimum bias pPb event in HIJING, for a proton beam of $(1-x_P)E_p$ and a Pb beam of $E_{\rm Pb}$, i.e. we reduce the proton energy for the underlying event such that $\sqrt{s_{NN}} = 2\sqrt{(1-x_p)E_p E_{\rm Pb}}$ [3];

3. shift both events (that are generated in their respective center of mass) to a common frame (the LHC laboratory frame);

4. the HIJING event, generated as minimum bias, is reweighted according to its impact parameter such that scaling in the number of collisions N_{coll}, expected for hard events, is fulfilled;

5. the PYTHIA and HIJING events are superimposed, resulting in a full pPb event with the weight given in the previous step.

Note that the momentum fraction $x_{\rm Pb}$ of the parton from the Pb participating in the $2 \to 2$ hard subprocess is unchanged. This is clearly a deficiency of the model,

[3] Here $E_{\rm p}$ and $E_{\rm Pb}$ does not have any relations ship to $E_{\rm T}^{\rm p}$ and $E_{\rm T}^{\rm Pb}$ variables used in the previous sections

which should accordingly be expected to fail for small N_{coll} (when the number of participating nucleons from the Pb is small) and for large x_{Pb} (for the Pb-going side in pseudorapidity).

The matching procedure based on x_{p} produces a connection between E_{T} deposition in the forward pseudorapidities, which is the common centrality classification variable used by experiments, and dijet production. To demonstrate that this simple procedure creates the necessary link between energy in the UE and energy in the jets the $E_{\mathrm{T}}^{4<|\eta|<5.2}$ distribution is plotted for two different bins of dijet energy. When dijet energy is large, $E_{\mathrm{T}}^{4<|\eta|<5.2}$ distribution shifts towards smaller values.

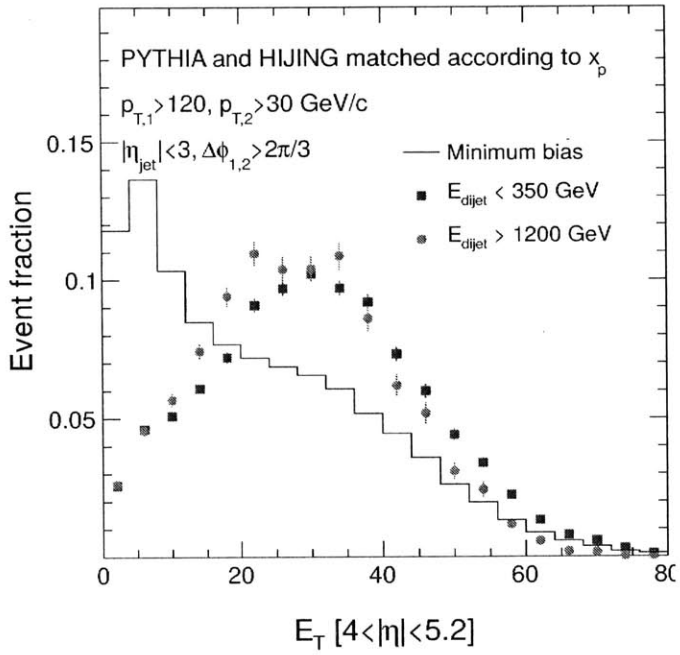

Figure 9-8: Distribution of $E_{\mathrm{T}}^{4<|\eta|<5.2}$ for $E_{dijet} = p_{T,1}cosh(\eta_1)+p_{T,2}cosh(\eta_2)$ selection.

The connection between jets and UE is built as a result of steps 2 and 3 of the procedure described above, i.e., by reducing the energy available in HIJING and by boosting the HIJING event to set their nucleon nucleon pseudorapidity at $\eta_{\mathrm{CM}}^{\mathrm{HIJING}} = 0.5 \ln\left((E_{\mathrm{p}}(1-x_{\mathrm{p}})/E_{\mathrm{Pb}})\right)$. Therefore, if x_{p} is large, then the energy created by HIJING in Pb-going-direction is reduced due to reduction in $\sqrt{s_{\mathrm{NN}}}$, but is enhanced due to boost of the UE towards that direction, while the energy in p-going-direction is reduced both by the change in $\sqrt{s_{\mathrm{NN}}}$ and by the boost.

The average total E_{T} in proton-going-direction, $\langle E_{\mathrm{T}}^{\mathrm{p}} \rangle$, Pb-going direction, $\langle E_{\mathrm{T}}^{\mathrm{p}} \rangle$ and the sum of the two is calculated as a function of x_{p} in two reference frames, in LHC laboratory frame and at center-of-mass frame of HIJING (Shown in the left panel of Fig. 9-9).

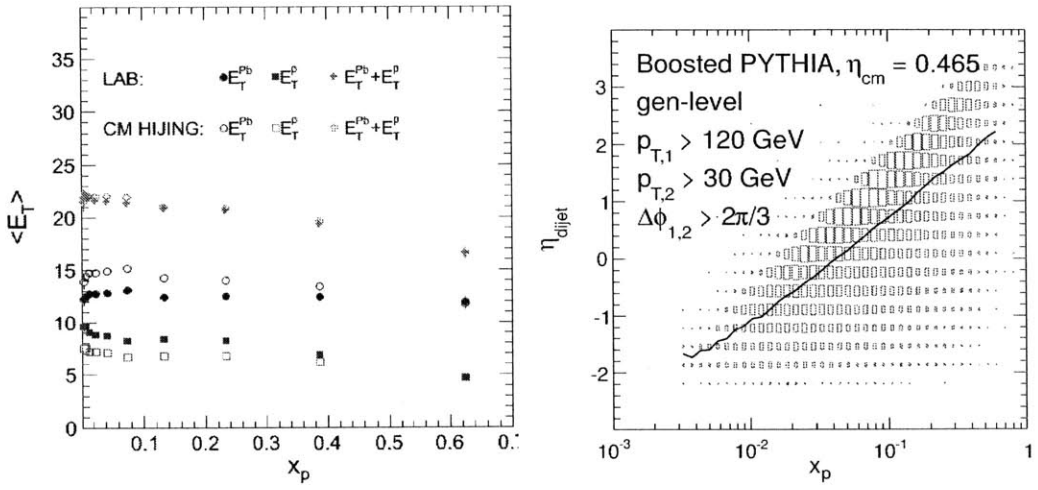

Figure 9-9: (Left) The average total E_{T} in proton-going-direction, $\langle E_{\mathrm{T}}^{\mathrm{p}} \rangle$, Pb-going direction, $\langle E_{\mathrm{T}}^{\mathrm{p}} \rangle$ and the sum of the two as a function of x_{p} in two reference frames, in LHC laboratory frame and at center-of-mass frame of HIJING. (Right) Correlation between η_{dijet} and x_{p}, where the black line shows the average value, $\langle \eta_{\mathrm{dijet}} \rangle$.

The change in E_{T} values are mild with x_{p}, but still large enough to create the effect observed in data, because η_{dijet} is extremely sensitive to x_{p}, as shown in the right panel of Fig. 9-9.

9.6.2 Comparison to CMS dijet results

In this section we consider the dijet measurements by CMS [110]. We generate hard events in PYTHIA with jets reconstructed within $|\eta| < 3$ using the anti-k_T sequential recombination algorithm [74, 75] with a distance parameter of 0.3, considering events required to have a dijet with a leading jet $p_{T,1} > 120$ GeV/c, a subleading jet $p_{T,2} > 30$ GeV/c, and an azimuthal distance between them $\Delta\phi_{1,2} > 2\pi/3$. Then, for the full PYTHIA+HIJING generated event, the transverse energy in the region $4 < |\eta| < 5$ is rescaled, to match that measured by CMS, by a factor that accounts for detector

resolution effects that are not corrected by CMS. It is this rescaled energy that is used to classify events in centrality.

In figure 9-10 we show the comparison of our results for the average dijet pseudorapidity ($\eta_{\rm dijet} = (\eta_1 + \eta_2)/2$) as a function of the total transverse energy deposition in the pseudorapidity range of $4 < |\eta| < 5$, compared with data measured by CMS [110]. The agreement is very good except for the lowest transverse energies, corresponding to peripheral collisions where the model is not expected to work as discussed in the previous section. In figure 9-11 we show the ratio of the dijet pseudorapidity distribution for events in a a given centrality class over the minimum bias distribution, compared to the CMS data. Again, a good overall agreement is found.

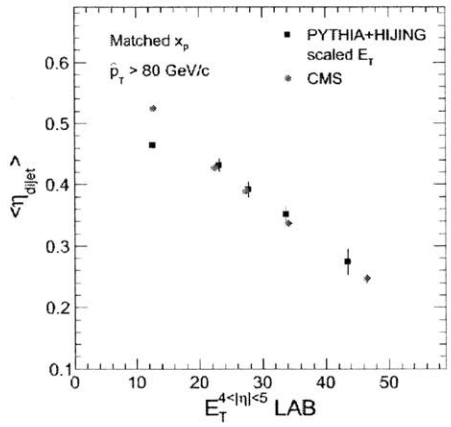

Figure 9-10: Average dijet pseudorapidity ($\eta_{\rm dijet} = (\eta_1 + \eta_2)/2$) as a function of the total transverse energy deposition in the pseudorapidity range of $4 < |\eta| < 5$ for PYTHIA+HIJING events matched according to x_p value (black squares) overlaid with data measured by CMS [110] (red circles).

CMS [110] also provided data on the average dijet pseudorapidity for a fixed energy in the p-going direction, $E_{\rm T}^{p}$ for $4 < \eta < 5$, as a function of the energy in the Pb-going direction, $E_{\rm T}^{\rm Pb}$ for $-5 < \eta < -4$. In figure 9-12 we show the comparison of the CMS data with our PYTHIA+HIJING results. Once more, the model captures the trend of data except for the lowest activity data where only one or two nucleons from the Pb nucleus contribute and the model – that corrects for energy only on the proton side – is clearly deficient due to the neglect of energy-momentum constraints for Pb.

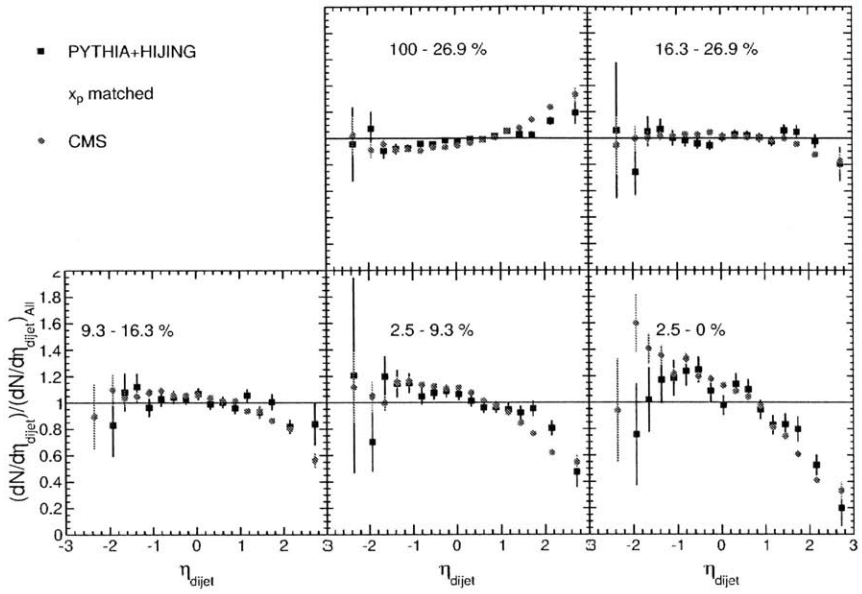

Figure 9-11: Ratios of dijet pseudorapidity ($\eta_{\rm dijet} = (\eta_1 + \eta_2)/2$) distributions with a selection on total forward energy deposition ($E_T^{[4<|\eta|<5]}$) to the dijet pseudorapidity distribution without any requirement on event activity. The calculation in PYTHIA+HIJING is shown by black squares and CMS data points [110] are shown by red circles.

9.6.3 Comparison to inclusive ATLAS jet results

In this section we consider the single-jet measurements by ATLAS [14]. We generate hard events in PYTHIA with jets reconstructed using the anti-k_T sequential recombination algorithm [74, 75] with a distance parameter of 0.4, in the region $|\eta_{\rm jet} - \eta_{\rm CM}| < 3$. The centrality criterium is, in this case, the total transverse energy in Pb-going direction within the pseudorapidity range of $-4.9 < \eta < -3.2$, thus less sensitive to energy constraints on the proton. Let us note that we use, for the different centrality classes, the number of collisions N_{coll} provided by ATLAS and not the one extracted from HIJING [4].

In figure 9-13 we show the results of the model for the nuclear modification factor $R_{p\rm Pb}$ of jets as a function of their transverse momentum, for different centrality classes,

[4] They are (11.94,9.86,8.38,6.934,4.82,2.29) for HIJING and (14.57,12.07,10.37,8.94,6.44,2.98) in the ATLAS paper [14], for the $0-10\%$, $10-20\%$, $20-30\%$, $30-40\%$, $40-60\%$ and $60-90\%$ centrality classes respectively.

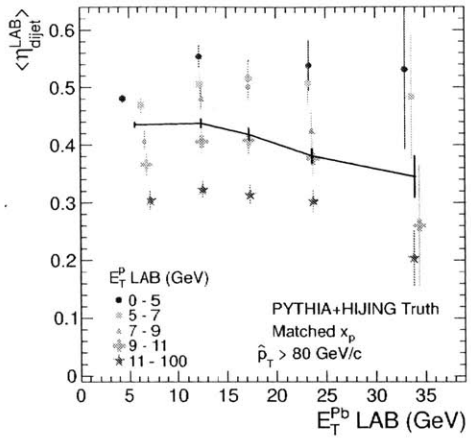

Figure 9-12: PYTHIA+HIJING with x_p matching. Colored markers show average dijet pseudorapidity ($\eta_{\rm dijet} = (\eta_1 + \eta_2)/2$) as a function of transverse energy deposition in the Pb-going direction, $E_{\rm T}^{\rm Pb}$, for bins of the transverse energy deposition in the p-going direction, $E_{\rm T}^{p}$. The choice of pseudorapidity intervals for $E_{\rm T}^{\rm Pb}$ and $E_{\rm T}^{p}$ are $-5 < \eta < -4$ and $4 < \eta < 5$ respectively. The black line shows average dijet pseudorapidity as a function of $E_{\rm T}^{\rm Pb}$ when the requirements on transverse energy in proton going direction are removed.

integrated over the whole pseudorapidity region $|\eta_{\rm jet} - \eta_{\rm CM}| < 3$. The effect of the centrality selection becomes evident.

In figures 9-14, 9-15 and 9-16 we show a comparison of the results of the model with ATLAS data [14] for the nuclear modification factor $\rm R_{pPb}$ of jets as a function of their transverse momentum in different pseudorapidity bins, for central, semicentral and peripheral collisions respectively. A good agreement with data is found for central collisions that deteriorates with decreasing centrality, until the model fails for peripheral collisions as expected from previous discussions.

9.7 Summary

In this Chapter pPb dijet measurements based on [110] were presented, which show no final state effects on jets, such as jet quenching effects similar to that observed in PbPb collisions. Dijet pseudorapidity results provide constraints and reevaluation of fits showed that these can provide improvements nPDF fits. Dijet pseudorapidity distributions are modified significantly when selection on $E_{\rm T}^{4<|\eta|<5.2}$ is applied. Fig-

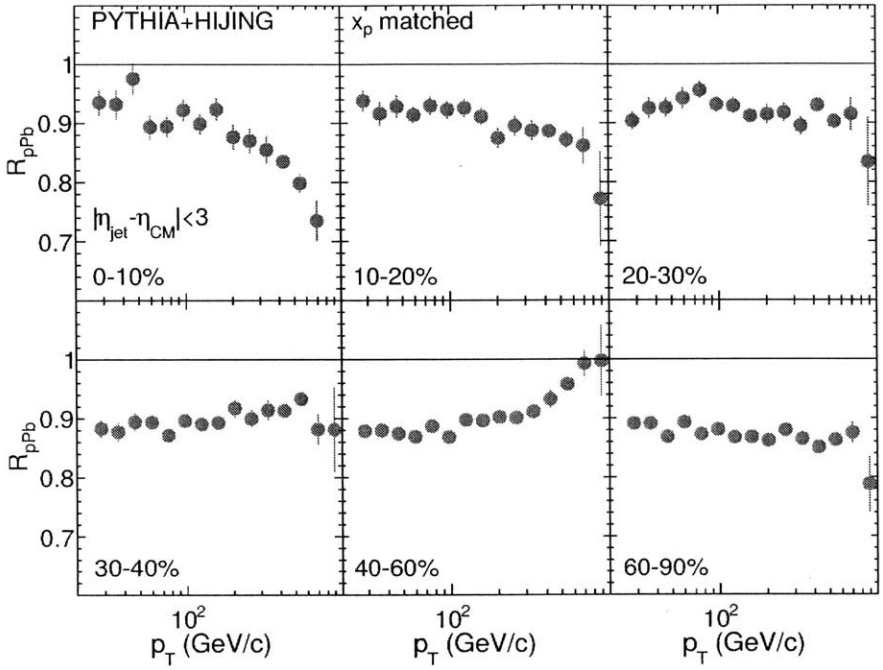

Figure 9-13: R_{pPb} calculation in PYTHIA+HIJING with x_p matching are shown for $0-10\%$, $10-20\%$, $20-30\%$, $30-40\%$, $40-60\%$ and $60-90\%$ centrality classes. The centrality classes are determined according to total transverse energy in Pb-going direction within the pseudorapidity range $-4.9 < \eta < -3.2$.

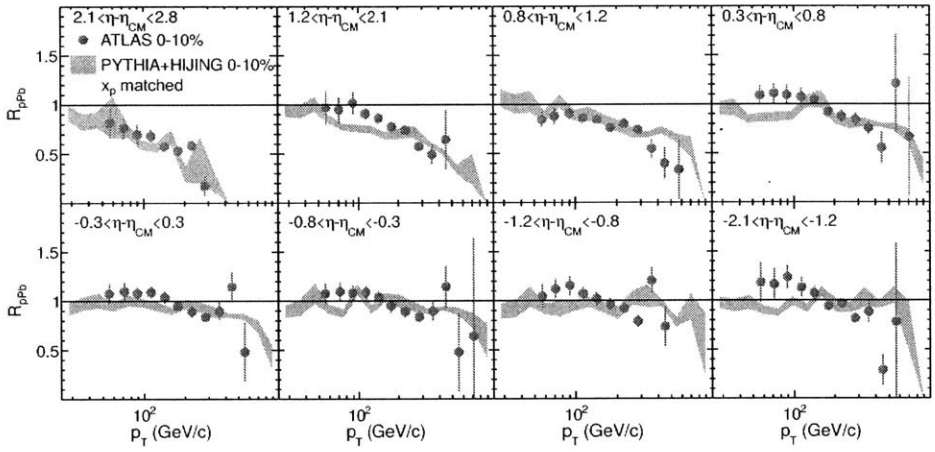

Figure 9-14: R_{pPb} calculation in PYTHIA+HIJING with x_p matching (grey bands) and the measured values by ATLAS ([14], red circles) are shown for the $0-10\%$ centrality class in bins of pseudorapidity in the center-of-mass frame. The centrality classes are determined according to total transverse energy in Pb-going direction within the pseudorapidity range $-4.9 < \eta < -3.2$.

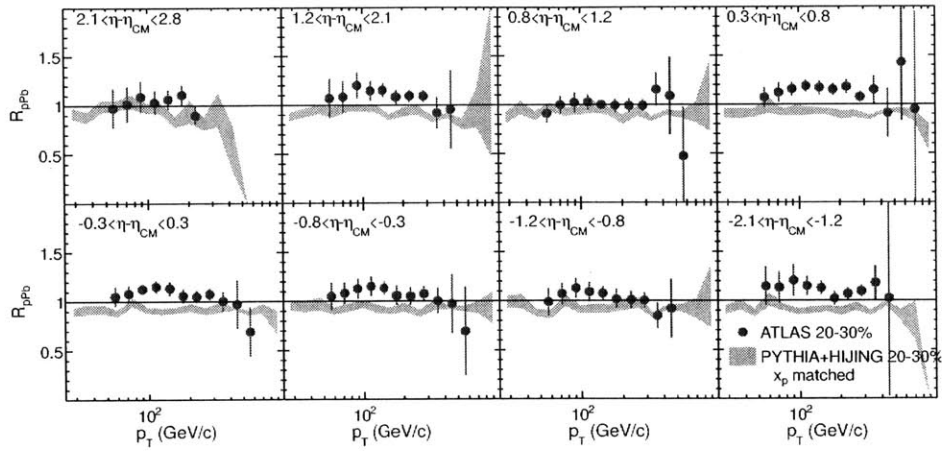

Figure 9-15: $R_{p\mathrm{Pb}}$ calculation in PYTHIA+HIJING with x_p matching (grey bands) and the measured values by ATLAS ([14], blue circles) are shown for the $20-30\%$ centrality class in bins of pseudorapidity in the center-of-mass frame. The centrality classes are determined according to total transverse energy in Pb-going direction within the pseudorapidity range $-4.9 < \eta < -3.2$.

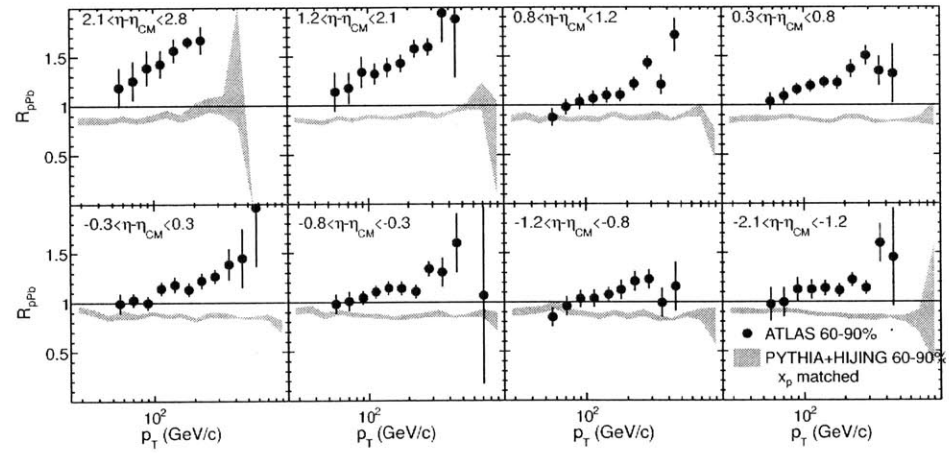

Figure 9-16: $R_{p\mathrm{Pb}}$ calculation in PYTHIA+HIJING with x_p matching (grey bands) and the measured values by ATLAS ([14], black circles) are shown for the $60-90\%$ centrality class in bins of pseudorapidity in the center-of-mass frame. The centrality classes are determined according to total transverse energy in Pb-going direction within the pseudorapidity range $-4.9 < \eta < -3.2$.

ure 9-17 summarizes all of the $E_{\mathrm{T}}^{4<|\eta|<5.2}$ dependent dijet results obtained with pPb collisions. A nearly constant width in the dijet azimuthal angle difference distributions and transverse momentum ratio of the dijets as a function of $E_{\mathrm{T}}^{4<|\eta|<5.2}$ is observed. The lower panels show the mean and standard deviation of the dijet pseu-

dorapidity distribution, measured using jets in the pseudorapidity interval $|\eta| < 3$ in the laboratory frame, as a function of the HF transverse energy. Those quantities change significantly with increasing forward calorimeter transverse energy, while the simulated p dijets embedded in HIJING MC, representing pPb collisions, show no noticeable changes.

Measurement of dijet pseudorapidity distributions with a "centrality" selection reveal kinematic biases which are modelled in Section 9.6.1 by combining PYTHIA and HIJING simulations according to x of parton in hard-scattering interaction from proton. Central inclusive jet data of ATLAS is described with the same model.

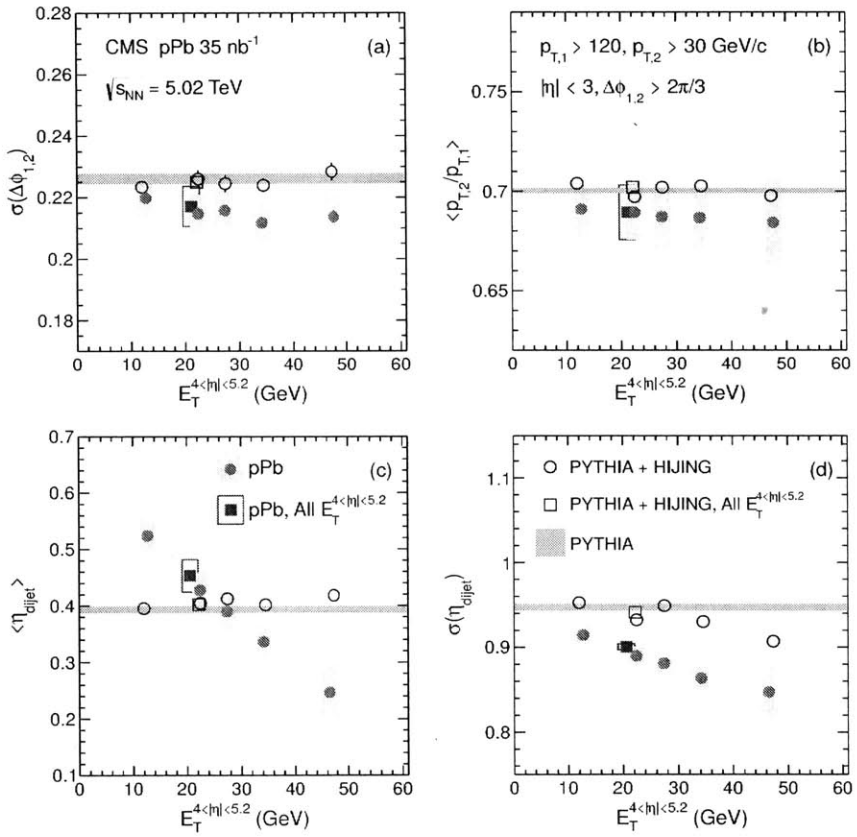

Figure 9-17: Summary of the dijet measurements as a function of $E_{\mathrm{T}}^{4<|\eta|<5.2}$. (a) Fitted $\Delta\phi_{1,2}$ width (σ in Eq. (7.3)). (b) Average ratio of dijet transverse momentum. (c) Mean of the η_{dijet} distribution. (d) Standard deviation of the η_{dijet} distribution. All panels show pPb data (red solid circles) compared to the PYTHIA + HIJING(black open circles) and PYTHIA (light grey band, where the band width indicates statistical uncertainty) simulations. The inclusive HF activity results for pPb and PYTHIA + HIJINGare shown as blue solid and black empty squares, respectively. The yellow, grey and blue boxes indicate the systematic uncertainties and the error bars denote the statistical uncertainties. Note that the legend is spread over the four subfigures.

Chapter 10

Angular scan of particle distributions with respect to dijets

This analysis aims to provide information that would aid the characterization of the energy loss mechanisms responsible for the increase in the fraction of unbalanced dijet pairs in central PbPb relative to pp collisions, as shown in Fig. 7-3.

As hard-scattered partons travel and shower in the QGP, leading and subleading jet can both trigger a coherent medium response and undergo interactions in the medium that modify the parton showers. However, the enhancement in unbalanced dijet pairs suggests that, on average, the subleading jet loses more energy than the leading jet. The modification in jet balance must be compensated by the remaining, unclustered constituents of the event, as each interaction conserves overall momentum.

This analysis aims to measure the distribution of particles which contribute to the overall p_{T} balance in the event, with respect to the direction of the leading and subleading jet. Tracks inside annuli, $\Delta_{min} < \Delta = \sqrt{(\eta_{\mathrm{jet}} - \eta_{\mathrm{track}})^2 + (\phi_{\mathrm{jet}} - \phi_{\mathrm{track}})^2} < \Delta_{max}$, around axis of leading and subleading jets are picked and the projection of their p_{T} on the dijet axis is calculated event-by-event. The radius of the annuli is increased and a scan of the whole acceptance is carried out at steps of $\delta\Delta = 0.2$. Event averages of these projections are taken to obtain the final results, but event-by-event fluctuations are discussed in Section 10.2. Additional information is provided by

simply counting the number of particles rather than measuring their p_{T} projection. A more detailed description of the observables are given in Section 10.1.

The main idea is to study central PbPb collisions with large A_J, and see where the "extra" energy lost by the subleading jet goes. The term "extra" here indicates a comparison of leading jet to subleading jet and at the same time a comparison of PbPb collisions to pp collisions. The p_{T} projections are non-zero also for pp and are dependent on R, as a result of the semi-hard splitting of the parton that creates the subleading jet to form a third jet. The structure of distributions in pp are discussed in Section 10.4. The modification of balance in PbPb compared to pp is presented in 10.5 as a function of centrality and A_J for $R = 0.3$ jets. To investigate how differences in jet fragmentation affect energy loss mechanisms, jets are clustered using several anti-k_{T} R parameters (0.2, 0.3, 0.4 and 0.5). The R dependent results are discussed in Section 10.6 with a focus on central events.

Sections 10.1, 10.3, 10.5, 10.6, and 10.7 are taken from [167].

10.1 Analysis

To select a dijet topology, the azimuth between the leading and subleading jets is required to be $\Delta\phi_{1,2} = |\phi_1 - \phi_2| > 5\pi/6$. Once leading and subleading jets are identified within the initial range of $|\eta| < 2$, both jets are then restricted to be within a tighter $|\eta|$. For measurements that offer comparison to a previous analysis [94], we use the previous selection of $|\eta| < 1.6$. For those that extend up to large angular distances Δ, a tighter requirement of $|\eta| < 0.6$ is applied, such that leading and subleading jets are far from the edge of the tracker and all ranges in Δ fall within the acceptance.

The particles that provide the p_{T} balance are correlated with the jet axes, but the particles that are not affected by the interaction of the partons with the medium are evenly distributed in azimuth relative to the individual directions of the leading and subleading jets. The total p_{T} of these particles is uncorrelated with the dijet pair. To differentiate the uncorrelated and correlated particles, we compare differences

in multiplicity in leading and subleading jet hemispheres. In addition, we measure modifications in the p_{T} spectrum of charged particles that contribute to the overall p_{T} balance in the event, as well as their angular distribution with respect to the dijet system. Using the azimuthal symmetry of the jet axes relative to the UE makes it possible to perform precise measurements for particles down to $p_{\mathrm{T}} = 0.5\mathrm{GeV}$, and angles as large as $\Delta = 1.8$. This provides constraints on energy loss mechanisms despite the small signal-to-background ratio.

The cancellation of the uncorrelated UE depends on azimuthal symmetry of the areas selected around the leading and subleading jets relative to the axis of projection. As mentioned above, to ensure this requirement, the dijet azimuthal angle (ϕ_{dijet}) is defined as the average ϕ of the leading and subleading jets after the subleading jet is reflected around the origin. In contrast with previous publications [94], ϕ_{dijet} is preferred over ϕ_1 (the ϕ of the leading jet) for the projection axis, because the latter choice breaks azimuthal symmetry, by generating particles near the leading jet that have larger projections at small angles relative to particles produced at the same distance to the subleading jet.

The perfect cancellation of contributions from particles to p_{T}flow, and to differences in hemisphere multiplicities from UE, take place only when there is no interaction between UE and the jets. This is the case in PYTHIA+HYDJET simulations. In data, due to the variations in path length in medium traversed by jets there are complicated correlations between particles from different interactions and jet directions. These correlations comprise a part of the signal probed in this analysis.

The observables used in this analysis are measured in bins of centrality and dijet imbalance. The dependence on centrality in PbPb collisions is investigated in terms of the emergence and enhancement of jet quenching effects as the size of the medium and energy density increase, and the dijet imbalance enriches events with subleading jets that lose more energy than the leading jet. To define centrality classes, collisions with inelastic hadronic interactions are divided into percentages according to the E_{T} of calorimeter towers summed in the HF, and events are assigned into classes of centrality based on these total sums in the HF. The distribution in this E_{T} is used to

divide the event sample into bins, each representing 0.5% of the total nucleus-nucleus interaction cross section. Following Refs. [94, 97], we quantify p_{T} imbalance through the asymmetry ratio A_J as described in Eq. 7.1. The A_J boundaries used in the analysis are 0.11, 0.22, 0.33 and 0.44, which correspond to $p_{\mathrm{T},2}/p_{\mathrm{T},1}$ values of 0.8, 0.64, 0.50 and 0.42, respectively.

10.1.1 Difference in multiplicities

The events are bisected with a plane perpendicular to ϕ_{dijet} into two hemispheres associated with the leading and subleading jets. The multiplicity difference is defined as the difference between the corrected number of tracks with $p_{\mathrm{T}} > 0.5\mathrm{GeV}$ ($N_{\mathrm{trk}}^{\mathrm{Corrected}} = \sum \mathrm{c}^{\mathrm{trk}}$) in these two hemispheres:

$$\Delta_{\mathrm{mult}} = N_{\mathrm{trk}}^{\mathrm{Corrected}}|_{|\phi_{\mathrm{trk}}-\phi_{\mathrm{dijet}}|>\pi/2} - N_{\mathrm{trk}}^{\mathrm{Corrected}}|_{|\phi_{\mathrm{trk}}-\phi_{\mathrm{dijet}}|<\pi/2}. \tag{10.1}$$

Positive Δ_{mult} means that an excess of particles is found in the hemisphere of the subleading jet, relative to the number of particles in the leading jet hemisphere. This quantity is measured event-by-event and then averaged in bins of the observables of interest. It is sensitive to the number of jets in a given hemisphere and their fragmentation, as well as to the additional particles produced in jet quenching or through some specific response of the QGP medium in one of the two hemispheres.

To select events that show consequences of jet quenching, the measurement is carried out as a function of A_J and collision centrality. The A_J-dependent measurement is performed for jets with a distance parameter of $R = 0.3$.

To see modifications in the p_{T} spectrum associated with the difference in multiplicities in two hemispheres, Δ_{mult} is measured for track p_{T} ranges of 0.5–1, 1–2, 2–4, 4–8, and 8–300GeV, and divided by the bin width. The measurement is repeated for different R parameters.

To be consistent with the measurement of p_{T} balance, the leading and subleading jets used in the A_J-dependent Δ_{mult} measurement are required to fall in the pseudo-

rapidity region of $|\eta| < 1.6$. The leading and subleading jets used in the R-dependent measurement are required to be within $|\eta| < 0.6$. Although in both cases jets with $|\eta| > 2$ are excluded, it is important to note that starting jet reconstruction with a cutoff $|\eta| < 1.6$, (or < 0.6) is different than using the $|\eta| < 2$ selection for determining the highest-p_{T} jets and then applying a tighter requirement, since events in which the leading or subleading jets are found in the range between $|\eta| = 1.6$ (or 0.6) and $|\eta| = 2.0$ are also excluded.

10.1.2 Transverse momentum balance

Detailed information about the p_{T} flow relative to the dijet system can be obtained by studying the contribution of tracks to the overall p_{T} balance in the event, as characterized by individual track p_{T} and angle relative to the jets. To calculate the p_{T} balance, the p_{T} of tracks are projected onto the dijet axis. For each track, this projection is defined as

$$p_{\mathrm{T}}^{\parallel} = -\mathrm{c}^{\mathrm{trk}}\, p_{\mathrm{T}}^{\mathrm{trk}} \cos\left(\phi_{\mathrm{trk}} - \phi_{\mathrm{dijet}}\right), \tag{10.2}$$

where, as mentioned in Chapter 8, the correction for reconstruction effects accounts for the misreconstruction rate and reconstruction efficiency for PbPb collisions, with values specified by Eq. 8.2. In addition, secondary particle and multiple reconstruction rates are corrected in pp collisions.

Particles that make a positive contribution in Δ_{mult} also have positive $p_{\mathrm{T}}^{\parallel}$, as the cosine function changes sign at $\pi/2$. These two observables therefore map onto each other with a weight in track p_{T} and $\cos\left(\phi_{\mathrm{trk}} - \phi_{\mathrm{dijet}}\right)$.

To study the angular recovery rate (rate at which imbalance is restored, as momentum contributions are included further from the jet cone) and the associated spectra of p_{T} balance, tracks that fall in annular regions around the jet axes are grouped together according to their p_{T}. In each event, $p_{\mathrm{T}}^{\parallel}$ values of these group of tracks are summed to obtain $\not{p}_{\mathrm{T}}^{\parallel}$. For each region, $\not{p}_{\mathrm{T}}^{\parallel}$ is calculated in track p_{T}ranges of 0.5–1, 1–2, 2–4, 4–8, and 8–300GeV. Annular regions are defined in $\Delta = \sqrt{(\phi_{\mathrm{trk}} - \phi_{\mathrm{jet}})^2 + (\eta_{\mathrm{trk}} - \eta_{\mathrm{jet}})^2}$

and binned between $\Delta = 0.0$–1.8 in steps of 0.2. In addition, the contribution from charged particles that fall outside of this range are all collected in an extra overflow bin. These particles lie in the range of $1.8 < \Delta < 3.6$, depending on the η of the dijet pair. No anti-k_{T} clustering is employed in the calculation of Δ, and tracks are defined to lie within circular regions in pseudorapidity and azimuth. The axes used to define the annuli differ from the projection axis, ϕ_{dijet}. For large Δ, the annuli around the leading and subleading jets can overlap, in which case, the track used in the overlap region when calculating $\not{p}_{\mathrm{T}}^{\parallel}$, is the one in the annulus at smaller radius. The overlaps do not occur before $\Delta = 5\pi/12$.

The $\not{p}_{\mathrm{T}}^{\parallel}$ is averaged over events with a specific A_J value separately for pp and PbPb collisions, and for PbPb collisions they are divided into classes of collision centrality. This average is denoted as $\langle \not{p}_{\mathrm{T}}^{\parallel} \rangle_{p_{\mathrm{T}}^{\mathrm{trk}},\Delta}$, to indicate that within each event the balance is calculated using a subset of tracks with specific Δ and p_{T}.

Using the track p_{T} and Δ parameters limits the selections on collision centrality and A_J because of the statistical imprecision of the data. For more detailed analysis of the dependance of track p_{T} on event properties, Δ binning can be removed by adding up the $\langle \not{p}_{\mathrm{T}}^{\parallel} \rangle_{p_{\mathrm{T}}^{\mathrm{trk}},\Delta}$ values for each Δ bin, which is identical to not having annular requirements in the first place, to obtain

$$\langle \not{p}_{\mathrm{T}}^{\parallel} \rangle_{p_{\mathrm{T}}^{\mathrm{trk}}} = \sum_{\Delta} \langle \not{p}_{\mathrm{T}}^{\parallel} \rangle_{p_{\mathrm{T}}^{\mathrm{trk}},\Delta}. \tag{10.3}$$

The p_{T}balance, as in Eq. 10.3, calculated for tracks in a given p_{T}range usually yields nonzero values, because of the differences in p_{T}spectra of particles in subleading jet hemisphere relative to the spectra in the leading jet hemisphere. Summing the signed $\langle \not{p}_{\mathrm{T}}^{\parallel} \rangle_{p_{\mathrm{T}}^{\mathrm{trk}}}$ values for each track p_{T}bin provides an overall p_{T}balance in the event for tracks with $0.5 < p_{\mathrm{T}} < 300GeV$, that takes values close to zero, because of momentum conservation. There can still be a deviation from zero because of the particles with $p_{\mathrm{T}} < 0.5$GeV, as well as for those particles that fall out of the tracker coverage in pseudorapidity that are not included in the measurement. This sum corresponds to

$$\langle \not{p}_{\mathrm{T}}^{\parallel} \rangle_{\Sigma} = \sum_{p_{\mathrm{T}}^{\mathrm{trk}}} \langle \not{p}_{\mathrm{T}}^{\parallel} \rangle_{p_{\mathrm{T}}^{\mathrm{trk}}}. \tag{10.4}$$

The angular distribution of p_{T}balance is studied differentially in bins of track $p_{\mathrm{T}}$by $\langle \not{p}_{\mathrm{T}}^{\parallel} \rangle_{p_{\mathrm{T}}^{\mathrm{trk}},\Delta}$, as described above, and adding up the contribution from different track p_{T}bins gives

$$\langle \not{p}_{\mathrm{T}}^{\parallel} \rangle_{\Delta} = \sum_{p_{\mathrm{T}}^{\mathrm{trk}}} \langle \not{p}_{\mathrm{T}}^{\parallel} \rangle_{p_{\mathrm{T}}^{\mathrm{trk}},\Delta}, \tag{10.5}$$

which defines the contribution of all tracks with $0.5 < p_{\mathrm{T}} < 300\mathrm{GeV}$ in a given annulus to total p_{T}balance. This $\langle \not{p}_{\mathrm{T}}^{\parallel} \rangle_{\Delta}$, summed over all Δ intervals, yields $\langle \not{p}_{\mathrm{T}}^{\parallel} \rangle_{\Sigma}$. Instead of summing all Δ bins, to calculate the recovery of balance as radius gets larger, the annuli can be summed from $\Delta = 0$ up to the angle of interest, and a cumulative balance inside a cone calculated, as

$$\langle \not{p}_{\mathrm{T}}^{\parallel} \rangle_{[0,\Delta]} = \sum_{\Delta'=0}^{\Delta'=\Delta} \langle \not{p}_{\mathrm{T}}^{\parallel} \rangle_{\Delta'}. \tag{10.6}$$

As mentioned previously, for consistency with the analysis in Ref. [94], in calculations that integrate over Δ , e.g., for, $\langle \not{p}_{\mathrm{T}}^{\parallel} \rangle_{p_{\mathrm{T}}^{\mathrm{trk}}}$ and $\langle \not{p}_{\mathrm{T}}^{\parallel} \rangle_{\Sigma}$, only events in which both leading and subleading jets fall within $|\eta| < 1.6$ are included in the measurement of p_{T}balance. For measurements where contributions of different annuli are studied, to ensure full tracker coverage around jets over $\Delta < 1.8$ for $\langle \not{p}_{\mathrm{T}}^{\parallel} \rangle_{p_{\mathrm{T}}^{\mathrm{trk}},\Delta}$, $\langle \not{p}_{\mathrm{T}}^{\parallel} \rangle_{\Delta}$, and $\langle \not{p}_{\mathrm{T}}^{\parallel} \rangle_{[0,\Delta]}$, tighter restrictions are required on the pseudorapidity of leading and subleading jets ($|\eta| < 0.6$) after they are found within $|\eta| < 2$.

10.1.3 Corrections steps for reconstruction effects

Having a good control of jets and tracks is not easily done and requires several levels of corrections. In Fig. 10-1 the flow chart of all corrections applied on tracks and jets for "missing-p_{T}" analysis is shown.

Corrections on reconstructed jets and tracks are applied in the following order:

1. L2-L3 and FF JEC is applied on jets.

2. Iterative factorized track correction table is derived. The algorithm uses the corrected jets from step 1. to define the minimum distance of a track to a jet, as this is one of the 5 parameters used in the derivation. Moreover, analysis selections on dijets are applied to obtain corrections from events that are as similar as events used in the analysis. Although, a table without dijet selection was also derived and the results of measurements did not change significant by switching between the two tables.

3. The residual discrepancy between yields of corrected tracks and primary particles within $\Delta R < 0.2$ of leading (subleading) is corrected. This correction depends on particle p_{T} and dijet asymmetry. It corrects the biases caused as a result of correlations between track and jet reconstruction which are discussed in Section 8.6.3.

4. A bin by bin correction to account for jet reconstruction biases is derived. The correction is the discrepancy in the results calculated in MC simulations with reconstructed jets compared to results with gen-jets, for both cases primary particles are used in combination to choice of jets. As primary particles are used in both cases track reconstruction effects do not come into play here. This bin by bin correction is subtracted from results in data.

10.2 Fluctuations of p_{T} projections

The analyses are focussed on calculating event averages rather than selecting on certain type of p_{T} balance distributions, because there are several sources of fluctuations in this observable. Although reconstruction effects increase the fluctuations, these are already present at generator-level PYTHIA, HYDJET and PYTHIA+HYDJET, because of the fact that our measurement is carried out using all the particles within $|\eta| < 2.4$ and $p_{\mathrm{T}} > 0.5$ GeV and a fraction of particles that contribute to the p_{T} balance are left

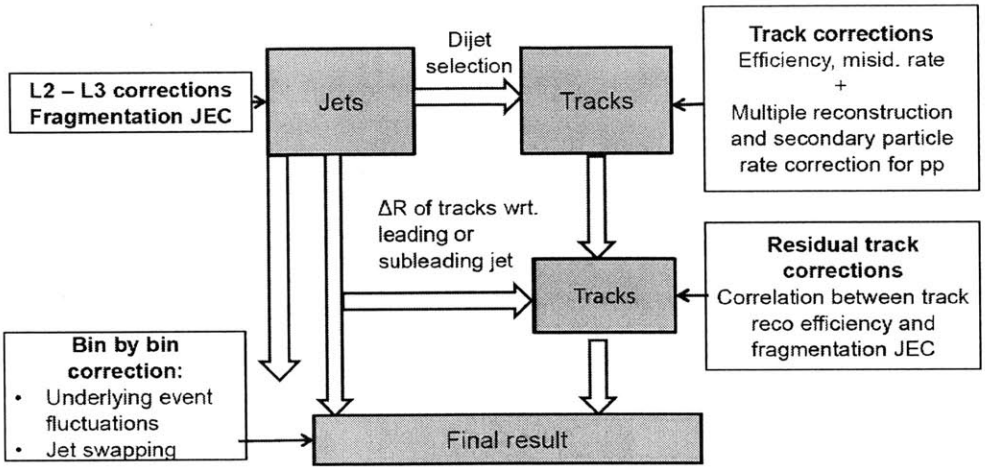

Figure 10-1: Chart of corrections starting from raw jets and tracks at the detector up to the measured values. Most of the items listed here are described in Chapter 8.

out of this range. In Fig. 10-2, the $\langle \not{p}_{\mathrm{T}}^{\parallel} \rangle_{p_{\mathrm{T}}^{\mathrm{trk}}}$ distributions are shown for each p_{T} range as well as $\langle \not{p}_{\mathrm{T}}^{\parallel} \rangle_{\Sigma}$ in the last panel for all particles (or tracks) with $p_{\mathrm{T}} > 0.5$ GeV. The distributions calculated at generator level are already very wide, for low-p_{T} particles the width of the fluctuations are dominated by underlying event particles in HYDJET (shown with red histogram), while for high-p_{T} particles fluctuations in PYTHIA projections are dominant (shown with blue histogram). The overall fluctuations in $\langle \not{p}_{\mathrm{T}}^{\parallel} \rangle_{\Sigma}$ in PYTHIA+HYDJET events are driven by the high-p_{T} particles that go outside of the $|\eta|$ acceptance.

The effects of jet and track reconstruction on the amount of fluctuations can be seen by comparing the black histograms for generator level PYTHIA + HYDJET to black dots which represent reconstructed result in PYTHIA+HYDJET simulations. The effects of jet reconstruction can be factorized by looking at the 2D correlation between $\langle \not{p}_{\mathrm{T}}^{\parallel} \rangle_{\Sigma}$ values obtained by using gen-particles with gen-jet, and by using gen-particles with reco-jets. The 2D distribution is shown in the left panel of Fig. 10-3. There are two bands, one diagonal and one anti-diagonal, the width of the bands are rather small meaning that jet reconstruction effects do not add much to the resolution, but result in obtaining a negative value with respect to the gen level calculation, due to swapping of leading and subleading jet directions (See 8.6.1).

The main source of increase in fluctuations in $\langle \not{p}_{\mathrm{T}}^{\parallel} \rangle_{\Sigma}$ comes from track reconstruction effects. To test this results obtained using reco jets and gen particles are compared to results obtained using reco jets and tracks. The correlations are shown in middle and right panels of Fig. 10-3, for raw tracks and tracks with corrections, respectively. The width of the correlation is much larger compared to what we observed for jet reconstruction effects. One can see that the effect of track corrections is having the slope of the mean of this correlation function to be equal to 1.

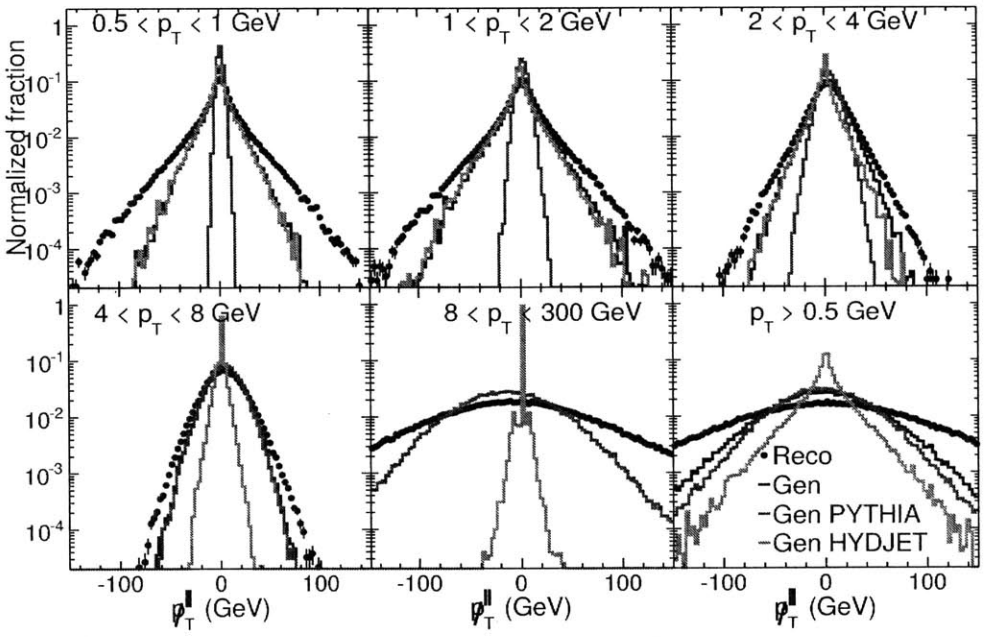

Figure 10-2: Distributions of $\langle \not{p}_{\mathrm{T}}^{\parallel} \rangle_{p_{\mathrm{T}}^{\mathrm{trk}}}$ and $\langle \not{p}_{\mathrm{T}}^{\parallel} \rangle_{\Sigma}$ for generator level PYTHIA, HYDJET and PYTHIA+HYDJET, shown as blue, red and black histograms, respectively, as well as fully reconstructed distributions from PYTHIA+HYDJET shown as filled dots.

10.3 Systematic uncertainties

The sources of major systematic uncertainty can be categorized into two groups; biases related to jet reconstruction and those related to track reconstruction. Effects associated with event selection and beam background rejection are found to be negligible.

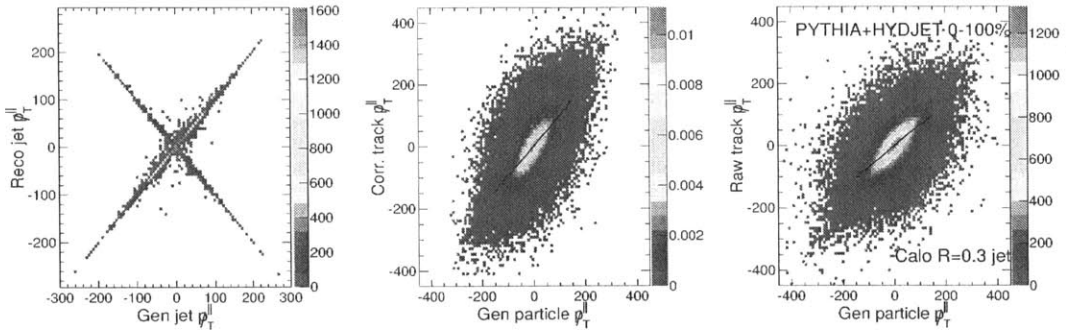

Figure 10-3: (Left) Correlation between $\langle p_{\mathrm{T}}^{\parallel} \rangle_{\Sigma}$ calculated using gen-jets with gen-particles and reconstructed jets with gen-particles. (Middle) Correlation between $\langle p_{\mathrm{T}}^{\parallel} \rangle_{\Sigma}$ calculated using reconstructed jets with gen-particles and reconstructed jets with raw tracks. (Right) Correlation between $\langle p_{\mathrm{T}}^{\parallel} \rangle_{\Sigma}$ calculated using reconstructed jets with gen-particles and reconstructed jets with corrected tracks.

The biases related to jet reconstruction are caused by smearing of jet p_{T}due to energy resolution and uncertainties in the JES. These factors can change the p_{T}-ordering of jets in the event, resulting in the interchanging of leading and subleading jets, or causing third jet to replace the subleading jet. The uncertainties are estimated as a function of centrality and A_J in each charged-particle p_{T}range, using PYTHIA and PYTHIA+HYDJET simulations to compare observables calculated with reconstructed jets to generator-level jets. This uncertainty is calculated the same was as the bin-by-bin correction is applied to data to account for the observed jet reconstruction bias. Although, it is not a major component jet reconstruction uncertainty also includes the effect of jet-angular resolution. The size of the bins in the Δ-dependent measurement is significantly larger than a typical angular resolution, which therefore has a negligible effect on the observables. Going from $R = 0.2$ to 0.5, the angular resolution, defined by the standard deviation of the $\Delta^{\mathrm{reco,gen}}$ distribution, increases from 0.020 to 0.025 for leading jets, and from 0.025 to 0.035 for subleading jets in pp. The same holds in 30–100% centrality PbPb collisions. In the most central 0–30% of events, the corresponding ranges are 0.020–0.035 and 0.025–0.045, respectively.

After implementing the fragmentation-dependent jet energy corrections there is up to 5% difference between the JES for quark and gluon jets at $p_{\mathrm{T}} < 50$GeV, and

Table 10.1: Systematic uncertainties in $\langle p_{\mathrm{T}}^{\parallel} \rangle_{\Delta}$ for jets clustered with distance parameter of 0.3 in pp, and in central and peripheral PbPb collisions, for different A_J selections. Uncertainties are shown as shifts in the values in units of GeV (rather than as fractions) for two Δ selections.

Values integrated over A_J

	pp		PbPb, 30–100%		PbPb, 0–30%	
Δ	<0,2	0.2–2.0	<0,2	0.2–2.0	<0,2	0.2–2.0
Jet reconstruction	<1	0.0–0.2	1	0.1–0.2	1	0.1–0.4
Data/MC differences for JES	1	0.1–0.2	2	0.1–0.3	2	0.1–0.3
Fragmentation dependent JES	<1	0.1–0.2	2	0.1–0.2	1	0.1–0.4
Track corrections	<1	< 0.1	1	0.0–0.2	2	0.2–0.9
Data/MC differences for tracking	1	0.0–0.1	1	0.1–0.2	1	0.1–0.2
Total	1	0.1–0.3	2	0.2–0.3	3	0.2–1.0

$A_J < 0.22$

	pp		PbPb, 30–100%		PbPb, 0–30%	
Δ	<0,2	0.2–2.0	<0,2	0.2–2.0	<0,2	0.2–2.0
Jet reconstruction	<1	0.1–0.2	1	0.1–0.2	1	0.1–0.4
Data/MC differences for JES	1	0.1–0.2	2	0.1–0.4	2	0.2–0.4
Fragmentation dependent JES	<1	0.1	2	0.1–0.4	1	0.1–0.5
Track corrections	<1	< 0.1	1	0.1	2	0.1–0.6
Data/MC differences for tracking	<1	0.0–0.1	1	0.1	1	0.1
Total	1	0.1–0.3	2	0.2–0.4	3	0.2–0.6

$A_J > 0.22$

	pp		PbPb, 30–100%		PbPb, 0–30%	
Δ	<0,2	0.2–2.0	<0,2	0.2–2.0	<0,2	0.2–2.0
Jet reconstruction	2	0.1–0.5	1	0.1–0.6	2	0.2–0.6
Data/MC differences for JES	2	0.1–0.3	3	0.2–0.5	3	0.3–0.6
Fragmentation dependent JES	1	0.1–0.5	1	0.1–0.7	1	0.2–0.6
Track corrections	<1	0.1	1	0.1–0.3	3	0.2–1.1
Data/MC differences for tracking	2	0.1–0.2	2	0.1–0.2	2	0.1–0.3
Total	3	0.3–0.8	3	0.3–0.9	4	0.4–1.4

the difference disappears for high-p_{T} jets. Additional checks are therefore pursued to account for possible discrepancies in the performance of jet energy corrections in data and in MC simulations. A modification in flavor content of jets due to quenching can lead to an under- or over-correction of the jet energy in data. Also, the uncertainty in the JES from differences in simulation and detector conditions is calculated to be 2% using a data-based "tag-and-probe" technique that depends on dijet balance in a

control sample of peripheral PbPb events [92]. The jet $p_{\mathrm{T}}$is changed up and down for leading and subleading jets in an asymmetric manner (leading JES is increased while subleading JES is decreased) as a function of jet p_{T}, to account for the differences in JES between quark and gluon jets and the data-based JES uncertainty. Because the number of charged particles is a parameter in these corrections, and can make the fragmentation-dependent jet energy corrections sensitive to quenching effects, the difference in the observables before and after corrections in MC events is compared to the corresponding change in data, and the discrepancy between data and simulation is quoted as an additional source of uncertainty.

Uncertainties related to track reconstruction are calculated in PYTHIA and PYTHIA+HYDJET by comparing the results with generator-level charged particles to those with reconstructed tracks, after applying the track corrections discussed in Section 8.4.2. The small uninstrumented regions in the detector, and the correlation between track reconstruction efficiency and JES are the main causes of discrepancies observed between results with generator-level particles and reconstructed tracks. The track corrections account for the inefficiencies due to uninstrumented regions. However, the bins used in η and ϕ to calculate the reconstruction efficiency are larger than the size of the uninstrumented regions, and as a result cannot completely correct the effect of these. An additional uncertainty is therefore added to account for the effect of differences in detector conditions and simulation of track reconstruction. This is achieved using the ratio of corrected to initial track $p_{\mathrm{T}}$and η spectra in data and simulations that are compared as track-quality selections are changed. The difference is found to be less than 5%, which is included in the systematic uncertainty.

To calculate the total uncertainty, the uncertainties from sources mentioned above are summed in quadrature. The contribution of each item is summarized in Tables 10.1–10.3 for the $\langle p_{\mathrm{T}}^{\parallel} \rangle_{\Delta}$ measurement. The systematic sources are given in terms of shifts in the value of each observable in a given bin in units of GeV instead of % changes, as the $\langle p_{\mathrm{T}}^{\parallel} \rangle_{\Delta}$ can vanish and can take values arbitrarily close to zero. Typically, $\langle p_{\mathrm{T}}^{\parallel} \rangle_{\Delta}$ is between 15–40GeV near the jet axes ($\Delta < 0.2$), and less than 10GeV at larger angles.

The dependence of uncertainties in dijet asymmetry and centrality is summarized in Table 10.1 for jets with a distance parameter $R = 0.3$. The jet energy resolution, can cause events to move across the A_J boundaries. Moreover, it is more likely for the leading jet in a highly imbalanced dijet event to be located in a region of an upward UE fluctuation in PbPb collisions. For these reasons, uncertainties related to jet reconstruction are larger in imbalanced dijet events. For well-balanced events, the uncertainty is comparable to that in the inclusive A_J selection, because the increase in effects from jet energy resolution balances the reduction of effects related to UE fluctuations. Uncertainties in track reconstruction are larger in imbalanced than in balanced events, because of the correlation of track reconstruction efficiency and reconstructed jet energy. When a high-p_{T} track that carries a significant fraction of jet $p_{\mathrm{T}}$is not reconstructed, the jet energy is under-corrected, and vice versa, the energy is over-corrected in events where the high-p_{T} track is found, because jet energy corrections are obtained for the average case where the high-p_{T} track might not be reconstructed. Events with highly imbalanced dijets can result from miscalculated jet energies caused by inefficiencies in track reconstruction. Centrality of PbPb collisions does not affect the uncertainties within the jet cone as much as at larger angles, where the signal-to-background ratio gets smaller. Track and jet reconstruction uncertainties, caused by over-correction of the leading jet p_{T}because of upward UE fluctuations, in particular, tend to increase in central collisions. Uncertainties are smaller in pp than in PbPb collisions because of the absence of a heavy-ion UE, and differences in jet and track reconstruction that provide better measurement of jet p_{T}, larger track reconstruction efficiency, and lower track misidentification rates.

Uncertainties for small Δ are dominated by charged particles with $p_{\mathrm{T}} > 8\mathrm{GeV}$, while at larger Δ, low-p_{T} particles make up a larger fraction of the total uncertainty in events when there is no selection made on charged-particle p_{T}. The contribution from each range of track $p_{\mathrm{T}}$to the uncertainty in $\langle p_{\mathrm{T}}^{\parallel} \rangle_{\Delta}$, in other words the uncertainty in $\langle p_{\mathrm{T}}^{\parallel} \rangle_{p_{\mathrm{T}}^{\mathrm{trk}},\Delta}$, is shown in Table 10.2 for $R = 0.3$, in events with 0–30% central PbPb collisions. Finally, as shown in Table 10.3, uncertainties in jet reconstruction and track reconstruction in MC events increase together with increasing R, as the UE

inside the jet cone gets larger. However, JES difference between quark and gluon jets is smaller for large R parameters, and uncertainties that account for JES differences in data and in MC events therefore decrease.

Table 10.2: Systematic uncertainties in $\langle p_{\mathrm{T}}^{\parallel} \rangle_{p_{\mathrm{T}}^{\mathrm{trk}},\Delta}$ in 0–30% PbPb collisions, for jets clustered with a distance parameter of 0.3, as a function of charged-particle p_{T}. Uncertainties are shown as shifts in the values in units of GeV (rather than as fractions) for two Δ selections.

	$0.5 < p_{\mathrm{T}} < 2$GeV		$2 < p_{\mathrm{T}} < 8$GeV		$p_{\mathrm{T}} > 8$GeV	
Δ	<0,2	0.2–2.0	<0,2	0.2–2.0	<0,2	0.2–2.0
Jet reconstruction	0,04	0.06–0.25	0,13	0.04–0.14	0,85	0.01–0.07
Data/MC differences for JES	0,14	0.07–0.24	0,42	0.03–0.11	0,97	0.01–0.12
Fragmentation dependent JES	0,03	0.10–0.14	1,1	0.05–0.23	0,19	0.02–0.06
Track corrections	0,09	0.08–0.64	0,27	0.06–0.13	1,78	0.01–0.07
Data/MC differences for tracking	0,04	0.03–0.08	1,2	0.01–0.05	1,16	0.00–0.02
Total	0,17	0.20–0.69	1,1	0.11–0.29	2,3	0.04–0.10

Table 10.3: Systematic uncertainties in $\langle p_{\mathrm{T}}^{\parallel} \rangle_{p_{\mathrm{T}}^{\mathrm{trk}},\Delta}$ in 0–30% PbPb collisions are shown for jets clustered with distance parameters of 0.2, 0.4 and 0.5. Uncertainties are shown as shifts in the values in units of GeV (rather than as fractions) for two Δ selections.

	$R = 0.2$		$R = 0.4$		$R = 0.5$	
Δ	<0,2	0.2–2.0	<0,2	0.2–2.0	<0,2	0.2–2.0
Jet reconstruction	1	0.1–0.4	1	0.1–0.5	1	0.1–0.7
Data/MC differences for JES	2	0.1–0.5	2	0.1–0.4	2	0.1–0.3
Fragmentation dependent JES	1	0.1–0.4	1	0.1–0.3	1	0.1–0.3
Track corrections	2	0.2–0.7	2	0.1–1.1	2	0.1–1.1
Data/MC differences for tracking	1	0.1–0.2	1	0.1	1	0.1
Total	3	0.2–0.9	3	0.3–1.1	3	0.2–1.1

Although uncertainties in differences in multiplicities are calculated separately, their values are not listed in a table, because they can be approximated from the uncertainties in $\langle p_{\mathrm{T}}^{\parallel} \rangle$ divided by the average charged particle p_{T}in that range. In 0–10% central events, for $R = 0.3$, the dominant source is jet reconstruction, with

an uncertainty caused by an upward fluctuation in the background under the leading jet, which is followed by the uncertainty in track reconstruction, and residual track reconstruction in data and in MC events that change by 0.5–1.5 particles, as a function of A_J. The uncertainties increase with R and with centrality from peripheral to central collisions.

10.4 Missing p_{T} in vacuum

In addition to being a means to search for a medium response to jet quenching in PbPb collisions, the angular scan of momentum balance with respect to the dijet system is interesting on its own right in pp collisions. The observables defined in Section 10.1 to study hard QCD processes. The shape of the transverse balance distribution in angle and the p_{T} spectra at a given angular direction, i.e. $\langle \not{p}_{\mathrm{T}}^{\parallel} \rangle_{p_{\mathrm{T}}^{\mathrm{trk}},\Delta}$, is sensitive to the multi-jet formation, as well as to the shape and fragmentation of leading and subleading jet.

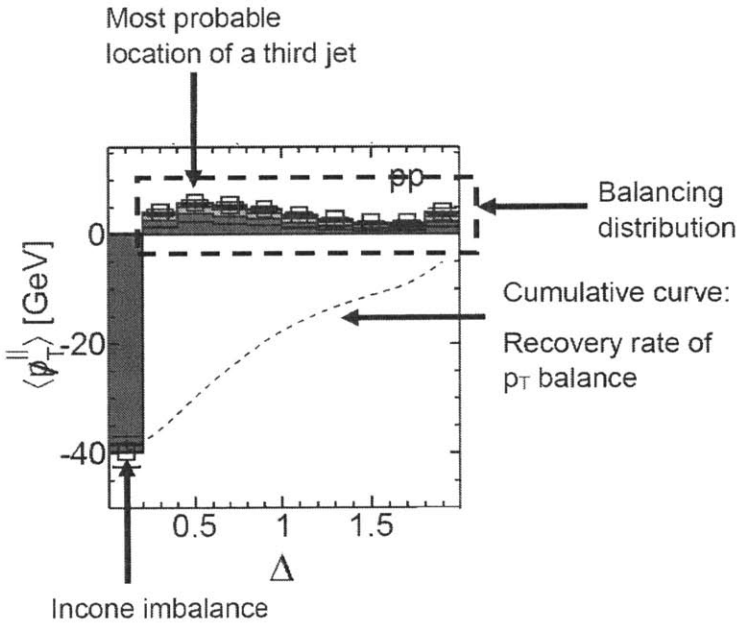

Figure 10-4: Characteristic features in $\langle \not{p}_{\mathrm{T}}^{\parallel} \rangle_{p_{\mathrm{T}}^{\mathrm{trk}},\Delta}$ distributions in pp collisions.

The distributions in pp collisions have characteristic features (marked in Fig. 10-4), and understanding these is important for interpreting the PbPb results. The magnitude of the $\langle \not{p}_{\mathrm{T}}^{\parallel} \rangle_{\Delta}$ in the first bin, with $\Delta < 0.2$, is related to the average dijet imbalance, and takes a negative value indicating that the momentum projection points along the direction of the leading jet. In the rest of the Δ bins, $\langle \not{p}_{\mathrm{T}}^{\parallel} \rangle_{\Delta}$ takes a positive value, and $\langle \not{p}_{\mathrm{T}}^{\parallel} \rangle_{p_{\mathrm{T}}^{\mathrm{trk}},\Delta}$ for lower track p_{T}make up larger fractions of $\langle \not{p}_{\mathrm{T}}^{\parallel} \rangle_{\Delta}$. We refer to the $\langle \not{p}_{\mathrm{T}}^{\parallel} \rangle_{p_{\mathrm{T}}^{\mathrm{trk}},\Delta}$ and $\langle \not{p}_{\mathrm{T}}^{\parallel} \rangle_{\Delta}$ for bins with $\Delta > 0.2$ as the "balancing distribution" of the corresponding quantity, because they reduce the large p_{T}imbalance observed in the first bin in Δ. The balancing distribution has a peak in the range $0.4 < \Delta < 0.6$, which is at the most likely Δ position for a third jet relative to the subleading jet.Dijet imbalance and the position of the third jet depends on the R parameter, therefore, these features can most easily be demonstrated with measurement of $\langle \not{p}_{\mathrm{T}}^{\parallel} \rangle_{p_{\mathrm{T}}^{\mathrm{trk}},\Delta}$ for different R, which is shown in Fig. 10-5. The difference of p_{T} of jets, $p_{\mathrm{T},1} - p_{\mathrm{T},2}$ shown in Fig. 10-6 decreases as R gets larger which reflects the reduction in the magnitude of first bin of $\langle \not{p}_{\mathrm{T}}^{\parallel} \rangle_{p_{\mathrm{T}}^{\mathrm{trk}},\Delta}$, which is shown in Fig. 10-5. Compare the position of the peak of balancing distribution. Moreover, the peaking point of the balancing distribution shifts towards larger Δ, as jet distance parameter R increases (from $\Delta =$ 0.2–0.4 for $R = 0.2$ jets, to $\Delta = 0.6$–1.0 for $R = 0.5$ jets). As stated for $R = 0.3$ jets in Section 10.5.1, the peak position is correlated with the most likely position of the third jet relative to the subleading jet, which is shown in Fig. 10-6. The peak of this distribution also moves to larger angles by increasing R.

Our measurement is not only sensitive to inter-jet properties but also to intra-jet structure. To demonstrate the sensitivity of $\langle \not{p}_{\mathrm{T}}^{\parallel} \rangle_{p_{\mathrm{T}}^{\mathrm{trk}},\Delta}$ on jet fragmentation and shapes $\langle \not{p}_{\mathrm{T}}^{\parallel} \rangle_{p_{\mathrm{T}}^{\mathrm{trk}},\Delta}$ is calculated in generator-level PYTHIA dijet events with q and g leading jets separately. As the fragmentation of q and g jets are significantly different, this is a test on $\langle \not{p}_{\mathrm{T}}^{\parallel} \rangle_{p_{\mathrm{T}}^{\mathrm{trk}},\Delta}$ differs for hard and soft fragmenting jets. In Fig. 10-7 the calculation for $R = 0.2 - 0.5$ are shown and can be compared to inclusive parton flavor results. Events with q jet have larger high-p_{T} track contribution in the first bin as a result leading jet fragmentation having more particles with $p_{\mathrm{T}} > 8$ GeV. As a result of having more particles with high-p_{T}, leading jet also has less particles with

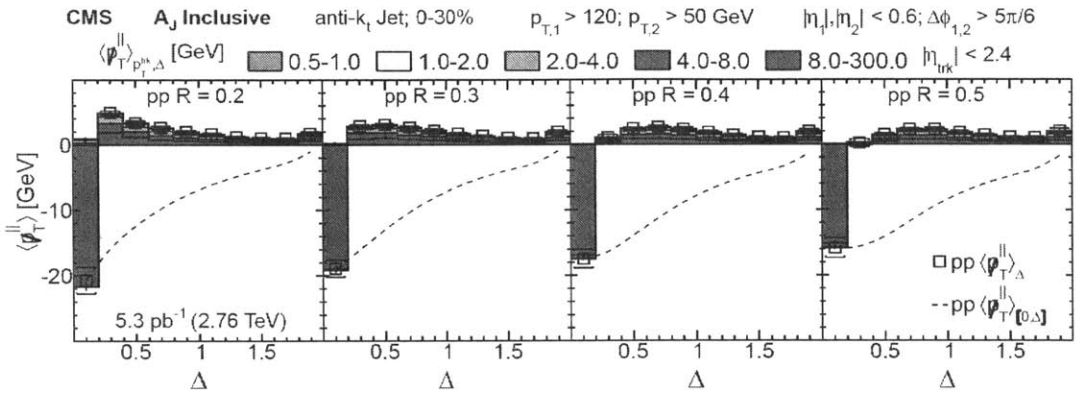

Figure 10-5: Distributions of $\langle p_{\mathrm{T}}^{\parallel} \rangle_{p_{\mathrm{T}}^{\mathrm{trk}},\Delta}$,$\langle p_{\mathrm{T}}^{\parallel} \rangle_{\Delta}$ and $\langle p_{\mathrm{T}}^{\parallel} \rangle_{[0,\Delta]}$ in pp collisions for $R = 0.2 - 0.5$. $\langle p_{\mathrm{T}}^{\parallel} \rangle_{p_{\mathrm{T}}^{\mathrm{trk}},\Delta}$ distributions correspond to five track-p_{T} ranges (colored boxes), for momentum ranges from $0.5 < p_{\mathrm{T}} < 1$GeV (light blue) to $8 < p_{\mathrm{T}} < 300$GeV (red), as a function of Δ. Also shown is $\langle p_{\mathrm{T}}^{\parallel} \rangle_{\Delta}$, the sum of $\langle p_{\mathrm{T}}^{\parallel} \rangle_{p_{\mathrm{T}}^{\mathrm{trk}},\Delta}$ over track-p_{T} ranges at a fixed Δ, as a function of Δ (open squares). Dashed lines show $\langle p_{\mathrm{T}}^{\parallel} \rangle_{[0,\Delta]}$ (i.e., integrating the $\langle p_{\mathrm{T}}^{\parallel} \rangle_{\Delta}$ over Δ from $\Delta = 0$ up to the point of interest). Error bars and brackets represent statistical and systematic uncertainties, respectively.

lower p_{T} then before, and this results in an excess in $2 - 8$ GeV range contribution to $\langle p_{\mathrm{T}}^{\parallel} \rangle_{p_{\mathrm{T}}^{\mathrm{trk}},\Delta}$ on the subleading jet side. In gluon jets an opposite direction change is observed. A gluon leading jet is also more likely to have a wider shape, this is reflected as a shift in the Δ, where $\langle p_{\mathrm{T}}^{\parallel} \rangle_{p_{\mathrm{T}}^{\mathrm{trk}},\Delta}$ changes sign, towards larger values when compared to the inclusive jet flavor results. The generic shift in the third jet location and decrease in the incone imbalance by increasing R discussed hold for both cases, but to observe the shift in the third jet location one has to look at the balancing distribution associated to high-p_{T} tracks.

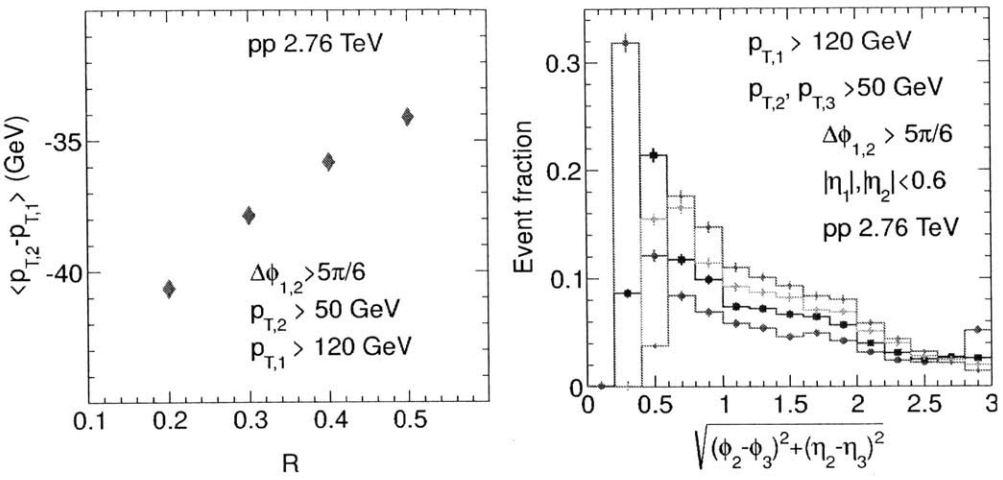

Figure 10-6: (Left) The p_{T} difference of leading and subleading jet as a function of R in pp collisions. (Right) The separation of third jet and subleading jet in $\eta-\phi$, i.e. $\sqrt{(\eta_2-\eta 3)^2+(\phi_2-\phi 3)^2}$ in pp collisions.

10.5 Modification of momentum flow in PbPb collisions

10.5.1 Dependence of the p_{T} balance in pp and PbPb on opening angles around jets

Angular distribution of the p_{T}relative to the axis defined by the parton direction is a key for studying QCD processes responsible for parton energy loss. In models, large-angle modifications in the event due to jet quenching have been accommodated qualitatively through a response triggered in the hydrodynamic medium by the deposited energy [217] and through the cascade of gluons created in medium-induced radiation processes [64, 159, 140, 66]. Moreover, some MC implementations of jet quenching that modify partonic showers in PYTHIA, such as Q-PYTHIA, can generate soft particles at angles $\Delta > 0.8$, but this treatment modifies the fragmentation functions more severely than found in data [41, 46]. Angular scales for different jet quenching mechanisms in perturbative QCD are related to momentum scales through time evolution of partonic interactions [171]. Especially for QCD cascades in a suf-

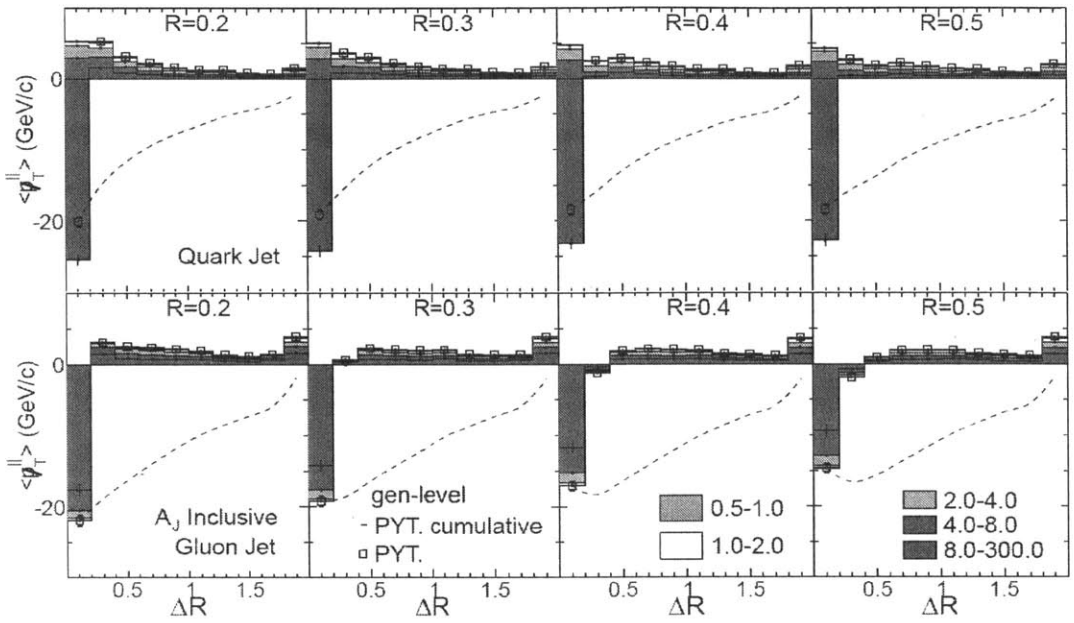

Figure 10-7: Upper row shows $\langle p_{\mathrm{T}}^{\parallel} \rangle_{p_{\mathrm{T}}^{\mathrm{trk}},\Delta}$, $\langle p_{\mathrm{T}}^{\parallel} \rangle_{\Delta}$ and $\langle p_{\mathrm{T}}^{\parallel} \rangle_{[0,\Delta]}$ in generator-level PYTHIA for events with leading jet matched to a quark. Lower row shows the same distributions for a gluon leading jet.

ficiently large medium, angular broadening is independent of the path length, and this mechanism might therefore produce a cumulative effect even after taking averages over different events where jets travel different path lengths in the QGP. The medium response may not have the same correlation between angular and momentum scales. The relative importance of each mechanism is unknown. Measuring the p_{T}spectra of $\langle p_{\mathrm{T}}^{\parallel} \rangle$ as a function of Δ from the jet axis, denoted as $\langle p_{\mathrm{T}}^{\parallel} \rangle_{p_{\mathrm{T}}^{\mathrm{trk}},\Delta}$, as discussed in Section 10.1, can provide information on the momentum scales at which certain quenching mechanisms become dominant.

The analysis is performed for pp collisions, and two PbPb centrality selections of 30–100% and 0–30%. The resulting differential distributions in $\langle p_{\mathrm{T}}^{\parallel} \rangle_{p_{\mathrm{T}}^{\mathrm{trk}},\Delta}$ are shown for different regions of track p_{T}(in terms of the colored boxes) as a function of Δ in the upper row of Fig. 10-8. The sum of $\langle p_{\mathrm{T}}^{\parallel} \rangle_{p_{\mathrm{T}}^{\mathrm{trk}},\Delta}$ for different $p_{\mathrm{T}}^{\mathrm{trk}}$ ranges as a function of Δ, $\langle p_{\mathrm{T}}^{\parallel} \rangle_{\Delta}$, are given by the open markers, and follow the leading jet at small Δ and subleading jet at large Δ. The cumulative values, $\langle p_{\mathrm{T}}^{\parallel} \rangle_{[0,\Delta]}$ (i.e., from

summing and smoothing the $\langle p_{\mathrm{T}}^{\parallel}\rangle_{\Delta}$ over bins in Δ, starting at $\Delta = 0$ and ending at the point of interest) are shown as dashed lines for pp and solid lines for PbPb. These lines demonstrate the evolution of the overall p_{T}balance from small to large distances relative to the jet axis, reaching an overall balance close to zero only at large radii. The cumulative curve in PbPb collisions for 0–30% centrality is slightly narrower than for pp collisions.

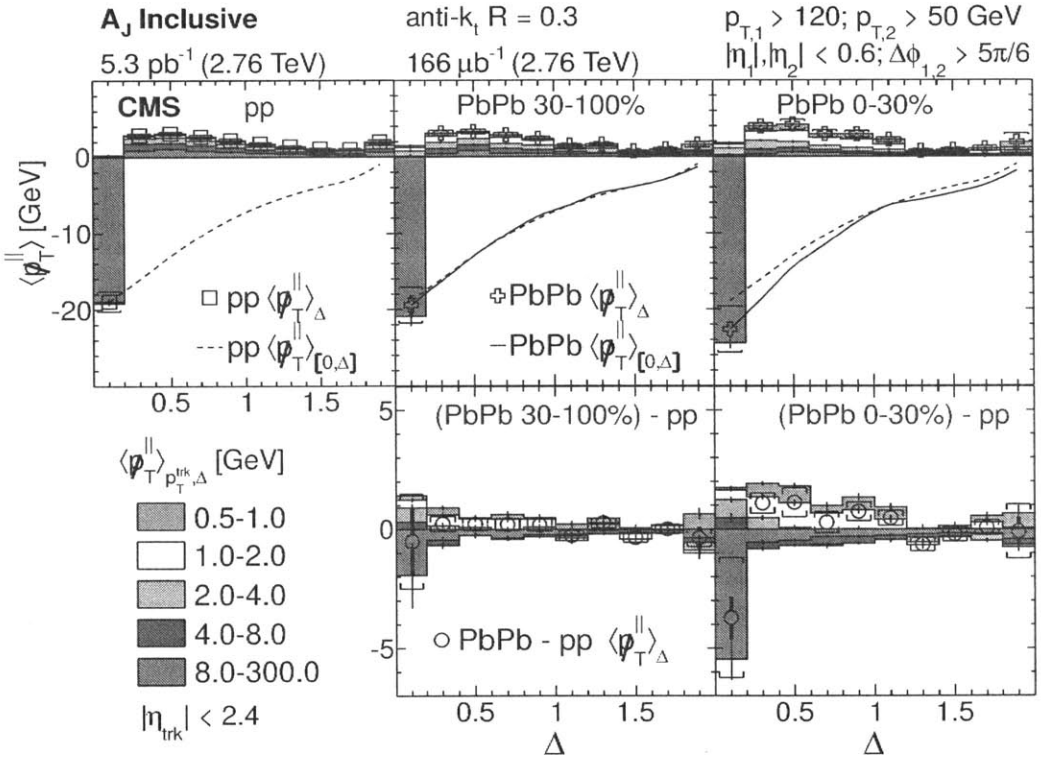

Figure 10-8: Upper row shows $\langle p_{\mathrm{T}}^{\parallel}\rangle_{p_{\mathrm{T}}^{\mathrm{trk}},\Delta}$, $\langle p_{\mathrm{T}}^{\parallel}\rangle_{\Delta}$, and $\langle p_{\mathrm{T}}^{\parallel}\rangle_{[0,\Delta]}$ distributions for pp, and for 30–100% and 0–30% PbPb data as a function of Δ. For further description of what colored boxes, empty markers and curves correspond to refer to 10-5. Lower row has the difference between the PbPb and pp.

The distributions in pp collisions have characteristic features, and understanding these is important for interpreting the PbPb results. The magnitude of the $\langle p_{\mathrm{T}}^{\parallel}\rangle_{\Delta}$ in the first bin, with $\Delta < 0.2$, is related to the average dijet imbalance, and takes a negative value indicating that the momentum projection points along the direction of the leading jet. In the rest of the Δ bins, $\langle p_{\mathrm{T}}^{\parallel}\rangle_{\Delta}$ takes a positive value, and $\langle p_{\mathrm{T}}^{\parallel}\rangle_{p_{\mathrm{T}}^{\mathrm{trk}},\Delta}$

for lower track p_{T}make up larger fractions of $\langle \not{p}_{\mathrm{T}}^{\parallel} \rangle_{\Delta}$. We refer to the $\langle \not{p}_{\mathrm{T}}^{\parallel} \rangle_{p_{\mathrm{T}}^{\mathrm{trk}},\Delta}$ and $\langle \not{p}_{\mathrm{T}}^{\parallel} \rangle_{\Delta}$ for bins with $\Delta > 0.2$ as the "balancing distribution" of the corresponding quantity, because they reduce the large p_{T}imbalance observed in the first bin in Δ. The balancing distribution has a peak in the range $0.4 < \Delta < 0.6$, which is at the most likely Δ position for a third jet relative to the subleading jet.

In PbPb collisions, the peak of the balancing $\langle \not{p}_{\mathrm{T}}^{\parallel} \rangle_{\Delta}$ distribution shifts towards smaller angles ($0.2 < \Delta < 0.4$). This can be due to the modification in the fragmentation of the leading and subleading jets after quenching, as it occurs at angles close to their axes, where the low-p_{T} particles make largest contributions. It is therefore not possible to claim a direct relation between the peak position of the balancing $\langle \not{p}_{\mathrm{T}}^{\parallel} \rangle_{\Delta}$ distribution and the location of other jets in the event, unless only the highest-p_{T}particles are considered, i.e., not likely to be related to the leading and subleading jets at large Δ values. The peak position of the balancing $\langle \not{p}_{\mathrm{T}}^{\parallel} \rangle_{p_{\mathrm{T}}^{\mathrm{trk}},\Delta}$ distribution of the highest-p_{T}particles is located at the same place as in pp collisions ($0.4 < \Delta < 0.6$), but with smaller magnitude. This suggests that the position of a third jet relative to the subleading jet is not modified significantly. However, the magnitude of $\langle \not{p}_{\mathrm{T}}^{\parallel} \rangle_{p_{\mathrm{T}}^{\mathrm{trk}},\Delta}$ for tracks with $8 < p_{\mathrm{T}} < 300$GeV associated with the third jet can be reduced for several reasons, such as quenching of the third jet, which makes its fragmentation softer, or a change in the ordering of the jets relative to original partonic conditions, i.e., leading parton losing more energy compared to the subleading parton, which causes the third jet to be found in the leading jet hemisphere, instead of the subleading jet hemisphere.

A comparison of pp and PbPb collisions is provided in the lower row of Fig. 10-8, showing the difference in PbPb and pp for $\langle \not{p}_{\mathrm{T}}^{\parallel} \rangle_{p_{\mathrm{T}}^{\mathrm{trk}},\Delta}$, and $\langle \not{p}_{\mathrm{T}}^{\parallel} \rangle_{\Delta}$ as a function of Δ. For central events, the first bin with $\Delta < 0.2$ $\langle \not{p}_{\mathrm{T}}^{\parallel} \rangle_{p_{\mathrm{T}}^{\mathrm{trk}},\Delta}$ for high-p_{T} tracks and $\langle \not{p}_{\mathrm{T}}^{\parallel} \rangle_{\Delta}$ point in the leading jet direction, although the excess is not significant. While in the second bin with $0.2 < \Delta < 0.4$, there is a significant positive excess in $\langle \not{p}_{\mathrm{T}}^{\parallel} \rangle_{\Delta}$. The excess towards the subleading jet in this bin may either be because the leading jet is narrower, or the subleading jet wider in PbPb collisions compared to pp collisions. The excess in $\langle \not{p}_{\mathrm{T}}^{\parallel} \rangle_{\Delta}$ along the subleading jet direction extends up to larger angles

($\Delta \approx 1$–1.2), with decreasing significance. In this angular range, there is an excess in $\langle p_{\mathrm{T}}^{\parallel} \rangle_{p_{\mathrm{T}}^{\mathrm{trk}},\Delta}$ for tracks with p_{T}that fall in the ranges of 0–0.5, 0.5–1, and 1–2GeV, and a depletion for particles with $p_{\mathrm{T}} > 4$GeV. This is consistent with results shown in the previous section and earlier CMS studies that demonstrate that the small-angle imbalance towards the leading jet is compensated by particles of small p_{T}emitted at large angles to the jet axes [94].

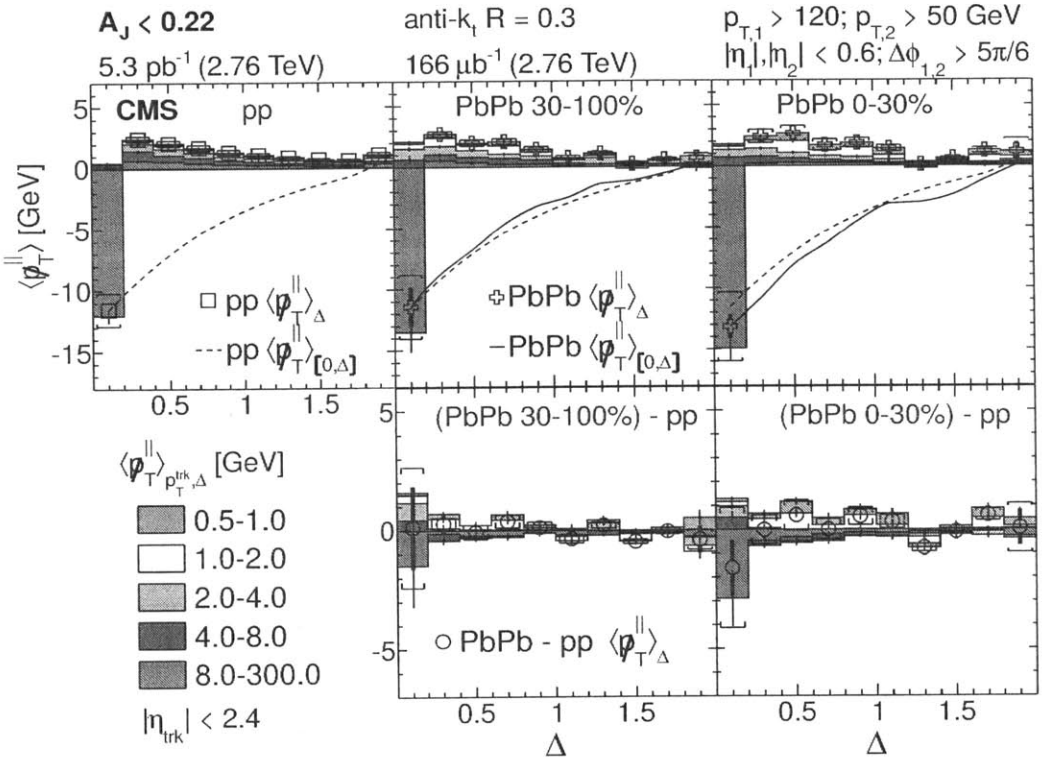

Figure 10-9: Same as Fig. 10-8, but with a balanced dijet selection ($A_J < 0.22$).

10.5.2 Study of the p_{T} balance in pp and PbPb collisions, as a function of opening angles around jets in bins of A_J

More information can be obtained by repeating the previous study as a function of dijet asymmetry A_J. The results for a sample containing more balanced dijets ($A_J < 0.22$) is shown in Fig. 10-9, again comparing pp data with two PbPb centrality

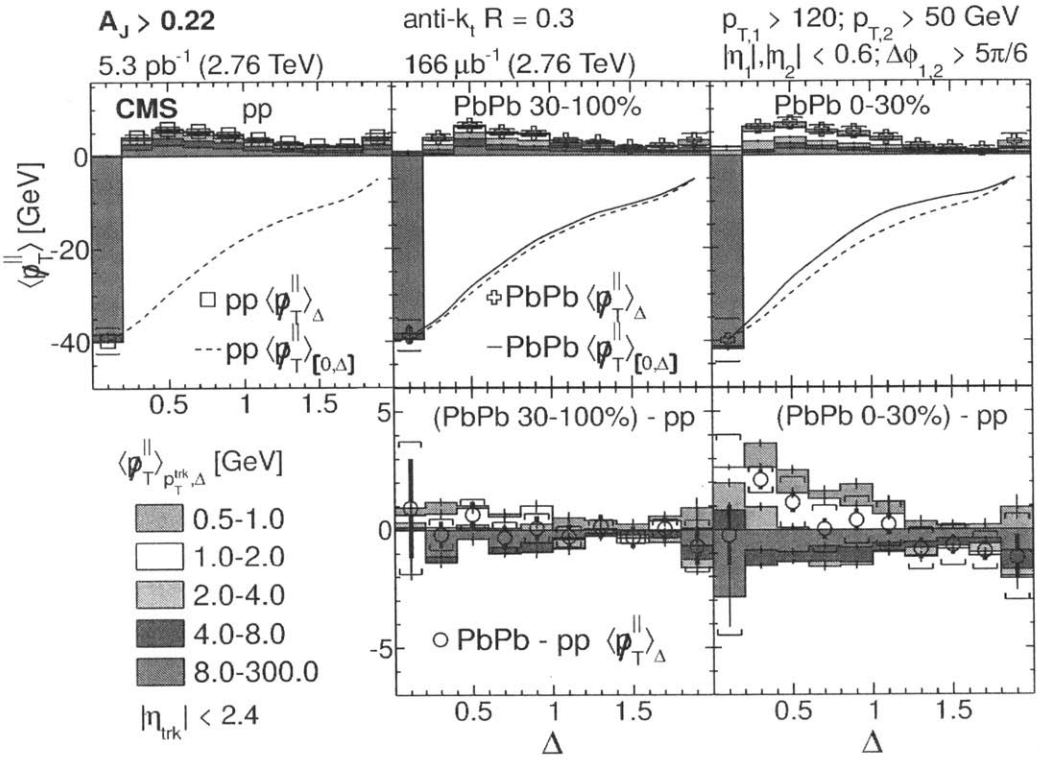

Figure 10-10: Same as Fig. 10-8, but with an unbalanced dijet selection ($A_J > 0.22$).

bins. As expected, $\langle p_{\mathrm{T}}^{\parallel} \rangle_\Delta$ and $\langle p_{\mathrm{T}}^{\parallel} \rangle_{p_{\mathrm{T}}^{\mathrm{trk}},\Delta}$ for all track p_{T}take smaller values compared to inclusive A_J selection, meaning that events with a more balanced dijet selection show an overall better p_{T}balance in both small $\Delta < 0.2$, as well as larger Δ. This is also seen in the difference in $\langle p_{\mathrm{T}}^{\parallel} \rangle_\Delta$ for PbPb and pp collisions, although, as before, an preference of $\langle p_{\mathrm{T}}^{\parallel} \rangle_{p_{\mathrm{T}}^{\mathrm{trk}},\Delta}$ for low-p_{T} tracks to point along the subleading side can be seen for central PbPb events.

Complementary to the selection of more balanced dijets, Fig. 10-10 shows a selection for unbalanced dijets with $A_J > 0.22$. The A_J selection is reflected in the overall larger contributions in the small- and large-angle regions relative to the jet axes. This large A_J selection, which enhances the fraction of jets having undergone significant energy loss in PbPb collisions, also enhances the differences between PbPb and pp, as shown in the lower row of Fig. 10-10.

It is important to note that in pp collisions, only 30% of selected dijet events

have $A_J > 0.22$, but this number increases to 42% for central PbPb selections. This again suggests the presence of an additional mechanism creating asymmetric dijets in PbPb, i.e., parton energy loss in the medium. Consistent with this picture, the A_J dependence of the $\langle \not{p}_{\mathrm{T}}^{\parallel} \rangle_{p_{\mathrm{T}}^{\mathrm{trk}},\Delta}$ distributions in PbPb and pp collisions and their difference suggests that asymmetric dijet systems in pp and PbPb collisions are created through different mechanisms, with semi-hard radiation (e.g.,, three-jet events) dominating pp collisions. In contrast, a large fraction of asymmetric dijet events in PbPb is created through a differential energy loss mechanism as the partons traverse the medium, which leads to the observed excess in $\langle \not{p}_{\mathrm{T}}^{\parallel} \rangle_{p_{\mathrm{T}}^{\mathrm{trk}},\Delta}$ for the low-p_{T} bins. The depletion of high-p_{T} particle contributions at large angles in PbPb is more dominant with $A_J > 0.22$ relative to an inclusive A_J selection, because of the difference in relative fractions of three-jet events among all selected events.

10.5.3 Dependence of dijet asymmetry on p_{T} balance and multiplicity difference in jet hemispheres

To study the p_{T}flow relative to the dijet system as a function of event properties, such as centrality and A_J, in more detail, the$\langle \not{p}_{\mathrm{T}}^{\parallel} \rangle_{p_{\mathrm{T}}^{\mathrm{trk}},\Delta}$ is summed over all annuli to obtain $\langle \not{p}_{\mathrm{T}}^{\parallel} \rangle_{p_{\mathrm{T}}^{\mathrm{trk}}}$, i.e., the average p_{T}balance in the event calculated for a given range of track p_{T}. In Fig. 10-11, we display $\langle \not{p}_{\mathrm{T}}^{\parallel} \rangle_{p_{\mathrm{T}}^{\mathrm{trk}}}$ for different ranges of track p_{T}(displayed in terms of the colored boxes) as a function of A_J, ranging from almost balanced to very unbalanced dijets in pp collisions, and in four selections of PbPb centrality from most peripheral to most central. The balance in the event for all tracks with $p_{\mathrm{T}} > 0.5$GeV, denoted as $\langle \not{p}_{\mathrm{T}}^{\parallel} \rangle_{\Sigma}$, which is obtained by adding up the $\langle \not{p}_{\mathrm{T}}^{\parallel} \rangle_{p_{\mathrm{T}}^{\mathrm{trk}}}$ for different p_{T} ranges, is also included, and shown as open markers, with associated systematic uncertainties as brackets around the points. In PbPb events, overall $p_{\mathrm{T}}$is balanced to better than 10GeV, i.e., $|\langle \not{p}_{\mathrm{T}}^{\parallel} \rangle_{\Sigma}| < 10$GeV for all A_J selections. The small negative trend in $\langle \not{p}_{\mathrm{T}}^{\parallel} \rangle_{\Sigma}$ as a function of A_J is observed also in pp events, and in generator-level PYTHIA events, once the p_{T}threshold set on charged particles and the acceptance of the tracker are imposed.

When selecting events containing dijets with $A_J > 0.11$, an expected excess of high-p_{T} particles in the direction of the leading jet (indicated by the red areas in Fig. 10-11) is seen for all selections in pp and PbPb collisions. For pp and peripheral PbPb collisions, this excess is mostly balanced by particles with intermediate $p_{\mathrm{T}}$of 2–8GeV. Going to more central collisions, $\langle \not{p}_{\mathrm{T}}^{\parallel} \rangle_{p_{\mathrm{T}}^{\mathrm{trk}}}$ on the subleading jet side is modified from the intermediate p_{T} range towards low p_{T} (0.5–2GeV). This effect is most pronounced for events with large A_J in central PbPb collisions.

The lower row of Fig. 10-11 shows the difference between $\langle \not{p}_{\mathrm{T}}^{\parallel} \rangle_{p_{\mathrm{T}}^{\mathrm{trk}}}$ in PbPb and pp collisions, after requiring the specific PbPb collision centralities and dijet imbalance. While the contributions from different p_{T} ranges are similar for pp and peripheral PbPb collisions, a difference can be seen for central collisions, where a significant excess of low-p_{T} charged particles is observed for asymmetric jets in PbPb collisions. Systematic uncertainties are shown only for $\langle \not{p}_{\mathrm{T}}^{\parallel} \rangle_{\Sigma}$, and not for $\langle \not{p}_{\mathrm{T}}^{\parallel} \rangle_{p_{\mathrm{T}}^{\mathrm{trk}}}$. Uncertainties in $\langle \not{p}_{\mathrm{T}}^{\parallel} \rangle_{\Sigma}$ provide an upper bound on systematic uncertainties for individual p_{T}ranges, as uncertainties in low-p_{T} particles are, in fact, significantly smaller. The excess observed in low-p_{T} particles in the range of 0.5–2GeV has therefore a significance of 3–4 standard deviations for $A_J > 0.11$ for most central events. The difference in $\langle \not{p}_{\mathrm{T}}^{\parallel} \rangle$ between PbPb and pp collisions for all tracks with $p_{\mathrm{T}} > 0.5$GeV is consistent with zero across all centrality and A_J selections.

The overall p_{T}balance observed through $\langle \not{p}_{\mathrm{T}}^{\parallel} \rangle_{\Sigma}$ in PbPb events agrees with pp events, within systematic and statistical uncertainties, over all ranges of A_J and centrality, while the $\langle \not{p}_{\mathrm{T}}^{\parallel} \rangle_{p_{\mathrm{T}}^{\mathrm{trk}}}$ distributions show excess of low-p_{T} particles. This implies that there are more particles in the subleading jet hemispheres compared to the leading jet hemispheres, because more particles are required to obtain the same p_{T}sum.

Figure 10-12 shows the mean difference in multiplicities between leading and subleading jet hemispheres, denoted as $\langle \Delta_{\mathrm{mult}} \rangle$, as a function of A_J and collision centrality. The $\langle \Delta_{\mathrm{mult}} \rangle$ is presented for both PbPb and pp collisions. Measurements in pp collisions are in good agreement with PYTHIA and PYTHIA+HYDJET simulations. In general, the $\langle \Delta_{\mathrm{mult}} \rangle$ increases as a function of A_J in pp, PbPb, PYTHIA, and PYTHIA+HYDJET events. The events in pp collisions with large A_J contain a

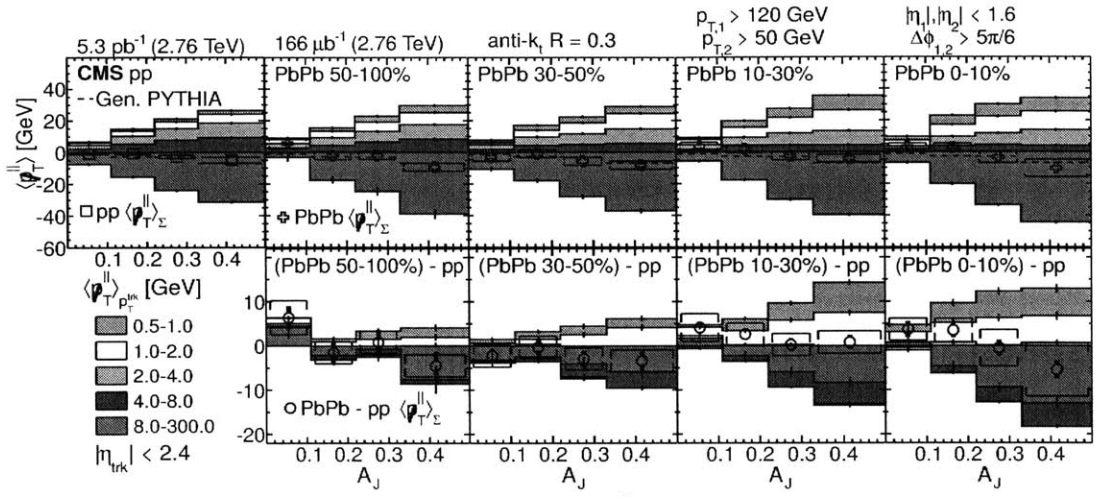

Figure 10-11: (Upper row) has $\langle p_{\mathrm{T}}^{\parallel} \rangle_{p_{\mathrm{T}}^{\mathrm{trk}}}$ and $\langle p_{\mathrm{T}}^{\parallel} \rangle_{\Sigma}$ in pp collisions (leftmost) and in four selections of PbPb for collision centralities from 50–100% to 0–10%. The open markers show $\langle p_{\mathrm{T}}^{\parallel} \rangle_{\Sigma}$, p_{T}balance for tracks with $0.5 < p_{\mathrm{T}} < 300$GeV, while the colored boxes show the $\langle p_{\mathrm{T}}^{\parallel} \rangle_{p_{\mathrm{T}}^{\mathrm{trk}}}$ contributions for different track p_{T}ranges. For each panel, $\langle p_{\mathrm{T}}^{\parallel} \rangle_{p_{\mathrm{T}}^{\mathrm{trk}}}$ and $\langle p_{\mathrm{T}}^{\parallel} \rangle_{\Sigma}$ values are shown as a function of dijet asymmetry. The lower row shows the difference between $\langle p_{\mathrm{T}}^{\parallel} \rangle_{p_{\mathrm{T}}^{\mathrm{trk}}}$ and $\langle p_{\mathrm{T}}^{\parallel} \rangle_{\Sigma}$ for PbPb and pp data. Error bars and brackets represent statistical and systematic uncertainties, respectively.

larger fraction of three-jet or multijet events, where more particles are produced in the direction of the subleading jet. The observed increase in $\langle \Delta_{\mathrm{mult}} \rangle$ for pp collisions with increasing A_J is therefore expected. Going from peripheral (50–100%) to central (0–10%) PbPb events, for a given A_J selection an excess in $\langle \Delta_{\mathrm{mult}} \rangle$ is visible compared to pp collisions. The difference in $\langle \Delta_{\mathrm{mult}} \rangle$ between pp and PbPb collisions increases monotonically as a function of A_J at all collision centralities, with the biggest effect seen for most central PbPb collisions. This is consistent with the expected dependence of medium-induced energy loss on collision centrality, where systems of the largest size (i.e., smallest centrality) should show the largest medium-related effects. The multiplicity difference is up to $\approx$15 particles in the most central 0–10 % collisions.

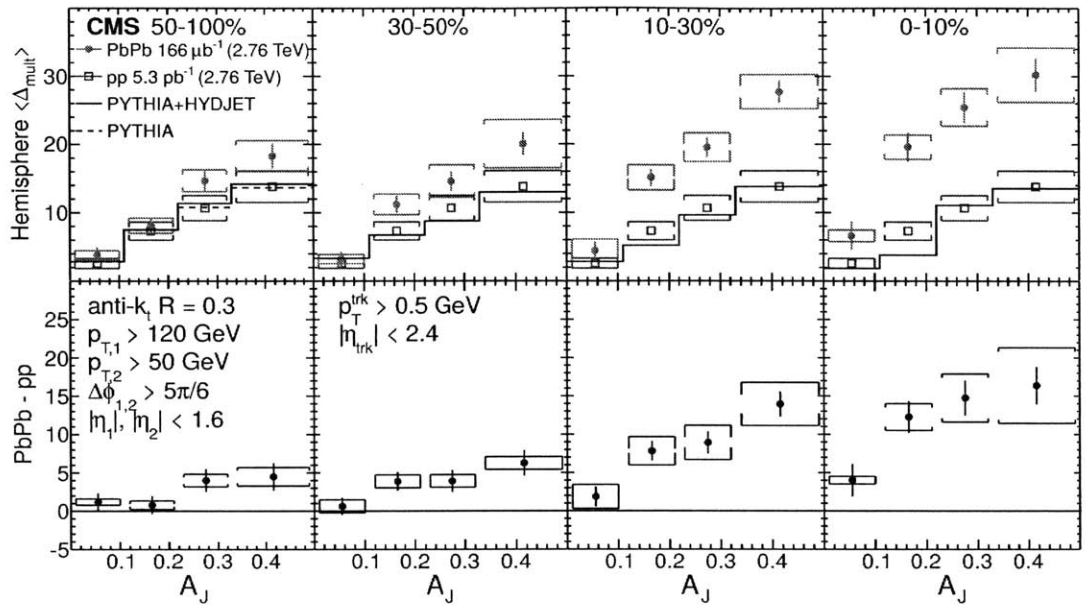

Figure 10-12: Upper panels show the comparison of the mean difference in multiplicity $\langle \Delta_{\mathrm{mult}} \rangle$ between the subleading jet hemisphere and leading jet hemisphere, as a function of dijet asymmetry A_J for pp (blue squares), PbPb (red filed circles), PYTHIA (dashed histogram), and PYTHIA+HYDJET events (black histogram). The centralities of PbPb collisions are 50–100%, 30–50%, 10–30 %, and 0–10%, respectively, from leftmost to rightmost panel. Lower panels provide the difference in $\langle \Delta_{\mathrm{mult}} \rangle$ between PbPb and pp collisions. Statistical and systematic uncertainties are shown as error bars and brackets, respectively.

10.6 R dependent measurement of momentum flow

The dependence of jet quenching effects on virtuality of the jets is harder to test, although it is supposed to be one of the main factors that drive the amount of quenching of jets [185, 178]. Measuring change in quenching effects by virtuality requires a jet-by-jet measurement of the width or mass of the jet. However, a jet-by-jet mass measurement is sensitive to underlying event fluctuations in PbPb and several reconstruction effects such as track reconstruction efficiency. It is certainly a direction to follow for future measurements, but at the moment R parameter can be used as a proxy for the mass of the jets. We have shown in Fig. 3-8 that by increasing R jets get wider and softer, which means that their mass also gets larger. However, measuring A_J as a function of R is not a clever direction to follow, because of the dependence

of A_J in vacuum on R as shown in Fig. 7-2. However, an interesting quantity one can measure, is the amount of energy lost by quenched jet into soft particles at large angles. This measurement is presented later in Chapter 10.

It is important to note that there is an overlap in the final set of dijet events obtained for different R parameters, and therefore it is not possible to interpret the dependence of the p_{T}-balance distributions on R as simply a dependence on jet size. A change in R can induce a modification in $\not{p}_{\mathrm{T}}$ in two ways: events that satisfy the dijet requirements for one R can fail for another R value, or events that satisfy the dijet requirements for both R parameters, but for which the ordering of jets change, can impact ϕ_{dijet}, as well as the value of parameters used in the binning of the measurements, such as A_J and Δ.

The requirements on the $p_{\mathrm{T}}$of leading and subleading jets are the main sources of variations in the final set of dijet events for different R parameters. For each R, a jet p_{T}selection translates into a different requirement on initial parton p_{T}. A smaller fraction of the initial energy of the parton is recovered using jets of smaller size. Although fewer events pass the dijet requirement for $R = 0.2$ jets, strictly speaking, such events do not form a subset of dijet events with larger R parameters. A small fraction of $R = 0.2$ dijet events (4–7% in PbPb collisions and 2–4% in pp collisions) does not satisfy the dijet requirements for other R values, mainly because jets fall outside of the η range or the $\Delta\phi$ requirement for the dijet pair. This can happen because of the merging of the subleading and third jets, and because of the resolution in jet angular direction. Such events make up a statistically negligible contribution to the results and are therefore not the focus of the discussion.

The fraction of events that pass the dijet selection both for the largest $R = 0.5$ and for other values are shown in the second column of Table 10.4, without matching the directions of the jets. Compared to pp collisions, the fraction of events that pass both cutoffs on jets is reduced in PbPb collisions more rapidly as R decreases. This observation is qualitatively consistent with the measurement showing that inclusive jet suppression is smaller in PbPb collisions for large R values [10], which can be interpreted as due to the recovery of part of the energy lost in the initial hard scatter

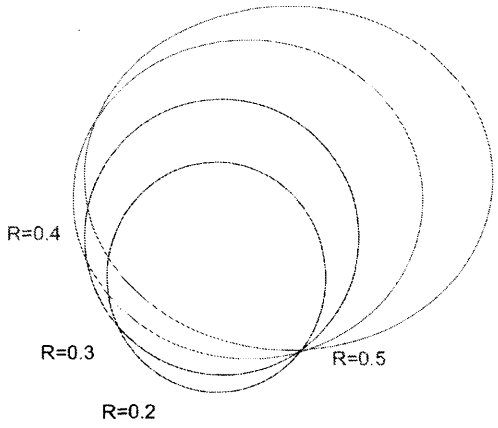

Figure 10-13: Venn diagram showing intersection of events with dijet selections with different R parameters.

Table 10.4: Overlap in event selections for 0-100% PbPb and pp collisions. The second column gives the percentage of events that pass dijet selections and a tight pseudorapidity requirement ($|\eta| < 0.6$) for $R = 0.5$, and an additional dijet selection also required for a smaller R value. In columns 3-6 the leading and subleading jets with $R = 0.5$ are matched to the leading and subleading jets with smaller R values, requiring only $R = 0.5$ selection on jets. The third column shows the percentage of these events where both leading and subleading jets point in the same direction ($\Delta_i = \sqrt{(\eta_i^R - \eta_i^{R=0.5})^2 + (\phi_i^R - \phi_i^{R=0.5})^2} < 0.5$ for $i = 1$ and 2). The fourth column shows percentage of events in which subleading jets with the given R parameter match the $R = 0.5$ leading jet, and the leading jet matches the $R = 0.5$ subleading jet.

R	Additional dijet selection [%]	Matched jet directions [%]	Swapped jet directions [%]
		PbPb	
0.2	48 , 2	83 , 5	10 , 3
0.3	62 , 2	90 , 4	7 , 3
0.4	77 , 1	94 , 3	3 , 2
		pp	
0.2	58 , 2	83 , 5	14 , 3
0.3	73 , 2	90 , 4	8 , 3
0.4	86 , 1	95 , 3	4 , 2

of partons.

The last column of Table 10.4 gives the fraction of events with swapped leading and subleading jets compared to those with $R = 0.5$. For these events, the $\not{p}_{\mathrm{T}}^{\parallel}$ has an opposite sign relative to the value for $R = 0.5$, as ϕ_{dijet} points in the opposite

Table 10.5: The average value of the ratio of $p_{\mathrm{T}}$of the leading and subleading jets at jet for a given R, to their $p_{\mathrm{T}}$for $R = 0.5$ are shown in the first and second, respectively, columns in 0-100% PbPb collisions. Same values shown for pp collisions in third and fourth columns. The leading jet is required to be matched to a leading jet of $R = 0.5$ in angular direction, and similarly for the subleading jet.

	PbPb		pp	
R	$\langle p_{\mathrm{T},1}^{R}/p_{\mathrm{T},1}^{R=0.5}\rangle$	$\langle p_{\mathrm{T},2}^{R}/p_{\mathrm{T},2}^{R=0.5}\rangle$	$\langle p_{\mathrm{T},1}^{R}/p_{\mathrm{T},1}^{R=0.5}\rangle$	$\langle p_{\mathrm{T},2}^{R}/p_{\mathrm{T},2}^{R=0.5}\rangle$
0.2	0.89 , 0.001	0.79 , 0.002	0.91 , 0.001	0.83 , 0.002
0.3	0.93 , 0.002	0.88 , 0.004	0.95 , 0.001	0.90 , 0.001
0.4	0.96 , 0.002	0.94 , 0.005	0.98 , 0.001	0.96 , 0.001

hemisphere. Especially in pp collisions, swapping of the leading and subleading jet is the main source of events in which the jet directions are not matched. In PbPb collisions, swapping is slightly less frequent than in pp collisions, suggesting that the third jet may be replacing the subleading jet. For events that satisfy dijet requirements for different R parameters, the $\not{p}_{\mathrm{T}}^{\parallel}$ in each event can still change as a function of R because of the swapping of jets in the dijet pairs, and the replacement of the subleading jet by the third jet.

Additional information can therefore be extracted by requiring the leading and subleading jets with a given R to be in the same direction as the corresponding jets found using $R = 0.5$. As shown in the third column of Table 10.4, the fraction of such events is similar for pp and PbPb collisions. These events produce almost no change in ϕ_{dijet} and the jet axes, which change only slightly due to jet angular resolution, and therefore yield approximately the same $\not{p}_{\mathrm{T}}^{\parallel}$. However, these events can accommodate the change in the $p_{\mathrm{T}}$of jets that originate from the same initial hard-scattered parton for different R parameters. For jets matched to each other spatially, the ratio of the $p_{\mathrm{T}}$of the leading or subleading jet at some given R to respective jets with $R = 0.5$, $\langle p_{\mathrm{T},1(2)}^{R}/p_{\mathrm{T},1(2)}^{R=0.5}\rangle$, is calculated and the values are shown in columns two and three in Table 10.5 for PbPb and columns four an five for pp collisions . As expected, in both PbPb and pp collisions, $\langle p_{\mathrm{T},1}^{R}/p_{\mathrm{T},1}^{R=0.5}\rangle$ and $\langle p_{\mathrm{T},2}^{R}/p_{\mathrm{T},2}^{R=0.5}\rangle$ are reduced as R gets smaller. In PbPb collisions, a smaller fraction of jet $p_{\mathrm{T}}$is recovered at small R for both the leading and subleading jets, which may be due to the broadening of quenched jets. This effect is larger for the subleading than for the leading jet.

As R parameters become smaller, leading and subleading jets fall below the p_{T}requirements. Most of the time, the leading jet satisfies the p_{T}selection for $R = 0.5$, but falls below the threshold for smaller R, because the subleading jet $p_{\mathrm{T}}$is already biased towards values above the 50GeV threshold by the leading jet with $p_{\mathrm{T}} > 120GeV$ in the event. However, as shown in Figs. 10-9 and 10-10, for $R = 0.3$ jets the $\langle p_{\mathrm{T}}^{\parallel} \rangle_{p_{\mathrm{T}}^{\mathrm{trk}},\Delta}$ signal is dominated by dijet events with large imbalance, which is true for all other R parameters as well. For events with $A_J > 0.22$, $\langle p_{\mathrm{T},2} \rangle \approx$ 70–80GeV is sufficiently close to the 50GeV threshold for subleading jets falling below the threshold to create sizable effects on the results.

To summarize the information given above, we do not exactly increase jet width with R, because of the significant overlap between the chosen events with different R parameters, and in the same event the jets might change resulting in swapping of jet pair in p_{T} order, and therefore, flipping of ϕ_{dijet}. However, the new events that pass the p_{T} requirements on jets are due to wider jets being added to the selected events, and therefore approximately it is possible to think of large R parameter dijet events as those with wider jets with softer fragmentation.

The dependence of $\langle p_{\mathrm{T}}^{\parallel} \rangle_{p_{\mathrm{T}}^{\mathrm{trk}},\Delta}$ on Δ and R is shown in Fig. 10-14, without any A_J requirement, for pp and for PbPb events with 0–30% centralities. In the PbPb system, the peak position of balancing distribution also shifts towards greater Δ, but less than in pp collisions due to the additional soft particles at small angles associated to the quenching of the dijet pair and reduction in the number of high-p_{T} particles associated with the third jet. In the PbPb − pp bottom panels, this manifests in the depletion of higher ranges at p_{T}, 4–8 and 8–300GeV, which shift to greater angular distance with increasing R. There is a modest increase observed in the excess in the p_{T}ranges of 0.5–1 and 1–2GeV with increasing R. The overall distribution in the low-p_{T} excess in PbPb relative to pp does not change significantly with the distance parameter, and especially not at larger angular distance Δ.

There is a hint that the $\langle p_{\mathrm{T}}^{\parallel} \rangle_{[0,\Delta]}$ distribution in central PbPb collisions, shown by the black curves in Fig. 10-14, is narrower than in pp collisions, shown by the dashed black curves, meaning that the slope is larger in PbPb relative to pp collisions. This

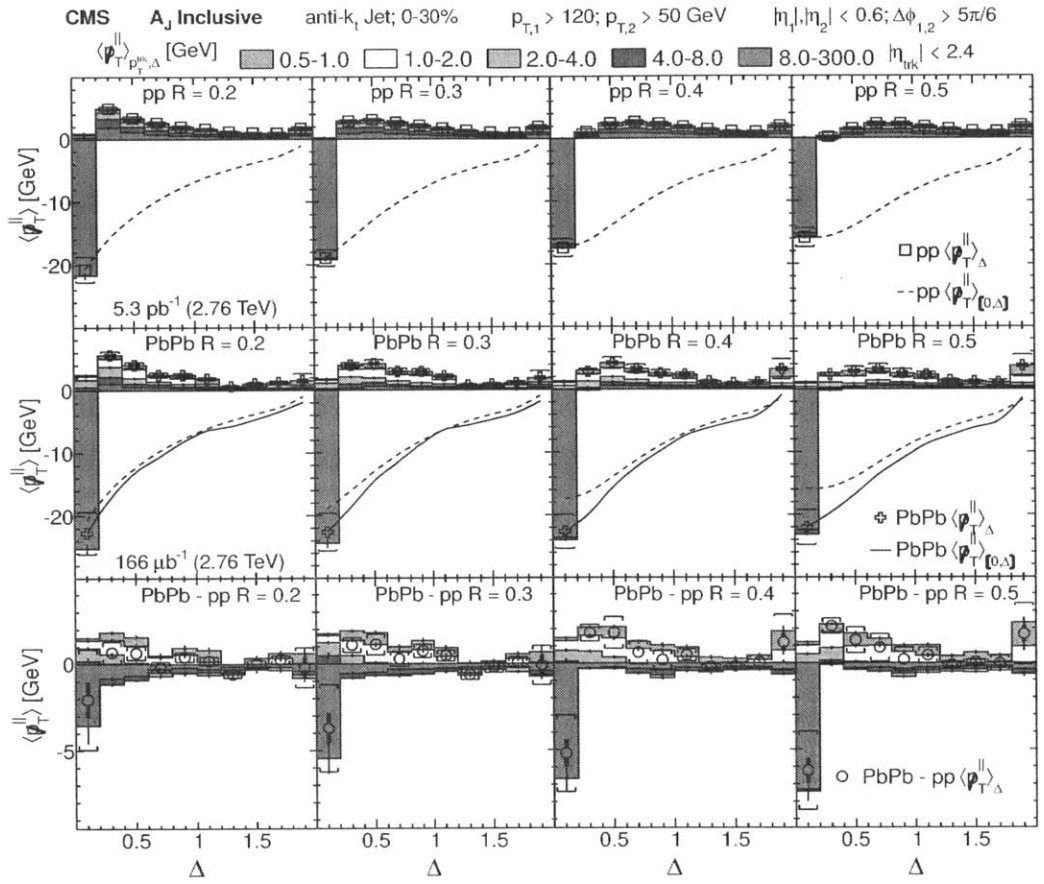

Figure 10-14: Upper row shows $\langle p_{\mathrm{T}}^{\parallel} \rangle_{p_{\mathrm{T}}^{\mathrm{trk}},\Delta}$, $\langle p_{\mathrm{T}}^{\parallel} \rangle_{\Delta}$ and $\langle p_{\mathrm{T}}^{\parallel} \rangle_{[0,\Delta]}$ in pp collisions as a function of Δ, for a distance parameter $R = 0.2$, 0.3, 0.4, and 0.5, from left to right. Middle row Provides same distributions in PbPb collisions of centrality range 0–30%. Lower row has the difference between PbPb and pp. Error bars and brackets represent statistical and systematic uncertainties, respectively. The results are inclusive in the dijet asymmetry parameter A_J. For further description of what colored boxes, empty markers and curves correspond to refer to 10-5.

becomes slightly more significant at $R = 0.5$, where bias in gluon or quark jets that have large angular width becomes smaller. This is also reflected in the increase in the magnitude of $\langle p_{\mathrm{T}}^{\parallel} \rangle_{\Delta}$ in the leading jet direction in the first bin, and in the subleading jet direction in the second bin. This modification is dominated by particles with $p_{\mathrm{T}} > 2$GeV, and may arise from quenching effects, causing leading jets to narrow or subleading jets to widen in central PbPb relative to pp collisions.

To summarize the dependence of differences in p_{T}balance among different R bins

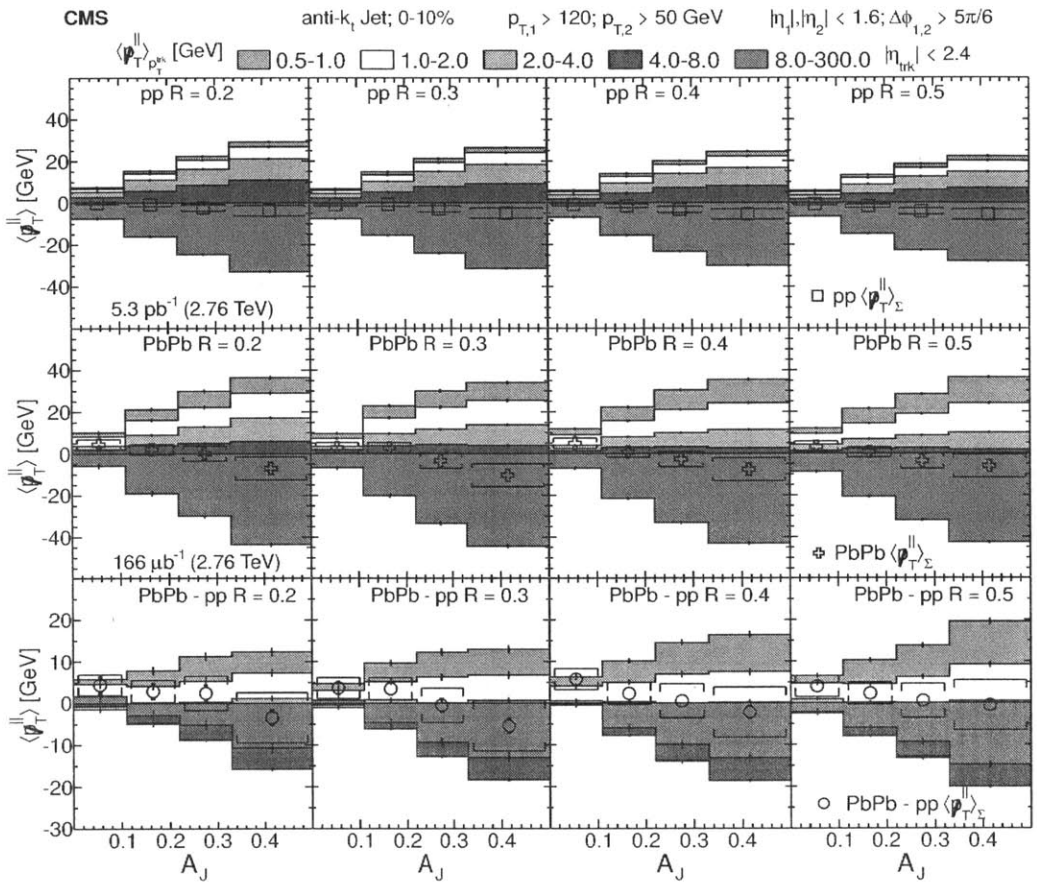

Figure 10-15: Upper row shows $\langle p_{\mathrm{T}}^{\parallel} \rangle_{p_{\mathrm{T}}^{\mathrm{trk}}}$ and $\langle p_{\mathrm{T}}^{\parallel} \rangle_{\Sigma}$ as a function of A_J in pp collisions for distance parameters $R = 0.2$, 0.3, 0.4, and 0.5, from left to right. Middle row provides the same distributions in PbPb collisions of centrality range 0–10%, for distance parameter $R = 0.2$, 0.3, 0.4, and 0.5, from left to right. Lower row has the difference PbPb − pp. For further description of what colored boxes, empty markers and curves correspond to refer to 10-11.

on A_J, and to investigate the observed changes in the associated track p_{T}spectrum in more central events, our measurement of the dependence of the p_{T}balance on R and A_J, is shown in Fig. 10-15 for pp and 0–10% central PbPb events, respectively, in the top and middle rows. The leftmost panels correspond to a selection of $R = 0.2$ jets, while the rightmost panels correspond to $R = 0.5$. For pp collisions, there is a slight decrease in the magnitude of signal in each p_{T} range as R increases. This behavior is consistent with the observed reduction in the incone $\langle p_{\mathrm{T}}^{\parallel} \rangle_{p_{\mathrm{T}}^{\mathrm{trk}},\Delta}$ for high-p_{T} tracks with $\Delta < 0.2$ shown in the top panels of Fig. 10-14 as a function of R, which was discussed

above, and is also observed in generator-level PYTHIA. This kind of behavior is not observed in central PbPb events.

The bottom row of Fig. 10-15 displays the difference between PbPb and pp results. The R parameter is correlated with a small change in the magnitude of the $\langle p_{\mathrm{T}}^{\parallel} \rangle_{p_{\mathrm{T}}^{\mathrm{trk}}}$ excess of low-p_{T} particles, as jets of larger R give a greater excess. When p_{T}ranges 0.5–2.0GeV are combined, the increase in the low-p_{T} excess becomes more significant. The systematic uncertainties shown in the plot are dominated primarily by the p_{T} range 8.0–300.0GeV, and as such cannot be used to characterize the significance of $\langle p_{\mathrm{T}}^{\parallel} \rangle_{p_{\mathrm{T}}^{\mathrm{trk}}}$ in the low track-p_{T} ranges, nor the slight dependence on the distance parameter in the low-p_{T} excess. The sum of track p_{T} ranges $\langle p_{\mathrm{T}}^{\parallel} \rangle_{\Sigma}$ is insensitive to the distance parameter, and the difference between PbPb and pp collisions is consistent with zero for all R values.

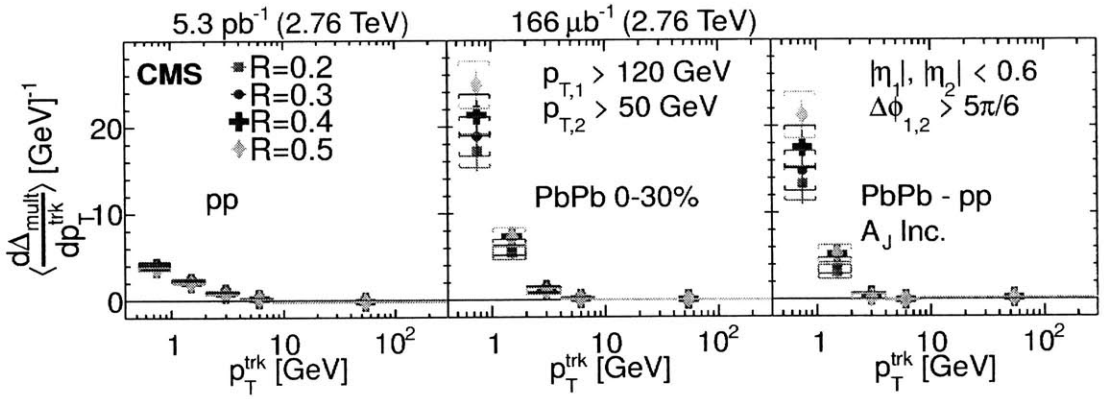

Figure 10-16: Difference in differential multiplicity $\langle \Delta_{\mathrm{mult}}/p_{\mathrm{T}^{\mathrm{trk}}} \rangle$ between the away-side and leading-jet hemispheres as a function of track p_{T}, using an inclusive dijet asymmetry selection. Left panel has measurements in pp for jet radii $R = 0.2$, 0.3, 0.4, and 0.5, and the middle panel displays similar measurements in PbPb. Right panel provides the difference in $\langle \Delta_{\mathrm{mult}}/p_{\mathrm{T}}^{\mathrm{trk}} \rangle$ between PbPb and pp collisions for each momentum range. Systematic uncertainties are shown as boxes. Error bars represent statistical uncertainties.

Finally, the multiplicity associated with excess of low-p_{T} particles shown in Figs. 10-14 and 10-15, and the charged-particle spectrum for $\langle \Delta_{\mathrm{mult}} \rangle$ are given in Fig. 10-16 for events with 0–30% centrality, without any A_J requirement, for several distance parameters in pp and PbPb collisions, and for their difference.

In pp collisions the fragmentation of leading jets with high p_{T}provides more high-p_{T} and fewer low-p_{T} particles in the hemisphere of the leading jet relative to the subleading-jet hemispheres. As a result, $\langle \Delta_{\mathrm{mult}}/p_{\mathrm{T}} \rangle$ has a positive value for charged particles with $p_{\mathrm{T}} < 8$GeV and a negative value for charged particles with $p_{\mathrm{T}} > 8$GeV. Also, in PbPb collisions, $\langle \Delta_{\mathrm{mult}}/p_{\mathrm{T}} \rangle$ is positive for particles with $p_{\mathrm{T}} < 8$GeV and becomes negative in the last bin, although the spectrum is much steeper, and has a large excess of soft particles. By taking the difference in $\langle \Delta_{\mathrm{mult}}/p_{\mathrm{T}} \rangle$ between PbPb and pp collisions, a significant excess (>5 standard deviations) is observed at $p_{\mathrm{T}} <$ 2GeV, and a depletion at $p_{\mathrm{T}} > 4$GeV, while there is only a slight excess in the range $2 < p_{\mathrm{T}} < 4$GeV. Changing R does not have an effect on the results in pp collisions, while in PbPb collisions there is a small enhancement in the excess for low-p_{T} charged particles as R is increased from 0.2 to 0.5.

10.7 Summary

The Δ dependent measurement of "missing-p_{T}", which is the sum of the projection of transverse momenta of charged particles with different p_{T} selections on the dijet axis, conveys information about several aspects of dijet events: in-cone fragmentation and jet shapes, transverse momentum flow at large angles and the intra-jet properties. The modification of these in PbPb collisions due to jet quenching can be studied by comparing the "missing-p_{T}" in PbPb to the pp collisions, and the effects of medium can be enhanced by studying central events and with large dijet asymmetry. The aim is to measure in what way the p_{T} spectra and angular distribution of charged particles in the event are modified, so that the dijet imbalance is enhanced but the overall transverse momentum in the event are conserved.

The modification in in-cone properties are seen as modification in the small Δ bins of size of a typical jet area, while the modification in transverse momentum flow which might happen due to medium response and large angle radiation shows up at large Δ values. The intra-jet properties are visible by looking at the peak position of balancing distribution for high p_{T} particles, which point at the angle of most likely

place of a third-jet in the event.

For a given dijet asymmetry, the imbalance in p_{T} in PbPb collisions is found to be compensated by particles at $p_{\mathrm{T}} = 0.5$–2 GeV, whereas in pp collisions most of the momentum balance is found in the p_{T} range of 2–8 GeV, reflecting a softening of the radiation responsible for the imbalance in p_{T} of the asymmetric dijet system in PbPb interactions. Correspondingly, a larger multiplicity of associated particles is seen in PbPb than in pp collisions. Both measurements show larger differences between PbPb and pp for more central PbPb collisions. The current data provide the first detailed study of the angular dependence of charged particle contributions to the asymmetry up to large angles from the jet axis, showing signs of medium response.

The dependence of jet quenching mechanisms on the opening angle on jets can be tested by repeating the measurement for a range of R parameters ($R = 0.2$, 0.3, 0.4 and 0.5). The increase in the magnitude of "missing-p_{T}" for $\Delta < 0.2$ as R gets larger is an indication of wider jets losing more energy, which results in more enhanced in dijet imbalance in PbPb compared to pp collisions. The modification of fragmentation and shapes of jets is also larger for larger R, as seen by an increase in difference in PbPb and pp in the second bin in Δ, i.e., $0.2 < \Delta < 0.4$ by increasing R. The results suggest that either the leading jet is getting narrower, or the subleading jet is getting broader after quenching, and more so for jets with wider opening angles.

Intra-jet properties can also be studied by the R dependent result, as in pp collisions, the balancing distribution shifts to larger Δ with increasing distance parameter R, because of the presence of a third jet further away from the dijet axis. The shift is more pronounced than in PbPb collisions, where there is an excess of low p_{T} particles close to the jet axes, because of the in-cone modification mentioned above. In order to be sensitive only to the third jet location and not the fragmentation modification, the peak position of contribution of only the high p_{T} charged particles in PbPb can be compared to pp collisions. The peak position of balancing distribution for charged particles is not modified significantly in PbPb compared to pp collisions meaning that the most likely position for a third jet is still the same.

To summarize, these results constrain the redistribution of transverse momentum

in the modelling of QCD energy loss processes of partons traversing the hot and dense medium created in heavy-ion collisions. It might be possible in the future to use this detailed measurement as a test for jet quenching MCs, as they develop to include a wider range of quenching mechanisms and a proper treatment of medium response. This measurement is especially challenging for quenched MCs due to the different aspects of event it is sensitive to.

Chapter 11

Conclusions

In this work two analyses on dijets, and the new information they made available on initial and final state interactions in heavy ion collisions, were discussed. In heavy ion collisions a high temperature, color charged medium is formed and jets produced in hard-scatterings propagate through the medium getting modified and leaving behind traces of their passage. The measurements of modification of intra-jet properties and global event shapes in the presence of jets in PbPb collisions can teach us about the mechanisms of interactions between partons in high T QCD. Indeed, studies of jet quenching have a long history, and experiments have reached a level of precision which allows very detailed measurements of the effects of passage of a jet through the medium. Effects of the medium produced in PbPb collisions become apparent through comparisons of PbPb collisions with baseline pp and pPb measurements. These comparisons allow us to factorize the effects of jet quenching from standard QCD processes that take place in vacuum, and from the initial state effects caused by modification of parton distributions inside the nucleus.

The measurements described here are carried out with three different collision systems, pp, pPb and PbPb, using the CMS detector at the LHC. The dijet measurement in PbPb collisions of total integrated luminosity of 166 μb^{-1} at nucleon-nucleon center of mass energy, $\sqrt{s_{\text{NN}}}$, of 2.76 TeV are compared to pp collisions of total integrated luminosity of 5.3 pb^{-1} at the same energy. The 35 nb^{-1} pPb data is collected at a different $\sqrt{s_{\text{NN}}} = 5.02$ TeV, and the properties of dijets in this collision system

are compared to NLO calculations, and PYTHIA and PYTHIA+HIJING simulations. Until pp and PbPb data at same $\sqrt{s_{NN}}$ become available, this is the preferred mode of operation to ensure reliability of results. Apart from having different $\sqrt{s_{NN}}$, these analyses also have different objectives, therefore, they are discussed separately. Measurement of properties of dijets in pPb are discussed in Chapter 9, and the analyses in PbPb collisions with a comparison to pp collisions are discussed in Chapter 10. Although, these measurements have different physics goals, they share the common feature of being based on a very basic QCD process, i.e. back-to-back production of partons, and the simple fact that these partons come from the same parent parton enables us to study a large variety of physics with dijets. Modifications in the p_{T} balance of dijets are signs of interactions of jets with the medium after the back-to-back partons are produced. In contrast, the absence of final state modifications dijet pseudorapidity distributions in pPb collisions enables us to perform a scan of nPDFs as a function of x of the parton in lead nucleus.

Before the pPb run at LHC, pPb collisions were seen simply as a reference for PbPb collisions, containing effects related to the modification of parton distributions inside the nucleus at the initial state. However, the observation of flow in pPb, which is one of the signs of formation of a strongly coupled medium in PbPb collisions, raised questions about whether a medium is formed in pPb collisions as well. The measurement of dijet properties in pPb collisions therefore has two parts: first we have checked whether or not jets are modified by a final state interaction, and based on lack of observation of any modification we use dijets to probe initial state properties. In order to do that we searched for an increase in the dijet p_{T} imbalance as event activity gets larger. Any modification is found to be less than 2% even in the highest activity events, which constitute 2.5% of total minimum bias interactions. Although this does not disprove the existence of a medium, it implies that jets are not modified significantly by final state interactions and therefore are suited for a study of initial state effects. The normalized dijet pseudorapidity distributions were compared to NLO CT10 PDFs and EPS09 nPDFs, and they agree with EPS09 results within systematic uncertainties while significantly disfavoring CT10 only calculation.

A side-result obtained in pPb measurement is the large modification in dijet pseudorapidity distributions with increasing event activity. For events with large forward energy, pseudorapidity of the dijet system shifts towards the Pb going direction. Although $10-20\%$ shift could have been interpreted as a sign of impact parameter dependent nPDF modification, the shift that is observed is an order of magnitude larger than the nPDF modification, therefore, that possibility is quickly invalidated. Owing to the simple relation between Bjoerken x values and dijet pseudorapidity, this measurement aided the interpretation of some other unexpected results observed by RHIC and LHC experiments. The large modification in dijet pseudorapidity is understood to arise from kinematics biases caused by event activity selection. This bias was modelled by combining PYTHIA and HIJING MC according to the x taken away from the parton in proton. This simple model reproduces experimental results on inclusive jet and dijet production at LHC, and might aid in the search for observables that are sensitive to impact parameter, but do not suffer from the same kinematic biases.

The dijet measurement in pp and PbPb collisions at 2.76 TeV, which is presented in Chapter 10, aims to provide detailed information on effects of jet quenching and the medium response to jet quenching. In this analysis, predecessor of which is known in the community as "missing-p_{T}", we make use of the observation that subleading jets on average lose more energy compared to the leading jets in the medium, hence jet quenching enhances the dijet p_{T} asymmetry. We search for the missing-p_{T} that is associated to the excess energy lost by the subleading jet, and try to pin down where it gets relocated, i.e. by what kind of reshuffling of p_{T} and location of particles does the overall p_{T} balance in the event gets recovered. We perform an angular scan of the distribution of charged particles around the dijet axis and measure the modification of their p_{T} spectra at a given angle up to distances of $\Delta = \sqrt{(\eta_{\mathrm{trk}} - \eta_{\mathrm{jet}})^2 + (\phi_{\mathrm{trk}} - \phi_{\mathrm{jet}})^2} = 1.8$. The distribution of charged particles in p_{T} and Δ in PbPb collisions are studied as a function of collision centrality and dijet p_{T} asymmetry, in order to enhance the effects of jet quenching. These distributions are compared to pp collisions. In PbPb collisions we observe enhancement of low p_{T}

particles with $p_{\mathrm{T}} < 2$ GeV around subleading jets up to large angles $\Delta \approx 1.2$. This effect has been qualitatively produced by medium-cascade calculation, radiation at large angles and by transferring the lost energy to excitations of hydro-modes. However, in order to make further statements on implications of this detailed result on jet quenching mechanisms, quantitative comparisons with MC models are needed. Unfortunately most of the MC models do not include the effect of the recoil of medium and they are not expected to reproduce the angular modification due to the medium response at such angles. However, the direction taken recently is to consider the excited medium particles in jet clustering[80, 220]. Therefore, with the new developments in MC implementations we will be able to make use of the information revealed with this measurement.

The anti-k_T R parameter can be seen as a jet-by-jet proxy for the width of the jets, and it allows one to study jet quenching for jets with different virtualities. Larger R parameter jets are wider, and jets with wide opening angles (larger virtualities) are expected to lose more energy according to several theoretical predictions [185, 178, 114]. Missing-p_{T} is measured for a range of R parameters of 0.2 to 0.5. The modification of p_{T} distributions of charged particles close to the dijet axis, $\Delta < 0.4$, is enhanced when going to larger R values. This might be an indication of either subleading jets getting broader in PbPb compared to pp collisions, or a result of leading jets getting narrower. Although, it sounds unintuitive for quenching effects to result in narrower leading jets, if narrow jets lose less energy than wide jets this might result in such an effect. In fact, it is also likely for both of these to happen at the same time, i.e. leading jets might get narrower while subleading jets get wider as a result of jet quenching. An interesting direction to follow based on this result would be measurements of the modification of jet shapes and fragmentation functions for leading and subleading jet separately for large R values, to help distinguish between the two possible explanations of R dependent results of "missing-p_{T}". In addition to the dependence of enhancement of modifications of particles close to the jet axes, a slight enhancement of large angle soft particle production on the subleading jet hemisphere was seen when going to larger R values, providing an indication of wider

jets losing more energy. The enhancement of quenching effects for $R = 0.5$ jets compared to smaller R values motivates the jet structure measurements in heavy ion collisions to be carried out with larger R parameters, instead of the commonly used $R = 0.3$ value.

A measurement that is as complicated as this one requires a good understanding of jet and track reconstruction effects. Detailed information of performance of track and jet reconstructions as well as the correction procedure for the reconstruction biases are presented. In the future with improvements in track reconstruction efficiencies that are recently achieved it will be possible to significantly reduce the fluctuations in the "missing-p_{T}" measurements. The angular scan of "missing-p_{T}" still suffers from statistical limitations, with the new PbPb data collected at the end of 2015 together with the improvements in reconstruction of jets and tracks in PbPb collisions, it will be possible to update this measurement with much better precision.

Bibliography

[1] The PYTHIA6 Z2 tune is identical to the Z1 tune described in [139], except that Z2 uses the CTEQ6L PDF, while Z1 uses CTEQ5L.

[2] Ct10 global analysis:additional figures and results.

[3] Displays of aleph events, 1996.

[4] Rhic scientists serve up 'perfect' liquid, April 2005. [Online; posted 18-April-2005].

[5] Particle-flow event reconstruction in cms and performance for jets, taus, and missing e_{T}. *CMS Physics Analysis Summary*, CMS-PAS-PFT-09-001, 2009.

[6] Measurement of Tracking Efficiency. 2010.

[7] Commissioning of the Particle-flow Event Reconstruction with the first LHC collisions recorded in the CMS detector. 2010.

[8] Georges Aad et al. Observation of a centrality-dependent dijet asymmetry in lead-lead collisions at $\sqrt{s_{\mathrm{NN}}} = 2.76$ TeV with the ATLAS detector at the LHC. *Phys. Rev. Lett.*, 105:252303, 2010.

[9] Georges Aad et al. Measurement of the centrality dependence of the charged particle pseudorapidity distribution in lead-lead collisions at $\sqrt{s_{NN}} = 2.76$ TeV with the ATLAS detector. *Phys. Lett.*, B710:363–382, 2012.

[10] Georges Aad et al. Measurement of the jet radius and transverse momentum dependence of inclusive jet suppression in lead-lead collisions at $\sqrt{s_{NN}}$= 2.76 TeV with the ATLAS detector. *Phys. Lett.*, B719:220–241, 2013.

[11] Georges Aad et al. Observation of Associated Near-Side and Away-Side Long-Range Correlations in $\sqrt{s_{NN}}$=5.02 TeV Proton-Lead Collisions with the ATLAS Detector. *Phys. Rev. Lett.*, 110(18):182302, 2013.

[12] Georges Aad et al. Measurement of inclusive jet charged-particle fragmentation functions in PbPb collisions at $\sqrt{s_{\mathrm{NN}}} = 2.76$ TeV with the ATLAS detector. *Phys. Lett. B*, 739:320, 2014.

[13] Georges Aad et al. Measurement of the centrality and pseudorapidity dependence of the integrated elliptic flow in lead-lead collisions at $\sqrt{s_{\rm NN}} = 2.76$ TeV with the ATLAS detector. *Eur. Phys. J.*, C74(8):2982, 2014.

[14] Georges Aad et al. Centrality and rapidity dependence of inclusive jet production in $\sqrt{s_{\rm NN}} = 5.02$ TeV proton-lead collisions with the ATLAS detector. *Phys. Lett.*, B748:392–413, 2015.

[15] Georges Aad et al. Search for New Phenomena in Dijet Mass and Angular Distributions from pp Collisions at $\sqrt{s} = 13$ TeV with the ATLAS Detector. 2015.

[16] Kenneth Aamodt et al. Centrality dependence of the charged-particle multiplicity density at mid-rapidity in Pb-Pb collisions at $\sqrt{s_{NN}} = 2.76$ TeV. *Phys. Rev. Lett.*, 106:032301, 2011.

[17] Betty Abelev et al. Pion, Kaon, and Proton Production in Central Pb–Pb Collisions at $\sqrt{s_{NN}} = 2.76$ TeV. *Phys. Rev. Lett.*, 109:252301, 2012.

[18] Betty Bezverkhny Abelev et al. Long-range angular correlations of π, K and p in p-Pb collisions at $\sqrt{s_{\rm NN}} = 5.02$ TeV. *Phys. Lett.*, B726:164–177, 2013.

[19] Jaroslav Adam et al. Centrality dependence of particle production in p-Pb collisions at $\sqrt{s_{\rm NN}} = 5.02$ TeV. *Phys. Rev.*, C91(6):064905, 2015.

[20] L. Adamczyk et al. Jet-Hadron Correlations in $\sqrt{s_{NN}} = 200$ GeV $p + p$ and Central $Au + Au$ Collisions. *Phys. Rev. Lett.*, 112(12):122301, 2014.

[21] L. Adamczyk et al. Effect of event selection on jetlike correlation measurement in d+Au collisions at $\sqrt{s_{\rm NN}} = 200$ GeV. *Phys. Lett.*, B743:333–339, 2015.

[22] L. Adamczyk et al. Long-range pseudorapidity dihadron correlations in d+Au collisions at $\sqrt{s_{\rm NN}} = 200$ GeV. *Phys. Lett.*, B747:265–271, 2015.

[23] John Adams et al. Experimental and theoretical challenges in the search for the quark gluon plasma: The STAR Collaboration's critical assessment of the evidence from RHIC collisions. *Nucl. Phys.*, A757:102–183, 2005.

[24] A. Adare et al. Medium modification of jet fragmentation in Au + Au collisions at $\sqrt{s_{NN}} = 200$ GeV measured in direct photon-hadron correlations. *Phys. Rev. Lett.*, 111(3):032301, 2013.

[25] A. Adare et al. Spectra and ratios of identified particles in Au+Au and d+Au collisions at $\sqrt{s_{NN}} = 200$ GeV. *Phys. Rev.*, C88(2):024906, 2013.

[26] A. Adare et al. Centrality categorization for Rp(d)+A in high-energy collisions. *Phys. Rev.*, C90(3):034902, 2014.

[27] A. Adare et al. Measurement of long-range angular correlation and quadrupole anisotropy of pions and (anti)protons in central d+Au collisions at $\sqrt{s_{NN}}$=200 GeV. *Phys. Rev. Lett.*, 114(19):192301, 2015.

[28] A. Adare et al. Measurements of elliptic and triangular flow in high-multiplicity ^{3}He+Au collisions at $\sqrt{s_{NN}}$ = 200 GeV. *Phys. Rev. Lett.*, 115(14):142301, 2015.

[29] K. Adcox et al. Suppression of hadrons with large transverse momentum in central AuAu collisions at $\sqrt{s_{\rm NN}}$ = 130 GeV. *Phys. Rev. Lett.*, 88:022301, 2002.

[30] K. Adcox et al. Formation of dense partonic matter in relativistic nucleus-nucleus collisions at RHIC: Experimental evaluation by the PHENIX collaboration. *Nucl. Phys.*, A757:184–283, 2005.

[31] C. Adler et al. Disappearance of back-to-back high $p_{\rm T}$hadron correlations in central Au+Au collisions at $\sqrt{s_{\rm NN}}$ = 200 GeV. *Phys. Rev. Lett.*, 90:082302, 2003.

[32] S. Agostinelli et al. Geant 4 – a simulation toolkit. *Nucl. Inst. Meth.*, A506:250, 2003.

[33] Mark G. Alford, Krishna Rajagopal, and Frank Wilczek. QCD at finite baryon density: Nucleon droplets and color superconductivity. *Phys. Lett.*, B422:247–256, 1998.

[34] B. Alver, M. Baker, C. Loizides, and P. Steinberg. The PHOBOS Glauber Monte Carlo. 2008.

[35] M. Alvioli, L. Frankfurt, V. Guzey, and M. Strikman. Revealing âĂIJflickeringâĂİ of the interaction strength in pA collisions at the CERN LHC. *Phys. Rev.*, C90:034914, 2014.

[36] Massimiliano Alvioli, Brian A. Cole, Leonid Frankfurt, D. V. Perepelitsa, and Mark Strikman. Evidence for x-dependent proton color fluctuations in pA collisions at the LHC. 2014.

[37] Bo Andersson, G. Gustafson, G. Ingelman, and T. Sjostrand. Parton Fragmentation and String Dynamics. *Phys. Rept.*, 97:31–145, 1983.

[38] A. Andronic, P. Braun-Munzinger, and J. Stachel. Hadron production in central nucleus-nucleus collisions at chemical freeze-out. *Nucl. Phys.*, A772:167–199, 2006.

[39] A. Andronic et al. Heavy-flavour and quarkonium production in the LHC era: from proton-proton to heavy-ion collisions. 2015.

[40] Y. Aoki, Z. Fodor, S. D. Katz, and K. K. Szabo. The QCD transition temperature: Results with physical masses in the continuum limit. *Phys. Lett.*, B643:46–54, 2006.

[41] Liliana Apolinario, Nestor Armesto, and Leticia Cunqueiro. Background subtraction and jet quenching on jet reconstruction. *Nucl. Phys. A*, 910-911:433, 2013.

[42] Eric Appelt. Measurements of charged-particle transverse momentum spectra in pbpb collisions at 2.76 tev and in ppb collisions at 5.02 tev with the cms detector. PhD Thesis, May 2014.

[43] FranÃğois Arleo and Jean-Philippe Guillet. npdf generator, 2010.

[44] N. Armesto, A. Capella, A. B. Kaidalov, J. Lopez-Albacete, and C. A. Salgado. Nuclear structure functions at small x from inelastic shadowing and diffraction. *Eur. Phys. J.*, C29:531–540, 2003.

[45] Nestor Armesto. Nuclear shadowing. *J. Phys.*, G32:R367–R394, 2006.

[46] Nestor Armesto, Leticia Cunqueiro, and Carlos A. Salgado. Q-PYTHIA: A medium-modified implementation of final state radiation. *Eur. Phys. J. C*, 63:679, 2009.

[47] Nestor Armesto, Doga Can GÃijlhan, and Jose Guilherme Milhano. Kinematic bias on centrality selection of jet events in pPb collisions at the LHC. *Phys. Lett.*, B747:441–445, 2015.

[48] NÃĺstor Armesto, Hannu Paukkunen, JosÃĺ Manuel PenÃŋn, Carlos A. Salgado, and PÃŋa Zurita. An analysis of the impact of LHC Run I proton-lead data on nuclear parton densities. 2015.

[49] Michele Arneodo. Nuclear effects in structure functions. *Phys. Rept.*, 240:301–393, 1994.

[50] Peter Arnold and Shahin Iqbal. The LPM effect in sequential bremsstrahlung. *JHEP*, 04:070, 2015.

[51] Peter Brockway Arnold, Guy D. Moore, and Laurence G. Yaffe. Photon emission from quark gluon plasma: Complete leading order results. *JHEP*, 12:009, 2001.

[52] I. Arsene et al. Quark-gluon plasma and color glass condensate at RHIC? The perspective from the BRAHMS experiment. *Nucl. Phys. A*, 757:1, 2005.

[53] B. B. Back et al. Charged particle pseudorapidity density distributions from Au+Au collisions at $\sqrt{s_{NN}}$ = 130-GeV. *Phys. Rev. Lett.*, 87:102303, 2001.

[54] B. B. Back et al. Centrality and pseudorapidity dependence of elliptic flow for charged hadrons in Au+Au collisions at s(NN)**(1/2) = 200-GeV. *Phys. Rev.*, C72:051901, 2005.

[55] B. B. Back et al. The PHOBOS perspective on discoveries at RHIC. *Nucl. Phys. A*, 757:28, 2005.

[56] M. Bahr et al. Herwig++ Physics and Manual. *Eur. Phys. J.*, C58:639–707, 2008.

[57] R. Baier, Yuri L. Dokshitzer, Alfred H. Mueller, S. Peigne, and D. Schiff. Radiative energy loss and p(T) broadening of high-energy partons in nuclei. *Nucl. Phys.*, B484:265–282, 1997.

[58] Rudolf Baier, Paul Romatschke, Dam Thanh Son, Andrei O. Starinets, and Mikhail A. Stephanov. Relativistic viscous hydrodynamics, conformal invariance, and holography. *JHEP*, 04:100, 2008.

[59] A. Bazavov et al. The chiral and deconfinement aspects of the QCD transition. *Phys. Rev.*, D85:054503, 2012.

[60] JÃijrgen Berges, BjÃűrn Schenke, SÃűren Schlichting, and Raju Venugopalan. Turbulent thermalization process in high-energy heavy-ion collisions. *Nucl. Phys.*, A931:348–353, 2014.

[61] Ante Bilandzic, Raimond Snellings, and Sergei Voloshin. Flow analysis with cumulants: Direct calculations. *Phys. Rev.*, C83:044913, 2011.

[62] J. D. Bjorken. Highly Relativistic Nucleus-Nucleus Collisions: The Central Rapidity Region. *Phys. Rev.*, D27:140–151, 1983.

[63] Jean-Paul Blaizot, Fabio Dominguez, Edmond Iancu, and Yacine Mehtar-Tani. Medium-induced gluon branching. *JHEP*, 01:143, 2013.

[64] Jean-Paul Blaizot, Leonard Fister, and Yacine Mehtar-Tani. Angular distribution of medium-induced QCD cascades. *Nucl. Phys. A*, 940:67, 2015.

[65] Jean-Paul Blaizot and Yacine Mehtar-Tani. Energy flow along the medium-induced parton cascade. 2015.

[66] Jean-Paul Blaizot, Yacine Mehtar-Tani, and Marcus A. C. Torres. Angular structure of the in-medium QCD cascade. *Phys. Rev. Lett.*, 114:222002, 2015.

[67] Elena Bruna. Measurements of jet structure and fragmentation from full jet reconstruction in heavy ion collisions at RHIC. *Nucl. Phys. A*, 830:267C, 2009.

[68] Karen M. Burke et al. Extracting the jet transport coefficient from jet quenching in high-energy heavy-ion collisions. *Phys. Rev.*, C90(1):014909, 2014.

[69] Adam Bzdak, Bjoern Schenke, Prithwish Tribedy, and Raju Venugopalan. Initial state geometry and the role of hydrodynamics in proton-proton, proton-nucleus and deuteron-nucleus collisions. *Phys. Rev.*, C87(6):064906, 2013.

[70] Adam Bzdak, Vladimir Skokov, and Stefan Bathe. Centrality dependence of high energy jets in p+Pb collisions at the LHC. 2014.

[71] et. al. C. Shen. The iebe-vishnu code package for relativistic heavy-ion collisions.

[72] M. Cacciari, G. Salam, and G Soyez. The anti-k_t jet clustering algorithm. *JHEP*, 04:063, 2008.

[73] Matteo Cacciari and Gavin P. Salam. Pileup subtraction using jet areas. *Phys. Lett. B*, 659:119, 2008.

[74] Matteo Cacciari, Gavin P. Salam, and Gregory Soyez. The Anti-k(t) jet clustering algorithm. *JHEP*, 04:063, 2008.

[75] Matteo Cacciari, Gavin P. Salam, and Gregory Soyez. FastJet User Manual. *Eur. Phys. J.*, C72:1896, 2012.

[76] J. Casalderrey-Solana, J.G. Milhano, and U. Wiedemann. Jet quenching via jet collimation. *J. Phys. G*, 38:124086, 2011.

[77] Jorge Casalderrey-Solana, Daniel Fernandez, and David Mateos. Cherenkov mesons as in-medium quark energy loss. *JHEP*, 11:091, 2010.

[78] Jorge Casalderrey-Solana, Doga Can Gulhan, JosÃĺ Guilherme Milhano, Daniel Pablos, and Krishna Rajagopal. A Hybrid Strong/Weak Coupling Approach to Jet Quenching. *JHEP*, 10:19, 2014. [Erratum: JHEP09,175(2015)].

[79] Jorge Casalderrey-Solana, Doga Can Gulhan, JosÃĺ Guilherme Milhano, Daniel Pablos, and Krishna Rajagopal. Predictions for Boson-Jet Observables and Fragmentation Function Ratios from a Hybrid Strong/Weak Coupling Model for Jet Quenching. 2015.

[80] Jorge Casalderrey-Solana, Doga Can Gulhan, Jose Guilherme Milhano, Daniel Pablos, and Krishna Rajagopal. Boson-Jet Correlations in a Hybrid Strong/Weak Coupling Model for Jet Quenching in Heavy Ion Collisions. In *7th International Conference on Hard and Electromagnetic Probes of High-Energy Nuclear Collisions (Hard Probes 2015) MontrÃĺal, QuÃębec, Canada, June 29-July 3, 2015*, 2015.

[81] Jorge Casalderrey-Solana, Michal P. Heller, David Mateos, and Wilke van der Schee. From full stopping to transparency in a holographic model of heavy ion collisions. *Phys. Rev. Lett.*, 111:181601, 2013.

[82] Jorge Casalderrey-Solana, Hong Liu, David Mateos, Krishna Rajagopal, and Urs Achim Wiedemann. Gauge/String Duality, Hot QCD and Heavy Ion Collisions. 2011.

[83] Jorge Casalderrey-Solana, Yacine Mehtar-Tani, Carlos A. Salgado, and Konrad Tywoniuk. New picture of jet quenching dictated by color coherence. *Phys. Lett.*, B725:357–360, 2013.

[84] Jorge Casalderrey-Solana, Jose Guilherme Milhano, and Paloma Quiroga-Arias. Out of Medium Fragmentation from Long-Lived Jet Showers. *Phys. Lett.*, B710:175–181, 2012.

[85] Jorge Casalderrey-Solana, Jose Guilherme Milhano, and Urs Achim Wiedemann. Jet Quenching via Jet Collimation. *J. Phys. G*, 38:035006, 2011.

[86] Jorge Casalderrey-Solana, Daniel Pablos, and Konrad Tywoniuk. Jet formation and interference in a thin QCD medium. 2015.

[87] S. Catani, Yuri L. Dokshitzer, M. Olsson, G. Turnock, and B. R. Webber. New clustering algorithm for multi - jet cross-sections in e+ e- annihilation. *Phys. Lett.*, B269:432–438, 1991.

[88] S. Chatrchyan et al. The CMS experiment at the CERN LHC. *JINST*, 3:S08004, 2008.

[89] S Chatrchyan et al. Alignment of the CMS Silicon Tracker during Commissioning with Cosmic Rays. *JINST*, 5:T03009, 2010.

[90] Serguei Chatrchyan et al. Dependence on pseudorapidity and centrality of charged hadron production in PbPb collisions at a nucleon-nucleon centre-of-mass energy of 2.76 TeV. *JHEP*, 08:141, 2011.

[91] Serguei Chatrchyan et al. Dependence on pseudorapidity and centrality of charged hadron production in PbPb collisions at a nucleon-nucleon centre-of-mass energy of 2.76 TeV. *JHEP*, 08:141, 2011.

[92] Serguei Chatrchyan et al. Determination of jet energy calibration and transverse momentum resolution in CMS. *JINST*, 06:P11002, 2011.

[93] Serguei Chatrchyan et al. Observation and studies of jet quenching in PbPb collisions at nucleon-nucleon center-of-mass energy = 2.76 TeV. *Phys. Rev.*, C84:024906, 2011.

[94] Serguei Chatrchyan et al. Observation and studies of jet quenching in PbPb collisions at $\sqrt{s_{\rm NN}} = 2.76$ TeV. *Phys. Rev. C*, 84:024906, 2011.

[95] Serguei Chatrchyan et al. Centrality dependence of dihadron correlations and azimuthal anisotropy harmonics in PbPb collisions at $\sqrt{s_{NN}} = 2.76$ TeV. *Eur. Phys. J.*, C72:2012, 2012.

[96] Serguei Chatrchyan et al. Jet momentum dependence of jet quenching in PbPb collisions at $\sqrt{s_{\rm NN}}$=2.76 TeV. *Phys. Lett. B*, 712:176, 2012.

[97] Serguei Chatrchyan et al. Jet momentum dependence of jet quenching in PbPb collisions at $\sqrt{s_{\rm NN}} = 2.76$ TeV. *Phys. Lett. B*, 712:176, 2012.

[98] Serguei Chatrchyan et al. Measurement of jet fragmentation into charged particles in pp and PbPb collisions at $\sqrt{s_{\rm NN}} = 2.76$ TeV. *JHEP*, 10:087, 2012.

[99] Serguei Chatrchyan et al. Measurement of the pseudorapidity and centrality dependence of the transverse energy density in PbPb collisions at $\sqrt{s_{\rm NN}} = 2.76$ TeV. *Phys. Rev. Lett.*, 109:152303, 2012.

[100] Serguei Chatrchyan et al. Observation of sequential Upsilon suppression in PbPb collisions. *Phys. Rev. Lett.*, 109:222301, 2012.

[101] Serguei Chatrchyan et al. Studies of jet quenching using isolated-photon+jet correlations in PbPb and pp collisions at $\sqrt{s_{\rm NN}} = 2.76$ TeV. *Phys. Lett. B*, 718:773, 2012.

[102] Serguei Chatrchyan et al. Measurement of the elliptic anisotropy of charged particles produced in PbPb collisions at $\sqrt{s}_{NN}$=2.76 TeV. *Phys. Rev.*, C87(1):014902, 2013.

[103] Serguei Chatrchyan et al. Multiplicity and transverse momentum dependence of two- and four-particle correlations in pPb and PbPb collisions. *Phys. Lett.*, B724:213–240, 2013.

[104] Serguei Chatrchyan et al. Observation of long-range near-side angular correlations in proton-lead collisions at the LHC. *Phys. Lett.*, B718:795–814, 2013.

[105] Serguei Chatrchyan et al. Description and performance of track and primary-vertex reconstruction with the CMS tracker. *JINST*, 9:P10009, 2014.

[106] Serguei Chatrchyan et al. Event activity dependence of Y(nS) production in $\sqrt{s_{NN}}$=5.02 TeV pPb and $\sqrt{s}$=2.76 TeV pp collisions. *JHEP*, 04:103, 2014.

[107] Serguei Chatrchyan et al. Measurement of jet fragmentation in PbPb and pp collisions at $\sqrt{s_{\rm NN}} = 2.76$ TeV. *Phys. Rev. C*, 90:024908, 2014.

[108] Serguei Chatrchyan et al. Modification of jet shapes in PbPb collisions at $\sqrt{s_{NN}} = 2.76$ TeV. *Phys. Lett. B*, 730:243, 2014.

[109] Serguei Chatrchyan et al. Studies of azimuthal dihadron correlations in ultra-central PbPb collisions at $\sqrt{s_{NN}} = 2.76$ TeV. *JHEP*, 02:088, 2014.

[110] Serguei Chatrchyan et al. Studies of dijet transverse momentum balance and pseudorapidity distributions in pPb collisions at $\sqrt{s_{\rm NN}} = 5.02$ TeV. *Eur. Phys. J.*, C74(7):2951, 2014.

[111] Paul M. Chesler, Kristan Jensen, Andreas Karch, and Laurence G. Yaffe. Light quark energy loss in strongly-coupled N = 4 supersymmetric Yang-Mills plasma. *Phys. Rev.*, D79:125015, 2009.

[112] Paul M. Chesler, Mindaugas Lekaveckas, and Krishna Rajagopal. Heavy quark energy loss far from equilibrium in a strongly coupled collision. *JHEP*, 10:013, 2013.

[113] Paul M. Chesler and Krishna Rajagopal. Jet quenching in strongly coupled plasma. *Phys. Rev.*, D90(2):025033, 2014.

[114] Paul M. Chesler and Krishna Rajagopal. On the Evolution of Jet Energy and Opening Angle in Strongly Coupled Plasma. 2015.

[115] Paul M. Chesler and Laurence G. Yaffe. Boost invariant flow, black hole formation, and far-from-equilibrium dynamics in N = 4 supersymmetric Yang-Mills theory. *Phys. Rev.*, D82:026006, 2010.

[116] Yang-Ting Chien and Ivan Vitev. Towards the Understanding of Jet Shapes and Cross Sections in Heavy Ion Collisions Using Soft-Collinear Effective Theory. 2015.

[117] CMS Collaboration. CMS physics: Technical Design Report Volume 1: Detector Performance and Software. *CERN-LHCC-2006-001*, 2006.

[118] CMS Collaboration. Vertex fitting in the cms tracker. Technical Report CMS-NOTE-2006-032, 2006.

[119] CMS Collaboration. Electromagnetic calorimeter commissioning and first results with 7TeV data. CMS Note CMS-NOTE-2010-012, 2010.

[120] CMS Collaboration. Identification and Filtering of Uncharacteristic Noise in the CMS Hadron Calorimeter. *JINST*, 5:T03014, 2010.

[121] CMS Collaboration. Jet performance in pp collisions at $\sqrt{s}$=7 TeV. CMS Physics Analysis Summary CMS-PAS-JME-10-003, 2010.

[122] CMS Collaboration. Determination of jet energy calibration and transverse momentum resolution in cms. *JINST*, 6:P11002, 2011.

[123] CMS Collaboration. Study of Isolated photon jet correlation in PbPb and pp collisions at 2.76TeV and pPb collisions at 5.02TeV. 2013.

[124] CMS Collaboration. Measurement of dijet azimuthal decorrelations in pp collisions at 8 TeV. 2015.

[125] The ATLAS collaboration. Measurement of correlations between dijet-asymmetry and event-shape variables in Pb+Pb collisions at $\sqrt{s_{\mathrm{NN}}}$=2.76 TeV with the ATLAS detector at the LHC. 2015.

[126] J. W. Cronin, Henry J. Frisch, M. J. Shochet, J. P. Boymond, R. Mermod, P. A. Piroue, and Richard L. Sumner. Production of hadrons with large transverse momentum at 200, 300, and 400 GeV. *Phys. Rev.*, D11:3105–3123, 1975.

[127] Daniel de Florian, Rodolfo Sassot, Marco Stratmann, and Pia Zurita. Global Analysis of Nuclear PDFs. In *Proceedings, 20th International Workshop on Deep-Inelastic Scattering and Related Subjects (DIS 2012)*, pages 421–424, 2012. [,421(2012)].

[128] David d'Enterria. Jet quenching. *Landolt-Boernstein, Springer-Verlag*, Vol. 1-23A:99, 2010.

[129] Francesco D'Eramo, Mindaugas Lekaveckas, Hong Liu, and Krishna Rajagopal. Momentum Broadening in Weakly Coupled Quark-Gluon Plasma (with a view to finding the quasiparticles within liquid quark-gluon plasma). *JHEP*, 05:031, 2013.

[130] Yuri L. Dokshitzer and Dmitri E. Kharzeev. The Gribov conception of quantum chromodynamics. *Ann. Rev. Nucl. Part. Sci.*, 54:487–524, 2004.

[131] Yuri L. Dokshitzer, G. D. Leder, S. Moretti, and B. R. Webber. Better jet clustering algorithms. *JHEP*, 08:001, 1997.

[132] Adrian Dumitru, Tuomas Lappi, and Larry McLerran. Are the angular correlations in pA collisions due to a Glasmion or Bose condensation? *Nucl. Phys.*, A922:140–149, 2014.

[133] Kevin Dusling, Wei Li, and Bjoern Schenke. Novel Collective Phenomena in High-Energy Proton-Proton and Proton-Nucleus Collisions. 2015.

[134] K. J. Eskola, H. Paukkunen, and C. A. Salgado. EPS09: A New Generation of NLO and LO Nuclear Parton Distribution Functions. *JHEP*, 04:065, 2009.

[135] Kari J. Eskola, Hannu Paukkunen, and Carlos A. Salgado. A perturbative QCD study of dijets in p+Pb collisions at the LHC. *JHEP*, 10:213, 2013.

[136] K.A. Olive et al. (Particle Data Group). *Chin. Phys. C*, 38:090001, (2014) and 2015 update.

[137] Elena Ferreiro, Edmond Iancu, Andrei Leonidov, and Larry McLerran. Nonlinear gluon evolution in the color glass condensate. 2. *Nucl. Phys.*, A703:489–538, 2002.

[138] Michael Fickinger, Grigory Ovanesyan, and Ivan Vitev. Angular distributions of higher order splitting functions in the vacuum and in dense QCD matter. *JHEP*, 07:059, 2013.

[139] R. Field. Early LHC underlying event data - findings and surprises. In William Trischuk, editor, *22nd Hadron Collider Physics Symposium (HCP 2010)*, Toronto, 2010.

[140] Leonard Fister and Edmond Iancu. Medium-induced jet evolution: wave turbulence and energy loss. *JHEP*, 03:082, 2015.

[141] L. Frankfurt, V. Guzey, and M. Strikman. Leading Twist Nuclear Shadowing Phenomena in Hard Processes with Nuclei. *Phys. Rept.*, 512:255–393, 2012.

[142] R. Fruhwirth, W. Waltenberger, and P. Vanlaer. Adaptive vertex fitting. *J. Phys.*, G34:N343, 2007.

[143] Kenji Fukushima and Tetsuo Hatsuda. The phase diagram of dense QCD. *Rept. Prog. Phys.*, 74:014001, 2011.

[144] Charles Gale, Sangyong Jeon, and Bjoern Schenke. Hydrodynamic Modeling of Heavy-Ion Collisions. *Int. J. Mod. Phys.*, A28:1340011, 2013.

[145] Charles Gale, Sangyong Jeon, BjÃűrn Schenke, Prithwish Tribedy, and Raju Venugopalan. Event-by-event anisotropic flow in heavy-ion collisions from combined Yang-Mills and viscous fluid dynamics. *Phys. Rev. Lett.*, 110(1):012302, 2013.

[146] Jun Gao, Marco Guzzi, Joey Huston, Hung-Liang Lai, Zhao Li, Pavel Nadolsky, Jon Pumplin, Daniel Stump, and C. P. Yuan. CT10 next-to-next-to-leading order global analysis of QCD. *Phys. Rev.*, D89(3):033009, 2014.

[147] Donald Geesaman et al. Reaching for the horizon: The 2015 long range plan for nuclear science. 2015.

[148] Francois Gelis, Edmond Iancu, Jamal Jalilian-Marian, and Raju Venugopalan. The Color Glass Condensate. *Ann. Rev. Nucl. Part. Sci.*, 60:463–489, 2010.

[149] Steven S. Gubser. Drag force in AdS/CFT. *Phys. Rev.*, D74:126005, 2006.

[150] Steven S. Gubser, Daniel R. Gulotta, Silviu S. Pufu, and Fabio D. Rocha. Gluon energy loss in the gauge-string duality. *JHEP*, 10:052, 2008.

[151] Miklos Gyulassy and Xin-Nian Wang. HIJING 1.0: A Monte Carlo program for parton and particle production in high-energy hadronic and nuclear collisions. *Comput. Phys. Commun.*, 83:307, 1994.

[152] Y. Hatta, E. Iancu, and A. H. Mueller. Jet evolution in the N=4 SYM plasma at strong coupling. *JHEP*, 05:037, 2008.

[153] Ulrich Heinz et al. Exploring the properties of the phases of QCD matter - research opportunities and priorities for the next decade. 2015.

[154] I. Helenius, K. J. Eskola, H. Honkanen, and C. A. Salgado. EPS09s and EKS98s: Impact parameter dependent nPDF sets. *Nucl. Phys.*, A904-905:999c–1002c, 2013.

[155] Ilkka Helenius, Kari J. Eskola, Heli Honkanen, and Carlos A. Salgado. Impact-Parameter Dependent Nuclear Parton Distribution Functions: EPS09s and EKS98s and Their Applications in Nuclear Hard Processes. *JHEP*, 07:073, 2012.

[156] C. P. Herzog, A. Karch, P. Kovtun, C. Kozcaz, and L. G. Yaffe. Energy loss of a heavy quark moving through N=4 supersymmetric Yang-Mills plasma. *JHEP*, 07:013, 2006.

[157] Diego M. Hofman and Juan Maldacena. Conformal collider physics: Energy and charge correlations. *JHEP*, 05:012, 2008.

[158] John E. Huth et al. Toward a standardization of jet definitions. In *1990 DPF Summer Study on High-energy Physics: Research Directions for the Decade (Snowmass 90) Snowmass, Colorado, June 25-July 13, 1990*, 1990.

[159] Edmond Iancu and Bin Wu. Thermalization of mini-jets in a quark-gluon plasma. *JHEP*, 10:155, 2015.

[160] W. Israel. Nonstationary Irreversible Thermodynamics:A Causal Relativistic Theory. *Ann. Phys.*, 100:310, 1976.

[161] Iu. Karpenko, P. Huovinen, and M. Bleicher. A 3+1 dimensional viscous hydrodynamic code for relativistic heavy ion collisions. *Comput. Phys. Commun.*, 185:3016–3027, 2014.

[162] Kolja Kauder. Di-jet imbalance measurements in central au+au collisions at $\sqrt{s_{NN}}$ =200 gev from star, 2015. Hard Probes.

[163] Vardan Khachatryan et al. CMS Tracking Performance Results from early LHC Operation. *Eur. Phys. J.*, C70:1165–1192, 2010.

[164] Vardan Khachatryan et al. Observation of Long-Range Near-Side Angular Correlations in Proton-Proton Collisions at the LHC. *JHEP*, 09:091, 2010.

[165] Vardan Khachatryan et al. Search for narrow resonances decaying to dijets in proton-proton collisions at sqrt(s) = 13 TeV. 2015.

[166] Vardan Khachatryan et al. Correlations between jets and charged particles in PbPb and pp collisions at sqrt(s[NN])= 2.76 TeV. 2016.

[167] Vardan Khachatryan et al. Measurement of transverse momentum relative to dijet systems in PbPb and pp collisions at $\sqrt{s_{\mathrm{NN}}} = 2.76$ TeV. *JHEP*, 01:006, 2016.

[168] Nikolaos Kidonakis, Gianluca Oderda, and George F. Sterman. Threshold resummation for dijet cross-sections. *Nucl. Phys.*, B525:299–332, 1998.

[169] B. Z. Kopeliovich, J. Nemchik, A. Schafer, and A. V. Tarasov. Cronin effect in hadron production off nuclei. *Phys. Rev. Lett.*, 88:232303, 2002.

[170] P. Kovtun, Dan T. Son, and Andrei O. Starinets. Viscosity in strongly interacting quantum field theories from black hole physics. *Phys. Rev. Lett.*, 94:111601, 2005.

[171] Aleksi Kurkela and Urs Achim Wiedemann. Picturing perturbative parton cascades in QCD matter. *Phys. Lett. B*, 740:172, 2015.

[172] Aleksi Kurkela and Yan Zhu. Isotropization and hydrodynamization in weakly coupled heavy-ion collisions. *Phys. Rev. Lett.*, 115(18):182301, 2015.

[173] Hung-Liang Lai, Marco Guzzi, Joey Huston, Zhao Li, Pavel M. Nadolsky, Jon Pumplin, and C. P. Yuan. New parton distributions for collider physics. *Phys. Rev.*, D82:074024, 2010.

[174] Yue Shi Lai. New cms background subtraction, 2014. Lisbon 3rd Heavy Ion Jet Workshop.

[175] Hong Liu, Krishna Rajagopal, and Urs Achim Wiedemann. Calculating the jet quenching parameter from AdS/CFT. *Phys. Rev. Lett.*, 97:182301, 2006.

[176] I. P. Lokhtin and A. M. Snigirev. A model of jet quenching in ultrarelativistic heavy ion collisions and high-p_{T}hadron spectra at RHIC. *Eur. Phys. J. C*, 45:211, 2006.

[177] Leif Lonnblad. ARIADNE version 4: A Program for simulation of QCD cascades implementing the color dipole model. *Comput. Phys. Commun.*, 71:15–31, 1992.

[178] A. Majumder and J. Putschke. Mass depletion: a new parameter for quantitative jet modification. 2014.

[179] A. Majumder and M. Van Leeuwen. The Theory and Phenomenology of Perturbative QCD Based Jet Quenching. *Prog. Part. Nucl. Phys.*, A66:41–92, 2011.

[180] A. D. Martin, W. J. Stirling, R. S. Thorne, and G. Watt. Parton distributions for the LHC. *Eur. Phys. J.*, C63:189–285, 2009.

[181] A. D. Martin, W. J. Stirling, R. S. Thorne, and G. Watt. Heavy-quark mass dependence in global PDF analyses and 3- and 4-flavour parton distributions. *Eur. Phys. J.*, C70:51–72, 2010.

[182] Gines Martinez-Garcia. Particle rapidity distribution in proton-nucleus collisions using the proton-contributor reference frame. 2014.

[183] Yacine Mehtar-Tani. Jet structure in heavy-ion collisions: A theory overview, 2015. Hard Probes.

[184] Yacine Mehtar-Tani, Jose Guilherme Milhano, and Konrad Tywoniuk. Jet physics in heavy-ion collisions. *Int. J. Mod. Phys.*, A28:1340013, 2013.

[185] JosÃĺ Guilherme Milhano and Korinna Christine Zapp. Origins of the di-jet asymmetry in heavy ion collisions. 2015.

[186] R. B. Neufeld. Mach cones in the quark-gluon plasma: Viscosity, speed of sound, and effects of finite source structure. *Phys. Rev.*, C79:054909, 2009.

[187] Jacquelyn Noronha-Hostler, Jorge Noronha, and Miklos Gyulassy. The unreasonable effectiveness of hydrodynamics in heavy ion collisions. 2015.

[188] P. R. Norton. The EMC effect. *Rept. Prog. Phys.*, 66:1253–1297, 2003.

[189] Hannu Paukkunen, Kari J. Eskola, and Carlos Salgado. Dijets in p + Pb collisions and their quantitative constraints for nuclear PDFs. *Nucl. Phys.*, A931:331–336, 2014.

[190] Dennis V. Perepelitsa and Peter A. Steinberg. Calculation of centrality bias factors in p+A collisions based on a positive correlation of hard process yields with underlying event activity. 2014.

[191] M. Peskin and D. Schroeder. *An Introduction to Quantum Field Theory.* Westview Press, Boulder, Colorado, 1995.

[192] P. Petreczky. Lattice QCD at finite temperature. In *Proceedings, 40th Rencontres de Moriond on QCD and High Energy Hadronic Interactions: La Thuile, Aosta Valley, Italy, March 12-19, 2005*, pages 399–402, 2005.

[193] Krishna Rajagopal. The Chiral phase transition in QCD: Critical phenomena and long wavelength pion oscillations. 1995.

[194] Krishna Rajagopal. Disorienting the chiral condensate at the QCD phase transition. In *QCD phase transitions. Proceedings, 25th International Workshop on Gross Properties of Nuclei and Nuclear Excitations, Hirschegg, Austria, January 13-18, 1997*, 1997.

[195] Thorsten Renk. Parton shower evolution in a 3-d hydrodynamical medium. *Phys. Rev.*, C78:034908, 2008.

[196] Gavin P. Salam. Towards Jetography. *Eur. Phys. J.*, C67:637–686, 2010.

[197] C. A. Salgado et al. Proton-Nucleus Collisions at the LHC: Scientific Opportunities and Requirements. *J. Phys.*, G39:015010, 2012.

[198] Carlos A. Salgado. Hard Probes of the Quark Gluon Plasma in Heavy Ion Collisions. 2011.

[199] Carlos A. Salgado and Urs Achim Wiedemann. Calculating quenching weights. *Phys. Rev.*, D68:014008, 2003.

[200] Bjoern Schenke, Charles Gale, and Sangyong Jeon. MARTINI: Monte Carlo simulation of jet evolution. *Acta Phys. Polon. Supp.*, 3:765–770, 2010.

[201] Bjoern Schenke, Prithwish Tribedy, and Raju Venugopalan. Fluctuating Glasma initial conditions and flow in heavy ion collisions. *Phys. Rev. Lett.*, 108:252301, 2012.

[202] Bjorn Schenke, Sangyong Jeon, and Charles Gale. Higher flow harmonics from (3+1)D event-by-event viscous hydrodynamics. *Phys. Rev.*, C85:024901, 2012.

[203] Bjorn Schenke, Sangyong Jeon, and Charles Gale. Higher flow harmonics from (3+1)D event-by-event viscous hydrodynamics. *Phys. Rev.*, C85:024901, 2012.

[204] Alexander SCHMAH. Jet production in au+au collisions at $\sqrt{s_{NN}} = 200$ gev, 2015. Hard Probes.

[205] Chun Shen, Ulrich W Heinz, Jean-Francois Paquet, and Charles Gale. Thermal photons as a quark-gluon plasma thermometer reexamined. *Phys. Rev.*, C89(4):044910, 2014.

[206] Edward V. Shuryak. Quantum Chromodynamics and the Theory of Superdense Matter. *Phys. Rept.*, 61:71–158, 1980.

[207] T. Sjostrand and Peter Z. Skands. Transverse-momentum-ordered showers and interleaved multiple interactions. *Eur. Phys. J.*, C39:129–154, 2005.

[208] Torbjorn Sjostrand. Jet Fragmentation of Nearby Partons. *Nucl. Phys.*, B248:469, 1984.

[209] Torbjorn Sjostrand, Stephen Mrenna, and Peter Z. Skands. PYTHIA 6.4 Physics and Manual. *JHEP*, 05:026, 2006.

[210] Huichao Song. Hydrodynamic modelling for relativistic heavy-ion collisions at RHIC and LHC. *Pramana*, 84:703–715, 2015.

[211] Huichao Song and Ulrich W. Heinz. Causal viscous hydrodynamics in 2+1 dimensions for relativistic heavy-ion collisions. *Phys. Rev.*, C77:064901, 2008.

[212] J. Stachel, A. Andronic, P. Braun-Munzinger, and K. Redlich. Confronting LHC data with the statistical hadronization model. *J. Phys. Conf. Ser.*, 509:012019, 2014.

[213] George F. Sterman and Steven Weinberg. Jets from Quantum Chromodynamics. *Phys. Rev. Lett.*, 39:1436, 1977.

[214] James Stirling. Parton distribution functions, 2010. Workshop: Implications of First LHC data.

[215] V.V. Sudakov. *Sov. Phys. J.E.T.P.*, 30:65, 1956.

[216] M Swartz, D Fehling, G Giurgiu, P Maksimovic, and V Chiochia. A new technique for the reconstruction, validation, and simulation of hits in the CMS Pixel Detector. *PoS*, Vertex 2007(CMS-NOTE-2007-033):035. 37 p, Jul 2007.

[217] Yasuki Tachibana and Tetsufumi Hirano. Momentum transport away from a jet in an expanding nuclear medium. *Phys. Rev. C*, 90:021902, 2014.

[218] Wilke van der Schee, Paul Romatschke, and Scott Pratt. Fully Dynamical Simulation of Central Nuclear Collisions. *Phys. Rev. Lett.*, 111(22):222302, 2013.

[219] Hendrik van Hees, Min He, and Ralf Rapp. Pseudo-Critical Enhancement of Thermal Photons in Relativistic Heavy-Ion Collisions. *Nucl. Phys.*, A933:256–271, 2015.

[220] Marco van Leeuwen. Jet Fragmentation and Jet Shapes in JEWEL and Q-PYTHIA. In *7th International Conference on Hard and Electromagnetic Probes of High-Energy Nuclear Collisions (Hard Probes 2015) MontrÃĺal, QuÃębec, Canada, June 29-July 3, 2015*, 2015.

[221] J.M. Stewart W. Israel. Transient relativistic thermodynamics and kinetic theory. *Ann. Phys.*, 118:341, 1979.

[222] Xin-Nian Wang and Xiao-feng Guo. Multiple parton scattering in nuclei: Parton energy loss. *Nucl. Phys.*, A696:788–832, 2001.

[223] Xin-Nian Wang and Miklos Gyulassy. HIJING: A Monte Carlo model for multiple jet production in pp, pA, and AA collisions. *Phys. Rev. D*, 44:3501, 1991.

[224] K. Werner, M. Bleicher, B. Guiot, Iu. Karpenko, and T. Pierog. Evidence for Flow from Hydrodynamic Simulations of p-Pb Collisions at 5.02 TeV from ν_2 Mass Splitting. *Phys. Rev. Lett.*, 112(23):232301, 2014.

[225] Simon Wicks, William Horowitz, Magdalena Djordjevic, and Miklos Gyulassy. Elastic, inelastic, and path length fluctuations in jet tomography. *Nucl. Phys.*, A784:426–442, 2007.

[226] B. G. Zakharov. Fully quantum treatment of the Landau-Pomeranchuk-Migdal effect in QED and QCD. *JETP Lett.*, 63:952–957, 1996.

[227] Korinna C. Zapp. JEWEL 2.0.0: directions for use. *Eur. Phys. J.*, C74(2):2762, 2014.

[228] Korinna Christine Zapp. Monte Carlo simulations of jet quenching in heavy ion collisions. *Nucl. Phys.*, A855:60–66, 2011.

[229] Korinna Christine Zapp, Johanna Stachel, and Urs Achim Wiedemann. A local Monte Carlo framework for coherent QCD parton energy loss. *JHEP*, 07:118, 2011.